Numerical modeling of high performance fiber reinforced cementitious composites

Numerical Modeling of High Performance Fiber Reinforced Cementitious Composites

Martin Trüb

Institute of Structural Engineering
Swiss Federal Institute of Technology

Zürich
July 2011

Preface

The devastating sequence of earthquakes that stuck the city of Christchurch, New Zealand, from September 2010 to June 2011 is the last example of seismic events occurring in countries with a long standing earthquake engineering tradition that fortunately claimed only a limited number of lives, but where the economic and social consequences have been very significant. Therefore, in recent years strong efforts within the earthquake engineering community have been directed toward the development of high-performance structural and non-structural systems, i.e. systems that for the same seismic action are less prone to damage. In this framework a significant contribution is being provided by material scientists with the development of so-called high performance materials, and High Performance Fibre Reinforced Cementitious Composites (HPFRCC) fall within this category. These are typically characterised by significant strain ductility in tension featuring strain hardening properties which make them particularly attractive for seismic applications.

Recognising the potential of HPFRCC, the former chair of Earthquake Engineering and Structural Dynamics at the ETH Zurich, started a research project aiming at developing new high-performance structural systems incorporating HPFRCC. During a first experimental part of the project, HPFRCC structural walls were tested under static-cyclic load reversals. The HPFRCC walls showed a superior performance compared to conventional reinforced concrete walls, however, the tests also made clear that to fully exploit the possibilities offered by the new material, new analysis tools needed to be developed.

Mr. Trübs doctoral dissertation meets this challenge by developing a new and original material model for the numerical simulation of the structural-scale (macro-scale) response of HPFRCC elements. The material model is designed for plane-stress quadrilateral finite elements and uses three different approaches for the description of the mechanical material behaviour: Up to cracking strength HPFRCC is modelled by means of a linear elastic law; the ensuing hardening phase is described using a rotating smeared-crack model and upon reaching tensile strength softening of the material and strain localisation within a single discrete crack are elegantly taken into account through the capabilities of the eXtended Finite Element Method (XFEM). While the three approaches taken singularly are well know, their combination to most accurately describe the tensile force-deformation-behaviour of HPFRCC is new and Mr. Trüb was able to compellingly solve the significant challenge of transitioning from one phase of the material behaviour to the next. So far, the proposed material model has been developed for monotonic behaviour allowing the seismic analysis of structures incorporating HPFRCC materials through non-linear static procedures. However, the more general theoretical framework set up by Mr. Trüb readily allows the extension of the model to full cyclic behaviour.

Pavia, July 2011 Alessandro Dazio

Summary

High Performance Fiber Reinforced Cementitious Composites (HPFRCCs) are a relatively new and innovative class of Fiber Reinforced Cementitious Composites which have been developed mainly in the last decade. Their most prominent feature, which also distinguishes them from traditional Fiber Reinforced Concrete, is that they are strain-hardening in direct tension. By consequence HPFRCCs are a lot more ductile than "normal" concrete, which makes them suitable for a number of structural applications.

In this thesis a general framework for the numerical simulation of High Performance Fiber Reinforced Cementitious Composites on a structural scale is developed. The proposed model focuses on the tensile response of the material and it is formulated for 8-node, quadrilateral Finite Elements and plane-stress conditions. One of the model's key features is that it distinguishes three different phases of behavior which are all modeled individually. The first part of the model treats the elastic behavior of HPFRCCs and it is formulated within the traditional theory of plane-stress elasticity. The second part of the model covers the strain-hardening and multiple cracking phase. It is based on a Rotating Smeared Crack Model with uncoupled components and explicit strain decomposition. The final part of the model captures crack localization and softening. It is based on a Discrete Cohesive Crack Model which is introduced by means of the eXtended Finite Element Method (XFEM). The XFEM is a relatively new finite element technique which allows for mesh-independent crack modeling. The basic idea behind it is to enrich the Finite Element approximation space with additional discontinuous shape functions which account for localized cracks. The transition between the Smeared Crack Model and the XFEM model is done by an innovative new method which performs a "splitting" of the integration points and thereby preserves the algorithmic stability. The simulation framework is completed by an Embedded Rebar Model which complements the HPFRCC model.

The proposed model is calibrated and validated by a number of experimental tests and the simulation results show an excellent agreement with the test measurements. The overall performance of the model is very satisfactory and the different phases of behavior are captured correctly. Furthermore, the numerical model proves to be robust and it shows no instabilities or numerical deficiencies such as mesh-sensitivity, stress-locking or spurious stress transfer.

Zusammenfassung

Hochleistungs-Faserbetone (HPFRCCs) bilden eine relativ neue und innovative Klasse faserverstärkter Betone die hauptsächlich in den letzten zehn Jahren entwickelt wurden. Ihr charakteristisches Merkmal welches sie von traditionellem Faserbeton unterscheidet ist, dass sie unter direktem Zug verfestigend sind. Auf Grund dessen sind Hochleistungs-Faserbetone viel duktiler als "normaler" Beton wodurch sie für eine Anzahl von strukturellen Anwendungen in Frage kommen.

In dieser Dissertation wird ein allgemeines Modell zur numerischen Simulation des Strukturverhaltens von Hochleistungs-Faserbetonen entwickelt. Das vorgeschlagene Modell ist für achtknotige, rechteckige Finite Elemente im ebenen Spannungszustand formuliert und konzentriert sich auf das Zugverhalten des Materials. Die grosse Besonderheit des Modells ist, dass es drei verschiedene Phasen des Verhaltens unterscheidet und jede davon individuell modelliert. Der erste Teil des Modells behandelt das elastische Verhalten von Hochleistungs-Faserbetonen und es ist innerhalb der klassischen Theorie des elastischen, ebenen Spannungszustandes formuliert. Der zweite Teil umfasst die Phase der Verfestigung und der multiplen Rissbildung. Er basiert auf der Methode der rotierenden, verschmierten Rissen mit entkoppelten Komponenten und einer expliziten Zerlegung der Dehnung. Der letzte Teil des Modells erfasst die Risslokalisierung und die damit verbundene Entfestigung. Er basiert auf diskreten, kohäsiven Rissen, welche mit Hilfe der "eXtended Finite Element Method" (XFEM) eingeführt werden. Die XFEM ist eine relativ neue Methode und sie erlaubt die maschenunabhängige Modellierung von Rissen. Die grundsätzliche Idee des Vorgehens ist es, die Menge der FE-Ansatzfunktionen um eine Anzahl von diskontinuierlichen Funktionen zu erweitern um dadurch den lokalisierten Rissen Rechnung zu tragen. Der Übergang zwischen den beiden Modellen geschieht über ein neuartiges Verfahren das die Integrationspunkte zerlegt und dadurch die Stabilität des numerischen Agorithmus gewährleistet. Des Weiteren wird das Materialmodell für Hochleistungs-Faserbeton mit einem Modell für eingebettete Armierung vervollständigt.

Durch eine Anzahl von Versuchen wird das numerische Modell kalibriert und validiert und die Simulationsergebnisse stimmen gut mit den Versuchsmessungen überein. Insgesamt ist das Verhalten des Modells sehr zufriedenstellend und die unterschiedlichen Phasen des Verhaltens werden korrekt abgebildet. Zudem zeigt sich, dass das numerische Modell robust ist und keine Instabilitäten oder numerischen Defekte wie Maschenabhängigkeiten, fehlerhaften Spannungsaufbau oder unechten Spannungsübertrag aufweist.

Contents

Chapter 1

Introduction

1.1 Defining the Problem

In recent years many so-called *High Performance Materials* have been developed by material scientists. These reach from cutting-edge polymers and very resistant structural glass to *High Performance Fiber Reinforced Cementitious Composites* (HPFRCCs) and *Ultra High Performance Fiber Reinforced Cementitious Composites* (UHPFRCCs). This presents a unique opportunity for civil engineers. There is an enormous potential in exploiting the excellent mechanical properties of these new High Performance Materials and in adopting them to engineering applications. This is especially true for the new High- and Ultra High Performance Fiber Reinforced Cementitious Composites because their production and handling (with the exception of SIFCON, see Section 2.3) is similar to that of traditional construction materials and their introduction into engineering practice is straightforward. Several of them such as *Engineered Cementitious Composite* (ECC), *Slurry Infiltrated Fiber Concrete* (SIFCON), *Reactive Powder Concrete* (RPC) and *Compact Reinforced Composite* (CRC) have been the subject of some research in the past, while others such as *Hybrid Fiber Concrete* (HFC) are currently under development and their mechanical properties are still a subject of ongoing research. The main features that distinguish HPFRCCs from traditional Steel Fiber Reinforced Concrete are their strain-hardening behavior in tension and their improved ductility and tensile strength.

Motivated by the perspectives of these excellent material properties preliminary tests on HFC structural walls under static-cyclic load reversals were performed at the Institute of Structural Engineering (IBK) at the ETH Zurich. The basic idea was to develop a structural wall that would require neither shear nor confinement reinforcement but which would still exhibit an excellent seismic behavior [BDT06, DBT08]. These tests confirmed the researchers' expectations. The HFC walls were able to undergo large inelastic deformation cycles without spalling of cover concrete and without any consequential buckling of the longitudinal reinforcement or shear failure. All three tested walls were designed completely without shear or confinement reinforcement and shear transfer was assured

only by the HFC matrix and the embedded steel fibers.

One of the findings of the performed investigation was that the numerical prediction of the structural response by means of standard Finite Element software and concrete models was largely inaccurate. Furthermore, a literature review revealed that there seems to be a need for a robust and accurate numerical model for High Performance Fiber Reinforced Cementitious Composites [Li02c, Bil04]. Therefore, it was decided to develop a numerical model for High Performance Fiber Reinforced Cementitious Composites which is the main subject of this thesis.

1.2 Aim and Scope

In spite of the excellent properties of High Performance Fiber Reinforced Cementitious Composites there are very few structural applications for this class of new materials. Although some adventurous enterprises were able to realize spectacular structures – which proved to be extremely satisfactory both in terms of mechanical behavior and economical profitability – civil engineers seem to lack the necessary innovative spirit and remain captives of their traditional formation where reinforced concrete and structural steel are still most commonly viewed as the only modern construction materials. Moreover, one of the primary obstacles preventing the widespread use of HPFRCCs is the lack of reliable numerical models for this class of materials.

This led to the primary goal of this thesis, which is the development and the experimental validation of a *structural-scale numerical model for High Performance Fiber Reinforced Cementitious Composites*. This model should be robust and capture all the essential characteristics of HPFRCCs which are namely *strain-hardening* (*multiple cracking*) as well as *strain-softening* (*localized cracking*). The latter is especially important because many HPFRCCs might potentially be used in seismic applications where the simulation of the structural response up to complete failure is essential. This has to do with the earthquake-specific "load scenario" which imposes displacements rather than forces. And especially in this scenario the capability of HPFRCC elements to sustain large, inelastic deformations constitutes a major advantage over traditional, reinforced concrete.

The objective of the developed model is to assist in the efficient planning of future experiments as well as to lay the groundwork for commercial HPFRCC Finite Element models. A number of possible applications for the new model are shown in Figure 1.1. Note that the latter are in accordance with the structural systems proposed in recent research [PM05].

Based on the most likely applications for HPFRCCs the model is formulated for *plane-stress* conditions. This will allow for an appropriate representation of beams, structural walls and beam–column connections with a reasonable degree of complexity but still manageable computational effort.

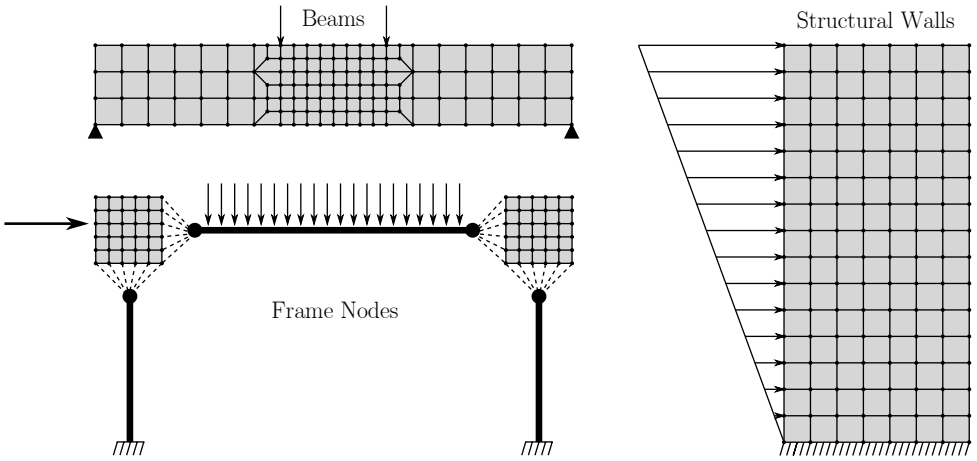

Figure 1.1: Different possible applications for the HPFRCC model

There are a number of requirements that the model should satisfy. The first of them is that the model should be linked to the physical behavior of HPFRCCs as closely as possible. This means that the different phases of behavior (i.e. multiple cracking, crack localization) should be directly reflected in the model. Also, the model input parameters should have a physical meaning.

A second requirement is that the model should use state-of-the-art Finite Element techniques, especially in respect to crack localization. The model should be insensitive to the Finite Element discretization and should not exhibit any pathological behavior at large crack openings such as *mesh-bias*, *spurious stress transfer* or *stress-locking*. Furthermore, no non-physical "regularization" parameters should be necessary. The main reason for these requirements is the fact that the existing models for HPFRCCs are prone to such problems as we will see in Section 3.4.

Finally, because the new model for HPFRCCs developed during this thesis is mainly a research tool no special emphasis is put on a commercial-grade graphical user interface. However, great care was taken that the computer code is well documented and easily extensible. The latter is achieved by following the *Object-Oriented Programming Paradigm*.

1.3 Limitations

The behavior of High Performance Fiber Reinforced Cementitious Composites is rather complex and it can be modeled on different scales with different levels of abstraction. This may range from a microscopic scale where the constituents of HPFRCCs (like aggregates and fibers) as well as their interaction are modeled explicitly, to a macroscopic scale where HPFRCCs are regarded as a continuum and single fibers cannot be discerned [Kab07].

The model that is developed in this thesis is an engineering model for the *structural-*

scale simulation of HPFRCC elements. On this scale the material is assumed to be homogeneous. This abstraction is made for both the intact HPFRCC bulk material, where microcracks are accounted for in an averaged (smeared) sense, as well as for the macroscopic cracks where the effect of the fibers is accounted for by a cohesive traction–separation law. For models on the microscopic scale where individual constituents are modeled the reader is referred to [NR95].

Another limitation of the model is that it focuses on the tensile behavior of HPFRCCs. The compressive behavior is assumed to be linear elastic. The main reason for this is the fact that the behavior of a vast majority of real world, concrete structures is limited by their tensile response [vM03]. However, the presented model can readily be extended by a nonlinear compression model such as for example the one presented in [Sir09], which is based on the theory of Plasticity.

There are also a number of limitations concerning the cohesive, localized cracks which are part of the model. The current implementation does not allow for branching or intersecting cracks, although it would be theoretically possible to do so (see [DMD$^+$00]). Furthermore, no specific focus was put on linking the material constituents (fibers, matrix) and their bond to the macroscopic cohesive law at the crack interface. An attempt to do so can be found in [Kab04, Kab07]. It was rather decided to take a phenomenological approach, which means that the cohesive traction–separation law is determined experimentally.

Finally, the model is designed for plane-stress conditions. The extension to a three-dimensional stress–strain state is theoretically possible but it is not part of this thesis.

1.4 Overview

As we have seen in Section 1.2 this thesis encompasses two major topics. On one hand there is the subject of High Performance Fiber Reinforced Cementitious Composites and on the other hand there is the field of numerical modeling of quasi-brittle materials.

In order to come up with a suitable numerical model for High Performance Fiber Reinforced Cementitious Composites the first task is therefore to fully understand the composition and behavior of Fiber Reinforced Cementitious Composites (FRCCs) and specifically HPFRCCs. For this reason *Chapter 2* will give an overview of the most important HPFRCCs and their characteristics. After summarizing the historical developments that led from FRCCs to HPFRCCs the key differences between the two materials are emphasized. Following this all modern HPFRCCs are described and for each of them some applications are given. The chapter is concluded by a comparison between the different HPFRCCs and some guidelines indicating which materials are suitable for which kinds of applications are given.

Chapter 3 is dedicated to the numerical modeling of quasi-brittle materials. First, the problem of crack localization and strain-softening is explained and the available modeling

approaches are introduced. The focus is then shifted towards the two methods that are used for the proposed HPFRCC model (namely the Smeared Crack Model and the eXtended Finite Element Method) and the theoretical basis for both of them are given. Finally, the chapter is concluded by a literature review of the currently available models for HPFRCCs and an improved model is presented.

In the next part of this thesis the new model for HPFRCCs is developed. In *Chapter 4* the basic framework for the model is set up and the formulation of the underlying isoparametric quadrilateral Finite Element is given. This serves both as a reference for further explanations and also as a short refresher of the Finite Element Method.

Chapter 5 then extends the linear, elastic model from Chapter 4 to account for the multiple cracking phase of High Performance Fiber Reinforced Cementitious Composites in tension. This is done by means of a Smeared Crack Model for strain-hardening materials.

Thereafter, the crack localization phase of the model is introduced in *Chapter 6*. Its development is explained step-by-step by first introducing a stress-free crack by means of the eXtended Finite Element Method, which is then modified to account for cohesive forces in the spirit of the Cohesive Crack Model. The chapter is concluded by defining the laws for crack propagation and explaining the issues related to the transfer of material history variables.

In order to be able to use the HPFRCC model for real world problems it has to be complemented by a model for mild steel reinforcement. This is done in *Chapter 7*.

After having explained all the necessary parts of the numerical model for HPFRCCs three applications are presented in *Chapter 8*. Starting with a simple wedge splitting test the model is then also applied to a 4-point bending test and a shear beam test. The validity of the model is verified and the computational results are compared to the experiments.

The final *Chapter 9* concludes this thesis with a summary of the most important findings and suggests a number of topics for further research.

Chapter 2

Fiber Reinforced Cementitious Composites (FRCC)

2.1 Introduction

This chapter will give a short overview of Fiber Reinforced Cementitious Composites (FRCCs). After a brief look at the history of FRCCs (Section 2.1.1) and proposing a classification in Section 2.1.3 the most important Fiber Reinforced Cementitious Composites are characterized (Sections 2.2 ff.) and some applications for each of them are presented.

2.1.1 History

Fiber Reinforced Cementitious Composites is a term commonly used for a broad class of materials. Every FRCC consists of two basic components: a cementitious base material called *matrix*, which is reinforced by steel or synthetic fibers. However, although the microscopic components of all Fiber Reinforced Cementitious Composites are more or less the same the individual materials can show a completely different macroscopic behavior as we will see in the following sections of this chapter.

The most common reason why fibers are added to a material is to improve its tensile performance i.e. its tensile ductility or its tensile strength. In fact the idea to use fibers in order to improve the tensile properties of brittle materials is old. Already in ancient times straw fibers were used to enhance the tensile strength of sun-baked bricks.

The scientific research on Fiber Reinforced Cementitious Composites reaches back to the 1960s [RM64]. In the early days of FRCCs straight steel fibers at relatively low volume contents were used to improve the mechanical properties of plain concrete. However, the early attempts were only of moderate success [vM03]. Although the fibers were able

to slightly increase the toughness of the composite its ductility remained more or less unchanged. The addition of larger volume contents of fibers was mainly prevented by workability problems.

In order to improve workability and restrict balling of fibers the quantity of cement was increased and the amount of coarse aggregates was reduced. Further improvement of the workability could be achieved by the introduction of high-range water-reducing admixtures (superplasticizers). As a direct consequence of the improved workability the volume content of fibers could also be increased. A further step towards better Fiber Reinforced Cementitious Composites was the utilization of more sophisticated fibers with better bond properties [RBCS80], as discussed in Section 2.1.2. The use of more carefully adjusted cementitious matrices with reduced amounts of coarse aggregates and carefully adjusted properties finally led to the High Performance Fiber Reinforced Cementitious Composites we know today (for term definition see Section 2.1.3).

Examples of modern Fiber Reinforced Cementitious Composites are: Slurry Infiltrated Fiber Concrete (Section 2.3), Engineered Cementitious Composites (Section 2.4), Compact Reinforced Composite (Section 2.6), Reactive Powder Concrete (Section 2.7), Multi-Scale Fiber-Reinforced Cementitious Compositesand Hybrid Fiber Concrete (Section 2.8).

For more details on the history of High Performance Fiber Reinforced Cementitious Composites the reader is referred to [Naa07] and a nice overview of Fiber Reinforced Cementitious Composites can be found in [BS92].

2.1.2 Fibers

Fibers are the key component of Fiber Reinforced Cementitious Composites. And they are used in many different shapes and sizes. The most commonly used ones are certainly steel fibers. However, there are also some Fiber Reinforced Cementitious Composites which use synthetic fibers made of Polypropylene, Polyethylene, Polyester, Carbon, Acrylic or Aramid. Asbestos fibers, which used to be popular, are now banned due to their detrimental influence on human health. Some FRCCs also use mineral and naturally occurring fiber. The latter two present somewhat of a special case and will not be treated here.

The majority of FRCCs in civil engineering applications contain steel fibers. However, today there is a vast number of different steel fibers to choose from. In contrast to the early days most modern steel fibers have some kind of deformed shape in order to improve their mechanical bond. Some common shapes are shown in Figure 2.1. They can be smooth, indented, crimped, coiled, with hooked ends, paddles, buttons or other anchorages. The most recent concept is to even use twisted fibers; a design which results in excellent performance as is presented in [Naa03].

Steel fibers generally have a length between 6 mm and 80 mm and a diameter ranging from 0.15 mm to 1.0 mm. A very common characteristic of fibers is also their *aspect ratio*. It is defined as the ratio between the length and the diameter of a fiber. The typical

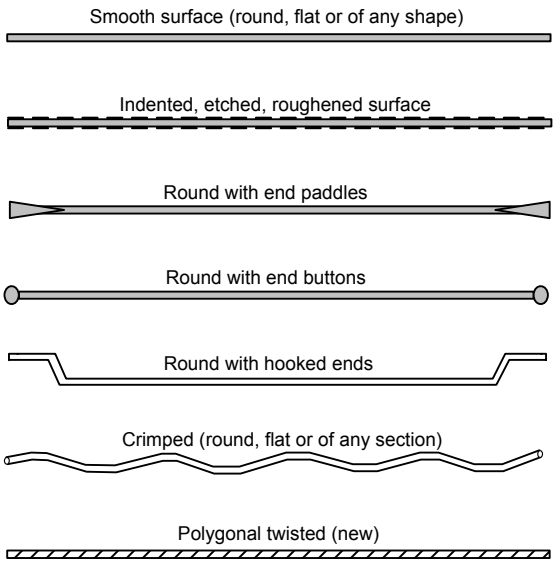

Figure 2.1: Possible shapes of steel fibers [Naa03]

aspect ratios for steel fibers range between 20 and 100. When it comes to quantities the amount of fibers in FRCCs is usually indicated by percents of total volume (vol.%) and the typical contents for Steel Fiber Reinforced Concretes are between 0.25 and 3 vol.%.

Synthetic fibers vary much more in size and their diameter can be anything from as little as 10 μm up to 0.8 mm. Their length is usually between 10 mm and 80 mm and typical quantities are 0.5 to 2 vol.%. The coarser fibers normally have an aspect ratio below 100 whereas the aspect ratio of fine fibers can easily exceed 100.

In order for a fiber to perform well in a FRCC it should have the following properties according to [Naa03]:

- A tensile strength of 2 to 3 orders of magnitude higher than that of the matrix
- A bond strength that is at least as high as the cracking strength of the matrix
- An elastic modulus that is much higher than that of the matrix (at least 3×)

Depending on the type and dimension of the fibers their effect on the mechanical properties of a FRCC can be very different. This concept will be elaborated in detail in Section 2.8.

2.1.3 Overview and Classification

In the literature there is some confusion about the terms used to describe different FRCCs. Many authors come up with new names for their material or use the same name in a different context. Therefore, this section will provide the most commonly used classification of FRCCs as proposed by [NR06] and define the terms as they are used within the

scope of this thesis.

High Performance Fiber Reinforced Cementitious Composites (HPFRCCs)

The most widely accepted proposition is to classify FRCCs by their stress–strain response in direct tension and their load–deflection response in flexure [NR06, SL04]. Following this approach a FRCC that is strain-hardening in direct tension is called *High Performance Fiber Reinforced Cementitious Composite* or HPFRCC (see Figure 2.2). One of the first stress–strain curves of a High Performance Fiber Reinforced Cementitious Composite was published by [NS79] in 1979 although it was not recognized as such at the time.

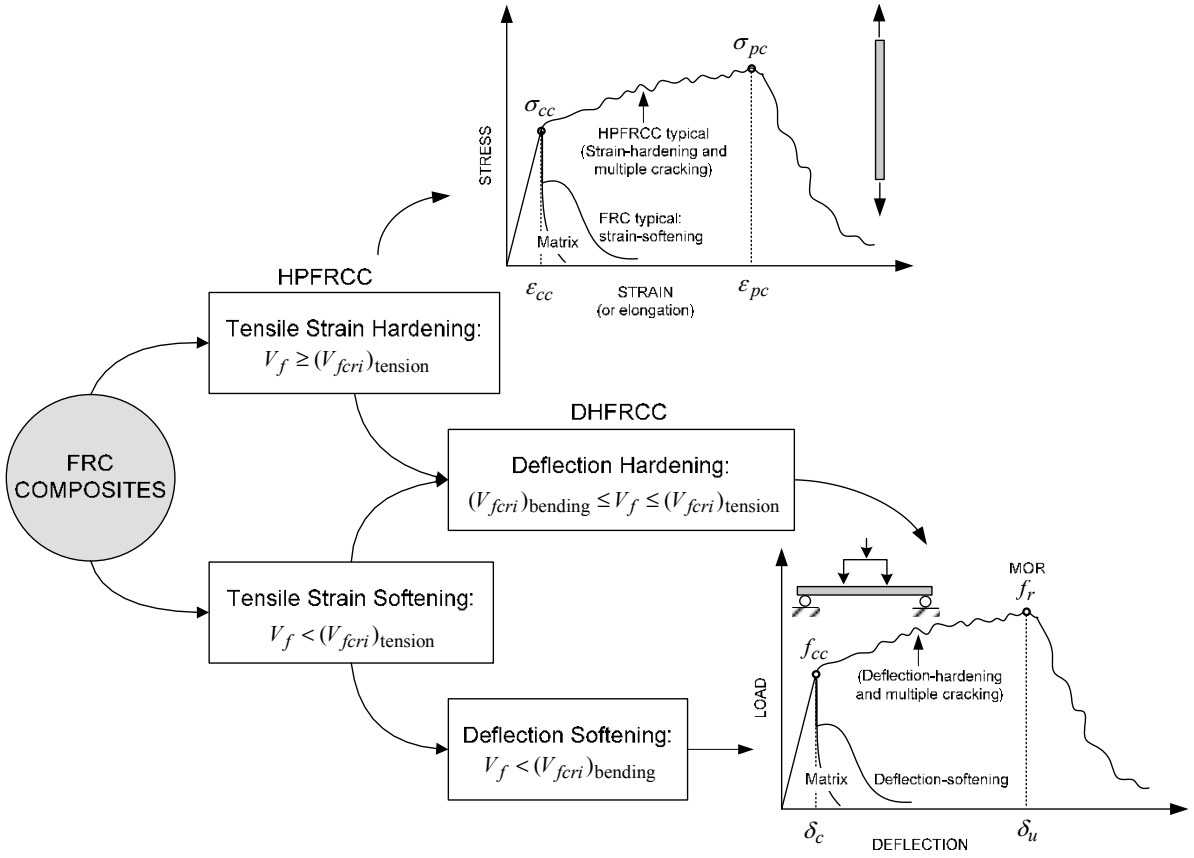

Figure 2.2: Classification of HPFRCCs taken from [NR06]

Some FRCCs are not strain-hardening in direct tension but they still show a hardening behavior in flexure. These are called *deflection-hardening* FRCCs and form the category of *Ductile Fiber Reinforced Cementitious Composites* (DFRCCs) [MM02]. However, it should be emphasized that deflection-hardening is also influenced by the dimension and cross-section geometry of a specimen and is therefore not a material property in the strict sense [SL04]. A Fiber Reinforced Cementitious Composite which falls into neither of these two categories is called deflection-softening FRCC. This thesis focuses on the numerical

modeling of *strain-hardening* Fiber Reinforced Cementitious Composites or in other words HPFRCCs.

The fundamental difference between strain-hardening composites and strain-softening composites is that the ductility of the latter is only effective on a material level and in general does not affect the overall structural ductility. Or in other words, the material does react in a ductile manner but because it is softening in tension the failure is restricted to a small area resulting in damage localization and formation of a limited fracture process zone with a large crack opening. On a structural level this kind of ductility has little benefit since the failure occurs locally and the rest of the structure remains elastic. Of course this can be remedied by the addition of structural reinforcement bars which transfer the large stresses form the localized fracture zone to other undamaged parts of the structure. Note that in some specific cases strain-softening FRCCs can improve structural ductility if they prevent shear failure and thereby produce a more ductile flexural failure.

Strain-hardening Fiber Reinforced Cementitious Composites on the other hand retard localization and lead to multiple cracking and structural ductility even without the addition of reinforcement bars. For this reason they are called High Performance Fiber Reinforced Cementitious Composites. Typical examples of HPFRCCs are *Slurry Infiltrated Fiber Concrete* (Section 2.3) and *Engineered Cementitious Composites* (Section 2.4).

Ultra High Performance Fiber Reinforced Cementitious Composites (UHPFRCCs)

Another important characteristic a Fiber Reinforced Cementitious Composite can have other than a strain-hardening behavior in tension is a very high compressive strength. The development of such concretes with extremely high compressive strengths called *Ultra High Strength Concretes* (UHSCs) was launched in the 1970s. In [Bac81] H.H. Bache presented a concept to create a concrete with an extremely high compressive strength by targeting a very dense packing of the particles in the concrete matrix. In order to achieve this goal Bache used a large amount of cement and fine particles such as silica fume. The application of superplasticizers ensured effective dense packing and sufficient workability even at low water-to-binder ratios. Bache also eliminated the coarse aggregates and used small-sized but extremely strong aggregates instead. The reason for not using large particles was that they are the major source of inhomogeneities which in turn are responsible for defects in the matrix and crack initiation. Bache called his invention *Densified Small Particle* concrete (DSP concrete), which was later commercialized under the name Densit® [Bac86]. Although considerable compressive strengths typically between 120 and 250 MPa can be obtained by this procedure DSP concrete has a significant drawback: With increasing compressive strength the brittleness increases as well.

The solution to this problem was found by adding steel fibers to the cementitious matrix, which increased the fracture energy and thereby reduced the brittleness. This idea gave birth to the materials called *Ultra High Performance Fiber Reinforced Cementitious*

Composites (UHPFRCCs). Most UHPFRCCs are also strain-hardening in tension (and therefore HPFRCCs) but they also exhibit the very high compressive strength of DSP concrete. Originating from this concept research continued following slightly different paths which led to the development of *Compact Reinforced Composites* (Section 2.6), *Reactive Powder Concrete* (Section 2.7), *Multi-Scale Fiber-Reinforced Cementitious Composites* and *Hybrid Fiber Concrete* (Section 2.8). A nice overview of UHPFRCCs can be found in [Ros00, Ros05].

As mentioned before, not all authors use the same terminology when it comes to FRCCs. For this reason the following section will define the terms as they are used in this thesis.

2.1.4 Terminology

Cementitious Materials are the binding component of a Fiber Reinforced Cementitious Composite. For our purposes these are: cement, mortar or concrete.

FRCC stands for *Fiber Reinforced Cementitious Composite* and describes a cementitious material that is reinforced by randomly oriented fibers. The FRCCs focused on in this thesis are mainly Steel Fiber Reinforced Cementitious Composites and to a smaller extent Synthetic Fiber Reinforced Cementitious Composites.

DFRCC denotes a subclass of FRCCs called *Ductile Fiber Reinforced Cementitious Composites* which are hardening under flexural conditions (deflection-hardening) but not strain-hardening in direct tension [MM02] (see also HPFRCCs). The expression *Ductile* emphasizes the fact that these composites exhibit multiple cracking which can be considered to be form of ductility.

HPFRCC is an acronym for *High Performance Fiber Reinforced Cementitious Composite*. It delimits a subclass of FRCCs which are strain-hardening in direct tension. Some authors also call them *pseudo* strain-hardening or *quasi* strain-hardening [Naa07]. Strain-hardening refers to a true material property and should not be confounded with hardening due to a redistribution of internal stresses such as within the cross-section of a beam (referred to as deflection-hardening).

UHSCs or *Ultra High Strength Concretes* are concretes with a very densely packed matrix which causes them to withstand high compressive loads. They usually contain large amounts of fly-ash and silica fume and can reach compressive strengths between 120 MPa and 250 MPa.

UHPFRCC stands for *Ultra High Performance Fiber Reinforced Cementitious Composite* and denotes a subclass of FRCCs that encompasses a number of Ultra High Strength Concretes that are reinforced with steel fibers. Many UHPFRCCs are also HPFRCCs and therefore exhibit strain-hardening and multiple cracking in direct tension.

SCC stands for *Self-Compacting Concrete* and summarizes a class of concretes which

do not need to be mechanically vibrated or compacted after casting. Their inherent flow characteristics guarantee excellent workability. Especially for FRCCs self-compacting properties are highly desirable because their workability is already negatively affected by the fibers. Also, mechanical vibration can cause unwanted segregation of the latter. SCCs are sometimes also called *Self Leveling Concretes* (SLCs).

Multiple Cracking means that a FRCC is capable of arresting the further opening of cracks by fiber bridging action and by consequence new cracks tend to form in the close vicinity. This is a fundamental property of HPFRCCs.

Localized Crack A *localized* crack is a crack at which the damage accumulates and where deformations start concentrating. It should be characterized by the crack opening displacement rather than a strain since the latter is gauge-dependent.

Brittle A material is called *brittle* if it looses its tensile strength immediately after first cracking under uniaxial tension and is no longer able to resist any stress.

Quasi-Brittle The expression *quasi-brittle* describes a material that starts softening directly after first cracking under uniaxial tension. However, quasi-brittle materials are still capable of transferring some reduced amount of stress which gradually decreases with increasing crack opening.

Ductile A *ductile* material is a material that does not fail immediately under uniaxial tension after reaching its first cracking strength. It first enters a strain-hardening phase, which is only then followed by a crack opening phase and localization of failure.

Tensile Toughness is a measure for the energy dissipation capacity of a material in tension. It is equal to the area under the stress-strain curve in uniaxial tension.

Damage Tolerance is an expression often used in conjunction with Engineered Cementitious Composites (Section 2.4). It refers to a material's insensitivity to initial defects (e.g. air inclusions) or stress concentrations (e.g. notches) [SL04].

2.2 Steel Fiber Reinforced Concrete (SFRC)

2.2.1 Material Description

The first Fiber Reinforced Cementitious Composite that was developed in the early 1960s was Steel Fiber Reinforced Concrete (SFRC). Although SFRC shows certain improvements compared to normal concrete it is not considered to be a High Performance Fiber Reinforced Cementitious Composite. SFRC consists of a normal strength concrete matrix (containing fine and coarse aggregates) which is reinforced by relatively long, straight

steel fibers at low volume contents. Sometimes the term Steel Fiber Reinforced Cementitious Composites (SFRCCs) is preferred to the term Steel Fiber Reinforced Concrete (SFRC) since it is a little more general and also includes fiber reinforced materials with no coarse aggregates such as fiber reinforced mortar. A nice overview of the material and its applications is given in [BS92, ACI73].

2.2.2 Mechanical Properties

The primary improvements of SFRC compared to normal concrete are: a higher toughness and energy absorption capacity, greater spalling and delamination resistance, improved durability characteristics through better crack control, as well as a higher ductility on the material level. However, the higher toughness and energy absorption capacity are mainly of interest for impact loading conditions and not for cyclic loading since the fiber pullout mechanism which is responsible for the higher toughness and energy absorption is not reversible.

Compared to normal concrete the tensile strength of SFRC is not improved significantly and SFRC still exhibits quasi-brittle failure (no strain-hardening). The reasons for this are the relatively low amount of fibers as well as the fact that the matrix contains too many coarse aggregates. However, compared to unreinforced concrete the failure is more ductile and exhibits a gradual softening behavior – hence the term *quasi-brittle* (see Figure 2.2 in Section 2.1.3).

2.2.3 Applications

SFRC is mainly used for non-structural elements such as pavements of industrial floors and runways, safety vaults, tunnel linings, slope stabilization and dam or pavement repairs, as well as for the repair and rehabilitation of marine structures [ACI73, Li02b, BS92]. Most of these applications either make use of the improved durability characteristics or the higher toughness of SFRC. Never the less, some structural applications have been examined and laboratory tests have shown that SFRC is able to improve the shear capacity of beams [Sha86, ND87, ND88, KEKK02, DPMW10] and reduce the necessary reinforcement detailing in beam–column connections [FPH95] (see Figure 2.3) as well as minimize bond-slip [HHK02] and prevent spalling of structural members.

A more recent application of SFRC is the strengthening of rectangular bridge piers. For circular and square bridge piers several strategies such as FRP (Fiber Reinforced Polymer) wrapping or welded steel plate jacketing are available. These methods improve the bond in the lap splice region by confining the concrete. However, they cannot be applied successfully to rectangular columns with a large aspect ratio. In [VM04a] a strengthening method for rectangular bridge piers with lap splices in the plastic hinge region is proposed. The basic idea is to replace the existing concrete cover in the lap splice region by a SFRC jacket. The authors of [VM04a] showed that by replacing the existing concrete cover with

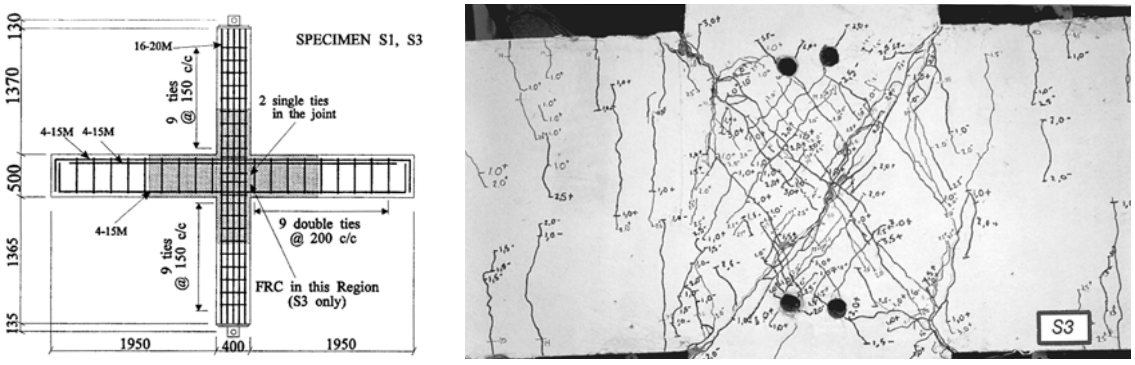

(a) (b)

Figure 2.3: FRC beam–column connection with reduced shear reinforcement [FPH95]

a FRC that has a compressive strength of 50 MPa and contains 30 mm long steel fibers (1 % Vol.) splitting failure in the lap splice region can be prevented and a more ductile behavior can be obtained.

Another interesting application of Steel Fiber Reinforced Cementitious Composites is presented in [PMCJ06]. In that paper different SFRCCs with twisted or hooked steel fibers are used in the plastic hinge region of a structural wall which is subjected to lateral load reversals. It was found that a SFRCC with 2 % vol. of hooked steel fibers allows for the total elimination of boundary confinement reinforcement and a more favorable crack distribution with no major shear-related damage.

In [CPM10a] and [CPM10b] the use of SFRCCs for punching shear resistance in slab-column connections is investigated. The first of these two companion papers focuses on a monotonically increasing load, whereas the second one considers lateral displacement reversals. It is shown that the use of a SFRCC with 1.5 % vol. of hooked steel fibers can significantly increase the punching shear strength and the rotation capacity of a slab-to-column connection.

2.3 Slurry Infiltrated Fiber Concrete (SIFCON)

2.3.1 Material Description

The experience with traditional FRCC showed that after fiber volume contents in excess of 2 % the fibers become difficult to place and create workability problems. In the early 1980s Lankard and co-workers experimented with a different procedure in order to solve this issue [LN84, Lan84, Lan85]. Instead of adding the fibers to the fresh concrete they were randomly placed in molds after which the latter were filled up with highly flowable cement slurry. This procedure allowed for much higher fiber volume contents and gave birth to a new class of FRCCs called Slurry Infiltrated Fiber Concrete or SIFCON. As

a result of the higher fiber content SIFCON shows strain-hardening behavior in direct tension and can therefore be considered to be the "oldest" HPFRCC.

The typical fibers used in SIFCON are 30 mm to 60 mm long hooked-end steel fibers with aspect ratios of 60 to 100. Traditionally they are randomly placed by hand or with a commercial fiber dispensing unit, although some attempts have also been made to artificially align the fibers [VMT96]. The unconventional casting procedure enables the use of very high fiber volume contents ranging from 5 % to 12 % and even up to 25 % if the fibers are aligned.

Because the cement matrix must infiltrate the relatively dense web of fibers it has to be highly flowable. This is achieved by using a cement based slurry which does not contain any coarse aggregates and has a w/c-ratio of about 0.3. Depending on the required compressive strength fly-ash or silica fume can also be added.

A product which is closely related to SIFCON and should be mentioned here is *Slurry Infiltrated Mat Concrete* or SIMCON. It is almost identical to SIFCON and the only difference is that instead of fibers a steel mat is placed into the mold prior to infiltration with the cement slurry.

A nice summary of SIFCON, including its mechanical properties and some applications, can be found in [BS92].

2.3.2 Mechanical Properties

Because of its high fiber content Slurry Infiltrated Fiber Concrete shows outstanding mechanical performance. Not only is it very ductile and strain-hardening in tension, but it also has an exceptionally high toughness. In fact the toughness of SIFCON and the related energy absorption capacity is 2 to 3 orders of magnitude larger than that of plain concrete.

The compressive behavior of SIFCON was investigated in [HN87]. It was found that the compressive strength can reach up to 190 MPa depending on the matrix constituents, but typical strengths are more in the order of 70 MPa. Especially the addition of silica fume was shown to increase the compressive strength. This can be explained by a denser matrix packing if silica fume is added, as was detailed in Section 2.1.3. The steel fibers also contribute to the compressive strength of SIFCON. Specifically the fibers oriented orthogonally to the principal direction of loading are responsible for a kind of "confining" effect which leads to strain-hardening in compression and a compressive strength which is approximately three times that of the pure matrix.

Being a High Performance Fiber Reinforced Cementitious Composite SIFCON shows the three distinct phases of tensile behavior typical for strain-hardening cementitious composites. In [NH89] the authors reported that they observed a prolonged phase of multiple cracking prior to reaching the peak load and the onset of softening. Because of the very high fiber content SIFCON can develop direct tensile strengths ranging between

9 MPa to 15 MPa. On average this corresponds to about twice the strength of the plane matrix. In [BS92] it is mentioned that there is a significant increase in tensile strength if a threshold of 10 % fiber volume content is surpassed. The tensile strength is also increased if a slurry containing silica fume is used since a denser matrix results in better packing of the fibers which in turn leads to an increased fiber–matrix bond (which in some cases can even lead to fiber fracture). Furthermore, hooked-end fibers perform a lot better that straight fibers and their use is strongly beneficial to the tensile strength. Another consequence of the strain-hardening behavior of SIFCON is its very high ductility. It is not uncommon that strains of 1 % to 2 % can be reached before the material starts softening.

When it comes to flexure the load carrying capacity of a SIFCON beam effectively approaches that of a traditional reinforced concrete beam. The only difference is that the softening phase of a SIFCON beam is shorter because in contrast to mild steel reinforcement bars the effective length of the fibers is limited. The flexural strength of Slurry Infiltrated Fiber Concrete is directly influenced by its high tensile strength, which leads to equivalent (elastic) flexural stresses of up to 90 MPa depending on the fiber volume content. The latter seems to be optimal at around 8 % to 10 %. In accordance with the observations made for direct tension and direct compression a denser matrix is beneficial in several ways. It increases the tensile strength on the tension side and it also increases the compressive strength on the compression side of a flexural member.

The fiber reinforcement in SIFCON is also very effective in increasing the shear strength. In fact the shear strength of Slurry Infiltrated Fiber Concrete is about three times as high as that of plain concrete. According to [BS92] experimental studies showed that SIFCON can withstand shear stresses as high as 28 MPa.

2.3.3 Applications

Due to the somewhat "extreme" nature of SIFCON and its particular fabrication method as well as the very high material costs the applications are limited to a few special cases. The most common are impact, blast and earthquake resistant structures. Some example applications are security vaults, explosive-resistant containers, the repair of structural components, bride deck and pavement rehabilitation, refractory applications and missile defense bunkers.

In the literature one can also find a couple of laboratory tests on SIFCON such as an attempt to use it for cast-in-place (CIP) beam–column joints in precast, earthquake resistant frames [NWA87] (see Figure 2.4b) or for overreinforced beams [NRF92] (see Figure 2.4a).

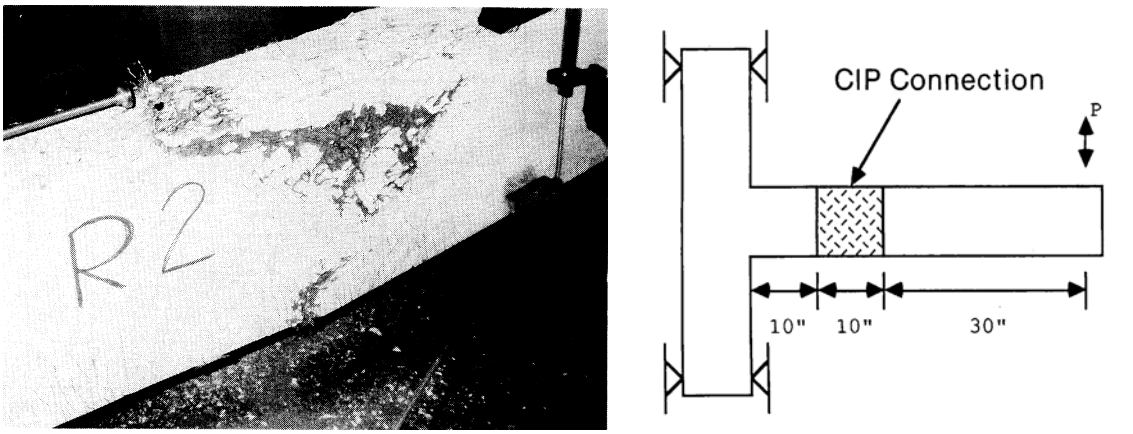

(a) Failure of a SIFCON beam [NRF92] (b) Concept of a SIFCON joint [NWA87]

Figure 2.4: Applications of SIFCON

2.4 Engineered Cementitious Composites (ECC)

Engineered Cementitious Composites (ECCs) are ultra-ductile Fiber Reinforced Cementitious Composites. Most of the research into the development of ECCs was done by Prof. Victor Li and co-workers at the University of Michigan and reaches back to the early 1990s [Li93]. The term *engineered* emphasizes the fact that ECC was engineered by using micromechanics and systematic microstructure tailoring in order to obtain certain macroscopic properties. An overview of the material and its applications can be found in [LK98, Li03, FL07].

2.4.1 Material Description

Like all other Fiber Reinforced Cementitious Composites ECCs consist of two primary components: fibers and a cementitious matrix. However, the properties of a FRCC are strongly influenced by the specific type of fiber and the matrix composition, as well as the interaction between these two components. In the case of ECCs this was taken into account by adjusting the fiber and matrix properties according to micromechanical theory in order to obtain the desired macromechanical behavior [Li03, YWYL08].

Using these micromechanical principles ECCs were specifically tailored to show an extremely ductile behavior in tension. Some authors call this behavior *pseudo strain-hardening*, referring to the post-yield strain-hardening usually exhibited by metals. Although the macroscopic performance of ECCs in the inelastic regime is very similar to the strain-hardening observed for metals the responsible micromechanical mechanism is a completely different one (hence the term *pseudo*). In metals strain-hardening is a consequence of a change in the atomic structure, whereas in ECCs it is produced by bridging of the cracks by the incorporated fibers and multiple cracking. Schematic stress-strain

curves of plain concrete, traditional FRC and an ECC are compared in the following Figure 2.5 taken from [FL07].

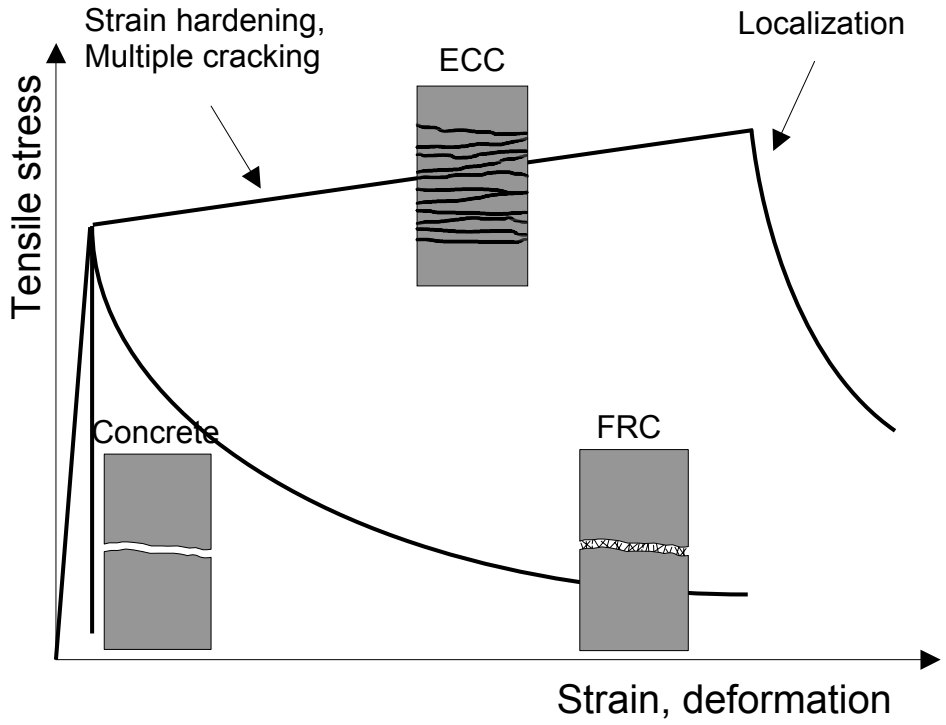

Figure 2.5: Typical stress-strain curves for concrete, traditional FRC and an ECC [FL07]

Depending on the matrix composition, the fiber geometry and the bond properties between the fibers and the matrix a certain minimal fiber volume content is necessary to achieve the typical strain-hardening behavior of HPFRCCs. If the fiber volume content is too low quasi-brittle failure, as it is exhibited by traditional FRC (see Figure 2.5), will occur. In this case damage localization and softening will set in immediately after formation of the first crack. Therefore, the fiber volume content is usually chosen just above the critical fiber volume fraction which – accounting for material heterogeneity – is typically around 2 % vol. This leads to a ductile, strain-hardening behavior but without using excessive amounts of fibers since the latter are rather expensive [Li02c].

In ECCs synthetic fibers such as UHMWPE (Ultra-High Molecular Weight Polyethylene) or PVA (Polyvinyl Alcohol) fibers with a length of 12 mm and a diameter of 0.038 mm are typically used. The difference between these two fiber types is that UHMWPE fibers show little chemical bond with the cement matrix, whereas the chemical bond strength between the PVA fibers and the matrix is considerable. Therefore, untreated PVA fibers are not adequate since they tend to get damaged by delamination during the pullout process and preliminary surface treatment in order to reduce the bond strength of the PVA fibers is therefore necessary [LWW01]. The performance of UHMWPE fibers, on the other hand, can be improved by surface treatment that increases the bond between

these fibers and the matrix, since the latter is small to begin with and the fibers have a high tensile strength [Li02a]. Engineered Cementitious Composites with UHMWPE are usually called PE-ECCs and Engineered Cementitious Composites with PVA are called PVA-ECCs.

The used fiber volume contents are usually somewhere around 2 %, but can go up to 4 %. Typically, the synthetic fibers in ECCs have a higher aspect ratio ($\approx$ 300) than the steel fibers used in Steel Fiber Reinforced Concrete. Their interfacial bond strength, on the other hand, is usually lower. As will be discussed later in this section a high aspect ratio is essential in minimizing the fiber volume content necessary for strain-hardening behavior.

The cementitious matrix in ECCs consists of a Portland cement paste or mortar with the addition of fly-ash and microsilica sand. In order to obtain the desired strain-hardening behavior described above the matrix must have a relatively low strength. If the matrix is too strong the bridging stress provided by the fibers is not high enough to produce multiple cracking. This is the case if the first cracking strength of the matrix exceeds the largest possible stress that can be transferred by the fibers.

In general no or very small sized aggregates are used for the cementitious matrix of ECCs. The main reason for this is to keep the fracture toughness of the matrix low, since a low fracture toughness is an essential condition for multiple cracking with economic fiber volume contents [LMW95, SLH$^+$09]. Adding larger aggregates would result in longer fracture paths and by consequence a higher fracture energy.

The function of the synthetic fibers is to lead to steady-state, multiple cracking which in turn is responsible for the strain-hardening behavior and large strain capacity of ECCs. In order to guarantee multiple cracking the bridging stress that can be transmitted by the fibers has to be larger than the first cracking strength of the intact matrix. This condition is referred to as the *strength criterion* for multiple cracking. It implies relatively strong fibers and a weak matrix in order to prevent premature rupture of the fibers. Also, it has to be guaranteed that the fibers are pulled out of the matrix instead of rupturing, which imposes certain limits on the fiber strength, the bond strength and the acceptable fiber length. A second less obvious criterion which has to be satisfied in order to assure steady-state cracking can be explained by using fracture mechanics. Without going into too much details, the requirement for steady-state cracking is that the crack tip propagates in a controlled manner without rupture or complete pullout of the fibers in the already formed part of the crack. Because the mode of crack propagation is governed by the energetics of crack extension this requirement for steady-state cracking is referred to as the *energy criterion* (for more information see [Li93]). If either the strength or the energy criterion is not satisfied damage localization and quasi-brittle failure will occur.

The critical fiber volume fraction which is necessary to ensure multiple cracking can be determined by following a fracture mechanics approach as described in [Li93]. It depends on the modulus of elasticity of the fibers, their aspect ratio and the interfacial bond strength between fibers and matrix. The larger these quantities are the fewer fibers are

necessary to assure multiple cracking. The fiber aspect ratio has the largest influence which explains why long and thin fibers are preferably used in PE-ECCs. The toughness of the cementitious matrix has an influence on the necessary fiber volume fraction as well. The higher the fracture energy of the matrix the more fibers are needed. A strong matrix therefore requires a large amount of fibers which is the reason why a relatively weak cement paste or mortar matrix is used for ECCs.

Most recently a number of special-purpose ECC derivatives have emerged. Apart from the characteristic high ductility these ECC materials also satisfy some specific additional requirement. They are namely: Self-consolidating ECC [KBL03], high early strength ECC and light-weight ECC [Li08].

2.4.2 Mechanical Properties

The most obvious beneficial mechanical property of ECCs is their extremely ductile strain-hardening response in tension. Experiments show that tensile strains exceeding 4 % (in extreme cases up to 8 %) can be reached before softening sets in. This means that structural elements made from ECC are extremely ductile and are able to bear very large imposed deformations such as for example those produced by an earthquake. The results of an extensive test series on ECCs including tensile, compressive and cyclic loading are reported in [KBD03, KB04].

The tensile strength of ECCs lies somewhere between 2 MPa and 8 MPa depending on the fiber volume content, the fiber type and the constituents of the matrix. For typical mix designs it is around 4 MPa. This is considerably less than the tensile strength reached by some UHPFRCCs (see Sections 2.6 and 2.8). This has to do with the low strength matrix that is necessary to obtain the desired strain-hardening behavior with low fiber volume contents.

The compressive strength of ECCs is similar to that of plain concrete (PE-ECC $\approx$ 40 MPa, PVA-ECC $\approx$ 80 MPa). However, the modulus of elasticity is typically lower ($\approx$ 20 GPa). The reason for this is that the elastic modulus of the matrix is lower than that of the aggregates used in concrete. And since ECCs contain no coarse aggregates their total elastic modulus is by consequence lower than that of traditional concrete [LMW95].

The flexural behavior of ECCs is a direct consequence of the tensile and compressive characteristics. It was investigated by [ML94] and the authors demonstrated analytically and experimentally that in third-point bending tests the modulus of rupture of ECCs can be as high as five times the first-cracking stress in direct tension. This can be verified by sectional analysis of ECC beams with a nonlinear stress–strain law in both tension and compression. Experimentally the nonlinear behavior can be observed by a spread of the multiple cracking zone with increasing load, beginning at the tension fiber and progressing towards the compression fiber up to about 90 % of the beam depth. This process leads to a redistribution of efforts within the cross-section of a beam and results in a higher structural resistance.

The experimental investigation by [LMN+94] demonstrated that Engineered Cementitious Composites with UHMWPE-fibers (Spectra) have a higher shear strength than conventional concrete, which leads to less requirements for the shear reinforcement in ECC structural members. With sufficiently high fiber volume contents the same shear strengths as with traditional shear reinforcement can be reached. However, due to the strain-hardening characteristic of ECCs the crack pattern is more favorable and exhibits a large number of distributed fine cracks instead of a single localized crack. As a result this leads to a relatively ductile failure. Because of the inherent ductility of ECCs the use of confinement reinforcement in order to increase the ductility of a failure zone is not necessary either. These two facts lead to less complicated and time consuming reinforcement detailing for PE-ECC structural members.

A very important mechanical property of ECCs is their deformation compatibility with embedded reinforcement bars [FL02b, LF99]. Because Engineered Cementitious Composites are highly ductile an ECC structure reinforced with traditional reinforcement bars exhibits a compatible deformation pattern even in the inelastic regime. As a direct consequence no bond splitting or interface delamination failure will occur. The cracking pattern and stress flow for a reinforced concrete and a reinforced ECC specimen are shown schematically in the following Figure 2.6.

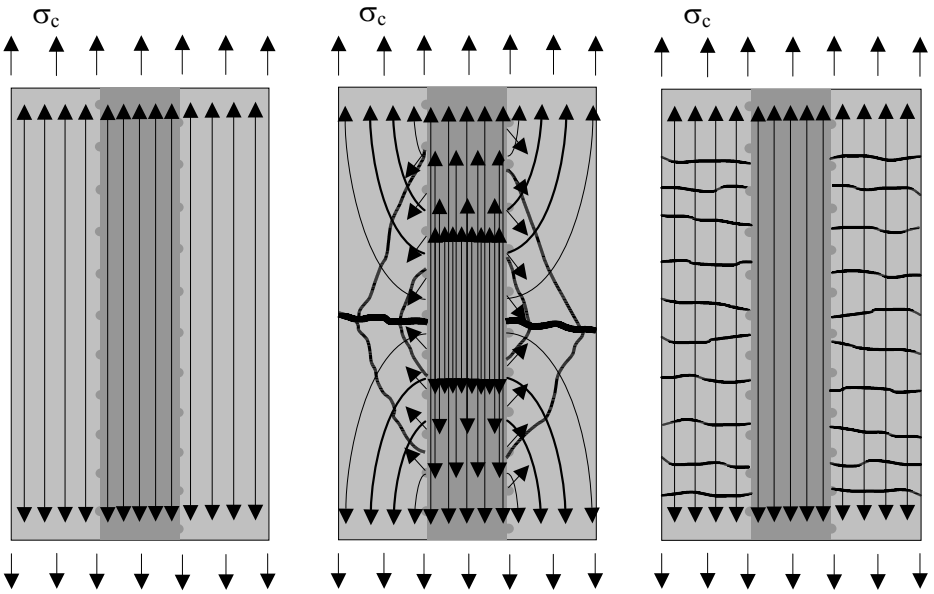

Figure 2.6: Cracking patterns in the inelastic deformation range [FL02b]

Another interesting mechanical property of ECC structural members is their energy dissipation capacity. ECCs have a higher energy dissipation capacity than plane concrete due to their multiple cracking behavior and fiber pullout. However, under cyclic loading conditions this is only of minor benefit because the process is not reversible (see Figure 2.7). More interesting is the increased energy dissipation capacity that results from the inherent spalling resistance of ECCs. Because ECCs do not spall, reinforcement bars

are somewhat stabilized against buckling which increases the likelihood that they undergo large plastic energy dissipation loops under cyclic loading [KB04, FL07].

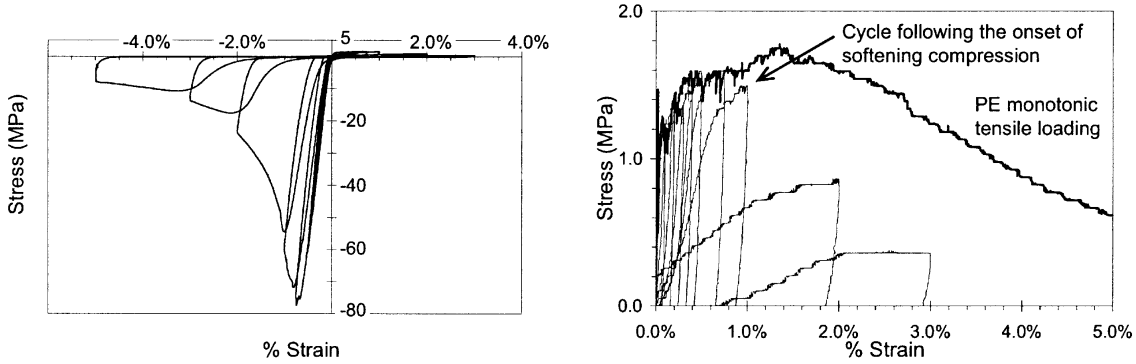

(a) Compression (b) Tension

Figure 2.7: Cyclic behavior of ECC (termed DFRCC in this study) taken from [KBD03]

2.4.3 Applications

An example of a structural application are ECC column members for earthquake resistant design. Compared to conventional reinforced concrete columns they show a more damage tolerant inelastic deformation behavior. Reinforced ECC column members are found to have a larger ductility, an enhanced energy dissipation capacity and less transverse reinforcement requirements than reinforced concrete members. They also show no spalling, interface delamination or bond splitting even at large deflections. Research on ECC column members is presented in [FL02a] and [FL03c].

Similar research was also performed on ECC column and frame members reinforced with Fiber Reinforced Polymer (FRP) rods instead of traditional steel reinforcement [FL03a, FL03b]. The main advantages of FRP rods over traditional steel reinforcement are that the residual displacements after large deformation cycles are smaller and that FRP is more resistant to corrosion than steel. The former can be of particular interest when certain service levels have to be satisfied after an earthquake. However, it should be noted that in contrast to steel rebars FRP rods do not exhibit any yielding which calls for a completely different design philosophy. Using ECCs instead of "normal" concrete in conjunction with FRP rods has similar advantages to steel reinforced ECC structures. Namely, there is no interface delamination or bond splitting which is a direct consequence of the compatible deformation between ECCs and FRP rods.

When investigating ECC shear beam members the same observations as for columns can be made [FMNS99, FSL$^+$00]. A direct comparison between a conventional shear beam and a ECC shear beam with identical reinforcement detailing is shown in Figures 2.8 and 2.9. The superior performance of the ECC beam is clearly apparent. The authors of [KWL98] investigated ECC shear beams as well and reached the same conclusions. Furthermore,

they also tested ECC shear joint connections and found that the extremely damage tolerant behavior of ECCs makes them an optimal material for such applications.

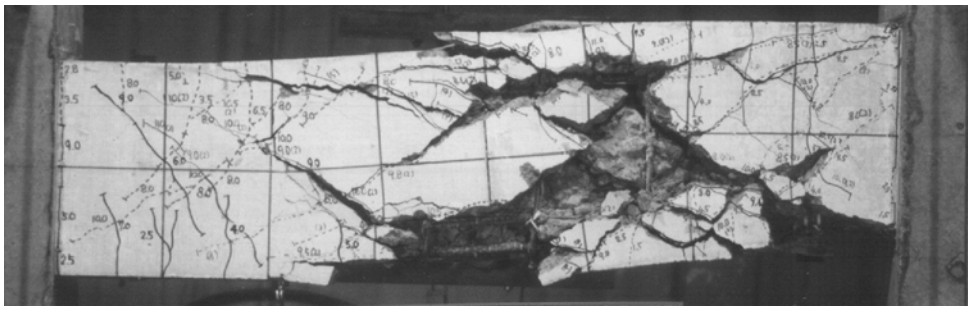

Reinforced Concrete Shear Beam

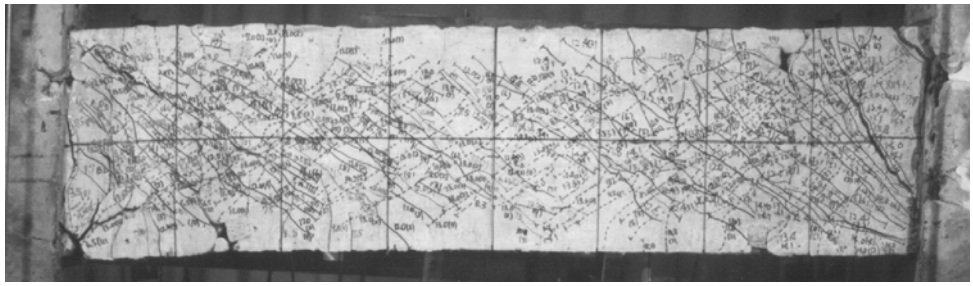

ECC Shear Beam

Figure 2.8: Comparison RC shear-beam and ECC shear-beam (from [FSL+00])

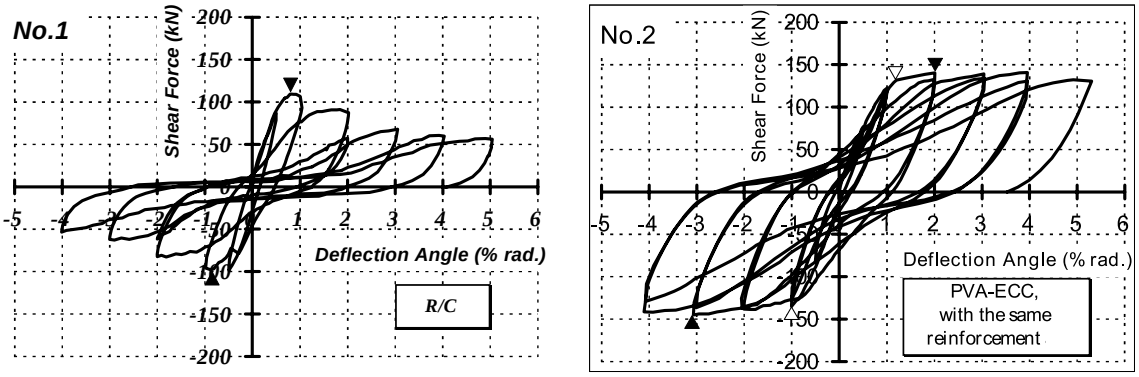

(a) RC (b) ECC

Figure 2.9: Comparison of the hysteretic response (from [FSL+00])

Another related application is the use of ECC elements (called Ductile Fiber-Reinforced Cement-Based Composite DFRCC in this study) in the plastic hinge region of segmentally precast bridge piers with unbonded posttensioning [RB03, BY04]. Again ECC elements are used for their extremely ductile behavior. The unbonded posttensioning reduces residual displacements while the ECC plastic hinge regions retain their integrity even at high deformation levels without spalling or crack localization. A schematic representation of the bridge pier system proposed by [BY04] is given in Figure 2.10a.

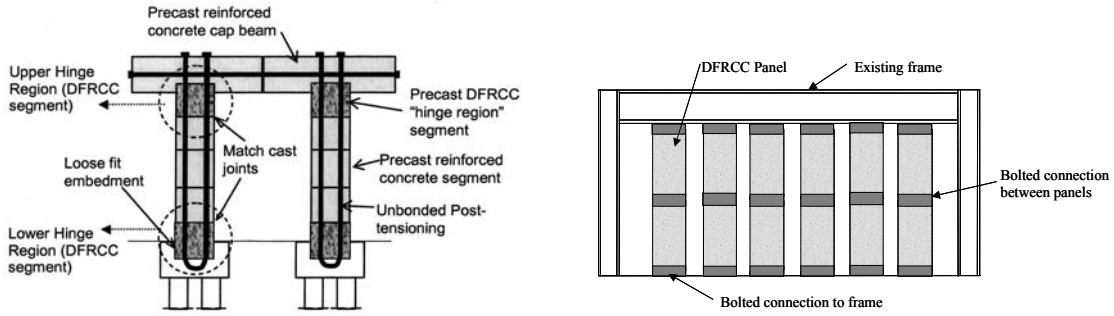

(a) Pier system by [BY04] (b) Infill panels by [KB03]

Figure 2.10: ECC applications (ECC is termed DFRCC in those studies)

Other applications strive to exploit the good energy dissipation capacities of ECC structural members. One example of this is the precast infill panel system with welded wire mesh reinforcement described in [KB02, KB03] (see Figure 2.10b). It is used for seismic retrofitting of critical buildings such as hospitals. The precast panels have good energy dissipation characteristics because ECCs prevent damage localization allowing the reinforcement to undergo large hysteretic energy dissipation cycles without risking premature failure. Other similar energy absorption devices made from an ECC are also presented in [NKKM04].

A very innovative application of ECCs is presented in [PMW00]. While investigating different connections between reinforced concrete columns and steel beams the authors also tested an ECC beam–column connection with Spectra fibers. The study shows that ECCs provide sufficient shear capacity to completely eliminate the transverse reinforcement in the joint region. An image of the beam-column joint at a high deformation level is given in Figure 2.11. The photo shows the very ductile behavior of the ECC joint exhibiting a multitude of fine cracks but no major damage even at a high deformation level (5 % story drift).

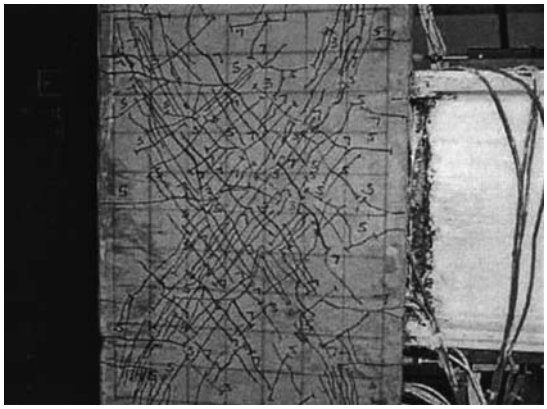

Figure 2.11: Steel-beam to ECC-column joint [PMW00]

2.5 High Performance Fiber Reinforced Concrete

2.5.1 Material Description

Beginning in the last decade the research group around Prof. Parra-Montesinos and Prof. Wight at the University of Michigan investigated several possible applications of different *High Performance Fiber Reinforced Concretes* with low fiber volume contents. Their goal was to reduce the reinforcement detailing and improve the deformation capacity of shear dominated structural members subjected to seismic loading.

In contrast to the other materials presented in this chapter there is no clear-cut definition for the term High Performance Fiber Reinforced Concrete (HPFRC). It is used here for a number of strain-hardening, fiber reinforced materials with a normal strength matrix and a low fiber volume fraction (typically in the range of 1.5% - 2%). A number of different fiber types can be used, but the most common are *Dramix*® hooked steel fibers, *Torex* twisted steel fibers and *Spectra* Ultra-High Molecular Weight Polyethylene (UHMWPE) fibers.

The synthetic Spectra fibers have a length between 15 mm and 38 mm, a diameter of 0.038 mm and a tensile strength of 2590 MPa. Torex fibers are made of twisted steel wire and have a length of 15 mm - 50 mm, an equivalent diameter between 0.2 mm and 0.7 mm and a tensile strength of 2470 MPa. Dramix® fibers are 30 mm long and are either employed in form of the normal strength ZP095 fibers with a diameter of 0.55 mm and a tensile strength of 1100 MPa, or in form of the high strength RC-80/30 fibers which have a reduced diameter of 0.38 MPa and a tensile strength of 2300 MPa.

Typically the matrix contains water, cement, fly-ash and sand but does not include coarse aggregates because the latter adversely affect the tensile performance of the composite [PM05].

2.5.2 Mechanical Properties

The mechanical properties vary between different HPFRCs but the compressive strength is typically around 50 MPa and the tensile strength ranges from 3 MPa to 5 MPa.

The most prominent feature of HPFRCs is their strain-hardening behavior in direct tension (see Figure 2.12a). What distinguishes them from most other HPFRCCs and UHPFRCCs it that they achieve strain-hardening behavior with less then 2% fibers by volume due to the strong bond (or anchorage) between the fibers and the matrix.

In compression HPFRCs show a smooth, post-peak softening behavior (see Figure 2.12b) and exhibit a large compressive strain capacity (up to 1% is possible).

From a practical standpoint the most useful features of HPFRCs are an increased shear strength which allows for a relaxation of the confinement reinforcement requirements and

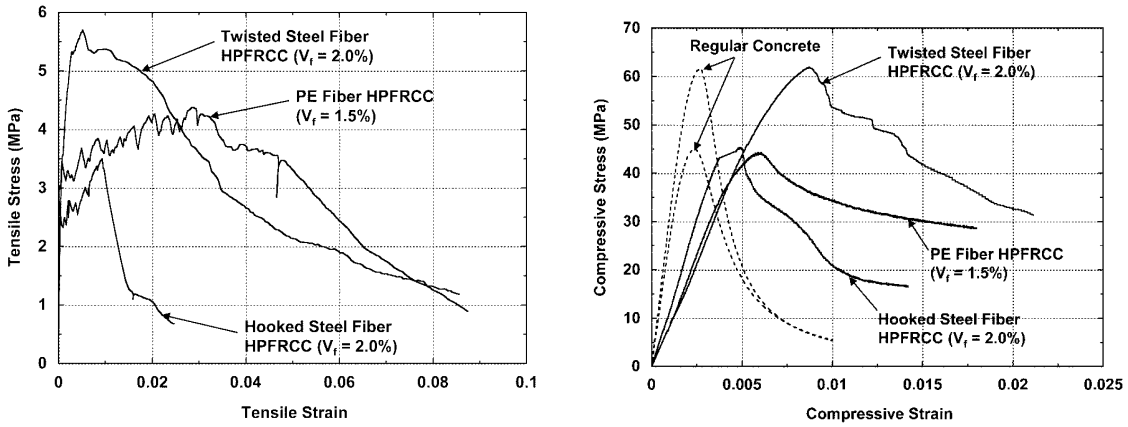

(a) Tensile behavior (b) Compressive behavior

Figure 2.12: Mechanical behavior of HPFRCs taken from [PM05]

an overall improved ductility. Some applications which make use of these mechanical properties are briefly discussed hereafter. A nice and more extensive summary can also be found in [PM05].

2.5.3 Applications

A classic type of structural elements which are subjected to large shear forces during seismic events are coupling beams. By consequence such coupling beams require rather intricate shear reinforcement detailing for seismic resistance. In [CPMW04] and [CPMW05] the authors showed that the shear reinforcement requirements can be relaxed and that the overall deformation behavior of coupling beams can be improved if HPFRC is used instead of normal reinforced concrete. Because site casting of fiber reinforced coupling beams may be difficult for the typical contractor a precast system is proposed. The cracking pattern of such a coupling beam (see Figure 2.13a) after severe cyclic loading is shown in Figure 2.13b. Note that in order to facilitate the testing procedure the coupling beam element depicted in Figure 2.13b was turned by 90 degrees.

A similar application are low-rise HPFRC structural walls [PMK04]. Here the use of HPFRC leads to walls which are characterized by an outstanding damage tolerance and a relatively large drift capacity even with considerably less shear reinforcement. The authors estimated that in their test setup about 70 % of the total shear force was carried by the High Performance Fiber Reinforced Concrete.

In [PMPC05] the use of HPFRC for beam–column joints is presented. The study shows that the shear capacity of the joint region and the bond strength between the reinforcement and the cementitious matrix can be increased if HPFRC is used instead of conventional concrete. This confirms the findings from [CNPM09] which indicate that the bond behavior between rebars and an HPFRC matrix is noticeably better than between

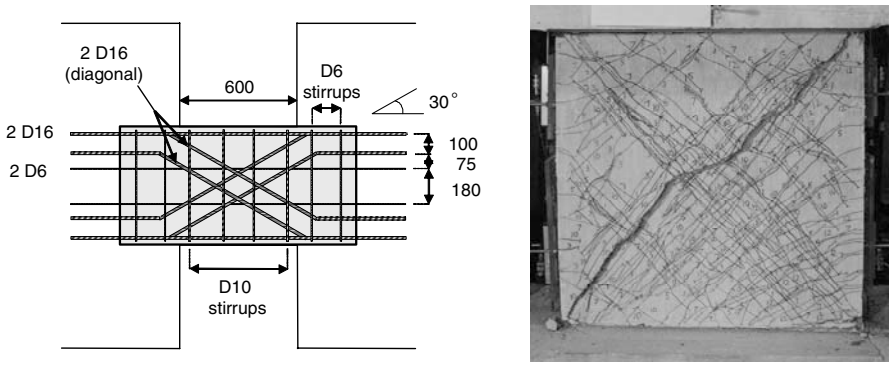

(a) Design (b) Cracking Pattern

Figure 2.13: HPFRC coupling beam taken from [CPMW04], all dimensions in [mm]

rebars and conventional concrete. Another advantage is that the transverse and the confinement reinforcement in the joint region can be reduced significantly. An image of the beam-column joint investigated in [PMPC05] at a high deformation level is given in Figure 2.14.

Figure 2.14: HPFRC beam–column joint [PMPC05]

A final application for HPFRC are cyclically loaded flexural members as presented in [PMC07]. The investigation showed that polyethylene HPFRC (Spectra fibers) flexural members with no transverse steel reinforcement exhibit stable hysteretic behavior with a large drift capacity and superior damage tolerance compared to traditional concrete. Furthermore, the HPFRC is effective in providing lateral support for the longitudinal reinforcement and it is able to sustain significant shear stress levels.

2.6 Compact Reinforced Composites (CRC)

In the early 1980s H.H. Bache from Portlands Cement and Concrete Laboratory in Aalborg, Denmark discovered that by adding large amounts of small fillers (like fly-ash and

silica fume) to a cementitious matrix the latter's density can be increased significantly. By consequence this procedure leads to a concrete with an extremely high compressive strength which H.H. Bache called *Densified Small Particle* (DSP) concrete [Bac81, Bac86]. One of the drawbacks of DSP concrete is that with its higher compressive strength its brittleness is magnified as well. In order to reduce this brittleness H.H. Bache added short steel fibers to the cementitious matrix which gave birth to an Ultra High Performance Fiber Reinforced Cementitious Composite he called *Compact Reinforced Composite* (CRC) [Bac88, Bac90, Bac95].

2.6.1 Material Description

In CRCs an extremely high amount of short stiff steel fibers is used. The first mixes of CRCs contained 6 mm long fibers ($\varnothing$ 0.15 mm) at volume contents between 5 % and 10 %.

The cementitious matrix of CRCs has all the characteristics of the already discussed DSP concrete. More specifically, these are an extremely dense packing of particles (see Figure 2.15a) which is achieved by adding large amounts of microsilica (up to 20 % vol.) and a low w/b-ratio of 0.16 to 0.18 thanks to the use of superplasticizers.

The aggregates used in CRCs need to be strong and small. If the strength of the aggregates is not sufficient fracture surfaces will pass through them which would mean that the high strength of the cementitious binder is not exploited to its maximal extent. Using small sized aggregates is based on the fact that cracks in concrete are always initiated by inhomogeneities where local stress concentrations can occur. And the smaller the aggregate grains the better the homogeneity of the matrix. For these two reasons hard and small aggregates such as quartz sand or calcined bauxite are usually used.

As already mentioned, an extremely high quantity of short stiff steel fibers is employed in CRCs. The fibers mainly have an influence on the tensile strength and ductility of CRCs on a material level. However, the fibers are not able to improve the ductility on a structural level significantly. The use of short fibers leads to a high tensile strength of the composite because the fibers have a similar size and spatial distribution as microcracks which enables them to effectively arrest microcrack propagation.

Maybe, at this point it is appropriate to emphasize the difference between ductility on a *material* level and ductility on a *structural* level. When talking about ductility on a material level the zone of failure is described. A cementitious composite is ductile on a material level if it fails gradually and not instantaneously (brittle failure) after formation of a crack. The material ductility can for example be visualized by tracing the stress vs. crack opening graph of a specimen loaded in tension. A material that provides structural ductility on the other hand is one that, in addition to exhibiting material ductility does not show localization of damage after the first crack is formed. This means that the inelastic deformation will not only occur in a small region but will have a tendency to spread within a structural element. A FRCC can only show inherent structural ductility

if it is strain-hardening. However, if structural ductility is not an inherent property of the cementitious composite itself it can be provided by using the traditional concept of reinforcement bars. This is exactly what is done in CRC structural elements.

The strain-hardening phase of CRCs is not very pronounced which means that CRC structural elements show little ductility on a structural level. In other words the short fibers in CRCs are very effective in producing a high tensile strength and ductility on a material level but they cannot improve the ductility on a structural level. For this reason reinforcement bars are incorporated into CRC structural members. Because the fibers create a locally ductile fracture zone it is possible to use very high reinforcement ratios and more closely spaced reinforcement bars in CRCs than in traditional concrete. Typically a reinforcement ratio of 10 % to 20 % is used. The short steel fibers create ductile fracture zones whereas the structural reinforcement bars distribute the crack zone deformations over the entire body of the element. The improvement in flexural strength going from a typical reinforced concrete beam to a heavily reinforced CRC beam is shown in Figure 2.15b.

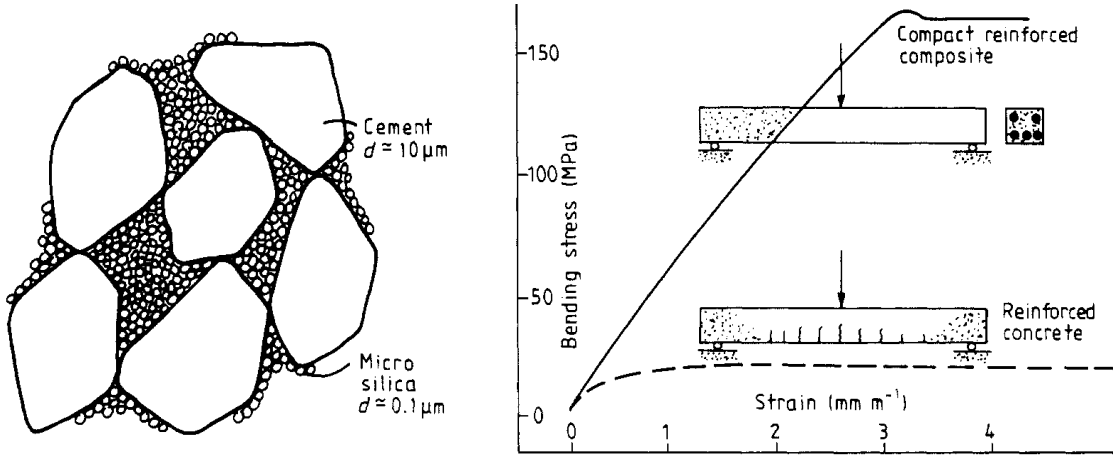

(a) Dense particle packing (b) Bending stress comparison

Figure 2.15: Characteristics of CRC [Bac88]

The reinforcement is also used during the compactation process. In CRCs the fresh concrete is normally vibrated by applying high-frequency vibration directly onto the reinforcement.

2.6.2 Mechanical Properties

Probably the most interesting mechanical property which distinguishes CRCs form other Fiber Reinforced Cementitious Composites is their relatively high direct tensile strength. Depending on the fiber content the maximum tensile strength can range from 6 MPa to 15 MPa. Crack initiation will usually start at a tensile stress of about 6 MPa to 7 MPa.

As expected, CRCs have the high compressive strength of Ultra High Strength Concretes such as DSP concrete. Depending on the quality of the aggregates and on the thermal curing conditions the compressive strength reaches from 150 MPa to 400 MPa. A compressive strength of 150 MPa is achieved with quartz aggregates whereas the 400 MPa are reached when using calcined bauxite and heat curing. The typical module of elasticity of CRCs is about 45 GPa.

One of the reasons why the combination of CRCs and high reinforcement contents is so successful are the good bond characteristics between the fiber reinforced matrix and the reinforcement bars. There are several reasons for this. The first is the high density of the matrix. The significant content of silica fume results in large contact surfaces and by consequence large frictional forces. Secondly, the short steel fibers provide ductility and control crack formation in the anchorage zone of the reinforcement bars. In fact, when using a high volume content of fibers (6 %) the material ductility of CRCs is sufficient to give the matrix approximately the same strain capacity before crack localization as mild steel has at yielding. This means that up to yielding of the longitudinal reinforcement there is no visible cracking. The good bond characteristics result in shorter rebar anchorage lengths which are typically between 5 and 10 bar diameters [AKL00]. It is also due to these good bond properties that the high reinforcement ratios used in CRCs are possible.

Because of the high tensile strength CRCs also have a high shear strength (see Section 2.9.1). In fact, in many structural applications the shear reinforcement can be omitted and the shear stresses are carried by the fiber reinforced matrix alone [Bac90].

Another important property of CRCs is their exceptional durability. The very dense matrix and the lack of capillarity lead to an extremely low permeability. This means that there is practically no corrosive agent transport and freezing–thawing problems can be eliminated. As a result CRC elements rarely have a concrete cover of more than 10 mm even if they are exposed to an aggressive environment.

CRC structural members have a problem in respect to their fire resistance. Because the matrix is so dense the water inside the pores cannot escape and high vapor pressures might build up. This can lead to spalling or explosive failure of CRC elements if they are exposed to high temperatures.

2.6.3 Applications

A commercial application of CRCs is *JointCast* [AKL00, Aar08]. The concept of JointCast is to exploit the good bond characteristics and the high strength of CRCs for in-situ cast joints between precast elements. JointCast is used for the assembly of moment resisting frames from precast elements and for joining precast slabs. The following Figure 2.16 shows two images of such a joint between precast floor slabs.

Although the CRC joints seem promising the major field of CRC applications are thin, precast structural elements such as staircases, balconies or bridge deck panels [KB05].

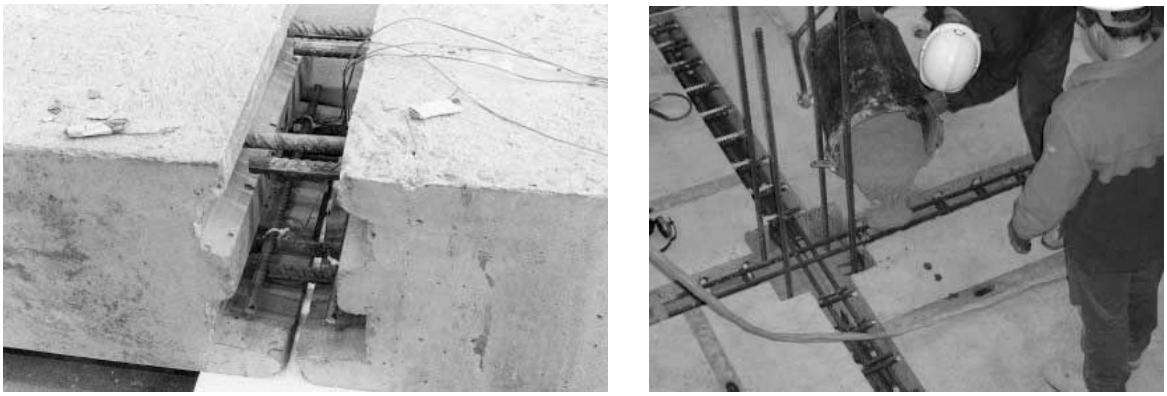

(a) (b)

Figure 2.16: Precast column and floor slabs are joined in-situ by JointCast [CRC]

These elements make use of the very high flexural strength of CRCs which allows them to be extremely thin and architecturally elegant. As of late, there has also been an increase in demand for CRC beams and columns as mentioned in [Aar08]. Another application of CRCs is their use for impact resistant structures such as defense shelters, gas tanks, nuclear reactor containment shields and crash barriers [BBA02].

2.7 Reactive Powder Concrete (RPC)

Reactive Powder Concrete (RPC) is an Ultra High Performance Fiber Reinforced Cementitious Composite that was developed in the 1990s by the French company Bouyges. RPC has many similarities with CRCs because both materials share the basic principles that are used for DSP (Densified Small Particle) concrete (see Section 2.6). However, from the common starting point of DSP concrete, CRCs and RPC evolved in two different directions. In CRCs the main improvement compared to DSP concrete is a higher tensile strength whereas in RPC it is a higher ductility. The two concepts that lead from DSP concrete to RPC are the following: Firstly the ductility of the concrete matrix is improved by the addition of medium sized straight steel fibers and secondly the compressive strength of the matrix is improved by applying heat and pressure treatment [RC95].

2.7.1 Material Description

The fibers used in RPC are straight steel fibers that have about the same diameter ($\varnothing$ 0.15 mm) as those used in CRCs but they have a higher aspect ratio. Their typical length is around 13 mm. Due to their larger size these fibers cannot be used at the same amounts as those in CRCs because workability considerations limit the fiber volume content to approximately 3 %. Therefore, the standard RPC mixes contain between 1.5 % and 3 % fibers by volume.

Needless to say, that the cementitious matrix of RPC shows the same characteristics as all the other Ultra High Strength Concretes such as a dense packing of particles, a very low w/b-ratio (0.08 for the densest RPC mixes) and a homogeneous matrix containing small but hard aggregates such as quartz sand as well as a large amount of silica fume. In addition to these "standard" matrix characteristics of UHPCs, the matrix strength of RPC is further improved by mechanical and thermal treatment during curing.

The mechanical treatment basically consists of applying pressure to the freshly cast concrete. This is shown to improve the RPC matrix because it increases its density by expelling entrapped air and excess water and consequently results in a higher compressive strength. Because applying pressure is a complicated procedure it is only used for precast elements that are fabricated under controlled laboratory conditions.

Normally RPC is also subjected to post-set thermal treatment. The heat treatment improves the microstructure of the hydrates by accelerating the pozzolanic reaction and increasing the amount of bound water [CMF95]. This can be more or less effective depending on the temperature that is applied.

Because the fibers in RPC are longer than those in CRCs they can improve the ductility on a larger scale. Having a larger aspect ratio they show better bond with the surrounding matrix and because of their greater length they have an effect on wider cracks. This means that even after formation of the first macrocrack strain-hardening can still be present leading to structures with sufficient ductility without the need for large amounts of conventional reinforcement like in CRCs. The drawback is that due to workability problems the medium sized fibers cannot be used in the same quantities as the short steel fibers in CRCs. By consequence the tensile strength of RPC is not as high as that of CRCs.

Lately the borders between different UHPFRCCs have started blurring since certain concepts which distinguished a specific Ultra High Performance Fiber Reinforced Cementitious Composite are also used for others and vice versa. For example there are mixes of CRCs that include medium sized fibers such as those in RPC and RPCs that are improved by the addition of short steel fibers.

One of the most recent derivatives of RPC is DUCTAL®, an Ultra High Performance Fiber Reinforced Cementitious Composite that was developed in a joint-venture by the French companies Bouygues, Lafarge and Rhodia. Although DUCTAL® is based on the original RPC recipe several improvements have been made. The most important are chemical surface treatment of the fibers in order to improve their bond with the surrounding matrix and the addition of organic fillers and mineral microfibers in order to increase the fracture energy of the matrix [ODA00, CRSQ03].

2.7.2 Mechanical Properties

There are basically two possible versions of RPC. The first one goes by the name RPC-200 and is suitable for use on a construction site. The other one called RPC-800 can only be produced under laboratory conditions and is used for precast elements [RC95]. The reasons why RPC-800 cannot be produced on a construction site are that it requires a compacting pressure during setting and heat treatment at high temperatures (250 to 400 °C) which are both difficult to apply in-situ.

RPC's most outstanding mechanical property is its extremely high compressive strength which is not rivaled by any other UHPFRCC. The compressive strength of RPC-200 is typically between 170 MPa and 230 MPa. RPC-800 can achieve compressive strengths of 490 MPa to 680 MPa with matrices containing quartz aggregates and even 650 MPa to 810 MPa when steel aggregates are used [DRB96, RC95]. Because of the high density of the concrete matrix the modulus of elasticity generally exceeds 50 GPa and can reach 75 GPa for the highest densities.

Compared to CRCs, RPC has a lower direct tensile strength. Typically it is between 8 MPa and 11 MPa. Because fibers are added in smaller quantities in RPC they cannot be as effective in arresting the propagation of microcracks as the short fibers in CRCs. Although the tensile strength is improved in comparison to conventional concrete the major improvement of adding fibers to RPC is not in terms of strength but in terms of ductility. The direct tension test presented in [CRSQ03] per example shows that DUCTAL® retains its tensile strength even at crack openings above 0.3 mm.

RPC and CRCs obviously share the same good durability characteristics since they have a similar high density matrix. The lack of capillarity prevents corrosive agent transport and freezing - thawing problems [RAS96].

2.7.3 Applications

Due to the fiber reinforcement of the matrix and the thereby provided ductility RPC structures without mild steel reinforcement can be envisioned. The large discrepancy between RPC's extraordinary compressive strength and its limited tensile strength can be remedied by prestressing techniques. The secondary tensile stresses due to shear can be carried by the inherent tensile strength of the fiber reinforced matrix which allows for the total omission of mild reinforcement [AB04]. Following this concept very light and slender structures can be constructed.

One possible example of this are very thin and delicate structures such as footbridges. The high strength of RPC and the lack of mild reinforcement make such a structure extremely light and easy to construct providing a serious alternative to steel structures. The Sherbrooke RPC footbridge in Canada was the first industrial structure of this kind

[ALAR98]. Two other examples of slender footbridges constructed with the RPC derivative DUCTAL® are given in the following Figure 2.17.

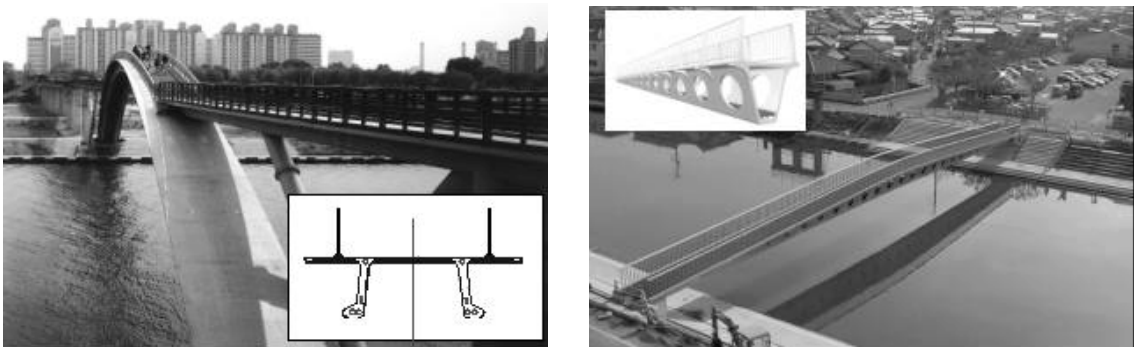

(a) Seonyu footbridge in Korea (b) Sakata Mirai footbridge Japan

Figure 2.17: Footbridges made of DUCTAL® [AB04]

DUCTAL® and RPC have also been used for long span beams and girders [AB04, VFG06]. When these elements are used repetitively in large structures the high strength and good durability characteristics make DUCTAL® a cost-effective solution.

The use of RPC for columns was investigated in [MF08] and led to the conclusion that RPC successfully prevents spalling of cover concrete and buckling of the longitudinal reinforcement which suggests that the elimination of tie reinforcement in RPC columns could be possible. Another application for RPC mentioned in the literature are impact resistant military structures (especially for RPC-800) [RC95] and safes [SMK05].

2.8 Hybrid Fiber Concrete (HFC)

Hybrid Fiber Concrete (HFC) is an Ultra High Performance Fiber Reinforced Cementitious Composite that was recently developed by Prof. J.G.M. van Mier from the ETH Zürich and Prof. J.C. Walraven from the Delft University of Technology [MWvM03]. The term *Hybrid* indicates that a mix of different fiber geometries is used. In contrast to traditional fiber reinforced concrete where adding fibers only leads to a higher toughness and better durability characteristics (less shrinkage and crack formation after curing) a well balanced mixture of HFC can significantly improve the strength of a structural element. By consequence HFC could be applied to a whole new field of structural applications. A good overview of the development of HFC including the micromechanical concepts behind it can be found in [vM03].

HFC can be seen as a synthesis of the three high performance materials DSP concrete, CRC and RPC because it combines the high compressive strength of DSP concrete with the high tensile strength of CRCs and the ductility of RPC. The combination of these three mechanical properties can be achieved by incorporating the concepts which are at

their origin into the design of HFC. This means that an extremely dense matrix like the one in DSP concrete is used. In addition short fibers like those in CRCs are added and they are complemented with longer fibers such as those employed in RPC.

2.8.1 Material Description

Hybrid Fiber Concrete is a very ductile Ultra High Performance Fiber Reinforced Cementitious Composite with a high compressive strength and a high tensile strength which exhibits strain-hardening in direct tension. Its development is nicely presented in [MWvM03]. The authors experimented with a High Performance Steel Fiber Reinforced Concrete that contained 6 mm long ($\varnothing$ 0.16 mm) straight, 13 mm long ($\varnothing$ 0.2 mm) straight and 60 mm long ($\varnothing$ 0.71 mm) hooked-end fibers. The fiber volume contents were between 1 % and 4 % and different fiber mixes were tested with a focus on the influence of each fiber type.

Most Hybrid Fiber Concretes use a mixture of steel fibers but some authors also experimented with synthetic fibers or a combination of synthetic and steel fibers [BG04, PMAG07].

The function of the different fiber types in the micromechanical behavior of HFC is illustrated in Figure 2.18. Because the short straight fibers have the same dimensions and a similar spatial distribution as potential microcracks they can effectively arrest their propagation. As a result the short fibers are the main reason for the high first-cracking tensile strength of HFC. Longer fibers on the other hand become active when macrocracks start forming. In a first phase they effectively arrest the propagation of these macrocracks and they are therefore responsible for the strain-hardening and multiple cracking behavior of HFC. In a second phase when localization and formation of a large macrocrack begins they bridge this crack and thereby produce a smooth softening curve and a ductile failure of the material [vM04b]. This last phase corresponds to the progressive pullout of the long hooked-end or crimped fibers. The same observations concerning the functions of long and short fibers were also made for synthetic fibers [BOS95].

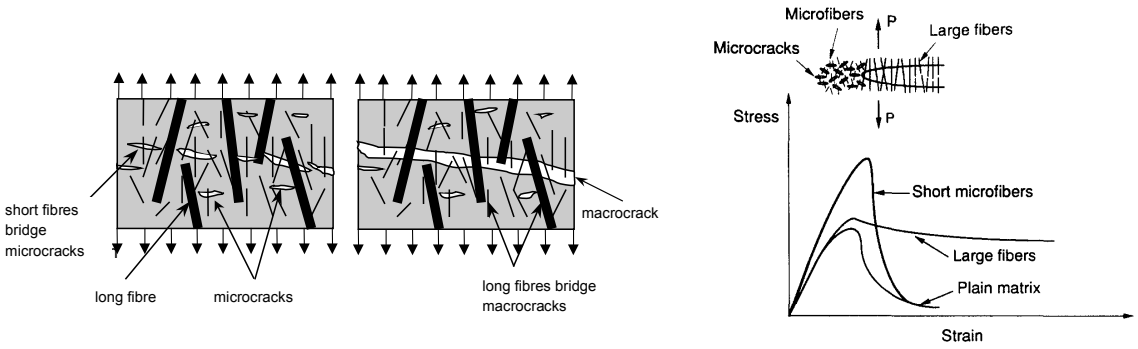

(a) Scale at which different fiber types are active [Mar06]

(b) Influence of different fibers on the tensile behavior [BOS95]

Figure 2.18: Different functions of short and long fibers

The concept of adding different fiber geometries in various volume contents makes the design of HFC very flexible. Basically, the fiber mix can be selected in such a way as to tailor a Fiber Reinforced Cementitious Composite with the desired mechanical properties. This means that there is not one unique HFC but many different mixes with individual characteristics. Because the properties can vary from one fiber mix to another the values given here should be seen as a rough indication of possible magnitudes.

The macroscopic behavior of HFC is not only governed by the fiber mix but the composition of the concrete matrix is of equal importance. The latter should be as dense as possible in order to maximize the bond between the matrix and the fibers. In other words the matrix should contain an important amount of fine aggregates that fill the voids between the larger aggregates and the fibers. The smaller the fiber diameter the more fine fillers have to be added. This can be nicely seen in Figure 2.19. Usually silica fume, fly-ash and a high dosage of cement as well as a fine granulometry of the aggregates are used for this purpose. The concrete matrix strength, the fiber pullout resistance and the tensile strength of the fibers have to be balanced delicately in order to guarantee sufficient fiber pullout forces but prevent rupture of the concrete matrix or the fibers. From an economic standpoint it is also reasonable to use the most efficient matrix possible since the fibers are the most expensive component and they should be exploited to the highest possible extent. Therefore, it is a lot more economic to maximize the bond between the fibers and the matrix by using a high-density (and slightly more expensive) matrix than to add more fiber to the concrete.

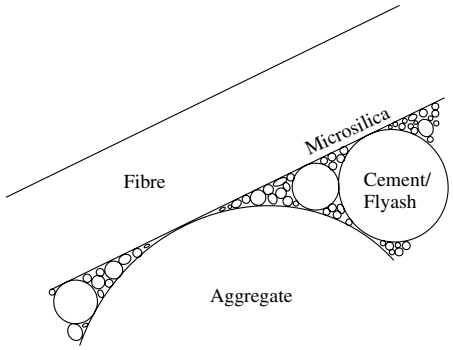

Figure 2.19: Dense packing of the concrete matrix close to a fiber [SvM07]

Because of the dense packing of particles HFC also exhibits a very high compressive strength making it an Ultra High Performance Fiber Reinforced Cementitious Composite. This is to be expected since adding fine particles to the concrete mixture and targeting a dense packing is the fundamental concept used in the design of UHPFRCCs. However, it should be noted that the developers of HFC did not intend to produce a concrete with a very large compressive strength but rather one with a high tensile strength and more importantly with a balanced ratio between tensile and compressive strength. The high compressive strength is a rather unwanted side effect that is a consequence of the desired good bond between the fibers and the matrix which makes a dense particle packing necessary.

Like all Ultra High Performance Fiber Reinforced Cementitious Composites, HFC contains a relatively large amount of cement and a relatively low w/b-ratio of about 0.2. Compared to conventional concrete the workability of HFC is reduced considerably by the addition of the long hooked-end fibers [SvM04]. The addition of short steel fibers on the other hand has little influence on the workability. In order to counteract the reduced workability a large amount of superplasticizer is used. Together with a careful matrix design HFC can achieve self-compacting properties which is an important design aspect of Hybrid Fiber Concrete. This guarantees reasonable workability of the fresh concrete while assuring compactness of the concrete matrix and preventing the formation of voids. It should be emphasized, that the balance of the mix is delicate since HFC has to be fluid enough to show self-compacting properties but it also has to be dense enough to prevent the segregation of fibers. In addition to the improved workability the self-compacting properties of HFC are also largely beneficial to achieving a homogeneous fiber distribution since compactation and vibration tend to accentuate the segregation of fibers.

HFC is very closely related to Multi-Scale Fiber-Reinforced Cementitious Composites (MSFRCCs) which are sometimes also called High Performance Multimodal Fiber Reinforced Cement Composites (HPMFRCCs) [Ros97, Ros05]. Rossi was the first to propose the use of multiple fiber geometries based on what he called the *multi-scale* concept [RAM87]. The basic idea of the multi-scale concept is that different fiber sizes are necessary for different stages of crack development since every fiber type can only be effective on a scale close to its own geometrical dimensions. In [Ros97] Rossi describes the results of a test series with a MSFRCC that contains short straight ($l = 5\ mm$, $\varnothing = 0.25\ mm$, 5 % Vol.) and long hooked-end fibers ($l = 25\ mm$, $\varnothing = 0.3\ mm$, 2 % Vol.). Since the theoretical concepts and mechanical properties of MSFRCCs and HFC are practically identical these two materials are not explicitly distinguished here. In fact the starting point for HFC were HPMFRCCs [SvMW00].

Most recently the "Laboratoire Central des Ponts et Chaussées" in Paris launched an extensive study to investigate the mechanical properties of a derivative of MSFRCCs which is commercially known under the name CEMTECH$_{\text{multiscale}}$® [RAPF05]. Some improvements that were made during the development of CEMTECH$_{\text{multiscale}}$® when compared to the earlier versions of MSFRCCs are the use of three fiber geometries instead of two, the use of higher fiber volume contents (11 % instead of 7 %) and the application of post set heat-treatment (a procedure typically used for RPC see Section 2.7).

2.8.2 Mechanical Properties

HFC shows a very ductile behavior on the material level as well as on the structural level. The ductility on the material level is mainly produced by the short and medium sized fibers whereas the ductility on the structural level can be attributed to the long hooked-end or crimped fibers. The ductility is apparent both in tension and in compression (for more details see following paragraphs).

Another interesting property of HFC is that it has a high toughness. The latter also implies a high energy dissipation capacity. However, for cyclic loading this is of minor importance since the fiber pullout process which creates the energy dissipation is not reversible. Of much greater importance for the energy dissipation capacity of a structural member is the fact that HFC does not spall due to its greater tensile strength and ductility. By consequence reinforcement bars in HFC members do not buckle and can undergo large hysteretic energy dissipation cycles [DBT08].

After casting the fresh HFC hardens very quickly. The early age compressive strength (after 1 day) is usually already somewhere between 80 MPa and 110 MPa. The early age splitting tensile strength reaches from 8 MPa to 10 MPa. A range of mechanical properties of HFC at an age of 28 days is given in the following Table 2.1:

Modulus of elasticity	40 – 50	GPa
Compressive strength	120 – 160	MPa
Tensile strength	8 – 15	MPa
Flexural strength	20 – 50	MPa

Table 2.1: Characteristic mechanical properties of HFC

Compressive Behavior

The high compressive strength of HFC mentioned in Section 2.8.1 can be explained by the very dense packing of particles in the concrete matrix and the low w/b-ratio as well as the short fibers which delay formation of microcracks and splitting cracks by providing some sort of "internal" confinement [vM04b]. In addition, HFC shows a very smooth post-peak softening behavior in compression (see Figure 2.20). This characteristic property is due to the long crimped fibers. The short fibers probably have a secondary effect by anchoring the long fibers more strongly in the concrete matrix. Even at extremely high strain levels the residual compressive strength remains important. This shows that HFC has a tendency to retain its integrity even after it has been strained significantly.

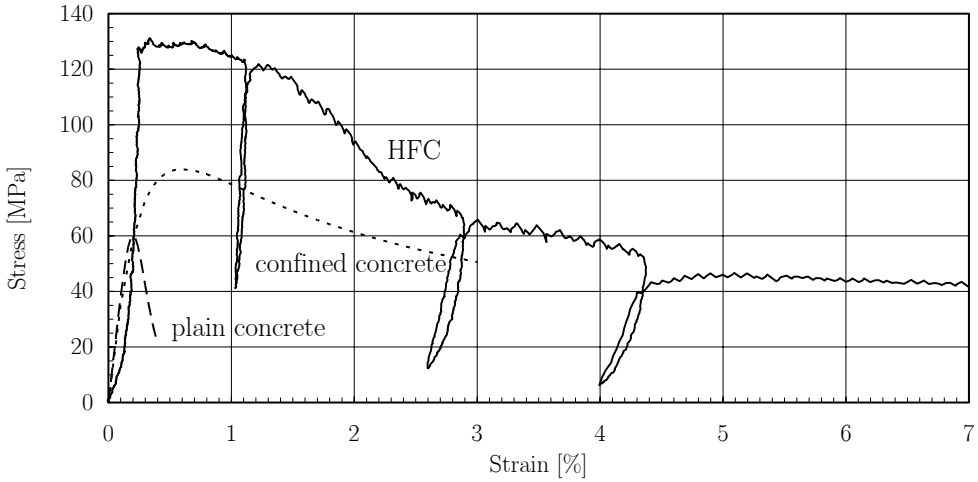

Figure 2.20: Compression test results of a HFC cube specimen [DBT08]

Tensile Behavior

According to [MWvM04b, Mar06] the tensile behavior of HFC can be separated into four different phases (see Figure 2.21):
The first phase (phase 0) represents the linear, elastic behavior of the uncracked concrete. In the second phase (phase A) the behavior is still more or less linear elastic. On the material level this phase corresponds to the appearance of the first microcracks but their propagation is effectively arrested by the short fibers. It is this effect that is responsible for the high tensile strength reached by HFC. This phase is sometimes also called the *stable microcracking* phase. The third phase (phase B) is characterized by the formation of a first macrocrack followed by multiple cracking. In this stage HFC exhibits strain-hardening which is mainly produced by the long hooked-end fibers. Before they can be pulled out of the concrete matrix their hooked ends have to be deformed which results in a fiber bridging stress that is higher than the first cracking stress of the matrix. The fourth and final phase (phase C) is characterized by the onset of strain-softening. The short straight fibers no longer participate because they have been pulled out of the matrix completely. At this point only the long fibers remain active and they are gradually pulled out of the matrix.

The phases proposed above are in accordance with the observations made on uniaxial tensile tests with Hybrid Fiber Concrete "dog-bone" specimens [MWvM04a]. As expected, using only short fibers leads to a massive increase in tensile strength whereas the test specimens with only long fibers showed strain-hardening and enhanced ductility. Using both short and long fibers leads to the best overall performance with both a higher tensile strength and an increased ductility.

The high tensile strength of HFC also leads to a high shear capacity. As a consequence it is most likely that less transverse reinforcement is necessary in HFC structural members and in most cases it can probably be omitted completely [BDT06].

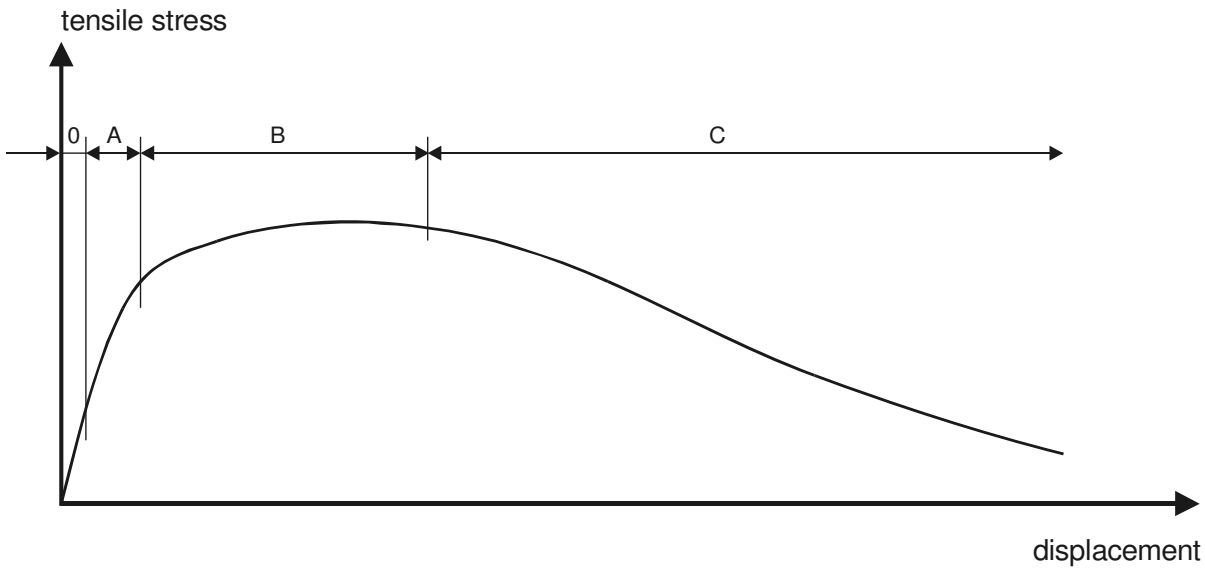

Figure 2.21: Phases of tensile behavior [Mar06]

Flexural Behavior

In analogy to the tensile response of HFC the flexural behavior is also strongly influenced by the used type of fibers and the fiber mix proportions. Figure 2.22a taken from [Mar06] shows the influence of different fibers. The percentage values in the plot represent the volume content of a specific fiber type and the values in brackets indicates the length of the respective fibers in mm. A complete discussion of this subject can be found in [MWvM03].

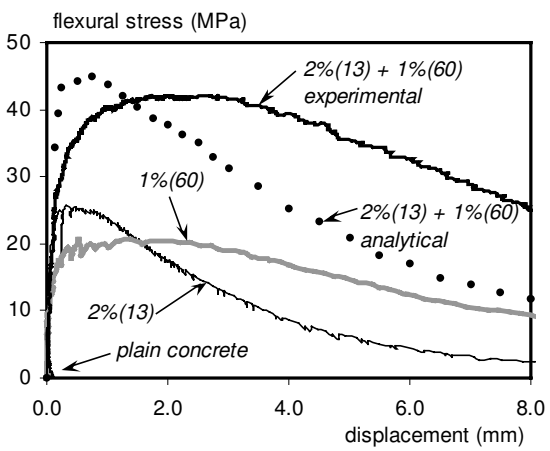

(a) Flexural response of HFC [Mar06]

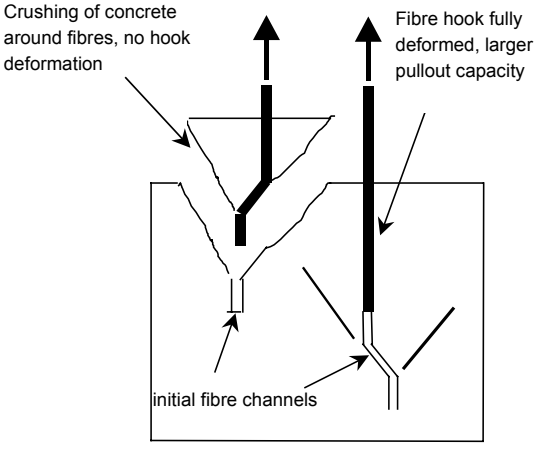

(b) Fiber synergy [Mar06]

Figure 2.22

In Figure 2.22a the influence of the long hooked-end fibers is shown by the curve labeled 1%(60). It is apparent that they are responsible for some flexural-hardening up to crack

openings of about 2 mm. Their addition to the mix results in a slightly higher flexural strength but more importantly they are responsible for some pronounced ductility as well as higher residual strengths at large crack openings.

The effect of the short fibers is illustrated by the curve labeled 2%(13) in Figure 2.22a. At small crack openings the short fibers are very effective resulting in a considerable increase in flexural strength. However, with growing crack opening their influence is reduced asymptotically until it becomes negligible at a crack opening of approximately 7 mm. This is easily explained by considering that at this point the crack opening approaches half the length of the fibers and by consequence almost all of the short fibers have been pulled out of the matrix completely. The long fibers on the other hand are still active at this crack opening.

As can be seen from the curve labeled 2%(13) + 1%(60) *experimental* in Figure 2.22a the combination of short and long fibers results in a more favorable behavior than the sum of the two fiber contributions (curve 2%(13) + 1%(60) *analytical*) indicates. The short fibers tend to reinforce the concrete in which the long hooked-end fibers are embedded. Thereby they activate more of the long fibers forcing their hooked ends to be deformed plastically rather than allowing pullout by destruction of the concrete matrix (see Figure 2.22b). This effect is know as *fiber synergy* [Mar06] which means that the combination of fibers in HFC produces a better performance than could be expected by the simple addition of each fiber types individual contribution.

2.8.3 Applications

Up to date there are very few applications of Hybrid Fiber Concrete due to its rather recent development. To the author's knowledge, the first study on a structural application of HFC was performed at the Institute of Structural Engineering at the ETH Zürich and is presented in [BDT06] and [DBT08]. The main goal of this study was to design and test a number of earthquake-resistant, structural HFC walls. The design of the HFC mix was done by members of the Institute for Building Materials at the ETH Zürich and is described in [SvM05, Stä08]. The most important findings were that the HFC structural walls performed very well under cyclic loading, displaying a large ductility even without shear or confinement reinforcement. The fibers in HFC prevented spalling of the cover concrete and they where able to sustain nominal shear stresses of up to 7.1 MPa. Figure 2.23 shows the test setup for a HFC structural wall as well as a photo of the wall during testing.

An application of Multi-Scale Fiber-Reinforced Cementitious Composites that could be found in the literature is its use for structures subjected to fatigue and impact loading [RP08]. The principal findings of that investigation were that MSFRCCs (fiber content 11 % vol.) perform much better than other HPFRCCs when they were subjected to high strain rates during impact loading.

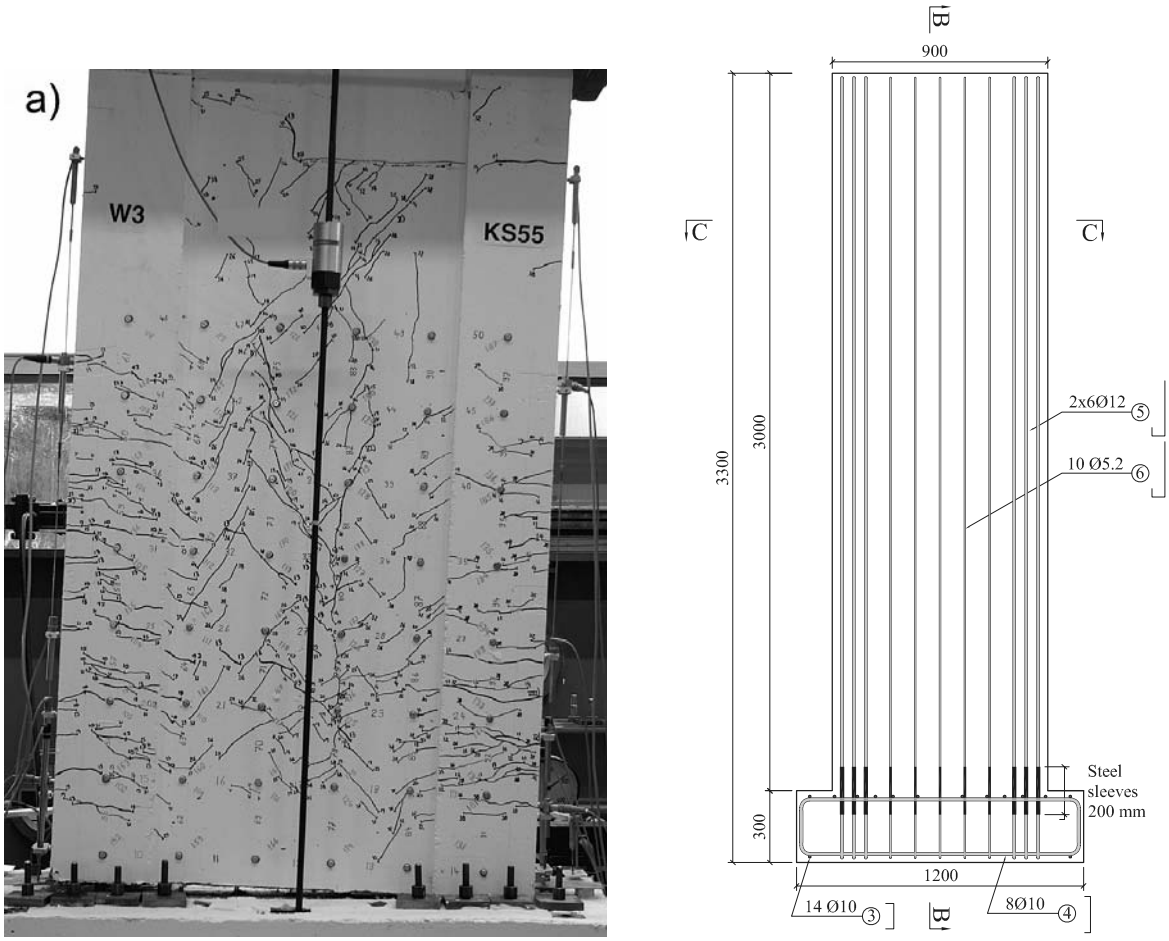

(a) Crack pattern at failure

(b) Reinforcement details

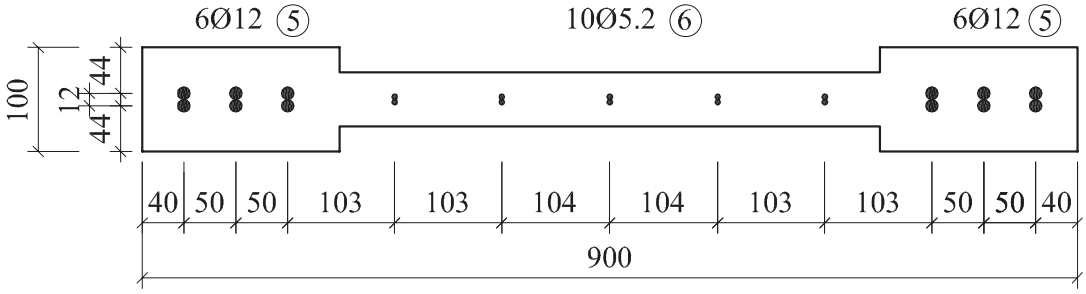

(c) Cross-section

Figure 2.23: HFC structural wall [BDT06], all dimensions in $[mm]$

2.9 Comparison

After having presented the most important Fiber Reinforced Cementitious Composites in the preceding sections of Chapter 2 this section will focus on comparing them against

each other in the light of possible applications. The following Figure 2.24 recapitulates the High Performance Fiber Reinforced Cementitious Composites of Sections 2.2 ff.

	Abbreviation	Name	Commercial Product	Period of Development
	SFRC	Steel Fiber Reinforced Concrete	-	1960s
	DSP	Densified Small Particle Concrete	Densit	1970s
Ultra High Performance Fiber Reinforced Cementitious Materials	CRC	Compact Reinforced Composite	-	1990s
	RPC	Reactive Powder Concrete	DUCTAL®	1990s
	MSFRCC	Mulit-Scale Fiber Reinforced Cementitious Composite	CEMTECH®	1990s
	HFC	Hybrid Fiber Concrete	-	2000+
High Performance Fiber Reinforced Cementitious Materials	SIFCON	Slurry Infiltrated Fiber Concrete	-	1980s
	ECC	Engineered Cementitious Composite	-	1990s
	HPFRC	High Performance Fiber Reinforced Concrete	-	2000+

Figure 2.24: Summary of Fiber Reinforced Cementitious Composites

Although DSP concrete and SFRC are not High Performance Fiber Reinforced Cementitious Composites they are still mentioned in the above recapitulation because they represent essential steps in the development of the other FRCCs. However, they will not be considered any further in the following comparative study.

In Figure 2.25 the HPFRCCs and UHPFRCCs are compared with respect to the fibers they contain. It is interesting to note that the Fiber Reinforced Cementitious Composites which contain the shortest fibers are also those which contain the highest fiber volume contents (with the exception of SIFCON). This has to do with workability considerations. Because short fibers do not affect the workability of concrete as much as long fiber do, they can be added in large quantities. Also note that the diameter of synthetic fibers is close to a magnitude smaller than the diameter of steel fibers with comparable length.

Material	Short fibers (6 mm Ø 0.16 mm)	Medium fibers (13-30 mm Ø 0.15-0.5 mm)	Long fibers (60 mm Ø 0.71 mm)	Fiber volume fraction	Fiber material
CRC	X			5 - 10 %	Steel
RPC		X		1.5 - 3 %	Steel
MSFRCC	X	X	X	7 - 11 %	Steel
HFC	X	X	X	1 - 6 %	Steel
SIFCON			X	5 - 12 %	Steel
ECC		X (but Ø 0.038 mm)		0.5 - 4 %	PVA / UHMWPE (synthetic fibres)
HPFRC		X (UHMWPE Ø 0.038 mm)		1.5 - 2 %	Steel / UHMWPE

Figure 2.25: Comparison of fibers in different HPFRCCs

2.9.1 General Comparison of FRCCs

The main criterion which distinguishes the UHPFRCCs from the HPFRCCs is their high compressive strength. It is achieved by a very dense packing of the particles in the matrix. As a consequence of the dense matrix not only the compressive strength but also the bond between matrix and reinforcement as well as the bond between matrix and fibers is significantly improved. A drawback of the high compressive strength is that the matrix becomes more brittle. These differences very clearly set ECCs, HPFRC and SIFCON (HPFRCC) apart from the UHPFRCCs. While the compressive strength of UHPFRCCs may be 5 to 10 times that of normal concrete the compressive strength of ECCs, HPFRC and SIFCON are of more or less the same order of magnitude. As already mentioned in Section 2.1.3 the concrete matrices of all the presented UHPFRCCs are very similar since they are all based on the common concept of high density particle packing. Or in other words: UHPFRCCs are all composed of a DSP matrix and are mainly set apart by the employed fibers and their respective volume content.

Originally all UHPFRCCs started out with the goal to improve a very specific mechanical property such as for example a very high compressive strength at limited brittleness in

the case of RPC – or a higher tensile strength which would result in a more reasonable ratio between the tensile and the compressive capacity of the material in the case of HFC. However, they all ended up with similar mechanical properties. What was the target property of one UHPFRCCs turned out to be just a beneficial side effect for another. The high compressive strength of HFC for example is only a by-product of the desired high tensile strength. The latter can only be achieved with a dense matrix with good bond characteristics which in turn increases the compressive strength as well.

When considering MSFRCCs or HFC which include different fiber geometries the mechanical properties can vary a lot depending on the used fiber cocktail. A MSFRCC with a large volume content of short fibers and few long fibers for example will approach the mechanical properties of CRCs. This emphasizes the fact that there are no clear boundaries between the different UHPFRCCs and it seems that especially HFC and MSFRCCs can be specifically tailored to approach the mechanical properties of the other UHPFRCCs. A different way of looking at it is that Multi-Scale Fiber-Reinforced Cementitious Composites are some kind of synthesis of the other UHPFRCCs. By not limiting the fiber cocktail to one specific type of fiber the fiber mix can be designed such as to resemble that of CRCs (with a large amount of very short fibers) or that of RPC (by using an important quantity of longer fibers) as well as anything in between.

The two material classes MSFRCCs and HFC are quite similar. Where Rossi used rather high fiber volume contents in his studies on MSFRCCs van Mier, Walraven and co-workers used smaller volume fractions in their experiments on HFC. Other than that the two materials seem to be almost the same and they also share a common theoretical basis. One small difference which merits mentioning is that HFC is self-compacting which is a characteristic that was not reported for MSFRCCs. In the following the discussion will be limited to HFC since there seem to be no fundamental differences between HFC and MMFRCCs.

2.9.2 Performance Properties of FRCCs

There are many different properties that might or might not be required of a FRCC depending on the specific application. The goal of this section is to discuss some performance requirements and to compare the different Fiber Reinforced Cementitious Composites in this light.

The following are the most sought-after properties of Fiber Reinforced Cementitious Composites for structural applications:

- Tensile strength
- Shear strength
- Compressive strength
- Stirrup replacement capacity
- Bond strength
- Spalling prevention capacity
- Energy dissipation capacity
- Ductility on a material level
- Ductility on a structural level

Tensile strength In case a Fiber Reinforced Cementitious Composite with a high tensile strength is desired the best choice would be CRCs respectively a HFC with a large volume content of short straight fibers. The highest possible tensile strength that can be reached is about 15 MPa. If even higher tensile strengths are required one can resort to SIFCON as long as the "unconventional" casting procedure is not an issue. The use of a HFC with additional medium and long fibers can ensure a higher residual tensile strength should this be required. Although the tensile strength of ECCs is slightly higher than that of traditional fiber reinforced concrete it rarely reaches 8 MPa. The same is true for RPC which makes the latter two high performance materials less suitable for applications requiring a high tensile strength.

Shear strength If the sought-after property is a high shear strength, then the most suitable Fiber Reinforced Cementitious Composite is one that has a high tensile strength. This can be understood by examining Figure 2.26 which shows a schematic failure envelope and different two-dimensional stress states at failure (represented by Moor's circle). It becomes evident that the state of pure shear τ_{pure} (represented by the circle that is concentric to the origin) is limited by the tensile strength σ_I of the composite, especially if there is a large difference between the tensile strength and the compressive strength as is typically the case for FRCCs. Another way of looking at it, is to understand that a state of pure shear is equivalent to a state of simultaneous tension and compression ($\sigma_I = -\sigma_{II}$) in the principal directions of the two-dimensional stress state. In FRCCs this leads to a failure in tension long before the compressive strength is reached. This is also in agreement with experimental evidence which suggests that Fiber Reinforced Cementitious Composites typically fracture in mode I (crack formation due to tensile stresses normal to the crack plane).

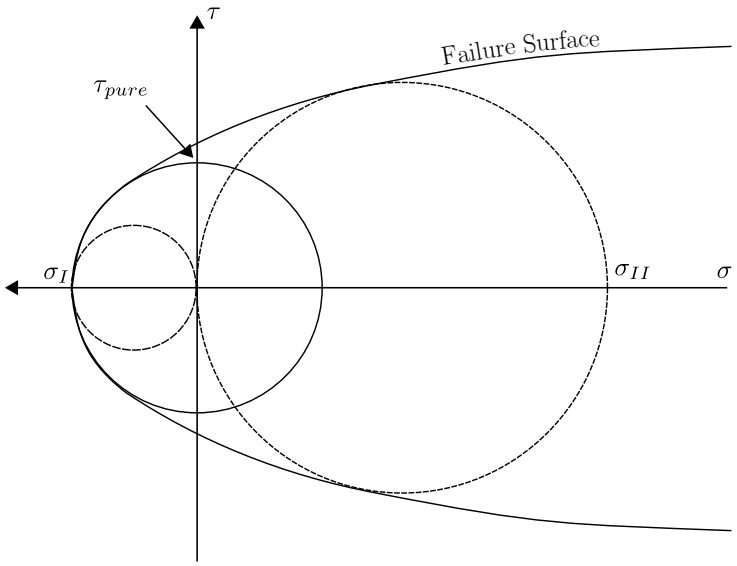

Figure 2.26: Limitation of the shear strength by the tensile strength

As a direct consequence, a FRCC with a high first cracking tensile strength also provides the best option when seeking a composite with a high shear strength. Therefore, the best choice would be a CRC or a HFC with a large volume fraction of short fibers. Of course the discussion above is limited to the linear elastic response of the material prior to cracking. Afterwards the shear transfer mechanism of the cracks becomes the key parameter in determining the shear strength. This post-cracking shear strength will most likely be positively influenced by any long steel fibers (bridging effect). However, this prediction is only based on engineering judgment as to the author's knowledge there is no experimental evidence on this subject.

Stirrup replacement A property which is directly linked to the shear strength is the capacity of a Fiber Reinforced Cementitious Composite to allow for a reduction or the complete elimination of stirrups in a structural element. If the inherent shear capacity of the FRCC is sufficiently large the often tedious and time consuming placement of stirrups can be circumvented. For the obvious same reasons as mentioned above CRCs and a HFC with short fibers are the most reasonable choices. However, other HPFRCCs such as HPFRC or RPC are also capable of alleviating stirrup requirements as has been shown in Sections 2.5 and 2.7.

Compressive strength If a high compressive strength is the desired property, then RPC is probably the most suitable choice. The fiber cocktail should consist of a moderate amount of medium sized fibers in order to improve toughness and prevent brittle failure. Under construction site conditions the compressive strength of RPC can range from 170 MPa to 230 MPa and under laboratory conditions (i.e. for precast elements) compressive strengths of 490 MPa to 680 MPa can be reached. However, the other UHPFRCCs such as CRCs and HFC can also be considered when looking for a high performance material with a high compressive strength. ECCs on the other hand are not very suitable since their compressive strength is more or less the same as that of conventional concrete.

Bond strength Another property that can be sought after in Fiber Reinforced Cementitious Composites is good bond behavior with reinforcement bars. As can be looked up in Section 2.6 on CRCs, there are three main characteristics of a FRCC that assure a strong bond with reinforcement bars. The first one is a dense matrix which increases the frictional forces and the second one is a certain ductility on a material level which guarantees a favorable stress and microcrack distribution in the vicinity of the rebars. Finally, a high tensile strength will delay cracking in the anchorage zone of a rebar which in turn will also increase the bond strength. All these requirements are met either by CRCs or by a HFC with an important content of short fibers.

Spalling prevention For seismic applications, among others, it can be interesting to prevent spalling of reinforced structural members. The most important reason for this is that the cover concrete prevents the longitudinal reinforcement from buckling during the compressive phase of a load cycle. However, the tensile strength which is required to prevent spalling is small. It is mostly sufficient if a FRCC member does not loose its outermost layer in a brittle manner but is able to maintain its integrity even after the tensile strength of the composite is reached. This is usually the case for all HPFRCCs and UHPFRCCs.

Energy dissipation The energy dissipation capacity of a FRCC structural member is strongly dependent on the loading conditions. Although the energy dissipation capacity of all FRCCs is much higher than that of plane concrete, this is only useful for non-cyclic loads since the fiber pullout process is not reversible. Some applications such as safety vaults or missile proof military bunkers make use of this kind of energy dissipation. However, it is more precise to talk about *toughness* than energy dissipation capacity in this context. The true reason why FRCCs can be extremely beneficial for the energy dissipation capacity of a structural element is its function in protecting the reinforcement. By preventing spalling and consequential buckling of the longitudinal reinforcement the FRCC cover layer can assure that the reinforcement bars are able to undergo large plastic deformation cycles. Basically all Fiber Reinforced Cementitious Composites are capable of producing this result.

Ductility on a material level One of the first properties that was sought-after in FRCCs was ductility. Already in the early days of Steel Fiber Reinforced Concrete development the main goal was to reduce the brittleness or in other words to improve the ductility of concrete by adding steel fibers. This characteristic is one that all mentioned Fiber Reinforced Cementitious Composites share since every composite that has a smooth post-peak softening behavior can be considered to fail in a ductile manner. This, however, is only ductility on a material level. If it is desirable to have a whole structure behave in a ductile manner, the sought-after property is ductility on a structural level.

Ductility on a structural level Structural ductility can be a desired property of a FRCCs for example in earthquake engineering where the load bearing capacity of a structure after it has been loaded far into the inelastic range is of interest. Inherent ductility on a structural level can only be provided by a material that has a pronounced strain-hardening phase. The reason for this is obvious. If the FRCC does not include any significant strain-hardening then damage localization will occur at first cracking and there will be no spread of cracking unless structural reinforcement is used. As a consequence the fracture process zone will be limited to a very small part of the structural element and the small amount of added ductility will not affect the overall structural response. All High Performance Fiber Reinforced Cementitious Composites show strain-hardening to some degree but the extent of the strain-hardening phase is strongly dependent on the

fiber cocktail. In general the more long fibers a FRCC contains the more pronounced its strain-hardening phase will be. Therefore ECCs, HPFRC, SIFCON or a HFC with a considerable amount of medium sized and long fibers in the fiber cocktail are the best candidates.

2.9.3 Conclusion

After this direct comparison it becomes obvious that HFC seems to combine two different aspects. Where CRCs are mainly of interest for applications where strength is required and ECCs are the optimal choice for applications that require ductility HFC shows a good performance in both these fields of application. This leads to the following conclusions:

> If an application requires a slender structural element consisting of a high performance composite that has a very high compressive, tensile and shear strength than CRCs are the optimal choice. If on the other hand an application requires a structural element of conventional strength but that has an extremely high inherent ability to maintain its integrity and prevent any premature and non-ductile failure mechanism than ECCs are the most suitable option. In case an application requires both these aspects HFC can be recommended.

Chapter 3

Numerical Modeling of Quasi-Brittle Materials

3.1 Introduction

With the invention of personal computers and their widespread use in civil engineering practice and research it has become a standard procedure to use numerical models for the simulation of all kinds of engineering problems. The most commonly used approach is probably the Finite Element Method (FEM) which was developed in the early 1960s. Among other things, it allows the static and dynamic simulation of structures with any complex geometry and arbitrary boundary conditions [Bat96].

Nowadays the technical performance and computational power of personal computers and the theoretical models have reached a level of sophistication that allows a relatively accurate prediction of structural responses up to failure. Such failure analysis is computationally very demanding because complicated nonlinear material models and a relatively complex two- or three-dimensional geometrical representation are often required. Also, the complete load path from initial cracking up to localized failure have to be tracked since damage history plays an important role.

In the following an introduction to numerical modeling of quasi-brittle materials is given. We recall that the final goal of this thesis is to come up with a numerical model for High Performance Fiber Reinforced Cementitious Composites (see Section 1.2). Therefore, special attention is accorded to those models that are deemed suitable for HPFRCCs. Nice overviews of nonlinear modeling and failure analysis of quasi-brittle materials can also be found in [Jir00, JP01] and [HC06].

After giving a general overview of the most popular models for quasi-brittle failure (Section 3.1) this chapter will focus on the theoretical background of the two models that are used in this thesis. These are the Smeared Crack Model (Section 3.2) and the eXtended

Finite Element Method (Section 3.3). The chapter is then concluded by a literature review of the existing models for HPFRCCs and the new model that was developed during this thesis is outlined (Section 3.4).

3.1.1 Strain Localization

As mentioned in Section 1.2 an accurate representation of the tensile softening behavior of High Performance Fiber Reinforced Cementitious Composites is essential. One of the fundamental issues that have to be tackled when modeling the softening behavior of quasi-brittle materials is a phenomenon called *strain localization* [Jir00, Wel01]. It can probably be explained best when considering a HPFRCC truss element loaded in pure tension. Let us distinguish the three different stages of material behavior depicted in Figure 3.1 which were already introduced in Section 2.1.3:

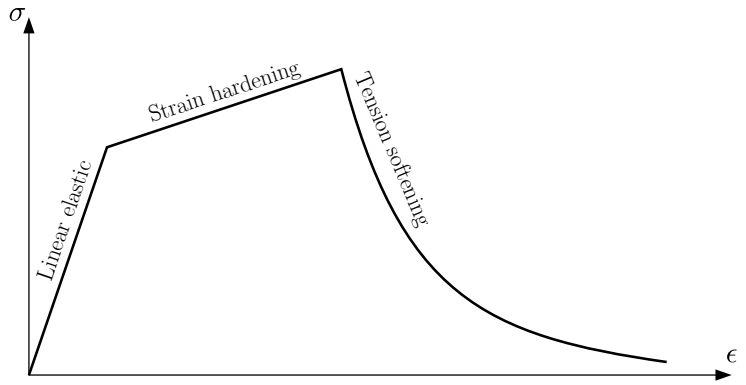

Figure 3.1: Phases of tensile behavior of a quasi-brittle material

1. In the first phase the truss is loaded within the linear, elastic regime and the stress and the strain are both constant throughout the entire length of the truss.

2. As the elastic limit is reached the truss changes into a regime of strain-hardening. Due to material and geometrical imperfections at first only a single section of the truss will pass from the elastic into the inelastic regime. However, since the load carrying capacity of the material is not reached yet (even if the stiffness is smaller and the increase in strain will therefore be larger) a next section will automatically pass into the hardening regime. This will continue until all sections are hardening and the strain profile is uniform again.

3. A completely different behavior will set in as the first section starts softening. Rather than forcing other sections to do the same the softening section is suddenly weaker than all the others. If the load level is maintained this will result in cataclysmic failure since whatever strain level the weaker section attains it will never be able to equilibrate the global forces (after the onset of softening the load carrying capacity of that section decreases with increasing strain as can be seen in Figure 3.1). Even if the

deformation of the specimen instead of the external load is controlled all deformation will "localize" in the weaker section causing the other sections to unload elastically. Hence the expression *strain localization*. A very graphic and detailed description of strain localization can also be found in [Jir00].

The main problem that is associated with strain localization is that all strain accumulates in one section while the strain in all other sections remains constant or decreases. By consequence this introduces a discontinuity in the strain profile in form of a "jump" between the softening section and the adjacent elastic sections. In the limit case when only an infinitely small section accumulates all the strain and all the other sections remain elastic the strain profile takes the form of the *Dirac delta-distribution* (see "strong discontinuity" in Figure 3.2). It is obvious that this representation of strain (finite displacement divided by zero length) is pathological and it no longer makes sense to talk about strain in this context. It is more reasonable to consider the displacement profile. The latter exhibits a jump at the softening section which means that a crack has formed at that location.

The initiation of localization marks the transition from a continuous to a discontinuous model. Mathematically this is accompanied by the *loss of ellipticity* of the underlying continuum mechanics differential equation. The problem becomes ill-posed. The moment of strain localization can also be seen as a classical bifurcation point where two configurations – namely a continuous and a discontinuous one – are possible at the same instant.

The same problem can also be explored from a different angle. A look at the energy dissipation during localization shows that continuum models are not able to describe a strong discontinuity accurately. This becomes obvious when recalling that the energy dissipation in a continuum is computed by integrating the product of the stress and the strain tensor over the volume domain of interest. Since a strong discontinuity has no width and therefore no volume there will obviously be no energy dissipation in the localization zone. This underlines the pathological behavior of a continuum model when applied to the description of strong discontinuities.

There are basically two approaches that can be followed to remedy the situation. Either a true discontinuity is introduced at the moment of localization (so called *strong discontinuity approach*) or the displacement profile is *regularized* (smoothened). The first approach is probably more realistic in a physical sense but it requires a discontinuous description of the underlying problem and the continuum model has to be abandoned. The second approach retains the continuum representation but it requires the introduction of an artificial parameter which in one way or another functions as a length scale for the localization zone (such as for example the numerical localization bandwidth in the Smeared Crack Model). Although some author's argue that this length scale can be physically interpreted as the width of the fracture process zone this is only true for small crack openings in the early phases of localization.

There are two different degrees of regularization. Either the displacement field is partially regularized making it continuous but not differentiable and leaving a discontinuity in

the strain field (e.g. Smeared Crack Models) or it is fully regularized (e.g. Nonlocal Models) which results in a continuous displacement field and a continuous strain field. In the following Figure 3.2 the three different models of a localization zone are shown schematically for the one-dimensional case.

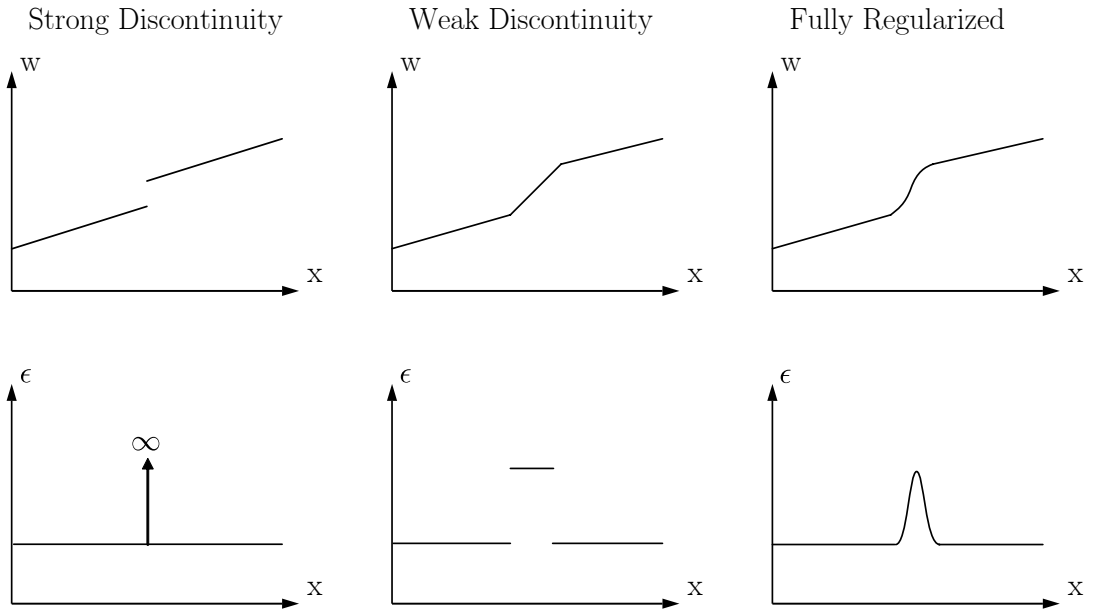

Figure 3.2: Different representations of the localization zone (adopted from [JP01])

The aspects discussed above have direct consequences on the implementation of a softening model in the Finite Element framework. When using a regularized model in Finite Element computations it is less obvious that a length scale has to be introduced since the Finite Element mesh already contains such a scale by the finite dimension of the elements. However, if no special measures are taken the softening model will show pathological mesh-size dependency. Even with advanced regularization techniques – which are usually based on fracture energy and should assure correct energy dissipation during the softening process – some undesirable side effects such as stress-locking, spurious damage growth and directional mesh-bias cannot be completely overcome (see Section 3.2).

The origin of the mentioned deficiencies of regularized models lies in the inaccurate kinematic representation of a strong discontinuity and the coupling of the strain tensor components which is inherent to continuum models. One solution is to introduce a real discontinuity upon initiation of softening which can remedy some of the problems mentioned above.

3.1.2 Overview of Modeling Approaches

While discussing the physical nature of a crack in the preceding section we concluded that the formation of a crack introduces a discontinuity into the displacement field of the

mechanical problem. We also addressed the problems associated with the transition from a hardening to a softening state and mentioned the two main classes of solutions: namely *Regularized Continuum Models* (partially and fully regularized) and *Strong Discontinuity Models* (a.k.a. Discrete Crack Models). In the following these models will be elaborated more thoroughly.

Regularized Continuum Models

A first class of models called Regularized Continuum Models assume that the discontinuity introduced by a crack can still be expressed by the kinematics of the continuum mechanics framework (see schematic representation Figure 3.3). This means that the physical reality of the discontinuity in the displacement field is mathematically transformed into a continuous representation. This is done by "smearing" the crack opening over a certain distance or in mathematical terms regularizing the strong discontinuity (compare with Section 3.1.1). By consequence the kinematics of the problem don't have to be modified to account for the cracks. The constitutive law is still expressed in terms of stresses and strains but it has to be modified to account for the contribution of the crack opening to the total strain. The most commonly used continuum based approaches for quasi-brittle materials are either the theory of *Damage and Plasticity* or the so-called *Smeared Crack Models* [Jir00]. Although Smeared Crack Models are usually presented in a physically intuitive manner it can be shown that they are in fact equivalent to an Isotropic Damage Model [dB02].

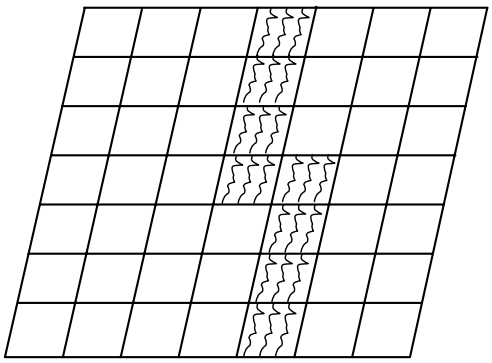

Figure 3.3: Schematic representation of the continuum model approach

The basic idea behind Smeared Crack Models is to decompose the total strain into a part representing the continuum and a part representing the crack (so-called cracking strain). The traction–separation law governing the crack (see Section 3.1.3) is transformed into a stress–strain law by smearing the crack opening displacement over a fixed distance (called the *numerical localization bandwidth*). Since the direction of the crack is usually not aligned with the global coordinate system several transformations between the global coordinate system and the local coordinate system associated with the crack are necessary. The final result of all Smeared Crack Models is a modified constitutive matrix which

accounts for the cracking. It is important to note that the kinematic equations of the underlying problem remain unchanged. Depending on whether or not the crack is allowed to change its orientation during loading one distinguishes between the Fixed Crack Model and the Rotating Crack Model. For a more detailed review of the different Smeared Crack Models see Section 3.2.

The theory of *Plasticity* is another framework that is commonly used to model quasi-brittle materials. It was originally developed for metals but due to its widespread use and relatively simple implementation it has also been adopted for quasi-brittle materials. The main components of a Plasticity Model are a *yield condition*, a *plastic flow rule* and a *hardening law*. The yield condition delimits the elastic domain and it is often graphically represented by a so-called *yield surface*. Once the strain reaches the yield surface any further deformation will produce an elastic strain increment (due to the internal redistribution of efforts) and a plastic strain increment (representing the cracking) as governed by the flow rule. The most commonly used flow rule is the *associated flow rule* which states that the plastic flow is perpendicular to the yield surface. If a material is hardening (or softening) a side effect of plastic flow is that the yield surface changes its shape during plastic deformation. This change is governed by the hardening law. One distinguishes between *isotropic* hardening and *kinematic* hardening. Isotropic hardening expresses a change of the size of the yield surface whereas kinematic hardening indicates a translation of the yield surface in the stress–strain space. A material can follow an isotropic hardening law, a kinematic hardening law or a combination of both. More information about the theory of Plasticity can be found in [Jir00].

Because the framework of Plasticity accounts for the accumulation of strains associated with the crack opening but does not account for the degradation of the material it can be combined with the theory of *Damage*. The basic goal behind Continuum Damage Models is to capture the progressive loss of material integrity due to the coalescence of microcracks. Macroscopically the latter manifests by a degradation of the material stiffness. The simplest Continuum Damage Model is the *Scalar Isotropic Damage Model*. It assumes that the material degrades isotropically and that the reduced stiffness can be expressed by multiplying the original elastic stiffness with a scalar reduction factor. In analogy to Plasticity Models a *loading function* which plays the role of the "yield condition" and governs the evolution of damage has to be specified. A more sophisticated class of damage models are the *Anisotropic Damage Models*. They take into account that a material tends to loose it integrity faster in the direction that exhibits large stretching which introduces an anisotropy into the material. A nice overview of Continuum Damage Models can be found in [dB02].

One major problem of the Plasticity Models and Continuum Damage Models is that in their pure form they do not conserve mesh-objectivity after strain-softening sets in. However, there are different remedies for this situation. The first one is to make the material law a function of the *numerical localization bandwidth* which is inherent to the Finite Element discretization. The numerical localization bandwidth is the width of the single layer of elements in which the deformations localize during a numerical simulation.

This procedure results in what are known as *Partially Regularized Continuum Models*. Although these models achieve mesh-size objectivity they may still suffer from directional bias (see [Jir00]). The alternative is to use a *Nonlocal Model* or a *Gradient-Enhanced Model* which are both examples of *Fully Regularized Continuum Models*. However, the latter are not part of this thesis and the reader is referred to [Jir00].

Discrete Crack Models (Strong Discontinuity Models)

An alternative to Regularized Continuum Models are the so-called *Discrete Crack Models*. They account for a crack by introducing a true (strong) discontinuity into the displacement field. The first models for discrete cracking within the Finite Element framework were only able to introduce cracks along element edges where the displacement field can easily be made discontinuous (see Figure 3.4a). Recently new methods which allow for crack formation with an arbitrary path through the mesh have been developed (see Figure 3.4b). Two of these new methods are the *Embedded Discontinuities Method* (EDM) and the *eXtended Finite Element Method* (XFEM).

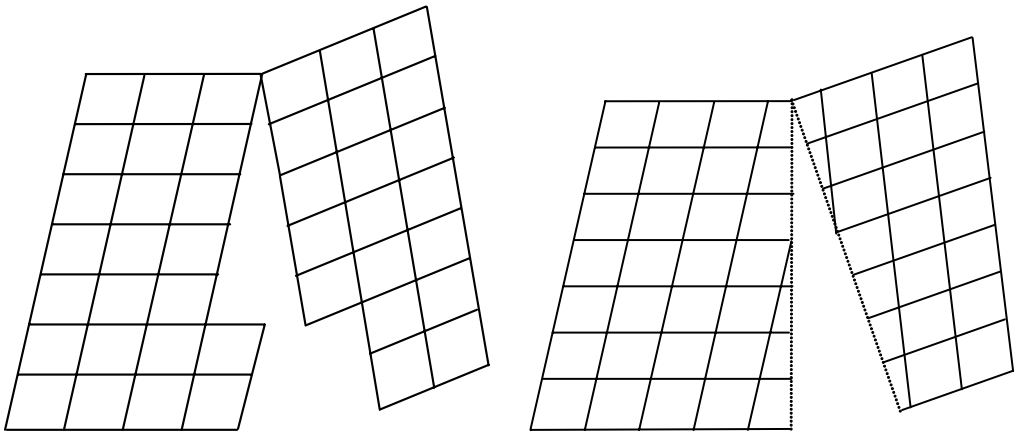

(a) Crack along element interfaces

(b) Crack crossing elements (EDM or XFEM)

Figure 3.4: Schematic representation of the Discrete Crack Model approaches

As already mentioned, the simplest approach is to introduce discontinuities only between elements where they can easily be modeled by means of Interface Elements. The drawback is that a discontinuity has to follow element boundaries and the correct prediction of crack propagation requires computationally expensive remeshing techniques. Furthermore, remeshing in nonlinear problems requires the transfer of results between different meshes which makes this method cumbersome. A variation of this concept is the *Incipient Discontinuity Method* which inserts a potential cohesive segment at the interface between all adjacent Finite Elements.

An alternative method is the use of elements with so-called *Embedded Discontinuities*. The Embedded Discontinuities Method (EDM) is based on the Enhanced Assumed Strain

(EAS) formulation which follows from the Hu-Washizu three-field variational principle [Wel01]. The strain field is enhanced with an incompatible strain mode that introduces a strong discontinuity. The advantage of this formulation is that a discontinuity can cross the Finite Element mesh in an arbitrary manner since it is introduced into the elements themselves. However, sensitivities to mesh alignment cannot be fully overcome [Wel01].

The third and most sophisticated approach is the eXtended Finite Element Method (XFEM). The XFEM is based on the Partition of Unity Method (PUM) pioneered by Melenk and Babuška in 1996 [MB96]. Similar to the EDM it allows the introduction of strong discontinuities with mesh-independent geometry. The main difference between the EDM and the XFEM formulation is that in the XFEM the displacement field instead of the strain field is enhanced. Furthermore, in contrast to the Embedded Discontinuities Method the strain field in the eXtended Finite Element Method is *conforming*. Also, the two parts of the mesh which separated by a discontinuity are completely dissociated in the XFEM which is not the case for the EDM.

An overview of Discrete Crack Models can be found in [JB02]. For more information about the XFEM the reader is referred to Section 3.3.

Since the Embedded Discontinuities Method and the eXtended Finite Element Method provide the possibility to include additional information about the solution into the Finite Element approximation space this procedure can in principle be used to introduce not only discrete but also regularized discontinuities. The latter are called *Embedded Localization Bands* [BFE88, PJ03]. The advantage of Embedded Localization Bands over the previously presented standard Regularized Continuum Models is that they are mesh-independent. An example of a model with Embedded Localization Bands and a full regularization using truncated harmonic functions is given in [Jir01]. In the same way that the EDM or the XFEM provide a mesh-independent counterpart to Interface Elements they also offer a mesh-independent alternative to Regularized Continuum Models in the form of Embedded Localization Bands.

A schematic overview of all the presented classes of models for localized failure is given in the following Figure 3.5.

3.1.3 Constitutive Laws

In Section 3.1.2 the different modeling approaches are classified by their underlying kinematic assumptions. It should be noted, that the individual kinematic models have direct implications on the constitutive law. In fact each type of model, or more specifically each kinematic representation of the localization zone (strong discontinuity, weak discontinuity, fully regularized) requires a specific type of constitutive law.

In models which represent a crack by a weak discontinuity the cracking zone is still regarded as a continuum which means that the kinematics remain unchanged. The deformations will naturally localize in a single layer of Finite Elements (numerical localization

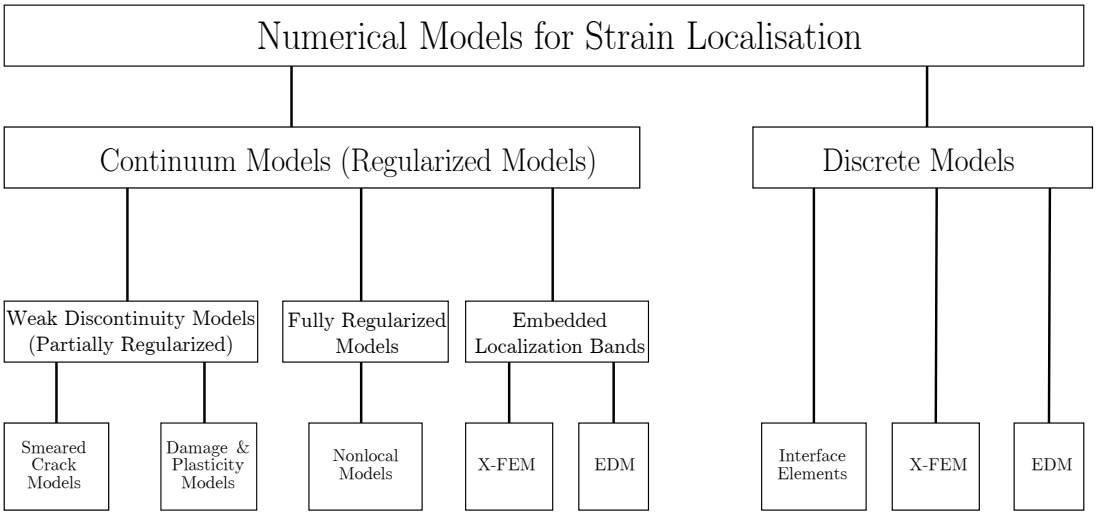

Figure 3.5: Overview of models for strain localization

band) and the weak discontinuity is automatically introduced because the strain interpolation field is normally discontinuous at element interfaces. However, in order to account for cracking the constitutive law (i.e. the stiffness and the stress–strain relationship) of the cracked elements has to be modified. For the reasons described in Section 3.1.1 an artificial parameter called the *numerical localization bandwidth* which functions as a length scale for the localization zone has to be introduced. The physical meaning of this length scale can probably be best understood when considering the Smeared Crack Model (see Section 3.2). Here the length scale provides the width over which the crack opening is smeared. Or in other words it is the reference length by which to transform the traction–separation law ($\underline{\sigma}$ – $\underline{\mathbf{w}}$) into a traction–strain law ($\underline{\sigma}$ – $\underline{\epsilon}$) such that it can be used in a continuum representation of the localization band. Models with fully regularized localization zones also take the "regularization" into account in their formulation of the constitutive equations. A Nonlocal Model for example provides a *nonlocal* constitutive law in which the nonlocal average of some material state parameter is used.

In a Strong Discontinuity Model (EDM, XFEM) two constitutive laws are required. One law which describes the behavior of the continuum (in form of a multi-dimensional stress–strain law) and one law which describes the traction–separation relationship governing the discontinuity (see Section 3.1.4). The simplest model is an elastic continuum combined with a tension free crack. The propagation of the crack tip can then be expressed within the framework of Linear Elastic Fracture Mechanics. However, for many practical problems Linear Elastic Fracture Mechanics are not very realistic. The situation can be improved by using a *Cohesive Crack Model* as it was proposed by Hillerborg and co-workers [HMP76]. The basic idea is to model the crack with a gradual loss of cohesion as the crack opening increases. This assumption can be justified for plain concrete but it is especially meaningful for Fiber Reinforced Cementitious Composites. A detailed explanation of the Cohesive Crack Model is given in Section 3.1.4. When using a Cohesive Crack Model the constitutive law for the continuum has to be supplemented by a traction–separation law.

This can either be done along the lines of the traction–separation laws used in Smeared Crack Models (linear, Hordijk etc. see Section 3.2) or by more sophisticated theories such as Damage and Plasticity.

3.1.4 The Cohesive Crack Model

In Section 3.1.2 some numerical modeling techniques for strain localization by a Discrete Crack Model were presented. One aspect that has not been discussed so far is the tip of the discontinuity (e.g. the crack tip). Linear Elastic Fracture Mechanics state that a stress singularity is present at the tip of a crack. This can cause numerical difficulties and assuring correct energy dissipation at the crack tip is problematic. A more realistic model was proposed by Dugdale [Dug60] and Barenblatt [Bar62]. They both considered an imaginary extension of the crack tip and applied cohesive forces to it. Later this concept was adopted by Hillerborg et al., who proposed the *Fictitious Crack Model* (sometimes also called the *Cohesive Crack Model*) for numerical crack growth simulations in concrete [HMP76].

The basic idea of the Cohesive Crack Model is relatively simple. Instead of immediately becoming stress free a crack is assumed to loose its cohesion gradually. A cohesive zone is introduced within which cohesive forces act on the surfaces of the newly formed crack (see Figure 3.6a). With increasing crack mouth opening the cohesive forces decrease until they vanish at a certain ultimate crack width. Having this in mind Hillerborg postulated that the cohesive forces acting on a crack are governed by a *traction–separation law*. The latter is directly related to the fracture energy of the material and it is therefore a means to assure correct energy dissipation. An example of a possible traction–separation law for normal concrete as proposed by [RCD86] is shown in Figure 3.6b.

The Cohesive Crack Model introduces a smooth transition of forces which is very beneficial in a numerical sense since it removes the stress singularity at the crack tip and also assures a controlled energy dissipation process. The final model represents a very clever way to combine fracture mechanics and Finite Element Analysis for crack propagation problems.

Although the Cohesive Crack Model could have been introduced for purely numerical reasons there is also a physical side to it. When looking at the formation of a crack under a microscope one will realize that this is not an instantaneous but rather a gradual process. At the tip of the crack a multitude of microscopic cracks (microcracks) will exist which gradually coalesced and finally join to form the extension of the macroscopic crack. In fracture mechanics this region at the crack tip is called the *fracture process zone*. The cohesive forces can be seen as a means to represent this fracture process zone at the crack tip. With increasing number and size of microcracks a steadily decreasing force can be transmitted across the fracture process zone, which explains the gradual loss of cohesion assumed by the Cohesive Crack Model.

The physical significance of the cohesive zone becomes even more obvious when considering Fiber Reinforced Cementitious Composites. Here the cohesive forces reflect the

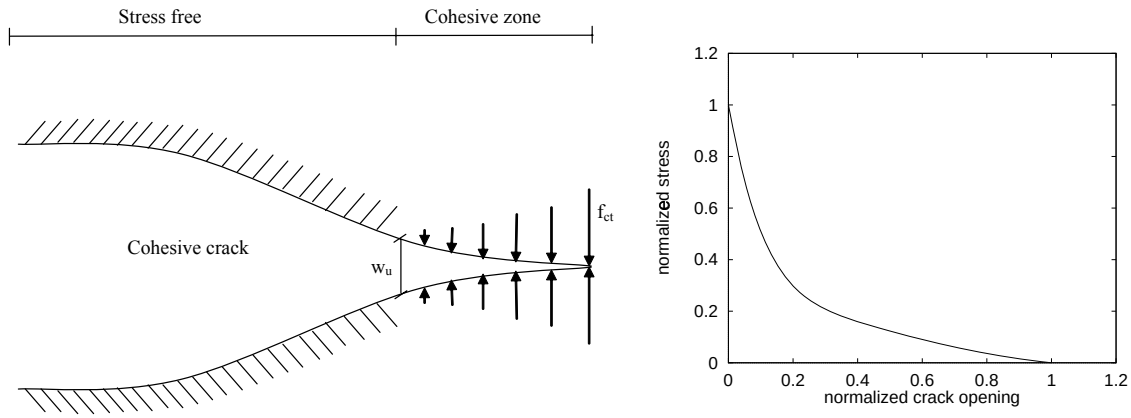

(a) Cohesive crack (adopted from [HMP76]) (b) Cohesive law (taken from [Jir00])

Figure 3.6

fiber bridging action, which decreases with increasing crack opening as a consequence of gradual fiber pullout.

Essentially the same principle is reflected in Smeared Crack Models (see Section 3.2). There cracking is also modeled as a continuous process and a gradual softening law is used in order to ensure correct energy dissipation.

3.2 Smeared Crack Models

The basic goal of Smeared Crack Models is to compute the softening behavior of materials in a Finite Element Analysis. In contrast to Discrete Crack Models where every crack is represented by a strong discontinuity the principal concept of the Smeared Crack Model is to represent a crack as an averaged strain over a certain cracking zone. In other words the influence of the crack is "smeared".

One can distinguish between three different commonly used Smeared Crack Models. The *Fixed Crack Model*, the *Multi-directional Fixed Crack Model* and the *Rotating Crack Model* [Rot91]. The Multi-directional Fixed Crack Model is an extension of the Fixed Crack Model which allows the formation of multiple cracks with different orientations at the same integration point. The main difference between the Fixed Crack Model and the Rotating Crack Model is that in the former the crack orientation is determined upon crack initiation and it is kept fixed whereas in the latter the orientation of a crack may change continuously. Although the Fixed Crack Model seems to be physically more meaningful (since a macroscopic crack has a given, irrevocable orientation) it does not necessarily yield more accurate results as we will see later in this chapter. Furthermore, the Rotating Crack Model has some procedural advantages over the Fixed Crack Model. The most prominent is probably that one does not have to worry about the complicated shear transfer mechanisms since in the Rotating Crack Model the axes of principal strain are

always aligned with the axes of principal stress (enforced coaxiality, see Section 3.2.4).

In his PhD thesis [Rot88] J.G. Rots demonstrated that the aforementioned three Smeared Crack Models can be unified in a single theoretical framework and that the individual models can be seen as limit cases of one generalized Smeared Crack Model. Before we can discuss the Fixed Crack Model (Section 3.2.2), the Multi-directional Fixed Crack Model (Section 3.2.3) and the Rotating Crack Model (Section 3.2.4) we will begin by explaining the fundamental concept behind Smeared Crack Models in the following Section 3.2.1.

3.2.1 The General Concept

The basic idea behind Smeared Crack Models is to represent a crack in form of a cracking strain which is smeared over a so-called *numerical localization band*. In order to do so the total strain has to be decomposed into an elastic strain and an inelastic cracking strain.

The Smeared Crack Model then postulates that the numerical localization band can be seen as the *fracture process zone* and assumes a gradual softening of this zone as proposed by the Cohesive Crack Model [HMP76]. For reasons of simplicity the softening stress–strain relationship of the fracture process zone is formulated in a coordinate system associated with the crack. This also allows for a more physical interpretation of the different cracking strain components. The first component is the tensile strain perpendicular to the cracking plain. It corresponds to the normal crack opening and it is associated with what is known as Mode I cracking in fracture mechanics (see Figure 3.7). In the three-dimensional case there are also two shear components (one in 2D) which correspond to Mode II and Mode III (only Mode II in 2D). A schematic representation of Mode II cracking and its corresponding Smeared Crack approximation are given in Figure 3.8.

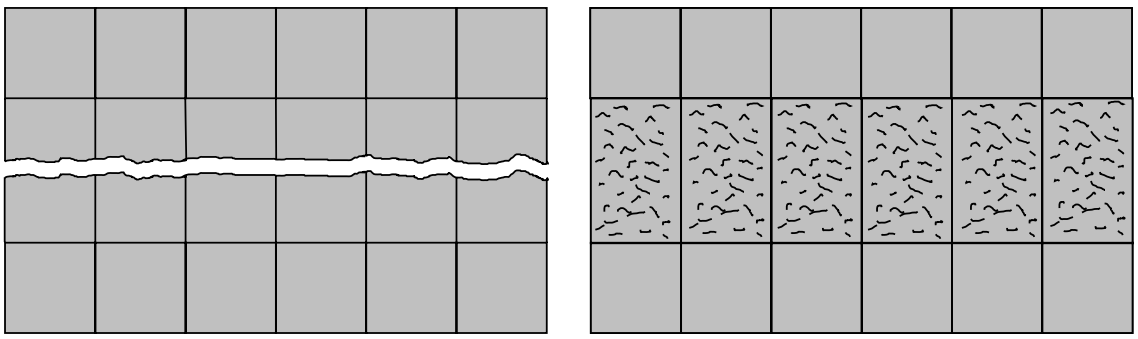

(a) Real crack (b) Smeared Crack approximation

Figure 3.7: Tensile cracking in the Smeared Crack Model (Mode I)

A further basic assumption of Smeared Crack Models is that the components of the softening stress–strain relationship are uncoupled in the local coordinate system associated with the crack. However, the model still allows for an *implicit* coupling of the components by using a cracking shear modulus that is a function of the Mode I cracking strain (see Section 3.2.2).

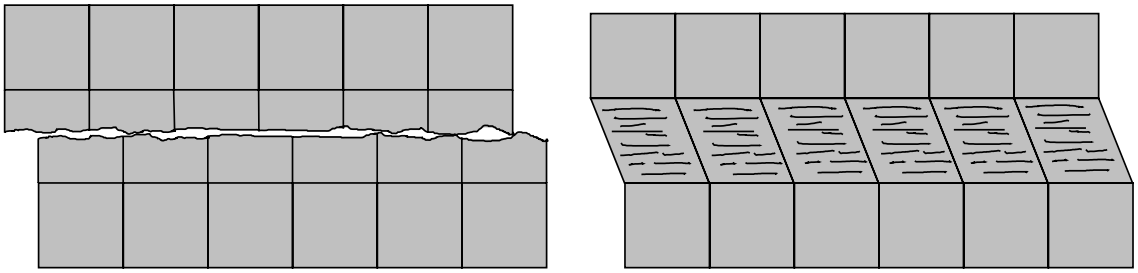

(a) Real crack (b) Smeared Crack approximation

Figure 3.8: Shear cracking in the Smeared Crack Model (Mode II)

Another important part of a Smeared Crack Model is a criterion for crack initiation. Usually initial crack formation is governed by a *cracking surface* which can be seen as the equivalent to a yield surface in the theory of Plasticity. The simplest but most frequently employed criterion is the constant tension cut-off criterion. It means that a crack is initiated as soon as the highest principal tensile stress reaches a certain limit value. This is also known as the *Rankine Criterion*.

Furthermore, it is necessary to describe the softening behavior of the crack in the spirit of the Cohesive Crack Model. This is done in form of a traction–separation law. Since the cracking behavior is expressed in a coordinate system associated with the crack and the constitutive relationships of Mode I and Mode II cracking are assumed to be uncoupled the traction–separation law is reduced to a scalar normal-stress vs. crack-opening law and a scalar shear-stress vs. crack-sliding law. The former basically expresses how much stress can be transmitted at a given crack opening. This will decrease from σ_{cc} at crack initiation until the crack becomes stress free after having reached a critical crack opening w_u. There are a number of different softening laws currently used in practice. These reach from simple models assuming a linear, bilinear or exponential decrease to more complicated ones such as *Hordijks Law* [Rot88].

One of the problems that arise with Smeared Crack Models is that they require the transformation of a discrete crack opening displacement into an equivalent cracking strain. Physically speaking a crack is a displacement discontinuity that is described by a traction–separation law ($\underline{\widetilde{\sigma}}_{cr} - \underline{\widetilde{\mathbf{w}}}$) in the Cohesive Crack Model. However, the Smeared Crack Model requires that this relationship is converted into a stress–strain law ($\underline{\widetilde{\sigma}}_{cr} - \underline{\widetilde{\epsilon}}_{cr}$) since a continuum representation of the crack is used. The critical issue is that every strain is dependent on the chosen "gage length". This poses a major problem because a crack represents a singularity with infinite strain (finite displacement over zero length). In order to solve this problem the already mentioned *numerical localization band* or *crack band* (see Section 3.1.1) is introduced [BO83]. The latter is assumed to represent the localized fracture process zone and it is taken as a gage length for the strain. In other words, the numerical localization bandwidth represents the width over which the cracking is spread. If the numerical localization band were not introduced the model would suffer from pathological mesh-size dependency (see Section 3.1.2).

Sometimes the numerical localization bandwidth is difficult to estimate a priori. In principle it should correspond to the width of the single layer of Finite Elements in which the deformations localize after cracking. Unfortunately, the width of the cracking zone is also dependent on the crack orientation with respect to the Finite Element mesh. In the simplest case when the crack localizes into a row of aligned elements the crack band is equal to the element size. However, if the crack passes through the mesh in a zigzag pattern a reasonable estimation of the numerical localization bandwidth becomes increasingly difficult. Also, special care has to be taken for higher order elements where the numerical integration scheme can have a strong influence on the choice of the cracking band. A table with some propositions is given in [Rot88].

While investigating the most favorable Finite Element formulation and meshing Rots found that crack localization is more accurately represented by many small elements with a constant strain interpolation than by fewer elements with higher order interpolation functions [Rot88]. The reason for this is that a discrete crack with "infinite strain over zero length" is more closely approximated by a constant strain over a narrow band than by a linear strain over a larger band. In addition, the constant strain formulation is also more compatible with the notion of "smearing" a crack, which implicitly assumes a constant cracking strain.

So far we have only discussed loading. When unloading occurs there are two basic options. The model either assumes secant unloading towards the origin or it assumes elastic unloading parallel to the linear, elastic stiffness. Of course, a case in-between these two extremes is also imaginable. Upon closure of a crack the cracking strain remains limited at zero since the crack faces cannot overlap. A nonlinear compressive behavior then has to be modeled within another theoretical framework such as for example the theory of Plasticity.

3.2.2 The Fixed Crack Model

As already mentioned, the main characteristic of the Fixed Crack Model is that the direction of cracking is determined upon crack initiation and it is kept fixed afterwards. Since the Fixed Crack Model also represents the theoretical bases for the other models it will be explained here in a bit more detail. This is done by applying the general concepts presented in Section 3.2.1 to the specific case of the Fixed Crack Model.

The first step is to decompose the total strain into a continuum strain of the uncracked bulk material $\underline{\epsilon}_{co}$ and a cracking strain that accounts for the cracks in the cracking band $\underline{\epsilon}_{cr}$. This is expressed in Equation (3.1). Note that all equations are formulated in incremental form as is customary for nonlinear Finite Element Analysis.

$$\Delta\underline{\epsilon} = \Delta\underline{\epsilon}_{co} + \Delta\underline{\epsilon}_{cr} \qquad \text{Decomposition of strain} \tag{3.1}$$

Next, the relationship between the strain in the local coordinate system associated with

the crack $\underline{\widetilde{\epsilon}}$ and the strain in the global coordinate system $\underline{\epsilon}$ is established (Equation 3.2a). The same is done for the local stress $\underline{\widetilde{\sigma}}$ and the global stress $\underline{\sigma}$ (Equation 3.2b). In Equations (3.2) $\mathbf{R}_\epsilon$ is the standard transformation matrix that performs a rotation of the strain vector from the local to the global coordinate system (or vice versa $\mathbf{R}_\epsilon^T$).

$$\Delta\underline{\epsilon} = \mathbf{R}_\epsilon \cdot \Delta\underline{\widetilde{\epsilon}} \qquad \text{Rotation of strain} \tag{3.2a}$$

$$\Delta\underline{\widetilde{\sigma}} = \mathbf{R}_\epsilon^T \cdot \Delta\underline{\sigma} \qquad \text{Rotation of stress} \tag{3.2b}$$

Furthermore, the constitutive models for the uncracked bulk material and for the crack are required. They are expressed in the traditional way by a constitutive matrix $\mathbf{D}_{co}$ resp. $\widetilde{\mathbf{D}}_{cr}$ as given by Equations (3.3). Note that since the constitutive laws are formulated incrementally $\mathbf{D}_{co}$ and $\widetilde{\mathbf{D}}_{cr}$ represent the tangent constitutive matrices at the current deformation state. For the case of a plane-stress analysis the constitutive matrix representing the cracks consists of a 2×2 matrix and it is conveniently formulated in the local coordinate system associated with the cracks. Since Mode I and Mode II are assumed to be uncoupled (see Section 3.2.1) the crack constitutive matrix is diagonal (has no off-diagonal terms). The constitutive law for the uncracked bulk material can be expressed by any kind of linear or nonlinear constitutive matrix.

$$\Delta\underline{\sigma}_{co} = \mathbf{D}_{co} \cdot \Delta\underline{\epsilon}_{co} \qquad \text{Bulk material constitutive law} \tag{3.3a}$$

$$\Delta\underline{\widetilde{\sigma}}_{cr} = \widetilde{\mathbf{D}}_{cr} \cdot \Delta\underline{\widetilde{\epsilon}}_{cr} \qquad \text{Crack constitutive law} \tag{3.3b}$$

Solving the system of the Equations (3.1), (3.2), (3.3) together with the fact that the local equilibrium of a cracked material point requires that $\Delta\underline{\widetilde{\sigma}}_{co} = \Delta\underline{\widetilde{\sigma}}_{cr} := \Delta\underline{\widetilde{\sigma}}$ leads to the following relationship between the total stress increment $\Delta\underline{\sigma}$ and the total strain increment $\Delta\underline{\epsilon}$ given in Equation (3.4).

$$\Delta\underline{\sigma} = \underbrace{\left[\mathbf{D}_{co} - \mathbf{D}_{co}\mathbf{R}_\epsilon \left(\widetilde{\mathbf{D}}_{cr} + \mathbf{R}_\epsilon^T \mathbf{D}_{co}\mathbf{R}_\epsilon\right)^{-1} \mathbf{R}_\epsilon^T \mathbf{D}_{co}\right]}_{\mathbf{D}_{smcr}} \cdot \Delta\underline{\epsilon} \tag{3.4}$$

From Equation (3.4) it can easily be seen that a new tangent constitutive matrix for the cracked material $\mathbf{D}_{smcr}$ can be determined by combining the tangent constitutive matrix of the uncracked bulk material with the tangent constitutive matrix accounting for the cracks. It is important to note that in general the tangent constitutive matrix accounting for the cracks is not constant but will change with increasing crack opening (resp. cracking strain). This variation is given by the aforementioned *traction–separation law* which will

be detailed later on. Another important observation that can be made from Equation 3.4 is that Smeared Crack Models account for cracking by modifying the constitutive matrix. This is in direct contrast to other methods such as the eXtended Finite Element Method (see Section 3.3) which modify the element kinematics to account for cracks.

After having established the tangent constitutive matrix the standard procedures for nonlinear Finite Element Analysis is followed. I.e. the tangent stiffness matrices of all Finite Elements are formed, assembled and subsequently used in a traditional iterative procedure for nonlinear analysis.

The only remaining question in the outlined procedure above is how to define the tangent constitutive matrix for the cracks $\widetilde{\mathbf{D}}_{cr}$. Taking into account the assumption of uncoupled components (see Section 3.2.1) the tension-softening behavior of the stress normal to the crack plane can be expressed by a scalar relationship between the Mode I cracking-stress and the Mode I cracking-strain. For this purpose a traction–separation law ($\widetilde{\sigma}_{cr}$ – $\widetilde{w}$) describing the behavior of a discrete crack in the softening regime in analogy to the Cohesive Crack Model is defined. For reasons of simplicity let us consider a linear softening law as shown in Figure 3.9 (and as given by Equation 3.5). However, in practice the appropriate choice of the softening law is essential [Rot86, RdB89].

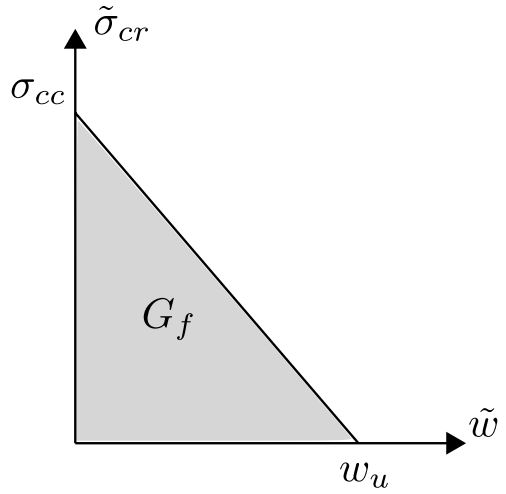

Figure 3.9: Linear softening traction–separation law

$$\widetilde{\sigma}_{cr} = \sigma_{cc} \cdot \left(1 - \frac{\widetilde{w}}{w_u}\right) = \sigma_{cc} - \frac{\sigma_{cc}}{w_u} \cdot \widetilde{w} \tag{3.5}$$

Often the ultimate crack opening w_u that marks the point at which a crack becomes stress free is difficult to determine experimentally. Therefore, the traction–separation law is usually defined by the tensile strength at crack initiation σ_{cc} (cracking strain), the shape of the softening curve (linear in this example) and the Mode I fracture energy G_f. Using the fracture energy as a parameter also has the advantage that it assures consumption of the correct amount of energy during the cracking process. The fracture energy is equal

to the area under the traction–separation curve as indicated in Figure 3.9. For the case of linear softening it is given by Equation (3.6). The derivation of the ultimate crack opening is then straightforward.

$$G_f = \sigma_{cc} \cdot \frac{w_u}{2} \quad \Rightarrow \quad w_u = 2 \cdot \frac{G_f}{\sigma_{cc}} \tag{3.6}$$

Next, the Mode I tangent softening modulus E_{cr}^I for the discrete crack is computed. It corresponds to the slope of traction–separation curve. In general it is a function of the crack opening $\widetilde{w}$ but in the case of this example it is constant and defined by Equation (3.7).

$$E_{cr}^I = -\frac{\sigma_{cc}}{w_u} = -\frac{1}{2}\frac{{\sigma_{cc}}^2}{G_f} \tag{3.7}$$

In the more general case of a nonlinear softening law the tangent softening modulus is typically expressed by using a parameter $k(\widetilde{w})$ that is a function of the crack opening and the shape of the softening curve (see Equation (3.8)).

$$E_{cr}^I = -\frac{1}{k}\frac{{\sigma_{cc}}^2}{G_f} \tag{3.8}$$

Up to this point all considerations were made for a discrete crack. Since the traditional Finite Element Analysis does not accept the singularity of a crack in the displacement field we now proceed by *smearing* the crack over the so-called *numerical localization bandwidth* h (see also Section 3.2.1). In order to guarantee mesh independence the numerical localization bandwidth needs to be determined from the mesh size and corresponds to the width of the single layer of Finite Elements into which the deformations localize. Note that the "smearing" implies a constant cracking strain over the cracking bandwidth. Following the outlined procedure the traction–separation law is transformed from a stress vs. crack-opening relationship $\widetilde{\sigma}_{cr}(\widetilde{w})$ into a stress vs. cracking-strain relationship $\widetilde{\sigma}_{cr}(\widetilde{\epsilon}_{cr})$ by dividing the crack opening by the width of the numerical localization bandwidth. This leads to the following tangent constitutive modulus given in Equation (3.9).

$$D_{cr}^I = -\frac{1}{k}\frac{{\sigma_{cc}}^2 \cdot h}{G_f} \tag{3.9}$$

As mentioned in Section 3.2.1 the Fixed Crack Model does not enforce coaxiality between the stress and the strain, therefore, shear transfer across cracks is possible. The latter is usually described by reducing the elastic shear modulus G with a factor β which is called the *shear retention factor*. This is expressed in Equation (3.10).

$$D_{cr}^{II} = \beta \cdot G \tag{3.10}$$

In the past the shear retention factor was sometimes assumed to be constant. The advantage of such a model is that it conserves the independence of the shear and the normal stresses in the cracking zone. However, it is physically not very realistic since the shear resistance along a crack is produced by friction and aggregate interlock, two phenomena which are clearly influenced by the crack opening. Moreover, it would mean that even cracks that have opened completely (no more stress transfer in tension) would still transmit shear forces. A better choice is to reduce the shear reduction factor linearly or exponentially with increasing Mode I crack opening. A linearly decreasing shear reduction factor is given in the following Equation (3.11) where $\widetilde{\epsilon}_{cr}$ is the Mode I cracking strain in the coordinate system associated with the crack and ϵ_u is the ultimate strain at which the crack becomes stress free.

$$\beta = 1 - \frac{\widetilde{\epsilon}_{cr}}{\epsilon_u} \tag{3.11}$$

Note that using a shear retention factor which depends on the Mode I cracking strain adds an implicit coupling to the constitutive law.

3.2.3 The Multi-directional Fixed Crack Model

The Multi-directional Fixed Crack Model is a simple extension of the Fixed Crack Model. It allows for the formation of multiple cracks with different orientations at the same integration point. The development is quite straight forward. The cracking strain is simply decomposed into separate strains for each of the multiple cracks. Every crack is monitored individually and a coordinate system transformation for each crack is performed.

In order to limit the total number of cracks at the same integration point an additional crack initiation criterion has to be introduced. It is called the *threshold angle criterion*. According to it a new crack can only form if the principal stress directions differ by more than the threshold angle from all preexisting cracks. This means that the formation of a new crack can be triggered in two ways: Either a new crack is initiated by a principal tensile stress that exceeds the first cracking stress (orthogonal cracking), or it is triggered by a rotation of the principal stress axes by more than the threshold angle [Rot88].

An important consequence of this is that the stress inside the material can at certain points exceed the first cracking stress because the threshold angle criterion is not fulfilled. In general this leads to an overly stiff response. However, the situation is certainly improved in comparison to the Fixed Crack Model where the same problem is much more pronounced.

An additional requirement for the Multi-directional Fixed Crack Model is to keep track of the damage that occurred during the cracking process. After several cracks have formed at an integration point subsequent cracks at the same location should not consume the same amount of fracture energy as was the case during formation of the first crack. Therefore,

it is assumed that the total fracture energy G_f is reduced by the amount that was already consumed during previous cracking activity at that integration point. In other words, only the tail part of the traction–separation law can be activated by a new crack. Note, that this only applies to the case of cracks which are triggered by a violation of the threshold angle criterion and not for ("orthogonal") cracks that are formed by violation of the first cracking stress criterion.

A further issue that deserves mentioning here, are the numerical problems that may arise during a simulation with Multi-directional Fixed Crack Models. Because there are a large number of possible combinations of loading and unloading when several cracks are active at the same integration point the uniqueness of a solution may be lost.

3.2.4 The Rotating Crack Model

In contrast to the Fixed Crack Models the Rotating Crack Model postulates that the crack direction is not "frozen" upon crack initiation. It is rather assumed that the crack changes its orientation in order to be aligned with the directions of principal strain. By consequence the axes of orthotropy are always coaxial with the directions of principal strain which implies that also the axes of principal stress are aligned with those of principal strain. This property is known as *enforced coaxiality*.

The main advantage of using a Rotating Crack Model is that there can be no artificial buildup of stresses above the ultimate cracking stress and there is no necessity to consider shear transfer because the shear components are always zero in the coordinate system associated with the crack.

J.G. Rots showed that the Rotating Crack Model can be seen as a limit case of the Multi-directional Fixed Crack Model [Rot88]. There are two basic assumptions that are necessary to unify the Rotating Crack Model with the Multi-directional Fixed Crack Model. The first one is that the threshold angle is set to zero and the second one is that the shear retention factor has to be determined in such a way as to ensure coaxiality. In other words, the shear retention factor is always chosen such as to eliminate the shear stress in the crack coordinate system. Furthermore, all previous cracks have to be removed from memory as soon as a new crack is activated. However, in analogy with the Multi-directional Fixed Crack Model the cracking energy is not recovered upon rotation.

3.2.5 Deficiencies of Smeared Crack Models

After having explained the general concept and functioning of the most important Smeared Crack Models this section will focus on some issues that are created by the model assumptions.

As a very general observation, one can state that the major deficiencies of Smeared Crack Models arise from using a continuum model for the description of a phenomenon which

is by its physical nature discontinuous. Or formulated differently: the cause for most of the problems with Smeared Crack Models is the artifice of "smearing" the cracks. The deficiencies are most pronounced at large crack openings because the kinematics of complete material separation are not adequately represented by the Finite Element interpolation fields.

The first consequences of the poor kinematic representation are the so-called *stress locking effect* and the related *spurious stress transfer*. Because the compatibility of the displacement field in a Finite Element Analysis has to be assured the cracking strain will influence both strain components of a Finite Element (except if the crack is oriented parallel to an element side). This can easily be shown by the example in Figure 3.10 (adopted from [Rot88]).

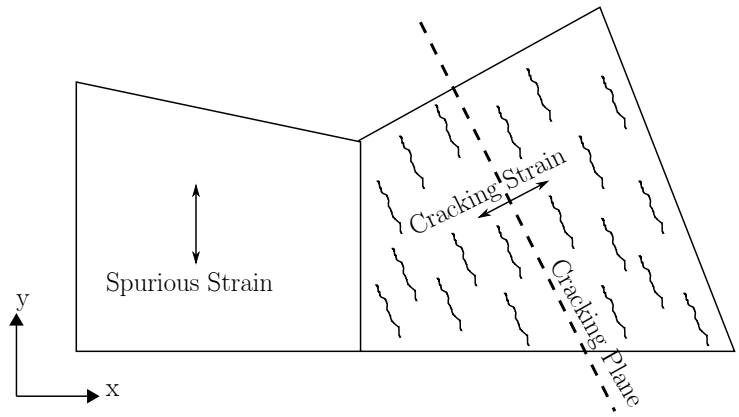

Figure 3.10: Spurious stress transfer (adopted from [Rot88])

Consider the two elements shown in Figure 3.10. One of them is crossed by a crack. Following the Smeared Crack Model the discrete crack is smeared over the right element as represented schematically in the figure. This creates a cracking strain. As becomes clear from the indicated direction the cracking strain does also have a component in the global y direction. Because of compatibility requirements between the left and the right element along their common edge the y component of the cracking strain in the right element will induce a vertical strain in the left element as well. The physical nature of the problem on the other hand dictates that all elements which are on the left side of the crack should be completely dissociated from those on the right side. It is clear that they should unload after crack formation rather than being loaded any further. It is interesting to note that even after the crack has reached the ultimate crack opening (at which point no stresses whatsoever should be transmitted) the spurious strains and resulting stresses will still continue to increase with increasing crack opening. This can even go so far as to lead to cracking of the left element as soon as it in turn reaches its cracking stress (*spurious cracking*).

The left element in the example on the other hand will resist against being strained by the spurious strain. The consequence is an overly stiff response in the softening regime with increasing imprecision as the crack opens.

Another deficiency that is strongly related to the same mechanism that creates stress locking is the so-called *mesh-induced bias*. It means that the direction of the fracture path is influenced by the mesh of the Finite Element model. It appears that the fracture path preferentially follow the principal directions of the mesh. This bias is more pronounced for the Rotating Crack Model than for the Fixed Crack Models since the cracks are free to rotate and align with the mesh.

A very comprehensive explanation of the reason for mesh bias is given by [JZ98]. Therein a triangular element that is crossed by a crack is investigated (see Figure 3.11).

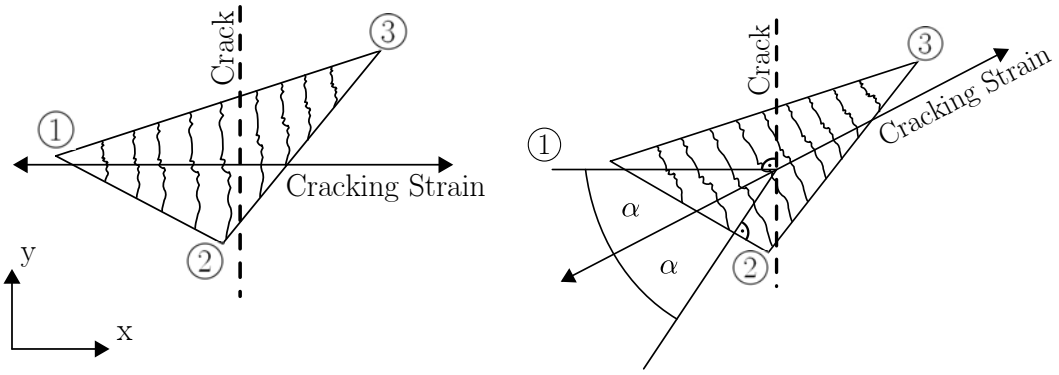

(a) Crack direction corresponding to the physical nature of the problem

(b) Crack direction in a FE-mesh when crack openings become large

Figure 3.11: Mesh bias (adopted from [JZ98])

The derivation of the general strain equations for this triangular element is straightforward and of little interest here. Therefore, the results are directly presented. For more details refer to [JZ98, Jir00]. Using area coordinates for the Finite Element interpolation fields the strain vector after cracking can be represented as given by Equation (3.12).

$$\begin{Bmatrix} \epsilon_x \\ \epsilon_y \\ \gamma_{xy} \end{Bmatrix} = \begin{Bmatrix} 1 \\ -\nu \\ 0 \end{Bmatrix} \cdot \frac{\widetilde{\sigma}_{cr}}{E} + \begin{Bmatrix} y_1 - y_2 \\ 0 \\ x_2 - x_1 \end{Bmatrix} \cdot \frac{\widetilde{w}}{2A} \tag{3.12}$$

Equation (3.12) shows the decomposition of the resulting strain vector into two parts. Firstly an elastic strain which depends only on the stress $\widetilde{\sigma}_{cr}$, the module of elasticity E and Poisson's ratio ν. And secondly a cracking strain which depends on the crack opening $\widetilde{w}$, the area of the triangular element A and the difference of nodal coordinates x_1, x_2 respectively y_1, y_2. The interesting thing about this result is the shear strain component. Although the physical nature of the problem clearly indicates that there should be no global shear strain (see Figure 3.11a) the Finite Element interpolation creates a shear strain term as soon as the crack opens ($\widetilde{w}$ is non-zero) and the element edge 1–2 is not parallel to the crack direction ($x_2 - x_1 \neq 0$). By consequence this spurious shear term creates a mesh bias by rotating the directions of principal strain. The limit case when $\widetilde{w}$ tends towards infinity is shown in Figure 3.11b. The derivation of this result in not

presented here but can be found in [Jir00]. Simply note that the limit angle α by which the cracking direction deviates from the true crack direction is half the angle between the element side 1–2 and the true crack direction. Although the existence of mesh-induced bias is demonstrated here for the very specific case of a triangular element quadrilateral meshes show the same deficiency.

Another problem with Smeared Crack Models is the appearance of spurious kinematic modes. This phenomenon manifests in form of Finite Element nodes "running out of control". As a consequence the global stiffness matrix becomes singular and the solution algorithm has to be stopped. According to [Rot88] this problem was found to exist for all types of elements and numerical integration schemes although no explanation of the cause was given.

3.3 The Extended Finite Element Method

The eXtended Finite Element Method (XFEM) is an extension of the Finite Element Method which allows for the incorporation of a priori knowledge about the analytical solution of a problem. The basic idea is to extend the set of standard Finite Element interpolation functions (shape functions) with additional so-called *enrichment functions*. The latter are chosen based on the expected form of the solution. The XFEM is a very general method and it can be applied to an infinite number of physical problems. Mostly it is used for cases where the incorporation of additional knowledge can improve the convergence or the accuracy of the solution, i.e. in situations where the solution field exhibits strong gradients, discontinuities or any other type of "rough" behavior. In the following we will focus on the application of the XFEM to cracking and modeling of strong discontinuities.

3.3.1 The General Concept

The eXtended Finite Element Method is based on the Partition of Unity Method (PUM) which was published by Melenk and Babuška in 1996 [MB96, BM97]. In fact the XFEM is a particular application of the PUM as we will see later.

Most of the development of the XFEM was done by professor Belytschko's group at the Northwestern University in Evanston, Illinois where the name *eXtended Finite Element Method* was coined. The first applications were oriented towards static crack growth in an elastic continuum [BB99, MDB99] but research has now been extended to various fields of physics such as hydromechanics and all sorts of interface problems.

In parallel to the eXtended Finite Element Method a practically identical method called the Generalized Finite Element Method (GFEM) was developed by Strouboulis and co-workers [SBC00, SCB01]. Like the XFEM the GFEM is also based on the Partition of

Unity Method. While the applications of Belytschko et al. were more oriented towards crack growth those of Strouboulis and co-workers were focusing on re-entrant corner singularities.

The advantage of using the eXtended Finite Element Method for the simulation of crack growth is that the crack geometry can be arbitrary with respect to the Finite Element mesh. As was already discussed in Section 3.1.1 a crack represents a strong discontinuity in the displacement field. The XFEM exploits this a priori knowledge about the solution and extends or in technical terms *enriches* the approximation space (the set of standard shape functions) with additional discontinuous functions. As a consequence the crack is modeled within the elements themselves making the crack path independent of the Finite Element mesh. Note that the enrichment is an enhancement of the kinematics of a Finite Element and it is independent of the constitutive law.

The huge success of the eXtended Finite Element Method as opposed to similar meshless methods such as the Element-Free Galerkin Method (EGM) [BLG94] can probably be explained by its compatibility with the "standard" Finite Element Method which is well known and commonly employed. Or in other words, the XFEM elegantly combines the advantages of meshless methods with the computational efficiency and robustness of the Finite Element Method.

Next, let us look at the mathematical background of the Partition of Unity Method. Before we can state the Partition of Unity Principle we need to introduce a few preliminary definitions.

A set of n functions φ_i $(i = 1 \dots n)$ which is uniquely defined on a domain Ω_{pu} is called a *Partition of Unity* if the property stated in Equation (3.13) is satisfied.

$$\sum_{i=1}^{n} \varphi_i(\underline{\mathbf{x}}) = 1 \quad \forall \underline{\mathbf{x}} \in \Omega_{pu} \tag{3.13}$$

Verbally this means that a set of functions form a Partition of Unity if the sum of their values at every location $\underline{\mathbf{x}}$ within the considered domain Ω_{pu} is equal to unity. An additional condition that has to be satisfied is that the functions in consideration are *linearly independent*.

An example of three functions $\varphi_{1,2,3}$ that form a Partition of Unity in the one-dimensional domain $\Omega_{pu} = [-1, 1]$ is given in the following:

$$\begin{aligned}
\varphi_1(x) &= \frac{1}{2}(1-x) - \frac{1}{2}(1-x^2) && \forall x \in [-1,1] \\
\varphi_2(x) &= \frac{1}{2}(1+x) - \frac{1}{2}(1-x^2) && \forall x \in [-1,1] \\
\varphi_3(x) &= (1-x^2) && \forall x \in [-1,1]
\end{aligned}$$

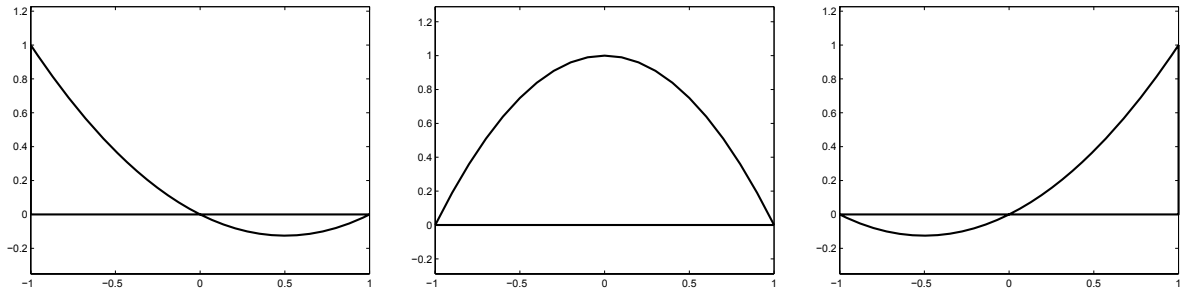

(a) φ_1 (b) φ_3 (c) φ_2

Figure 3.12: Example of three functions forming a Partition of Unity

A plot of these three functions is given in Figure 3.12. It is easily verified that the sum of all three functions is effectively equal to unity on the entire domain $[-1, 1]$. The same principle is also valid for the multi-dimensional case. In 2D for example the coordinate x simply becomes a vector $\underline{\mathbf{x}}$ and the domain Ω_{pu} becomes a surface. Note that Finite Element shape functions always form a Partition of Unity because this is necessary to represent rigid body displacements. In fact, the three functions depicted above are nothing other than the 2nd-order polynomial shape functions for an isoparametric 3-node truss element.

The Partition of Unity Principle states that any unknown field (e.g. horizontal displacement field $u(\underline{\mathbf{x}})$) in a given domain Ω_{pu} can be interpolated as given in Equation (3.14).

$$u(\underline{\mathbf{x}}) = \sum_{i=1}^{n} \varphi_i(\underline{\mathbf{x}}) \left(a_i + \sum_{j=1}^{m} \Psi_j(\underline{\mathbf{x}}) b_{ij} \right) \tag{3.14}$$

Where the φ_i are a set of n functions which form a Partition of Unity, a_i and b_{ij} are discrete nodal values in the domain Ω_{pu} and Ψ_j are a set of m so-called *enrichment functions*. Let us consider the case where only one enrichment function is used. The interpolation field can then be expressed by Equation (3.15).

$$u(\underline{\mathbf{x}}) = \underbrace{\sum_{i=1}^{n} \varphi_i(\underline{\mathbf{x}}) a_i}_{\text{standard}} + \underbrace{\sum_{i=1}^{n} \varphi_i(\underline{\mathbf{x}}) \Psi(\underline{\mathbf{x}}) b_i}_{\text{enrichment}} \tag{3.15}$$

This shows that the interpolation field can be decomposed into a standard part which interpolates the standard nodal degrees of freedom a_i and an enriched part which adds the contribution of the enriched nodal degrees of freedom b_i. Since the functions φ_i form a Partition of Unity the enrichment function Ψ can be reproduced exactly (all $a_i = 0$ and all $b_i = 1$).

It is by the way not necessary to use the same Partition of Unity for the standard and the enriched degrees of freedom. The Partition of Unity Principle can therefore also be

written in the form of Equation (3.16).

$$u(\underline{\mathbf{x}}) = \sum_{i=1}^{n} \varphi_i(\underline{\mathbf{x}}) a_i + \sum_{i=1}^{n} \hat{\varphi}_i(\underline{\mathbf{x}}) \Psi(\underline{\mathbf{x}}) b_i \tag{3.16}$$

The idea of the eXtended Finite Element Method is to use the Partition of Unity Principle in the Finite Element framework. Instead of the functions φ_i which form a *global* Partition of Unity on the entire domain Ω_{pu} an assembly of overlapping patches which form *local* Partitions of Unity on the local domains Ω_e of the individual Finite Elements is used. Because the standard Finite Element shape functions N_i already form local Partitions of Unity they are usually also directly used as Partition of Unity Functions for the enrichment. The advantage of using local Partitions of Unity is that a specific enrichment can be added locally without modifying the entire computational domain and thereby taxing the solution speed with unnecessary additional degrees of freedom in regions where the enrichment is not needed. As a consequence the global stiffness matrix of the Finite Element problem remains sparse. Note that the enrichment function Ψ still has global character and is defined over the entire domain. It is localized by multiplying it with the local Partition of Unity Functions which perform the task of "windowing" the enrichment function so to speak. Furthermore, the enrichment function is completely mesh-independent. As a final result the hereby produced *local enrichment* inherits the good approximation capabilities from the global enrichment function but it also inherits the local character from the Partition of Unity Functions. One other very important and fundamental property of the Partition of Unity Method is that it automatically enforces continuity of the enriched interpolation field across element boundaries and thereby produces *conforming* elements.

The application of the PUM to the specific case of the XFEM can be written as given by Equation (3.17) [BL05].

$$u(\underline{\mathbf{x}}) = \sum_{\text{all nodes}} N_i(\underline{\mathbf{x}}) u_i + \sum_{\text{all enriched nodes}} N_i(\underline{\mathbf{x}}) \Psi(\underline{\mathbf{x}}) e_i \tag{3.17}$$

Any unknown field u in the computational domain Ω is expressed by the nodal values u_i and e_i which are interpolated appropriately. The interpolation of the standard field is done by the customary Finite Element shape functions N_i. In a certain subdomain (the enriched domain Ω_{enr}) the unknown field is enriched by an additional function Ψ whose magnitude is determined by additional nodal degrees of freedom e_i. This means that in the enriched domain an additional field is superimposed. The character of this field is given by the enrichment function Ψ. The multiplication with the standard shape functions acts as a filter activating the enrichment function only in the region where it is necessary (windowing it). In order to avoid confusions concerning the used terminology in this thesis let us clarify the following: The function Ψ which describes the "character" or "type" of the global enrichment is called *enrichment function* or *global enrichment*

function. The functions which result from the multiplication of the local Partition of Unity Functions (e.g. standard shape functions) with the global enrichment function are called *local enrichment functions* or *enriched shape functions* and are usually denoted by $N_{enr,i}$ (see Equation 3.18). The local enrichment functions take the role of shape functions for the enrichment field which is superimposed on the standard field.

$$N_{enr,i}(\underline{\mathbf{x}}) = N_i(\underline{\mathbf{x}})\Psi(\underline{\mathbf{x}}) \tag{3.18}$$

The enrichment function Ψ can have many different forms and it will depend on the underlying problem and the a priori knowledge about the solution. However, there is one restriction. The enrichment function should not be contained in the standard interpolation space. If this were the case the system of equations would become linearly dependent which would mean that the solution would loose its uniqueness resulting in a singular stiffness matrix. Apart from that any form of enrichment function (even a discontinuous one) can be envisaged.

Let us consider the example of a truss element with standard linear shape functions as shown in Figure 3.13. As we discussed before these shape functions form a local Partition of Unity.

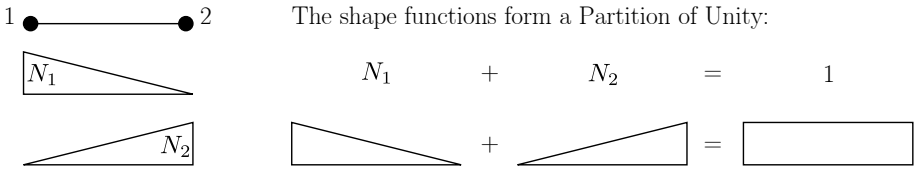

Figure 3.13: Standard truss element with linear shape functions

Next, we will enrich this element by a discontinuous shape function called the *Heaviside function*. The Heaviside function takes the value 0 on the left side of the discontinuity and the value 1 on the right side of the discontinuity. In the example a discontinuity shall be present at the location indicated by a dashed line in Figure 3.14. The latter shows the chosen discontinuous global enrichment function Ψ (Heaviside function) as well as the local enrichment functions which are obtained by multiplying the standard shape functions N_i with the enrichment function (local Partition of Unity Principle). Figure 3.14 also shows that the enrichment function can be reproduced exactly as was mentioned earlier. Note that both local enrichment functions depicted in Figure 3.14 are associated with additional degrees of freedom at the corresponding nodes. The global character of the enrichment function can be seen more clearly in the example shown in Figure 3.17 on Page 87 where more than one element is present.

In standard Finite Element Analysis the shape functions are constructed in such a way that the nodal degrees of freedom directly correspond to the value of the interpolated field (e.g. the displacement field) at the location of the corresponding node. If the PUM is applied without modification this physical interpretation is unfortunately lost since the contribution of the enrichment field is added to the standard field. However, by applying

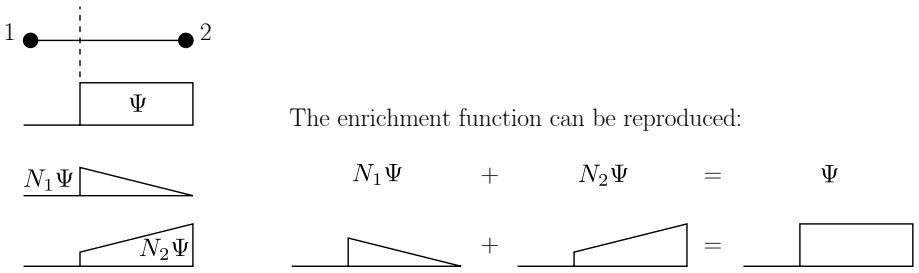

Figure 3.14: Enrichment function Ψ and resulting local enrichment functions

a suitable *shift* to the basis of the local enrichment the aforementioned characteristic of the standard degrees of freedom can be recovered. In order to achieve this goal it has to be ensured that the local enrichment takes the value 0 at the location of the node with which it is associated. This is done by subtracting the value of the global enrichment function at the location of the corresponding node (which is denoted by $\underline{\mathbf{x}}_i$). The modified local Partition of Unity Principle from Equation 3.17 then becomes Equation (3.19).

$$u(\underline{\mathbf{x}}) = \sum_{\text{all nodes}} N_i(\underline{\mathbf{x}}) u_i + \sum_{\text{all enriched nodes}} \underbrace{N_i(\underline{\mathbf{x}}) \Big(\Psi(\underline{\mathbf{x}}) - \Psi(\underline{\mathbf{x}}_i) \Big)}_{N^s_{enr,i}(\underline{\mathbf{x}})} e_i \tag{3.19}$$

This shift of the basis is admissible since it modifies the enrichment only by a multiple of the standard Finite Element shape functions. Applying the principle from Equation (3.19) to the previously introduced truss example results in the following Figure 3.15. The latter also shows that the enrichment is in fact only shifted by a multiple of the associated standard shape function.

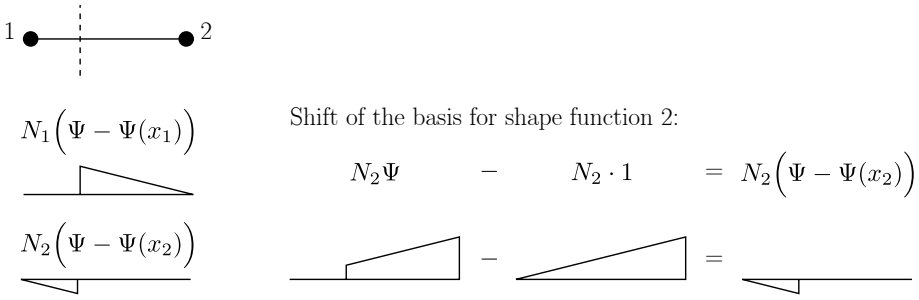

Figure 3.15: Final enrichment for a discontinuous truss element after shift of its basis

Putting everything together this finally yields the following Equation (3.20) for the displacement field interpolation of the eXtended Finite Element Method (the shifted enriched shape functions $N^s_{enr,i}$ are given by Equation 3.19).

$$u(\underline{\mathbf{x}}) = \sum_{\text{all nodes}} N_i(\underline{\mathbf{x}}) u_i + \sum_{\text{all enriched nodes}} N^s_{enr,i}(\underline{\mathbf{x}}) e_i \tag{3.20}$$

Let us emphasize that in the eXtended Finite Element Method the local enrichment functions (like the standard shape functions) are associated with degrees of freedom and those in turn are associated with nodes. Because continuity of the interpolation field at the nodes is required the domain of influence of a degree of freedom (called its *support*) extends to all elements connected to the corresponding node. In other words, the enrichment influences all elements that are directly connected to the node with which an enriched degree of freedom is associated. That is also the reason why one usually talks about *nodal enrichment* in the XFEM. Also, this once more underlines the local character of the enrichment. The given example with a Heaviside enrichment shown in Figure 3.14 presents a special case because after shifting the enriched shape functions are zero outside of the element where the discontinuity is located. As a consequence they do not need to be considered in the adjacent elements. However, for most other enrichments (or for the Heaviside enrichment in 2D) this is not the case.

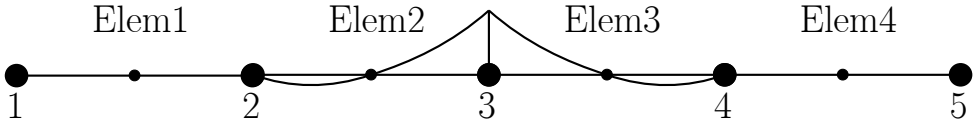

Figure 3.16: Support of node number 3

The concept of the "support" of a node is illustrated in Figure 3.16 which shows a mesh consisting of four three-node truss elements (two external nodes and one internal node) with quadratic shape functions. The influence of node 3 extends to the elements 2 and 3. Therefore, the support of node 3 consists of elements 2 and 3. The same is true for the enriched shape functions which influence the field of all elements in the support of the respective node.

3.3.2 An Illustrative Example

In the following the fundamental notions and basic principles of the XFEM introduced in Section 3.3.1 will be illustrated by an example. Although the eXtended Finite Element Method can be used to incorporate any type of function into the displacement field of a Finite Element problem the example is oriented towards crack modeling which means that a strong discontinuity i.e. a "jump" is introduced.

Let us assume that the discontinuous displacement field $u(x)$ shown in Figure 3.17 should be reproduced by a number of eXtended Finite Elements. The nodal values of the target displacement field are indicated in the figure (u_i). The "jump" in the field is clearly apparent and it separates the computational domain into a negative part Ω^- and a positive part Ω^+. Figure 3.17 also shows the enrichment function Ψ which should be incorporated into the Finite Element solution space. The global character of the enrichment function is clearly apparent. However, due to fact that the XFEM uses a local Partition of Unity the nodes of the Finite Element mesh only have to be enriched locally (indicated by circled dots). In the rest of the domain the enrichment function is constant. As such, it is

already contained in the standard approximation space and therefore requires no further enrichment.

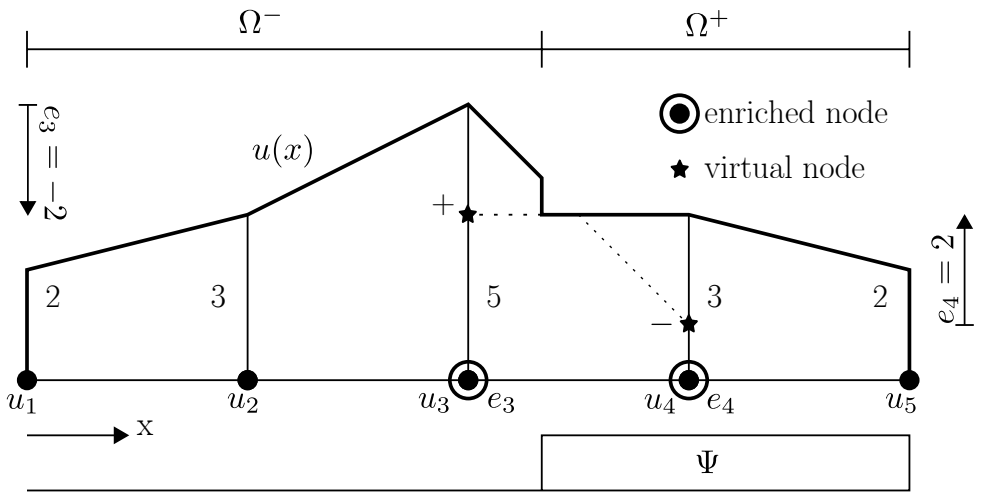

Figure 3.17: Discontinuous displacement field and Finite Element configuration

Let us first focus on the elements with a continuous displacement field. Figure 3.18 shows how the displacement field of those elements can be reproduced by the standard Finite Element shape functions. The linear shape functions introduced in Figure 3.13 are used. The nodal degrees of freedom can be directly identified in Figure 3.17 and they indicate the number of times a specific shape function has to be taken in order to reproduce the displacement field. Up to this point the procedure corresponds to the standard Finite Element Method.

Next, we will discuss the element which contains the discontinuity. Following Equation (3.20) and using the standard shape functions N_i and the shifted local enrichment functions $N^s_{enr,i}$ from the previous truss example (see Figure 3.15) the displacement field in the discontinuous element can be expressed by Equation (3.21).

$$u(x) = \underbrace{N_1(x)u_3 + N_2(x)u_4}_{\text{standard}} + \underbrace{N^s_{enr,1}e_3 + N^s_{enr,2}e_4}_{\text{enriched}} \tag{3.21}$$

The values of the standard degrees of freedom correspond to the nodal values of the target field ($u_3 = 5$; $u_4 = 3$) as was the case for non-enriched elements. The extended (additional) degrees of freedom can also be retrieved from the displacement field as shown in Figure 3.17. To understand this the notion of *virtual nodes* has to be introduced. A virtual node is a node that is associated with the extrapolation of the positive displacement field into the negative domain and vice-versa. The positive and negative virtual nodes are indicated in Figure 3.17 by a ★ and the corresponding sign. It can be shown that the values of the enriched degrees of freedom correspond to the difference between the "standard" nodal displacements and the virtual nodal displacements. In our example this yields $e_3 = -2$ and $e_4 = 2$. The signs are determined by subtracting the nodal

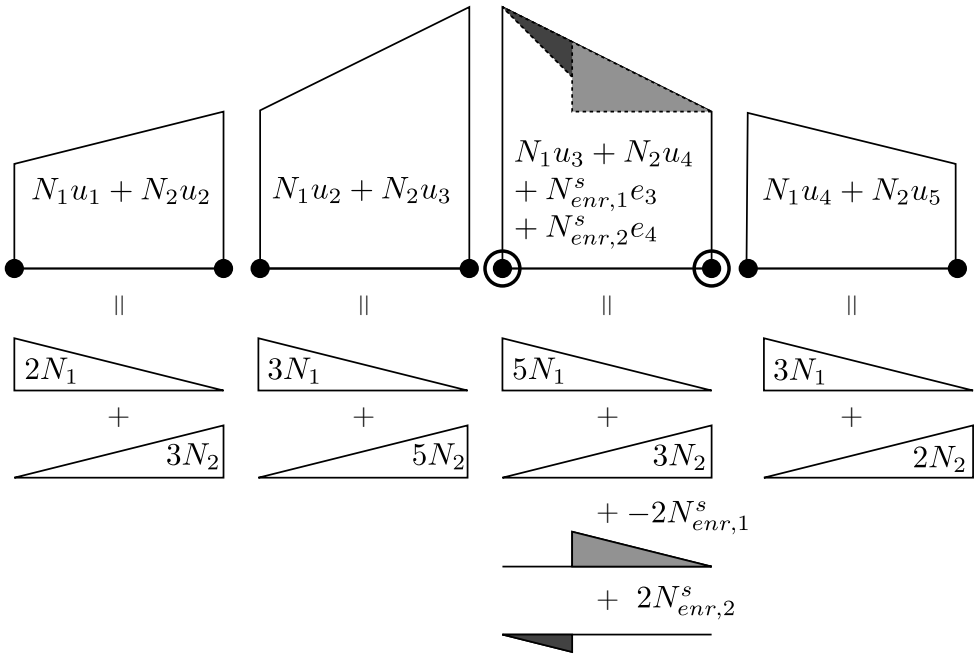

Figure 3.18: Decomposition of the displacement field

values associated with the negative domain Ω^- from the corresponding values associated with the positive domain Ω^+. This has to do with the convention that a "jump" is considered positive if the value increases going from the negative to the positive domain. The concept of virtual nodes and its graphical representation in Figure 3.17 inspires an interesting interpretation of the XFEM. In crack-related applications the XFEM can be seen as the use of two completely independent overlapping Finite Element meshes.

Using the values $e_3 = -2$ and $e_4 = 2$ for the enriched degrees of freedom leads to the decomposition of the discontinuous displacement field of the "cut" element as show in Figure 3.18. It can easily be verified that the assembly of continuous and discontinuous shape functions reproduces the discontinuous displacement field. We can therefore conclude, that the eXtended Finite Element Method is capable of reproducing a discontinuous displacement field by the local enrichment of selected nodes.

The displacement "jump" w at the location of the discontinuity x_w is directly related to the enriched degrees of freedom. In fact, it can easily be computed as derived in the

following Equations (3.22).

$$w = u^+(x_w) - u^-(x_w) \tag{3.22a}$$
$$w = \sum_{\text{enr}} N_i(x_w)\Psi^+(x_w)e_i - \sum_{\text{enr}} N_i(x_w)\Psi^-(x_w)e_i \tag{3.22b}$$
$$w = \Big(\Psi^+(x_w) - \Psi^-(x_w)\Big) \sum_{\text{enr}} N_i(x_w)e_i \tag{3.22c}$$
$$w = \Delta\Psi \sum_{\text{enr}} N_i(x_w)e_i \tag{3.22d}$$

At the location of the displacement discontinuity x_w the displacement value is equivocal. The "jump" corresponds to the difference between the value of the positive domain u^+ and the negative domain u^- as stated in Equation (3.22a). Substituting the basic equation of the XFEM (3.17) for $u^+(x_w)$ and $u^-(x_w)$ as well as using the fact that all contributions of the standard shape functions cancel out (they are not equivocal) this leads to Equation (3.22b). The enrichment function is also equivocal at the location of the discontinuity and the positive and negative values are analogously defined as Ψ^+ and Ψ^-. Equation (3.22c) is then directly obtained by simple algebraic transformation of (3.22b). Finally, the result can also be expressed in function of the magnitude of the discontinuity of the global enrichment function $\Delta\Psi$ as expressed in Equation (3.22d). Note that a positive displacement "jump" increases from the negative to the positive domain.

Applying Equation (3.22d) to the example of Figure 3.17 where the enrichment is equal to the Heaviside function gives:

$$w = (1-0) \cdot \Big(\frac{2}{3} \cdot -2 + \frac{1}{3} \cdot 2\Big) = -\frac{2}{3}$$

This is of course in accordance with Figure 3.17.

3.3.3 XFEM in 2D

In the preceding Section 3.3.2 the eXtended Finite Element Method was applied to a one-dimensional example because this is the best way to illustrate and understand it. However, apart from the educative value there exist no practical one-dimensional applications worth mentioning. The reason for this is that the advantages of a mesh-independent representation of a discontinuity in the one-dimensional case are negligible since adapting the mesh to accommodate the discontinuity is straightforward. The XFEM only develops its full potential in two- or three-dimensional applications.

Figure 3.19 shows a mesh of two-dimensional rectangular Finite Elements. It is crossed by a discontinuity (e.g. a crack) which is indicated by a bold line. Although the discontinuity

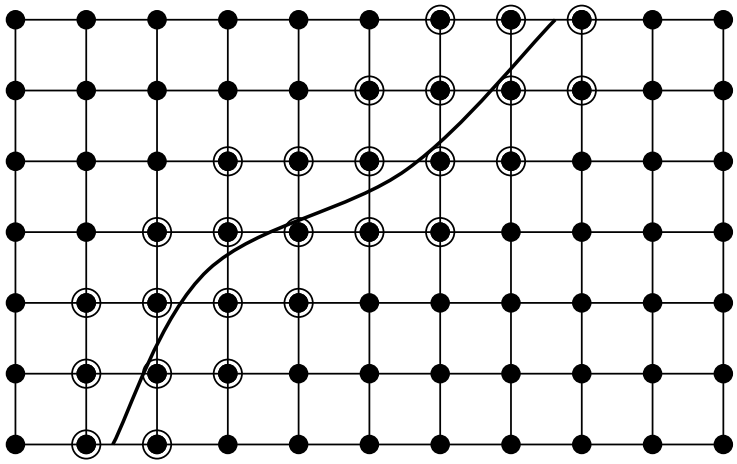

Figure 3.19: Discontinuity in a 2D XFEM mesh and local enrichment of nodes

is crossing the mesh in an arbitrary way it can be accounted for by the eXtended Finite Element Method. In order to do so the nodes marked by a circled dot in Figure 3.19 are enriched with additional degrees of freedom and the corresponding discontinuous shape functions (compare Section 3.3.1). In virtue of the local Partition of Unity Method the enrichment is only performed in the vicinity of the crack. Therefore, only the nodes of those elements that are crossed by the discontinuity are enriched.

In analogy to the one-dimensional case the two-dimensional Heaviside function is used as an enrichment function in order to introduce a strong discontinuity. However, since 4-node quadrilateral elements have four shape functions there will also be four enriched degrees of freedom per unknown field component (e.g. $u(x, y)$, $v(x, y)$) and four associated discontinuous shape functions. Furthermore, the discontinuity within an element can only be reproduced correctly if all nodes of that specific element are enriched and the Partition of Unity Principle is satisfied. Elements that have all their nodes enriched are called *enriched elements*. Note that not all elements in Figure 3.19 match this description. There are also a number of elements which are only partially enriched. They are called partially enriched elements or *blending elements* [CWB03] and will be discussed later.

As already mentioned, only the nodes of those elements which are crossed by the discontinuity have to be enriched (local enrichment). Because the discontinuous shape functions and the enriched degrees of freedom are associated with nodes it is more appropriate to state that only those nodes whose support is crossed by the discontinuity are enriched. Remember that the support of a node is the union of all elements connected to it. If the tip of the discontinuity only touches an element edge the nodes of that element must not be enriched since there is no discontinuity in that element yet. This leads to the following enrichment criterion for strong discontinuities (i.e. cracks):

> A node is enriched with the Heaviside function whenever a strong discontinuity completely bisects its support.

The fact that only selective nodes are enriched has certain implications on the global flow

of a Finite Element program based on the XFEM. In crack growth problems for example the global number of degrees of freedom is not constant since additional degrees of freedom have to be added whenever the crack propagates. As a consequence a Finite Element software implementing the XFEM has to account for a changing number of degrees of freedom which makes it impossible to use most existing codes without modification.

If the path of a discontinuity is very close to an element edge this can lead to numerical problems. The reason for this is that the added enrichment function would almost correspond to a constant function. However, a constant function (without "jumps") is already included in the standard approximation space and as a consequence adding such a function would lead to a linear dependency of the equilibrium equations and a singular stiffness matrix. Therefore, the so-called *area criterion* is usually used [Dol99, DMB00]. The area criterion is relatively straightforward and expresses the idea illustrated in Figure 3.20a. One determines the fraction of the total area A of the nodal support which lies on either side of the discontinuity (A^+/A and A^-/A). If one of the two is less than a certain threshold value (usually 10^{-4}) the corresponding node is not enriched. In order to compute the areas A^+ and A^- a *Delaunay triangulation* is usually performed (Figure 3.20b). As we will see in Section 6.2.6 the same subtriangulation is also necessary for the numerical integration of the weak form of the equilibrium equations.

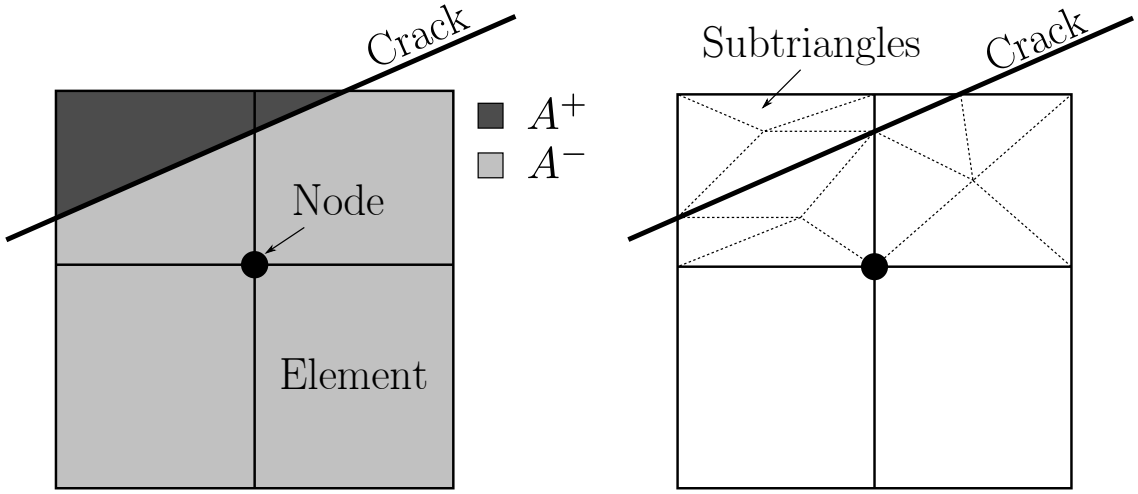

(a) Areas for the area criterion (b) Triangulation of intersected elements

Figure 3.20: Support of a node cut by a discontinuity

If the discontinuity ends within an element a special crack tip enrichment is required. For more information about this subject refer to Section 3.3.4 on enrichment functions.

In Section 3.3.2 the notion of two overlapping meshes was introduced to visualize the XFEM. In two dimensions this interpretation becomes even more intuitive as the following example illustrated in Figure 3.21 shows [JB02].

In the example a physical body and its representation by an eXtended Finite Element are depicted at three different states. The first one (Figure 3.21a) corresponds to the

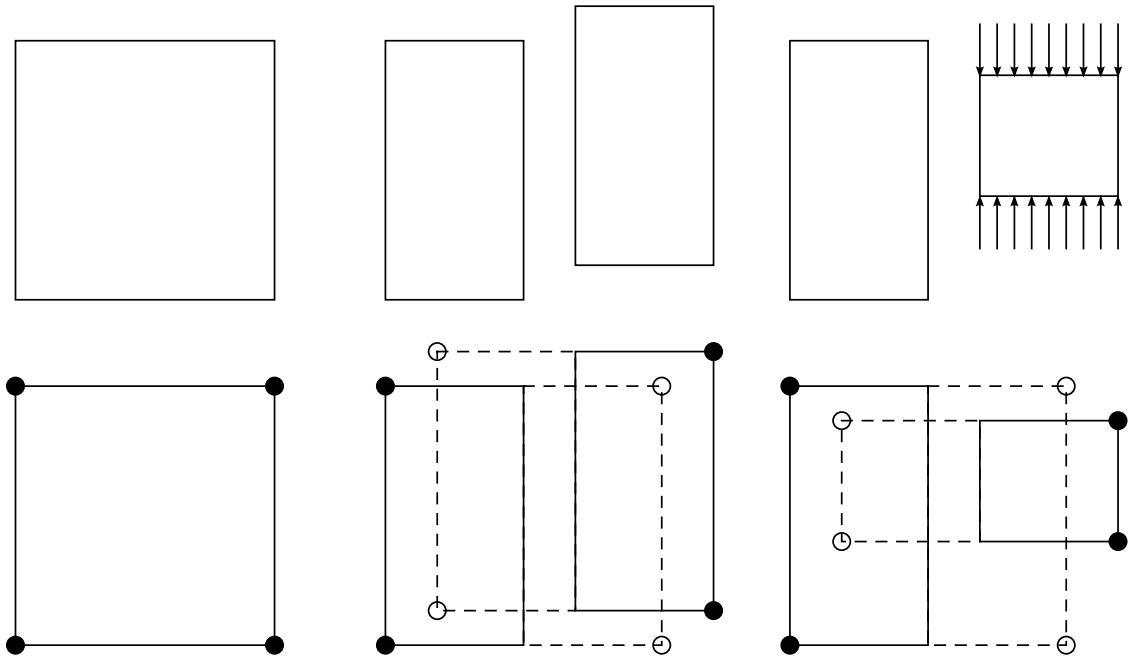

(a) Undeformed (b) Rigid body separation (c) Uncoupled straining

Figure 3.21: Interpretation of the XFEM as overlapping meshes (adopted from [JB02])

undeformed state. The second one (Figure 3.21b) represents the case where the body is crossed by a non-cohesive crack and it is separated by a rigid body movement. The individual halves are not strained and remain traction-free. The third situation corresponds to a separation of the body into two halves followed by a sequential straining of only one of the two pieces (Figure 3.21c). For each situation the corresponding XFEM solution is interpreted as overlapping meshes with virtual nodes. Note that although the first and the second situation can also be resolved correctly by the Embedded Discontinuities Method (EDM) this is not the case for the third loading condition. A certain coupling between the two sides cannot be completely avoid when using the EDM (see [JB02]).

At the beginning of this section we introduced the notion of "partially enriched elements" which should be discussed here in a bit more detail. If the standard Finite Element shape functions are used as Partition of Unity Functions in the eXtended Finite Element Method the local Partition of Unity Principle over the domain of a Finite Element is only fulfilled if all nodes of that element are enriched. This requirement is essential in order to be able to reproduce the discontinuity introduced by the enrichment function. However, in a Finite Element mesh there will also be some elements which are located in the transition zone between the normal mesh and the fully enriched region (where the enriched shape functions form a Partition of Unity). These elements only have some enriched nodes and they are therefore called *partially enriched elements* or *blending elements* [CWB03]. This situation is illustrated in Figure 3.22.

In general partially enriched elements cannot reproduce the enrichment function. Nor-

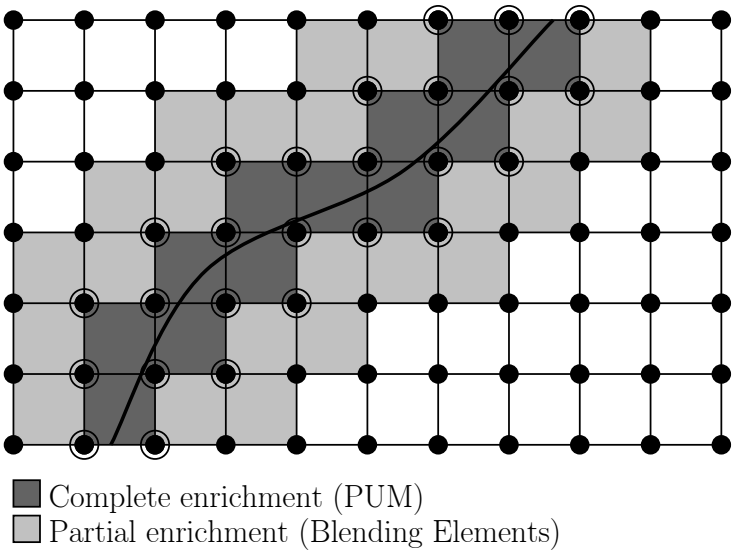

Figure 3.22: Completely enriched and partially enriched elements

mally this is also not necessary because the enrichment is not needed in those areas. Nevertheless, it is important to realize that the partially enriched elements are also affected by the enrichment because their displacement field approximation contains some enriched shape functions (shape functions influence the entire support of a node). Crack modeling with the Heaviside function represents a somewhat special case because, as we have seen in Section 3.3.1, the enriched shape functions are zero outside of the discontinuous elements (after shifting the basis). However, this is not the case for most other enrichments. As a consequence the enriched shape functions can produce spurious terms in the displacement field of the adjacent elements. These spurious terms might be prevented but only if the standard shape functions are able to compensate for the spurious terms induced by the enriched shape functions. For polynomial enrichment functions and polynomial standard shape functions the spurious terms can be removed if the polynomial order O of the standard shape functions is at least as high as that of the enriched shape functions. This is expressed mathematically as:

$$O(N) \geq O(N_{enr}) \qquad \text{or}$$
$$O(N) \geq O(\varphi \cdot \Psi)$$

For the case of a Heaviside enrichment in combination with the standard linear shape functions as Partition of Unity Functions the order of the enriched shape functions remains the same as that of the standard shape functions (since multiplication by a constant does not alter the order of a function). Therefore, the Heaviside enrichment does not create any spurious terms in the blending zone between the enriched and the standard part of the mesh. However, for other enrichment functions this can become a serious problem and special blending elements are required to obtain good overall performance [CWB03].

The latter can for example be constructed on the basis of the *Enhanced Assumed Strain (EAS) formulation*. An alternative is to use standard shape functions that have a higher order than the Partition of Unity Functions.

A final, challenging issue with the two-dimensional XFEM (even more challenging for three-dimensional applications) is the description of the geometry of a crack. One possible approach is to combine the XFEM with the so-called *Level Set Method*. The latter is based on the work by Osher and Sethian [OS88, Set99] and the basic idea behind it is to describe a geometrical shape by the "zero level set" of a scalar function (called the *Level Set Function*). The "zero level set" is the set of all points for which the Level Set Function $F_{ls}(\underline{\mathbf{x}})$ takes the value 0. Therefore, the geometrical shape of interest is mathematically described by the equation $F_{ls}(\underline{\mathbf{x}}) = 0 \quad \forall \underline{\mathbf{x}} \in \Omega$ where $\underline{\mathbf{x}}$ is the vector of coordinates of any point within the computational domain. For a circle with a radius of 3 which has its center at the coordinates $(6, 4)$ a possible Level Set Function would for example be $F_{ls}(\underline{\mathbf{x}}) = \sqrt{(6-x)^2 + (4-y)^2} - 3$. The big advantage of using Level Set Functions is that if they are cleverly formulated they can directly provide information about how certain points are situated with respect to the described shape. In the above case for example the Level Set Function takes negative values for points within the circle and positive values for points outside of the circle.

3.3.4 Enrichment Functions

We have seen that the eXtended Finite Element Method is a very general framework which allows the incorporation of a priori knowledge about the solution into the approximation space. Because the method is based on the Partition of Unity Principle the enrichment is automatically *conforming* (continuous across element boundaries) independent of the chosen enrichment function. A second important characteristic of the XFEM is that the enrichment is local since the Partition of Unity Functions act as windowing functions in this context. In the following a few of the most important enrichment functions with an emphasis on crack problems are presented. However, the choice of enrichment functions is not limited to those given here and any other type of function could be incorporated into the approximation space. The only restriction is that the enrichment should not already be contained in the standard approximation space. Or in other words, no enriched shape function should by a linear combination of the standard shape functions because this would lead to a singular system of equations.

Strong Discontinuity Enrichment

One possible class of enrichment functions are discontinuous functions. They are used to incorporate strong discontinuities into the displacement field of a Finite Element model (e.g. for crack problems). Basically any discontinuous function will do. The most popular choices are: The *Heaviside function* and the *sign function* which in some of the literature

is also called *Haar function* (see Figure 3.23). The Heaviside function takes the value 0 on one side of the discontinuity and the value 1 on the other side whereas the "sign" function takes the values -1 and 1.

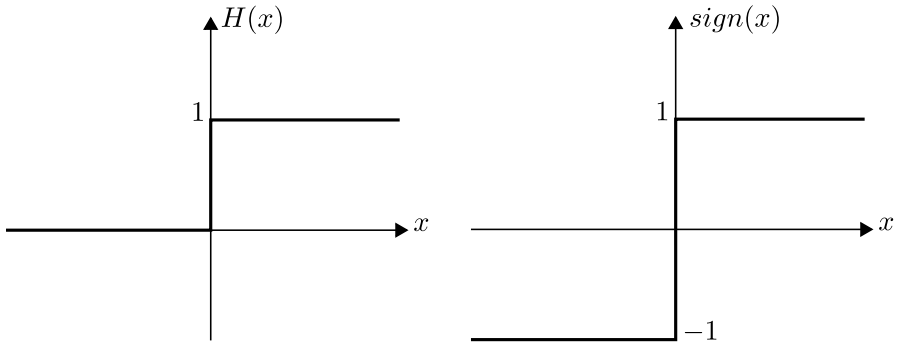

(a) Heaviside function (b) Sign function

Figure 3.23: Discontinuous enrichment functions

There is really no major difference between the Heaviside function and the sign function since they both add a discontinuous "character" to the solution. The magnitude of the "jump" in the enrichment function is not important. The only small difference is that the sign function is especially apt to be used in combination with a Level Set representation of the crack geometry (for an explanation of Level Sets see Section 3.3.3).

An interesting concept is the use of discontinuous functions in combination with higher order shape functions. In this case the magnitude of the displacement "jump" can vary at the polynomial order of the Partition of Unity Functions [MDB99]. This can be understood by looking at the equation for the separation vector (Equations 3.22d or 6.21) which clearly indicates that the variation of the separation vector is governed by the polynomial order of the Partition of Unity Functions. The path of the crack on the other hand is restricted to the polynomial order of the standard shape functions of the underlying Finite Element [SBCB03]. The reason for this is that both separated parts of an intersected Finite Element need to be mapped to the parent, natural element. For an isoparametric element this is done by means of the standard shape functions which can only map shapes corresponding to their polynomial order.

Junction Enrichment

Another special enrichment is needed if discontinuities are branching or intersecting [DMD+00]. Figure 3.24 shows a branching crack. The crack from bottom-left to top-right is considered to be a continuous crack while the crack from top-left to bottom-right is considered to be a secondary branch. The necessary nodes for the primary crack are enriched by a Heaviside function H_I as if the secondary crack were not present. The respective nodes for the secondary branch are also enriched by a Heaviside enrichment H_{II} as if the primary crack were not present except for those nodes in whose support the

junction is located. There a special *junction enrichment* J has to be added (indicated by additional squares in Figure 3.24). Note, that some nodes outside of the element containing the junction might contain enriched degrees of freedom from both cracks. However, no special "interaction" treatment is required.

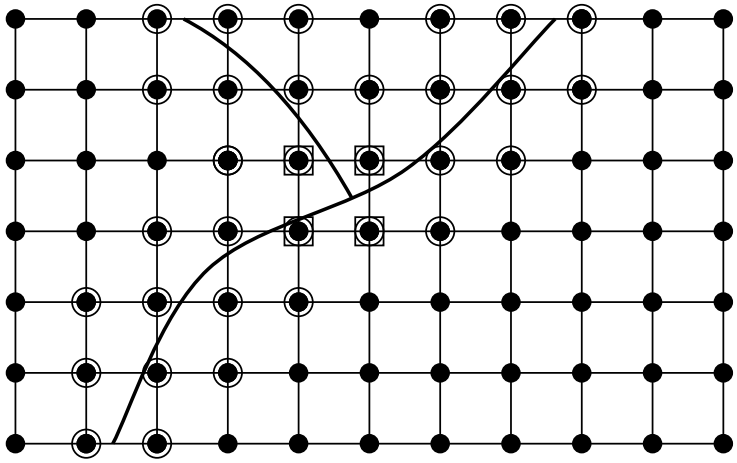

Figure 3.24: Junction of two cracks

The junction enrichment is illustrated in Figure 3.25. It can easily be constructed from a combination of the two Heaviside functions of the individual crack branches. Note that the representation in Figure 3.25 is only schematic. The separating lines would in fact correspond to the true geometry of the cracks. The element containing the junction has to be enriched with both the Heaviside enrichment for the primary crack (H_I) and the junction enrichment (J). In fact, it can easily be shown that there need to be three sets of shape functions (1 standard and 2 enriched) to represent a junction.

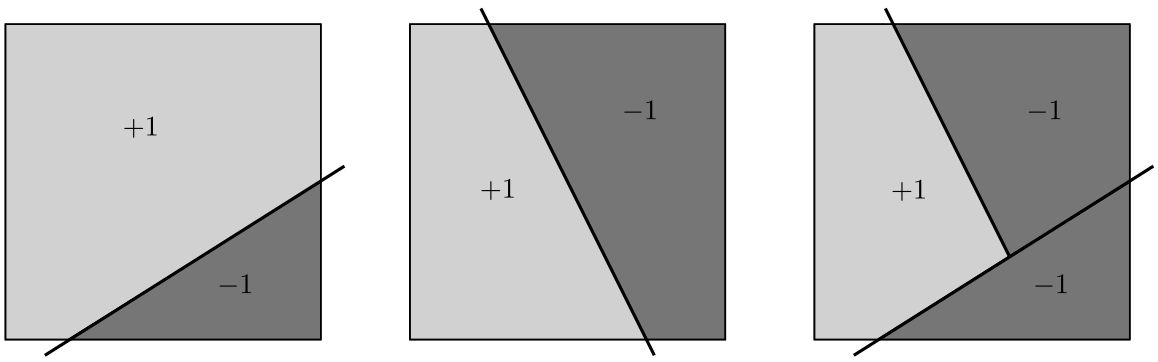

(a) H_I (b) H_{II} (c) J

Figure 3.25: Enrichment functions for each crack and for the junction

For each crack that branches from the primary crack an additional enrichment of type J has to be added to the element containing the junction. An intersection of two cracks can be seen as a primary crack joined by two secondary cracks which branch at the same location. Therefore an intersection requires four sets of shape functions: One set

of standard shape function N, one set of Heaviside-enriched shape functions N_H for the primary crack and one set of junction-enriched shape functions $N_{J,i}$ for each of the two secondary cracks.

Crack Tip Enrichment

A further class of enrichment functions used in crack growth simulations are crack tip enrichments. The most commonly used ones are the asymptotic near-tip field functions from Linear Elastic Fracture Mechanics (Westergaard solution). This type of enrichment was first used in combination with the XFEM by [BB99]. The near-tip displacement field in an elastic continuum is spanned by the following four functions:

$$B_1(r,\theta) = \sqrt{r}\sin\frac{\theta}{2} \qquad B_2(r,\theta) = \sqrt{r}\cos\frac{\theta}{2}$$
$$B_3(r,\theta) = \sqrt{r}\sin\frac{\theta}{2}\cos\theta \qquad B_4(r,\theta) = \sqrt{r}\cos\frac{\theta}{2}\cos\theta$$

Here r is the radius and θ is the angle in a polar coordinate system associated with the crack tip. The angle θ is contained in the range $[-\pi,\ \pi]$. The first function B_1 is a so-called *branch function* and it is discontinuous along the crack line. The displacement "jump" diminishes towards the tip of the crack until it is 0 at the exact location of the tip. The other three functions B_2 to B_4 are added to improve the accuracy of the solution. Incorporating a crack tip enrichment hence requires four enriched shape functions per node.

An alternative to the above mentioned branch function is the use of a smooth ramp function $R(\widetilde{x},\widetilde{y})$ which is multiplied by the $sign(x,y)$ function as proposed in [DMB00]. The smooth ramp function is given by:

$$R(\widetilde{x},\widetilde{y}) = \begin{cases} 3\left(\frac{\widetilde{x}}{l_c}\right)^2 + 2\left(\frac{\widetilde{x}}{l_c}\right)^3 & \text{for} \quad \widetilde{x} \le 0 \\ 0 & \text{for} \quad \widetilde{x} > 0 \end{cases}$$

Where $\widetilde{x}$ and $\widetilde{y}$ are Cartesian coordinates associated with the crack tip and l_c is the characteristic length of the element containing the crack tip. The enrichment function Ψ is then defined as:

$$\Psi(x,y) = R(\widetilde{x},\widetilde{y}) \cdot sign(x,y)$$

The ramp function assures that the discontinuity reduces to 0 at the crack tip whereas the sign function introduces the discontinuity along the line of the crack. In order to improve the accuracy of the solution the discontinuous ramp function can also be used

in combination with the three continuous terms of the near-tip asymptotic field. The advantage of the discontinuous ramp function over the branch function is that it requires no mapping to align the discontinuity with the edges of the crack.

The crack tip enrichment (branch or ramp function) is added to the approximation space of the elements containing a crack tip. In other words the nodes whose support is not bisected but only slit by the discontinuity are enriched with the crack tip enrichment. When comparing the condition for the crack tip enrichment with the condition for the crack body enrichment (Sign or Heaviside function) one can notice that exactly those nodes which are not enriched by the first are enriched by the second enrichment. In order to improve the accuracy of the solution – especially for nonlinear fracture mechanics problems or for very fine meshes – the asymptotic near-tip field enrichment can also be extended to several elements in the vicinity of the crack tip.

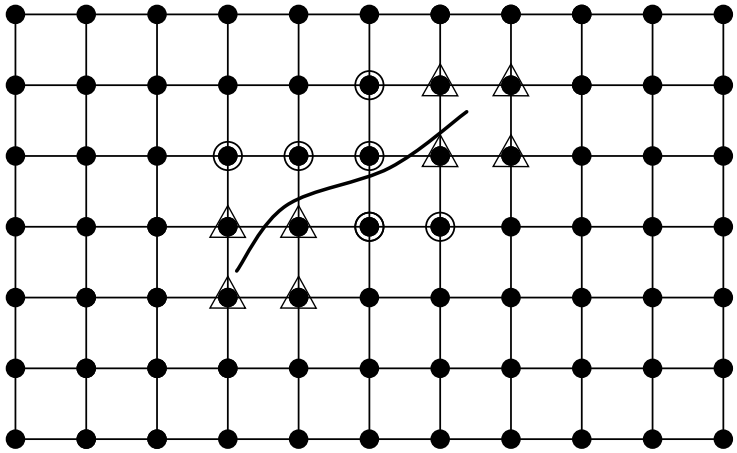

Figure 3.26: Crack tip enrichment (triangle) and crack body enrichment (circle)

Figure 3.26 shows the enrichment of a crack with two tips. The enrichment of every node is chosen on the basis of whether its support is completely bisected (Heaviside enrichment indicated by a circle) or just slit (tip-enrichment indicated by a triangle).

Weak Discontinuity Enrichment

A final enrichment worth mentioning is the continuous but kinked v-shaped function (see Figure 3.27). Since it is continuous but its derivative contains a discontinuity it can be used to model weak discontinuities such as localization bands [BMUP01]. However, its main field of application is to bi-material problems or material phase interfaces. Usually the "absolute value function" $abs(x)$ is used.

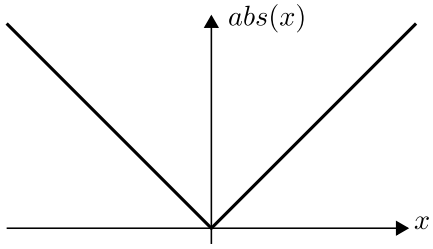

Figure 3.27: "Absolute value" function

3.3.5 Literature Overview of the XFEM

After having explained the basic principles of the eXtended Finite Element Method a short historical overview of the most important contributions with a special emphasis on crack modeling is given. Other summaries can also be found in [KX03, BL05, Fuh04] and [AH08].

Partition of Unity Method The fundamentals of the eXtended Finite Element Method were published in 1996 by Melenk and Babuška. In their milestone paper [MB96] they introduce the Partition of Unity Method (PUM) on which the entire XFEM is based. This was then soon followed by a second paper on the same subject [BM97]. Within these papers the mathematical basis for the PUM is outlined and the required proofs as well as some examples are given. However, these papers approach the subject from a very theoretical point of view.

Crack-tip enrichment The first paper which was directly considering an engineering problem is the seminal paper by Belytschko and Black published in 1999 [BB99]. In it the authors tackle the problem of crack growth simulation by Finite Elements. The main idea in the paper is to incorporate a set of functions which span the asymptotic near-tip field of a crack into the Finite Element approximation space. This set consists of a discontinuous branch function and three continuous trigonometric functions spanning the near-tip field encountered in Linear Elastic Fracture Mechanics (see Section 3.3.4). The crack surfaces are assumed to be tension-free. One of the drawbacks of this approach is that it requires a relatively complicated mapping procedure for each crack segment. Because of this the proposed method is combined with a remeshing technique which is applied at a certain distance away from the crack tip.

Jump enrichment The method proposed in [BB99] is further improved in [MDB99]. A discontinuous function called the generalized Haar function is added to the approximation space of the elements completely crossed by the crack. The generalized Haar function takes the value -1 on one side of the crack and the value $+1$ on the other side. By introducing

such a discontinuous enrichment remeshing can be avoided. The asymptotic near-tip field is then exclusively used to enrich those nodes in the vicinity of the crack tip.

Ramp enrichment A further contribution to the XFEM is made in [DMB00]. For kinked cracks the near-tip branch function requires a mapping procedure for each segment. By using a discontinuous ramp function instead of the branch function the mapping procedure which is necessary to align the enrichment function with the crack segments can be avoided. However, the accuracy of the solution near the crack tip is slightly reduced. The paper also presents the application of the XFEM to Mindlin-Reissner plates.

Intersecting cracks In [DMD$^+$00] the concept of crack modeling with the XFEM is extended to intersecting and branching cracks. The intersection is accounted for by an additional junction enrichment. The paper also discusses the representation of holes by the XFEM.

Cracks One of the most often cited papers about the XFEM is [BMUP01]. It is an overview paper which more or less summarizes and unifies the earlier contributions to the XFEM. Therein the enrichment by discontinuous step functions as well as the enrichment by near-tip field functions is described. The paper also addresses the issue of intersecting and branching discontinuities as well as the incorporation of weak discontinuities. Furthermore, the case of a discontinuity along a slip line is illustrated.

Frictional contact The first to consider nonlinear crack behavior were [DMB01]. In their paper the procedure for crack growth simulations is extended to cracks with frictional contact.

Cohesive cracks There are several papers which introduce cohesive forces to the crack representation within the XFEM. The earliest and most important ones are [WS01] and [MB02]. In both these studies the employed traction–separation law is similar to the ones used in Smeared Crack Models. In [MP03] a Cohesive Crack Model with a damage-type constitutive law is used in combination with the XFEM. Furthermore, the model uses discontinuous polynomial functions for the crack tip enrichment and it is argued that the near-tip asymptotic fields are only accurate for the linear, elastic solution.

Curved cracks In [SBCB03] the description and the implementation of curved cracks is treated. The formulation of elements with curved discontinuities evolves naturally when higher order interpolation functions are used for the standard Finite Element displacement field. Another paper that treats curved cracks but this time with cohesive forces is [ZB03]. A further contribution of the latter paper is to drop the branch functions because they can

create blending problems (see Section 3.3.3). Instead a linear discontinuous enrichment function which is constrained to become zero at the crack tip is used.

Crack coalescence A very interesting application of the Cohesive Crack Model in combination with the XFEM is proposed by [RdBN03]. There the XFEM is used to simulate the growth and coalescence of cracks. By introducing the concept of cohesive segments the entire fracture process beginning with crack nucleation at different locations followed by crack growth and finally coalescence is simulated. In [dBRN06] the same concept is extended to dynamic crack propagation.

Multiple cracks In a similar fashion the authors of [BZMB04] considered multiple crack growth and coalescence of cracks in solids governed by linear, elastic fracture mechanics. The proposed procedure handles crack tip, jump and junction enrichments and a criterion for determining the active cracks based on energy dissipation is presented.

Blending elements In [CWB03] the problems associated with partially enriched elements and a proposed methodology for constructing suitable blending elements (see Section 3.3.3) is presented.

Dynamic crack growth A method for dynamic crack growth simulation is introduced in [BCXZ03]. The elements are based on the enrichment proposed in [ZB03] which eliminates the need for the near tip asymptotic field enrichment. An interesting feature of the method proposed in [BCXZ03] is that the criterion for crack propagation is not based on stress intensity factors or nonlocal stresses but on the loss of hyperbolicity of the governing equations (which marks the starting point of localization). In other words the propagation of the cracks is purely driven by the material model of the continuum.

Level Set Method A further fundamental contribution to the XFEM is its combination with the *Level Set Method* [OS88, Set99]. This procedure is used to model cracks in [SCMB01a] and to model holes and inclusions in [SCMB01b]. The combination of the XFEM and Level Sets is then further elaborated in [VBB03] where it is extended by the notion of *Vector Level Sets* which can be used as a more elegant way to describe crack growth.

3D cracks One large field of application for the XFEM is the simulation of three-dimensional crack growth. The first paper on the subject was published by Sukumar et al. [SMMB00]. In it planar cracks in three-dimensional elastic continua are analyzed. A few years later the method is improved and the crack geometry and evolution are described by Level Sets and the *Fast Marching Method* (FMM) [SCM03]. This method is also applied to non-planar three-dimensional cracks as described in [MGB02] and [GMB02]. The above

mentioned applications illustrate the huge capabilities of the XFEM in providing a means to model discontinuities independent of the Finite Element mesh.

Continuous–discontinuous models Some of the latest research on the XFEM goes in the direction of combining it with Regularized Continuum Models [Wel01, WdBS01, WSdB02, Sim03, SWS03, SS04, CMP07]. The basic idea is to use regularized Continuum Damage Models (rate-dependent or nonlocal) in the early stages of failure. As soon as a critical level of damage is accumulated a strong discontinuity is introduced by the XFEM. On one hand this procedure profits from a good continuum representation of the diffuse damage mechanisms in the early stages of failure. On the other hand it also allows for the complete decoupling of regions separated by a crack in the later stages of failure preventing spurious damage growth.

3.4 Numerical Modeling of HPFRCC

Although the literature on numerical modeling of concrete is abundant there are only a handful of publications on the structural-scale simulation of High Performance Fiber Reinforced Cementitious Composites. Some research was done on the micromechanical modeling of HPFRCCs in an attempt to link the microstructure (fibers, matrix, bond, etc.) to the composite behavior (e.g. [KLL00]). However, methods for the simulation of the *structural* response of HPFRCC elements subjected to a two- or three-dimensional stress state are scarce and mostly limited to ECCs (see Section 2.4). In the following Section 3.4.1 the most commonly used structural-scale models for High Performance Fiber Reinforced Cementitious Composites are presented. A summary can also be found in [Kab03]. The section is then concluded by introducing the new model for HPFRCCs that was developed during this thesis.

3.4.1 Literature Review of HPFRCC Models

Coaxial Rotating Crack Model One modeling approach for High Performance Fiber Reinforced Cementitious Composites (such as ECCs) is proposed by Han, Feenstra and Billington [HFB03]. It is based on a coaxial Rotating Crack Model within the general framework of Smeared Crack Models. The basic assumption of the Rotating Crack Model is that the strain tensor and the axes of orthotropy (cracks) are always coaxial (see Section 3.2.4). Under this assumption the cracks can be represented by a scalar, nonlinear stress–strain law. The latter can either be determined experimentally (by a cyclic uniaxial tensile test) or analytically (e.g. [KLL00]). The advantages of this model are that it is computationally efficient, robust and that it can be incorporated into standard Finite Element codes. The model is validated in [HFB03] by comparison with ECC cantilever-beam tests ([FL03a]) and the results showed to be sufficiently accurate.

Hybrid Rotating–Fixed Smeared Crack Model An improvement of the model by [HFB03] is proposed in [HET09]. The basic idea is to use a hybrid between a Rotating Crack Model and a Fixed Crack Model. The Rotating Crack Model is used during the first stage of behavior when the HPFRCCs are exhibiting multiple cracking and strain-hardening. As soon as crack localization takes place the model switches to a Fixed Crack Model. Mesh-size sensitivity is counteracted by regularizing the constitutive model with the size of the Finite Element mesh. The model is validated with experiments on reinforced HPFRCC shear walls under reversed cyclic loading.

Model Based on Plasticity and Embedded Discontinuities Another very interesting model for the numerical simulation of ECCs is proposed by Kabele and Horii [KH96]. In their work they identify two phases of cracking behavior: first a phase of multiple cracking resulting in a pseudo strain-hardening behavior followed by a phase of crack localization and tension-softening. Since both phases of behavior are completely different they are also treated differently in the proposed numerical model. The pseudo strain-hardening phase is modeled within the framework of hardening Plasticity by employing a Rankine yield criterion with associated flow rule and kinematic hardening. The phase of localization and softening is represented by cracked elements with embedded displacement discontinuities (Embedded Discontinuities Method).

Model Based on a Fixed Smeared Crack Model and Crack Bands In [KTIH99] another computational method for the simulation of ECC is presented. Similarly to the model presented in the previous paragraph a distinction between the multiple cracking phase and crack localization is made. The former is modeled by a Fixed Smeared Crack Model. This has the advantage that sliding along cracks can be accounted for explicitly. In the proposed approach shear-stress transfer across sliding cracks is determined by a micromechanical model. Localized cracks are modeled separately by a Crack Band Model (Smeared Crack Model) and shear-stress transfer is also accounted for during this phase. Von Mises Plasticity with isotropic hardening is used as a constitutive law in compression without any extensive justification. In [KTIH99] this model is successfully applied to ECC shear panels and an ECC cover concrete layer.

Model Based on an Equivalent Continuum and Crack Bands In [Kab00, Kab02] the model from the preceding paragraph is further improved to include micromechanical concepts not only for the shear transfer but also the normal crack bridging stress. This is done by modeling the multiple cracking phase by an *equivalent continuum*. The basic idea behind this concept is that a *Representative Volume Element* (RVE) is defined which represents a sort of "averaged" material point. The constitutive law for this material point is then obtained by linking the micromechanics within the RVE to an equivalent macroscopic stress–strain relationship. Localized cracks are again modeled by a Crack Band Model. This concept of representing ECCs by a cascade of models on different scales

and then "plugging" the smaller scale model into the larger scale model is presented in [Kab04, Kab07] in even more detail and an application is shown in [Kab06].

Model Based on Sequentially Linear Analysis A different approach is taken in [Bil09]. This paper compares two different models by performing a case study on an ECC-beam. The first model is a total-strain based Smeared Crack Model similar to the ones already discussed and the second one is based on *sequentially linear analysis*. Although both models seem to capture the strain-hardening behavior pretty well some problems are encountered during the crack localization and softening phase. The Smeared Crack Model exhibits convergence problems whereas the linear sequential analysis shows some mesh sensitivity.

Isotropic Damage Model A further possibility to model High Performance Fiber Reinforced Cementitious Composites is presented in [BvZ07]. In this paper a model based on Continuum Damage Mechanics is developed. More specifically an Isotropic Damage Model is used to account for cracking in both the strain-hardening and the strain-softening regime. In order to deal with the issues associated with crack localization and mesh-size dependency a material length scale equal to half the fiber length is introduced as a means of regularization. The model is validated with three-point bending tests and an Iosipescu shear beam test [vZ07].

Plasticity Model A final model worth mentioning is the one presented in [Sir09]. It is based on the general framework of Plasticity. Starting out with a traditional four-parameter Plasticity model an extension to High Performance Fiber Reinforced Cementitious Composites is developed. The model includes softening in compression and both hardening and post-peak softening in tension. The advantage of this model is that once the yield surface is defined and the flow rule as well as the hardening respectively softening laws are formulated the model is computationally efficient and easy to implement in a commercial software package. However, the model uses a phenomenological approach and does not capture the physical reality of crack formation and localization.

3.4.2 Outline of the Proposed Model for HPFRCC

Recapitulating Section 3.4.1 it seems that the most popular and most often used models for HPFRCC structural elements are variants of the Smeared Crack Model. Throughout all studies it is recognized that Smeared Crack Models perform well during the strain-hardening phase of the behavior of HPFRCCs but they exhibit a number of problems after crack localization such as mesh-size sensitivity, convergence problems or difficult choices for regularization parameters. This becomes most evident in [DHB03] where the influence of different parameters of a Smeared Crack Model for HPFRCC elements is explicitly investigated. However, this problem is not unique to HPFRCCs but it is a

general deficiency of Smeared Crack Models because they try to capture a discrete crack by a continuum representation. For more information on the shortcomings of Smeared Crack Models (e.g. mesh-sensitivity, mesh-bias, stress-locking etc.) refer to Section 3.2.5 and [Rot88]. The goal of this thesis is to propose a model that solves these issues.

As we have seen in Section 2.1.3 High Performance Fiber Reinforced Cementitious Composites show three different phases of tensile behavior which are namely an elastic phase, a strain-hardening and a multiple cracking phase followed by a phase of crack localization and softening. It seems reasonable to model each of these phases individually as was also recognized by a number of authors mentioned in Section 3.4.1. Therefore, the model developed in this thesis uses the following approach which is also illustrated in Figure 3.28:

- the elastic phase is modeled by a linear, elastic plane-stress continuum model
- the multiple cracking phase is modeled by a Smeared Crack Model
- the crack localization phase is modeled by discrete cohesive cracks with the eXtended Finite Element Method

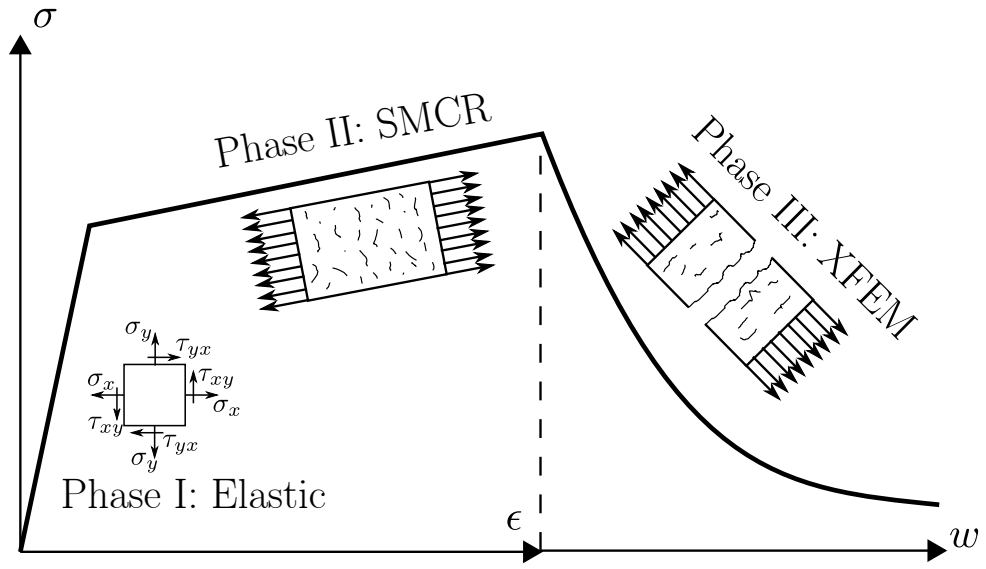

Figure 3.28: Outline of the new model for HPFRCCs

The most significant advantage of this new model over the ones presented in Section 3.4.1 is a more accurate and phenomenologically correct treatment of crack localization and softening. The different parts of the model will be presented in the following Chapter 4 (elastic), Chapter 5 (hardening) and Chapter 6 (softening).

Chapter 4

Elastic Model (FE Basics)

4.1 Introduction

In this chapter a model for the elastic phase of the behavior of HPFRCCs in accordance with the suggested decomposition in Section 3.4.2 is presented. We will start out by defining a Finite Element that is used for the model and explain how it captures the elastic behavior of a HPFRCC structural element. Although the Finite Element Method is well known [Bat96] it is important to be familiar with the details of the procedure in order to understand the extensions that are made in the following Chapter 6 where the eXtended Finite Element Method is used to capture localized cracking.

In perspective of the most common practical applications for HPFRCCs (some of which were mentioned in Chapter 2) it was decided to develop a two-dimensional Finite Element model for the state of plane-stress. This means that the model can be used to predict the behavior of structural elements for which the stress components perpendicular to the main plain of action are zero or insignificant. Hence, the proposed model can be used for panels, wall structures and beams.

Because the model uses the eXtended Finite Element Method for crack localization (see Chapter 6) it was not possible to develop a "user" element for an existing Finite Element code. Therefore, it was decided to write a custom Finite Element program from scratch using the programming language *Python* [vR06]. Python is a free and open-source programming language developed by Guido van Rossum which allows fast coding and features the *Object-Oriented Programming* paradigm (OOP). The program developed during this thesis follows this OOP paradigm making future extension by other researchers much more convenient. It is important to note that the program was written for scientific purposes rather than commercial use and its intent is to demonstrate the validity of the proposed model. For this reason no emphasis was put on computational efficiency or speed and no graphical user interface is provided.

The developed Finite Element program uses isoparametric, plane-stress, 8-node quadri-

lateral elements. The main reason for using 8-node and not 4-node elements is that they are able to reproduce a linear strain field variation over an element (instead of a constant strain field) which is the typical situation for most applications (e.g. beams) and results in smother strain and stress profiles as well as better convergence performance. The implemented quadrilateral element is presented in the following Section 4.2.

4.2 Isoparametric Quadrilateral Finite Element

This Section will provide the theoretical basis for the implemented Finite Element and will serve as a reference for the following chapters. It can be seen as a short summary of Finite Element Analysis but of course the main goal is not to give an extensive lecture on the Finite Element Method but rather to summarize the most important concepts and directly apply them to the specific case of the aforementioned isoparametric, 8-node quadrilateral element. Most of the developments can also be found in [Bat96].

The standard Finite Element Analysis procedure with isoparametric plane-stress elements consists of the following basic steps:

1. Discretization
2. Selection of shape functions (interpolation functions)
3. Formulation of the shape function matrix $\mathbf{N}$
4. Formulation of the strain–displacement transformation matrix $\mathbf{B}$
5. Computation of the element stiffness matrix $\mathbf{K}_e$ and force vector $\underline{\mathbf{F}}_e$
6. Assembly
7. Solution of the global system of equations
8. Update of the element state and computation of secondary results
9. Equilibrium check (not mandatory for linear analysis)

The individual steps are explained in more detail in the following Sections 4.2.1 – 4.2.9.

4.2.1 Discretization

The first step in the Finite Element procedure is to discretize the computational domain. This means that a structure is subdivided into a number of Finite Elements which are defined by the geometric location of their nodes. The isoparametric 8-node elements used in this thesis are defined by four corner nodes and four intermediate nodes on the element edges. Every edge passes through three adjacent nodes and the element's shape is completely defined by the location of the nodes. By consequence each edge can be

parabolic. An example of a quadrilateral Finite Element and the used node numbering is shown in the following Figure 4.1a.

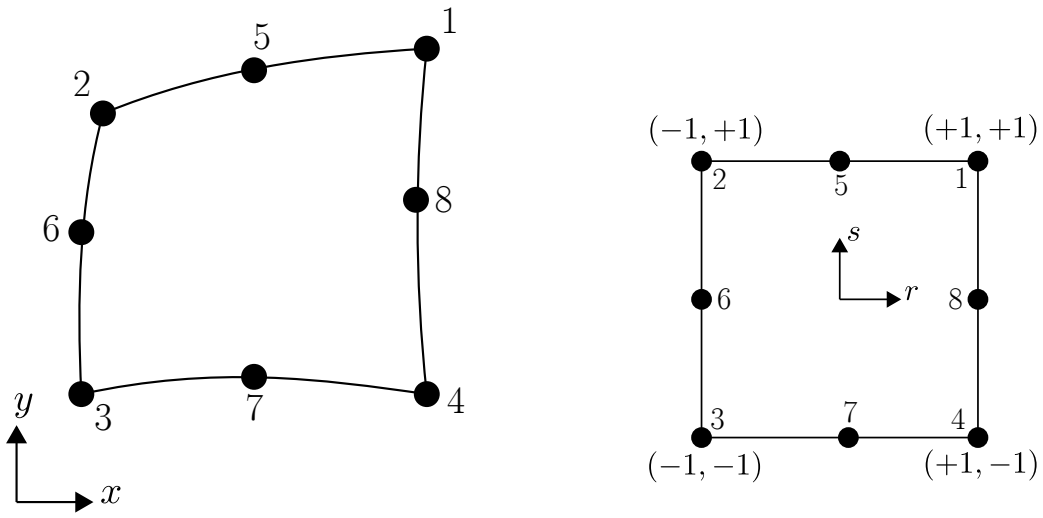

(a) Real domain (b) Parent domain

Figure 4.1: Isoparametric 8-node quadrilateral element

Figure 4.1b shows what is called the *parent element*. Since every element within a structure can theoretically be different a parent element is defined. The latter is formulated in a coordinate system of *natural coordinates* r, s which both range from -1 to 1. The real element is then obtained from the parent element by a coordinate mapping procedure which uniquely relates the natural coordinates r, s to the real coordinates x, y. This mapping procedure will be introduced in Section 4.2.2.

At each node of an element a number of degrees of freedom are introduced. This constitutes the basic step in the discretization process. It is assumed that a continuum with its infinite number of degrees of freedom can be approximated by a discrete number of nodes and their associated degrees of freedom. Each node i of the considered plane-stress element has two associated displacement degrees of freedom denoted by u_i and v_i in the directions of the global x- and y-axis respectively. From this we can define a displacement vector $\underline{\mathbf{d}}_e$ which contains all nodal degrees of freedom of an element as given in Equation (4.1).

$$\underline{\mathbf{d}}_e = (u_1, v_1, u_2, v_2, u_3, v_3, u_4, v_4, u_5, v_5, u_6, v_6, u_7, v_7, u_8, v_8) \tag{4.1}$$

Note that the degrees of freedom are ordered by node.

4.2.2 Shape Functions

The next step is to choose a set of so-called *shape functions* N_i which are used to approximate the unknown fields within the element. Sometimes these shape functions are also called *interpolation functions* since they interpolate the nodal values in order to find a value at any position within the element. The element presented here is called *isoparametric* because all unknowns of the element (including the geometry) are interpolated using the same set of interpolation functions.

Note that every node of the element has an associated shape function. The Finite Element Method then uses the following procedure: Any unknown field is interpolated by multiplying the nodal value of the respective unknown with the associated nodal shape function and then summing up the contributions of all shape functions. This is shown exemplarily in Equations (4.2) for the interpolation of the geometry i.e. the nodal coordinates (x_i, y_i).

$$x(r,s) = \sum_{1}^{8} N_i(r,s)x_i \qquad y(r,s) = \sum_{1}^{8} N_i(r,s)y_i \tag{4.2}$$

This constitutes a mapping procedure for the geometry and can be understood as follows: Any given point within the parent element has a pair of coordinates (r, s). The corresponding point in the real element is obtained by computing the values of the shape functions N_i at the coordinates (r, s) and then multiplying them with the coordinates (x_i, y_i) of the associated nodes. Finally, the contributions of all nodes are summed up to yield the global coordinates (x, y).

This procedure is not only used for the interpolation of the geometry but for all unknown fields. For the displacement fields this yields the following Equations (4.3).

$$u(r,s) = \sum_{1}^{8} N_i(r,s)u_i \qquad v(r,s) = \sum_{1}^{8} N_i(r,s)v_i \tag{4.3}$$

Since we are formulating an isoparametric element the same shape functions N_i as for the geometry are used. The displacements of any point (r, s) within the element are again found by interpolating the nodal displacements values u_i and v_i.

The main requirement for a set of shape functions is that they form a Partition of Unity (see Section 3.3.1). This means that the sum of all shape functions is always equal to unity at every point within the element. Another typical requirement is that a shape function has the value 1 at the location of its associated node and that all other shape functions are reduced to zero at that location. This condition will guarantee that the nodal value and the value of the interpolation field at the node location coincide.

Using these conditions the shape functions for the 8-node quadrilateral element can easily be determined [Bat96]. They are given in Equations (4.4).

$$N_1(r,s) = 1/4 \cdot (1+r)(1+s) - 1/4 \cdot (1-r^2)(1+s) - 1/4 \cdot (1-s^2)(1+r) \tag{4.4a}$$
$$N_2(r,s) = 1/4 \cdot (1-r)(1+s) - 1/4 \cdot (1-r^2)(1+s) - 1/4 \cdot (1-s^2)(1-r) \tag{4.4b}$$
$$N_3(r,s) = 1/4 \cdot (1-r)(1-s) - 1/4 \cdot (1-r^2)(1-s) - 1/4 \cdot (1-s^2)(1-r) \tag{4.4c}$$
$$N_4(r,s) = 1/4 \cdot (1+r)(1-s) - 1/4 \cdot (1-r^2)(1-s) - 1/4 \cdot (1-s^2)(1+r) \tag{4.4d}$$
$$N_5(r,s) = 1/2 \cdot (1-r^2)(1+s) \tag{4.4e}$$
$$N_6(r,s) = 1/2 \cdot (1-s^2)(1-r) \tag{4.4f}$$
$$N_7(r,s) = 1/2 \cdot (1-r^2)(1-s) \tag{4.4g}$$
$$N_8(r,s) = 1/2 \cdot (1-s^2)(1+r) \tag{4.4h}$$

It can easily be verified that the Equations (4.4) satisfy the requirements mentioned above.

4.2.3 Shape Function Matrix

The next step is to gather the shape functions from Equations (4.4) into the so-called *shape function matrix* $\mathbf{N}$. For the 8-node isoparametric plane-stress element this is given in Equation (4.5).

$$\mathbf{N} = \begin{bmatrix} N_1 & 0 & N_2 & 0 & N_3 & 0 & N_4 & 0 & N_5 & 0 & N_6 & 0 & N_7 & 0 & N_8 & 0 \\ 0 & N_1 & 0 & N_2 & 0 & N_3 & 0 & N_4 & 0 & N_5 & 0 & N_6 & 0 & N_7 & 0 & N_8 \end{bmatrix} \tag{4.5}$$

This matrix allows the more convenient and computer friendly computation of the unknown fields. Note that the shape functions $N_i(r,s)$ are still functions of r, s so the shape function matrix $\mathbf{N}(r,s)$ is also a function of r, s.

Using this compact notation and combining Equations (4.3) and (4.5) the displacement vector $\underline{\mathbf{u}}$ of any given point (r,s) in the quadrilateral element can be computed as shown in Equation (4.6) where $\underline{\mathbf{d}}_e$ is the vector of nodal displacement unknowns introduced in Equation (4.1).

$$\underline{\mathbf{u}}(r,s) = \begin{Bmatrix} u(r,s) \\ v(r,s) \end{Bmatrix} = \mathbf{N}(r,s) \cdot \underline{\mathbf{d}}_e \tag{4.6}$$

This relationship stipulates that the displacement of any point (r,s) can be computed from the nodal displacements.

4.2.4 Strain–Displacement Transformation Matrix

By using the kinematic equations of the underlying mechanical problem the strain field can be computed from the displacement field. For the plain-stress problem considered here the kinematic equations linking the strain $\underline{\epsilon}$ to the displacement $\underline{\mathbf{u}}$ are given by Equation (4.7).

$$\underline{\epsilon}(r,s) = \begin{Bmatrix} \epsilon_x \\ \epsilon_y \\ \gamma_{xy} \end{Bmatrix} = \begin{bmatrix} \partial/\partial x & 0 \\ 0 & \partial/\partial y \\ \partial/\partial y & \partial/\partial x \end{bmatrix} \begin{Bmatrix} u(r,s) \\ v(r,s) \end{Bmatrix} \tag{4.7}$$

In Equation (4.7) ∂ denotes the partial differential operator. Together with Equation (4.6) the strain can be computed as expressed by Equation (4.8).

$$\underline{\epsilon}(r,s) = \begin{bmatrix} \partial/\partial x & 0 \\ 0 & \partial/\partial y \\ \partial/\partial y & \partial/\partial x \end{bmatrix} \cdot \mathbf{N}(r,s) \cdot \underline{\mathbf{d}}_e \tag{4.8}$$

Usually a new matrix called the *strain–displacement transformation matrix* $\mathbf{B}$ is introduced. It is constructed by applying the differential operators from Equation 4.8 to the shape function matrix $\mathbf{N}$ (Equation 4.5). Following this procedure the strain can be computed directly from the nodal displacements by the following Equation (4.9a).

$$\underline{\epsilon}(r,s) = \mathbf{B}(r,s) \cdot \underline{\mathbf{d}}_e \qquad \text{with} \tag{4.9a}$$

$$\mathbf{B} = \begin{bmatrix} N_1^x & 0 & N_2^x & 0 & \cdots & N_7^x & 0 & N_8^x & 0 \\ 0 & N_1^y & 0 & N_2^y & \cdots & 0 & N_7^y & 0 & N_8^y \\ N_1^y & N_1^x & N_2^y & N_2^x & \cdots & N_7^y & N_7^x & N_8^y & N_8^x \end{bmatrix} \tag{4.9b}$$

$$N_i^x := \partial N_i/\partial x \qquad N_i^y := \partial N_i/\partial y \tag{4.9c}$$

The high indices denote a derivation by the indicated coordinate. The problem with the derivation by x and y is that the shape functions N_i are expressed in natural coordinates (r,s) and not real coordinates (x,y). However, r and s are functions of x and y.

In order to solve this problem the so-called *Jacobi transformation* is applied to the differentials. This transformation links the differential operators in the natural coordinate system to the differential operators in the global coordinate system. Using the standard procedure for the derivation of vector functions and respecting the chain rule it becomes clear that the natural differentials can be linked to the real differentials by Equations (4.10).

$$\frac{\partial}{\partial r} = \frac{\partial}{\partial x} \cdot \frac{\partial x}{\partial r} + \frac{\partial}{\partial y} \cdot \frac{\partial y}{\partial r} \qquad \frac{\partial}{\partial s} = \frac{\partial}{\partial x} \cdot \frac{\partial x}{\partial s} + \frac{\partial}{\partial y} \cdot \frac{\partial y}{\partial s} \tag{4.10}$$

Using matrix notation Equations (4.10) can be rewritten as Equation (4.11).

$$\begin{Bmatrix} \partial/\partial r \\ \partial/\partial s \end{Bmatrix} = \underbrace{\begin{bmatrix} \partial x/\partial r & \partial y/\partial r \\ \partial x/\partial s & \partial y/\partial s \end{bmatrix}}_{\mathbf{J}} \cdot \begin{Bmatrix} \partial/\partial x \\ \partial/\partial y \end{Bmatrix} \tag{4.11}$$

In Equation (4.11) the Jacobi transformation matrix $\mathbf{J}$ is introduced (to be precise it is the transposed of the Jacobi-matrix found in the mathematical literature). Of course the inverse transformation is given by Equation (4.12).

$$\begin{Bmatrix} \partial/\partial x \\ \partial/\partial y \end{Bmatrix} = \mathbf{J}^{-1} \cdot \begin{Bmatrix} \partial/\partial r \\ \partial/\partial s \end{Bmatrix} \tag{4.12}$$

Applying this result to Equation (4.9c) the shape function derivatives by x and y can be replaced by their natural counterparts.

$$\begin{Bmatrix} N_i^x(r,s) \\ N_i^y(r,s) \end{Bmatrix} = \mathbf{J}^{-1} \begin{Bmatrix} N_i^r(r,s) \\ N_i^s(r,s) \end{Bmatrix} \tag{4.13}$$

The determination of the shape function derivatives in the natural coordinate system is straight forward. Using Equation (4.4) this yields Equations (4.14) and (4.15).

$$N_1^r(r,s) = +1/4 \cdot (1+s) - 1/4 \cdot (1-s^2) + 1/2 \cdot r(1+s) \tag{4.14a}$$
$$N_2^r(r,s) = -1/4 \cdot (1+s) + 1/4 \cdot (1-s^2) + 1/2 \cdot r(1+s) \tag{4.14b}$$
$$N_3^r(r,s) = -1/4 \cdot (1-s) + 1/4 \cdot (1-s^2) + 1/2 \cdot r(1-s) \tag{4.14c}$$
$$N_4^r(r,s) = +1/4 \cdot (1-s) - 1/4 \cdot (1-s^2) + 1/2 \cdot r(1-s) \tag{4.14d}$$
$$N_5^r(r,s) = -r(1+s) \tag{4.14e}$$
$$N_6^r(r,s) = -1/2 \cdot (1-s^2) \tag{4.14f}$$
$$N_7^r(r,s) = -r(1-s) \tag{4.14g}$$
$$N_8^r(r,s) = +1/2 \cdot (1-s^2) \tag{4.14h}$$

$$N_1^s(r,s) = +1/4\cdot(1+r) - 1/4\cdot(1-r^2) + 1/2\cdot s(1+r) \tag{4.15a}$$
$$N_2^s(r,s) = +1/4\cdot(1-r) - 1/4\cdot(1-r^2) + 1/2\cdot s(1-r) \tag{4.15b}$$
$$N_3^s(r,s) = -1/4\cdot(1-r) + 1/4\cdot(1-r^2) + 1/2\cdot s(1-r) \tag{4.15c}$$
$$N_4^s(r,s) = -1/4\cdot(1+r) + 1/4\cdot(1-r^2) + 1/2\cdot s(1+r) \tag{4.15d}$$
$$N_5^s(r,s) = +1/2\cdot(1-r^2) \tag{4.15e}$$
$$N_6^s(r,s) = -s(1-r) \tag{4.15f}$$
$$N_7^s(r,s) = -1/2\cdot(1-r^2) \tag{4.15g}$$
$$N_8^s(r,s) = -s(1+r) \tag{4.15h}$$

What remains to be determined are the terms of the Jacobi transformation matrix in Equation (4.11). For this purpose the coordinate interpolation procedure given in Equations (4.2) can be used. Performing the necessary derivations we find Equations (4.16).

$$\frac{\partial x}{\partial r} = \sum_1^8 \frac{\partial N_i(r,s)}{\partial r} x_i = \sum_1^8 N_i^r(r,s) x_i \tag{4.16a}$$

$$\frac{\partial x}{\partial s} = \sum_1^8 \frac{\partial N_i(r,s)}{\partial s} x_i = \sum_1^8 N_i^s(r,s) x_i \tag{4.16b}$$

$$\frac{\partial y}{\partial r} = \sum_1^8 \frac{\partial N_i(r,s)}{\partial r} y_i = \sum_1^8 N_i^r(r,s) y_i \tag{4.16c}$$

$$\frac{\partial y}{\partial s} = \sum_1^8 \frac{\partial N_i(r,s)}{\partial s} y_i = \sum_1^8 N_i^s(r,s) y_i \tag{4.16d}$$

The terms of the Jacobi matrix in Equation (4.16) can be computed numerically at the location of a point of interest (r,s) for which the strain should be determined.

4.2.5 Element Stiffness Matrix and Force Vector

As a next step the *element stiffness matrix* $\mathbf{K}_e$ and the *element force vector* $\underline{\mathbf{F}}_e$ are computed. These two key quantities can be derived from the *weak form of equilibrium* of a Finite Element (sometimes also called the integral form of equilibrium). It is given in Equation (4.17).

$$\int_{\Omega_e} \delta\underline{\epsilon}^T \cdot \underline{\sigma}\ d\Omega_e = \int_{\Omega_e} \delta\underline{\mathbf{u}}^T \cdot \underline{\mathbf{f}}\ d\Omega_e + \delta\underline{\mathbf{d}}_e{}^T \cdot \underline{\mathbf{P}}_e \tag{4.17}$$

The weak form of equilibrium can be interpreted as the equilibrium of the internal and the external virtual work over the domain of a Finite Element Ω_e. Let us assume that a Finite Element which is in equilibrium is subjected to an infinitesimal, virtual nodal displacement $\delta\underline{\mathbf{d}}_e$. This nodal displacement will cause an infinitesimal, virtual displacement field variation $\delta\underline{\mathbf{u}}$ which in turn will cause an infinitesimal, virtual strain field variation $\delta\underline{\epsilon}$. For an element subjected to this virtual deformation the weak form of equilibrium states that the external virtual work done by the element nodal forces $\underline{\mathbf{P}}_e$ and the element surface forces $\underline{\mathbf{f}}$ should be equal to the internal virtual work done by internal stresses $\underline{\sigma}$.

By further assuming a *linear, elastic constitutive law* (as it is postulated for this phase of the behavior of HPFRCCs in Section 4.1) the stress and strain fields can be linked by the following Equation (4.18).

$$\underline{\sigma} = \mathbf{D}\underline{\epsilon} \tag{4.18}$$

In the case of the linear, elastic, plane-stress conditions used here the constitutive matrix $\mathbf{D}$ is given by Equation 4.19 [Bat96].

$$\mathbf{D} = \frac{E}{1-\nu^2}\begin{bmatrix} 1 & \nu & 0 \\ \nu & 1 & 0 \\ 0 & 0 & \frac{1-\nu}{2} \end{bmatrix} \tag{4.19}$$

Substituting Equation (4.18) into Equation (4.17) the latter becomes Equation (4.20).

$$\int_{\Omega_e} \delta\underline{\epsilon}^T \cdot \mathbf{D} \cdot \underline{\epsilon}\ d\Omega_e = \int_{\Omega_e} \delta\underline{\mathbf{u}}^T \cdot \underline{\mathbf{f}}\ d\Omega_e + \delta\underline{\mathbf{d}}_e{}^T \cdot \underline{\mathbf{P}}_e \tag{4.20}$$

The next step is to discretize the integral form of equilibrium in Equation (4.20) following the *Bubnov-Galerkin* approach [Bat96]. This means that the displacement field and the strain field are replaced by their Finite Element approximations given in Equations (4.6) and (4.9a). Note that the same interpolation is used for both the virtual and the real fields. The discretized equation of equilibrium is given by Equation (4.21).

$$\int_{\Omega_e} (\mathbf{B} \cdot \delta\underline{\mathbf{d}}_e)^T \cdot \mathbf{D} \cdot \mathbf{B} \cdot \underline{\mathbf{d}}_e\ d\Omega_e = \int_{\Omega_e} (\mathbf{N} \cdot \delta\underline{\mathbf{d}}_e)^T \cdot \underline{\mathbf{f}}\ d\Omega_e + \delta\underline{\mathbf{d}}_e{}^T \cdot \underline{\mathbf{P}}_e \tag{4.21}$$

And after some simple algebraic transformation this becomes Equation (4.22).

$$\delta\underline{\mathbf{d}}_e^T \cdot \int_{\Omega_e} \mathbf{B}^T\mathbf{D}\mathbf{B}\ d\Omega_e \cdot \underline{\mathbf{d}}_e = \delta\underline{\mathbf{d}}_e^T \int_{\Omega_e} \mathbf{N}^T\underline{\mathbf{f}}\ d\Omega_e + \delta\underline{\mathbf{d}}_e{}^T \cdot \underline{\mathbf{P}}_e \tag{4.22}$$

It is clear that Equation (4.22) must hold for any arbitrary variation of the virtual nodal displacements $\delta\underline{\mathbf{d}}_e$ which finally leads to the *Finite Element Equilibrium Equation* (4.23).

$$\underbrace{\int_{\Omega_e} \mathbf{B}^T\mathbf{D}\mathbf{B}\; d\Omega_e}_{\mathbf{K}_e} \cdot \underline{\mathbf{d}}_e = \underbrace{\int_{\Omega_e} \mathbf{N}^T\underline{\mathbf{f}}\; d\Omega_e}_{\underline{\mathbf{F}}_e} + \underline{\mathbf{P}}_e \tag{4.23}$$

The matrix $\mathbf{K}_e$ is called the *element stiffness matrix* and it expresses the relationship between any externally applied forces and the resulting nodal displacements. The vector $\underline{\mathbf{F}}_e$ is called the *element force vector* and it represents the work-equivalent nodal forces of any arbitrary element loads. $\underline{\mathbf{P}}_e$ is the vector of external forces acting on the element nodes.

The next question that arises is how to compute the integrals for the element stiffness matrix and the element load vector. We recall that both the shape function matrix $\mathbf{N}(r,s)$ (see Equation (4.5)) as well as the strain–displacement transformation matrix $\mathbf{B}(r,s)$ (see Equation (4.9a)) are functions of the natural coordinates (r,s). Therefore, it is reasonable to compute the integrals in the natural domain instead of the real domain. This requires a coordinate transformation of the integration domain. Without going into any details the infinitesimal volume element $d\Omega_e$ can be expressed by the differentials of the natural domain as given in Equation (4.24).

$$d\Omega = t \cdot dx \cdot dy = \det(\mathbf{J}) \cdot t \cdot dr \cdot ds \tag{4.24}$$

The variable t represents the thickness of the plane-stress element. As long as the thickness does not vary within the element there is no need to integrate over it since the stress and strain are considered to be constant over that dimension (part of the plane-stress assumptions). It is sufficient to multiply the area of the domain with the thickness of the element.

After performing a coordinate system transformation from the real to the natural domain using Equation (4.24) and considering that the natural domain is spanned by $r \in (-1,1)$ and $s \in (-1,1)$ the element stiffness matrix and the element force vector can be expressed by Equation (4.25).

$$\mathbf{K}_e = \int_{r=-1}^{1}\int_{s=-1}^{1} \mathbf{B}^T(r,s)\mathbf{D}(r,s)\mathbf{B}(r,s)\det\mathbf{J}(r,s)\; t\; drds \tag{4.25a}$$

$$\underline{\mathbf{F}}_e = \int_{r=-1}^{1}\int_{s=-1}^{1} \mathbf{N}^T(r,s)\underline{\mathbf{f}}(r,s)\det\mathbf{J}(r,s)\; t\; drds \tag{4.25b}$$

The integrals in Equation (4.25) can be computed with a numerical integration scheme. Two of the most popular numerical integration schemes in Finite Element Analysis are

the *Gauss-Legendre* and the *Gauss-Lobatto* integration rules. Here the Gauss-Legendre quadrature is chosen. The basic principle behind these numerical integration schemes is to compute the values of the integrand at several specific and well chosen locations (called *Gauss points*) and then multiplying them with the respective Gauss point's representative surface (called its weight).

The Gauss-Legendre scheme is able to integrate a regular polynomial function of the order $2n-1$ correctly if n Gauss points are used. The plane-stress 8-node elements used here will at most produce a stiffness matrix of the 4^{th} order in both r and s as long as the distortion remains constant ($\mathbf{J}$ constant). Therefore, a 3×3 Gauss-Legendre integration rule is required to integrate the stiffness matrix exactly. For more heavily distorted elements the 3×3 integration scheme is only an approximation. However, with mesh-refinement the solution will rapidly converge towards the exact solution. The following Table 4.1 gives the locations and weights of the Gauss-Legendre integration points in a 3×3 quadrature over the natural domain $r \in (-1, 1)$, $s \in (-1, 1)$.

r_{gp}	s_{gp}	α_{gp}
$+\sqrt{3/5}$	$+\sqrt{3/5}$	$5/9 \cdot 5/9$
$-\sqrt{3/5}$	$+\sqrt{3/5}$	$5/9 \cdot 5/9$
$-\sqrt{3/5}$	$-\sqrt{3/5}$	$5/9 \cdot 5/9$
$+\sqrt{3/5}$	$-\sqrt{3/5}$	$5/9 \cdot 5/9$
0	$+\sqrt{3/5}$	$8/9 \cdot 5/9$
$-\sqrt{3/5}$	0	$5/9 \cdot 8/9$
0	$-\sqrt{3/5}$	$8/9 \cdot 5/9$
$+\sqrt{3/5}$	0	$5/9 \cdot 8/9$
0	0	$8/9 \cdot 8/9$

Table 4.1: Gauss-Legendre Quadrature 3×3

Replacing the analytical integral in Equations (4.25) with the numerical integration scheme the element stiffness matrix and the force vector can be computed as the sums over all Gauss points given in Equations (4.26).

$$\mathbf{K}_e = \sum_{\text{Gauss points}} \mathbf{B}^T(r_{gp}, s_{gp})\mathbf{D}(r_{gp}, s_{gp})\mathbf{B}(r_{gp}, s_{gp}) \cdot t \cdot \det \mathbf{J}(r_{gp}, s_{gp})\alpha_{gp} \tag{4.26a}$$

$$\underline{\mathbf{F}}_e = \sum_{\text{Gauss points}} \mathbf{N}^T(r_{gp}, s_{gp})\underline{\mathbf{f}}(r_{gp}, s_{gp}) \cdot t \cdot \det \mathbf{J}(r_{gp}, s_{gp})\alpha_{gp} \tag{4.26b}$$

In Equation (4.26) (r_{gp}, s_{gp}) are the natural coordinates of a Gauss point and α_{gp} is its respective weight. This final results shows that the element stiffness matrix is computed by

evaluating the strain–displacement transformation matrix and the Jacobi transformation matrix at a number of discrete integration points.

4.2.6 Assembly

The next step in the Finite Element procedure is the *assembly* of all elements to a global structure. Since elements connecting to the same node and sharing the same degrees of freedom act in parallel the contributions of each individual element to the global stiffness matrix and the global force vector can simply be added up. Special care has to be taken that the element contributions are added at the correct location within the global system of equations. For this purpose it is easiest to number all degrees of freedom of the system sequentially. Each number then corresponds to one equation. By identifying which element degree of freedom corresponds to which global degree of freedom the stiffness matrix terms and the force vector terms can be added to the correct global equation. For more detailed information about the assembly procedure the reader is referred to [Bat96].

4.2.7 Solution of the Global System of Equations

After introducing the appropriate support conditions and possible external nodal loads the global system of equations can be solved for the unknown nodal degrees of freedom. The easiest way to take support conditions into account is to omit the equations which correspond to a blocked degree of freedom. These equations can later be used to determine the reaction forces of the support. More complicated support conditions such as springs or constraint equations could also be taken into account but they are not discussed here (for more information see [Bat96]).

The global system of equations can be solved by inverting the reduced global stiffness matrix (reduced by the equations corresponding to the blocked support conditions). The most commonly used method for inverting the global stiffness matrix is the *Gauss elimination* algorithm. More information about this procedure can be found in any textbook on linear algebra.

Solving the global system of equations yields the nodal displacement unknowns. By identifying the matching global (system) and local (element) unknowns the nodal displacements of each element can be determined.

4.2.8 Secondary Results

Once the primary nodal displacement unknowns have been determined the next step in the procedure it to compute other secondary unknowns of the element. The previously introduced Equations (4.6), (4.9a) and (4.18) can be used to compute the displacements,

strains and stresses at any arbitrary position within the element in function of the element nodal displacements. For clarity they are repeated here:

$$\begin{aligned} \underline{\mathbf{u}}(r,s) &= \mathbf{N}(r,s) \cdot \underline{\mathbf{d}}_e \\ \underline{\epsilon}(r,s) &= \mathbf{B}(r,s) \cdot \underline{\mathbf{d}}_e \\ \underline{\sigma}(r,s) &= \mathbf{D} \cdot \underline{\epsilon}(r,s) \qquad \text{(for lin. el. analysis)} \end{aligned}$$

Typically the secondary results are only computed at the locations of the Gauss points and the rest of the field is interpolated.

4.2.9 Equilibrium Check

The final step is checking for nodal equilibrium within the structure. This means that each node of the structure is checked and it is verified that all element reactions $\underline{\mathbf{R}}_e$ and all externally applied equivalent nodal loads $\underline{\mathbf{F}}_e$ and nodal loads $\underline{\mathbf{P}}_e$ sum up to zero. This step is not mandatory for linear analysis since the nodal equilibrium is automatically satisfied if the material law is linear. If the material law is nonlinear the deformation state predicted with a tangent constitutive matrix will deviate from the true equilibrium state and a corrective procedure such as a Newton-Raphson equilibrium iteration has to be implemented [Bat96].

The element reaction forces $\underline{\mathbf{R}}_e$ are computed by virtue of the principle of virtual work as expressed in Equation (4.27).

$$\underline{\mathbf{R}}_e = \int_{\Omega_e} \mathbf{B}^T \underline{\sigma} \; d\Omega_e \tag{4.27}$$

Or with numerical integration over the natural domain this becomes Equation (4.28).

$$\underline{\mathbf{R}}_e = \sum_{\text{Gauss points}} \mathbf{B}^T(r_{gp}, s_{gp}) \underline{\sigma}(r_{gp}, s_{gp}) \cdot t \cdot \det \mathbf{J}(r_{gp}, s_{gp}) \alpha_{gp} \tag{4.28}$$

Once the equilibrium at every node is satisfied the Finite Element Analysis ends and the results can be plotted.

Chapter 5

Multiple Cracking Model

5.1 Introduction

After having introduced a model for the elastic phase in Chapter 4 in this chapter we will extend the model to capture the characteristic strain-hardening phase of High Performance Fiber Reinforced Cementitious Composites in tension. As proposed in Section 3.4.2 the strain-hardening phase is modeled by a Smeared Crack Model or more precisely a Rotating Crack Model.

Using a Smeared Crack Model for the strain-hardening phase makes sense from both a physical and also from a modeling point of view. A HPFRCC structural member that undergoes strain-hardening will exhibit a large number of very fine parallel cracks (known as multiple cracking) that are distributed all over the heavily strained zones. Due to fiber bridging action the cracks do not localize and stresses can be redistributed in the structure. Also the crack width (e.g. $\approx 10^{-4}\ m$ for ECCs) and the crack-to-crack distance (e.g. $\approx 10^{-3}\ m$ for ECCs) are typically much smaller than the geometry of the analyzed structure. Therefore, it is reasonable and justified to use a continuum representation of the multiple cracking and strain-hardening phase in the sense of a *Representative Volume Element* [BO83, Kab07]. The effect of the cracks is thereby taken into account in an averaged way. It would make no sense to account for every small crack individually as this would firstly be highly inefficient and secondly these cracks are active on a meso-scale and their effect is only perceived as an additional strain at the scale of the structure. This is in contrast to localized cracks which truly represent a loss of cohesion of the structure and which ultimately separate the continuum into two disconnected parts. Therefore, localized cracks are modeled by a discrete crack approach as will be shown in Chapter 6.

For the model presented here it was decided to use a Rotating Crack Model for the strain-hardening phase. There are two reasons for this. Firstly the multiple, fine cracks that form in a HPFRCC during the strain-hardening phase can be seen as the coalescence of a number of microcracks. The latter can easily close and open depending on the direction

of loading. With rotating principal stress directions some microcracks become inactive whereas others are activated and start opening. On the scale of the structure this leads to a rotation of the perceived cracking direction. Note that as with every model this is only an approximation but one that seems reasonable from a macroscopic point of view. This is especially true if one keeps in mind that the rotation of the principal stresses in a structural element is normally a very gradual process. However, it is important to guarantee that the correct amount of energy is consumed during cracking and that no energy can be recovered through rotation of the principal stress directions.

The second reason for using a Rotating Crack Model and not a Fixed Crack Model (see Sections 3.2.2 and 3.2.4) is a purely practical one. As we have seen in Section 3.2.2 the Fixed Crack Model requires the introduction of a shear retention factor or a crack-sliding vs. shear-stress relationship which is experimentally difficult to determine and might add a level of sophistication to the model that is hard to relate to the physical reality of the material. The Rotating Crack Model on the other hand does not need this parameter as it assumes permanent coaxiality between the directions of principal strain and principal stress.

Using a Rotating Crack Model for the strain-hardening phase of High Performance Fiber Reinforced Cementitious Composites is in accordance with the majority of HPFRCC models suggested by other authors (see Section 3.4.1). However, it is very important to note that in contrast to the existing models the one proposed here only uses a Smeared Crack Model for the strain-hardening phase of HPFRCCs and not for the crack localization and softening phase. This is motivated by the fact that once a crack localizes it changes its nature and should no longer be described by a continuum model because this contradicts the physical reality of a crack and leads to a number of numerical problems as elaborated in Section 3.2.5.

The proposed Rotating Crack Model is presented in the following Section 5.2. It is formulated to be used in conjunction with the isoparametric, quadrilateral plane-stress elements introduced in Chapter 4.

5.2 Smeared Crack Hardening Model

The Rotating Crack Model for the strain-hardening phase of High Performance Fiber Reinforced Cementitious Composites that is presented in this section is an adaptation of the Smeared Crack Model given in [Rot88] and closely follows the implementation proposed in [JZ98]. It should be noted, that in contrast to the classical Smeared Crack Models the model presented hereafter is not used for crack localization and softening. By consequence there is no need to introduce a numerical localization bandwidth (see Section 3.2.1). Furthermore, accounting for cracking in an averaged or "smeared" way closely reflects the physical reality of multiple cracking in strain-hardening HPFRCCs whereas the smearing of a crack in the traditional Smeared Crack Models is only an

artifice that is used to capture a discrete crack by a continuum representation. However, although the Rotating Crack Model presented here is used for strain-hardening it shares most of its theoretical basis with the conventional Smeared Crack Models which were presented in Section 3.2.

As we have seen in Section 3.2 Smeared Crack Models account for cracking by modifying the constitutive relationship to include the cracking strain. We should therefore keep in mind, that in the setting of a nonlinear (incremental) Finite Element Analysis there are two things that are required from the Smeared Crack constitutive law. Firstly this is an *algorithmic stress* function which returns the global stress increment $\Delta\underline{\sigma}$ in function of the global strain increment $\Delta\underline{\epsilon}$. And secondly this is a tangent constitutive matrix $\mathbf{D}$ at any given global strain state $\underline{\epsilon}$. The algorithmic stress function and the tangent stiffness matrix for a Rotating Crack Model for our isoparametric quadrilateral element from Chapter 4 are presented in the following.

5.2.1 Strain Decomposition

Let $\underline{\epsilon}_{tot}$ be the total strain at any unknown target state of the material. The first fundamental concept of the proposed Rotating Crack Model is a decomposition of the total strain $\underline{\epsilon}_{tot}$ into a concrete strain $\underline{\epsilon}_{co}$ and a cracking strain $\underline{\epsilon}_{cr}$. This allows for the individual treatment of the concrete and the cracks (different constitutive laws). By doing so the model achieves great flexibility and consistently separates the cracking behavior from the bulk material behavior. One way to look at this, is to think of the cracking strain as being superimposed on the standard concrete behavior. From a physical point of view this makes perfect sense since the effect of multiple cracking is macroscopically observed as an additional strain in the direction of cracking. This is schematically illustrated in Figure 5.1.

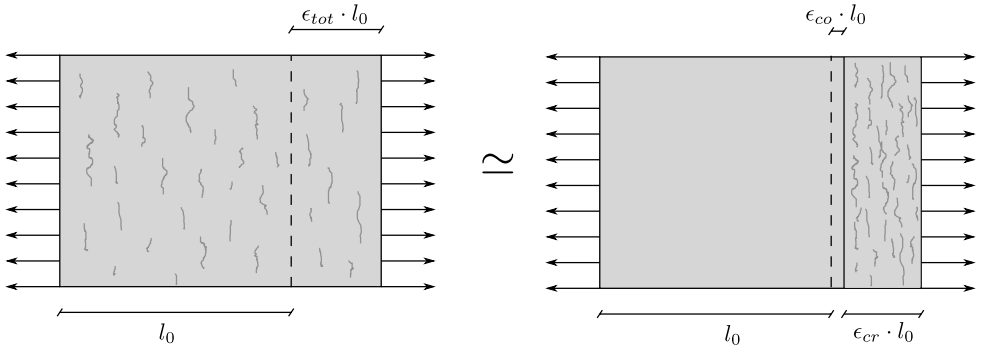

Figure 5.1: Schematic representation of the strain decomposition

Mathematically the strain decomposition is expressed by Equation (5.1) which must hold true for any state of the material.

$$\underline{\epsilon}_{tot} = \underline{\epsilon}_{co} + \underline{\epsilon}_{cr} \tag{5.1}$$

The nonlinear Finite Element solution technique requires that the problem is formulated in incremental form. Departing from a state of *equilibrium* at which the total strain $\underline{\epsilon}_{tot}^{eq}$ and also the individual strain components $\underline{\epsilon}_{co}^{eq}$, $\underline{\epsilon}_{cr}^{eq}$ are known a total strain increment $\Delta\underline{\epsilon}_{tot}$ is applied (as part of the Finite Element solution procedure) leading to the target state expressed in Equation (5.2a). This will entail an a priori unknown increment of the concrete strain $\Delta\underline{\epsilon}_{co}$ and of the cracking $\Delta\underline{\epsilon}_{cr}$ strain as given by Equations (5.2b) and (5.2c).

$$\underline{\epsilon}_{tot} = \underline{\epsilon}_{tot}^{eq} + \Delta\underline{\epsilon}_{tot} \tag{5.2a}$$
$$\underline{\epsilon}_{co} = \underline{\epsilon}_{co}^{eq} + \Delta\underline{\epsilon}_{co} \tag{5.2b}$$
$$\underline{\epsilon}_{cr} = \underline{\epsilon}_{cr}^{eq} + \Delta\underline{\epsilon}_{cr} \tag{5.2c}$$

5.2.2 Rotation into the Crack System

The second fundamental assumption of the Rotating Crack Model is that the cracking direction is always coaxial with the directions of principal strain (see Section 3.2.4). For the herein developed plane-stress model this means that every material point can have two orthogonal sets of cracks each one corresponding to one of the principal directions of total strain. This is shown schematically in Figure 5.2.

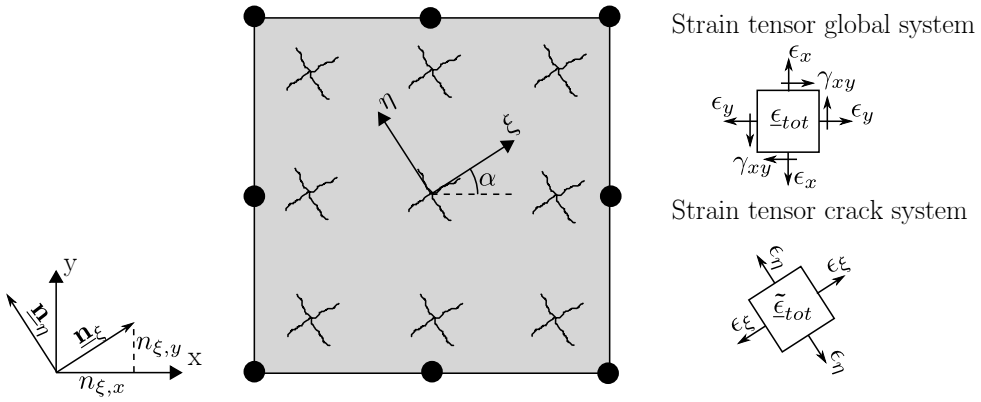

Figure 5.2: Crack system in the direction of principal strain

Figure 5.2 shows an element that is cracking in both directions of principal strain. In the global coordinate system (x, y) the strain is given by $\underline{\epsilon}_{tot} = (\epsilon_x, \epsilon_y, \gamma_{xy})$ (engineering notation). Because the crack directions are coaxial with the directions of principal strain the strain state in the coordinate system associated with the cracks (ξ, η) is given by $\underline{\tilde{\epsilon}}_{tot} = (\epsilon_\xi, \epsilon_\eta)$ and does not have any shear component as shown in Figure 5.2. The crack directions are defined by the unit direction vectors $\underline{\mathbf{n}}_\xi = (n_{\xi,x}, n_{\xi,y})$ and $\underline{\mathbf{n}}_\eta = (n_{\eta,x}, n_{\eta,y})$. Note that the components of the direction vectors are directly linked to the angle of rotation of the coordinate system α as given by Equation (5.3).

$$\underline{\mathbf{n}}_\xi = \begin{Bmatrix} n_{\xi,x} \\ n_{\xi,y} \end{Bmatrix} = \begin{Bmatrix} \cos\alpha \\ \sin\alpha \end{Bmatrix} \qquad \underline{\mathbf{n}}_\eta = \begin{Bmatrix} n_{\eta,x} \\ n_{\eta,y} \end{Bmatrix} = \begin{Bmatrix} -\sin\alpha \\ \cos\alpha \end{Bmatrix} \tag{5.3}$$

With changing state of total strain the principal directions will rotate and with them the crack directions will rotate as well. This means that for a given strain increment $\Delta\underline{\epsilon}_{tot}$ the principal directions of total strain will in general rotate and lead to a rotation of the cracks. However, since the cracks are always coaxial with the principal directions their new orientation can easily be obtained by determining the principal directions of the target strain state $\underline{\epsilon}_{tot}$. The components of the unit vector in the first principal direction $\underline{\mathbf{n}}_\xi = (n_{\xi,x}, n_{\xi,y})$ are given by Equation (5.4) and the unit vector of the second principal direction is given by $\underline{\mathbf{n}}_\eta = (-n_{\xi,y}, n_{\xi,x})$ due to its orthogonality with $\underline{\mathbf{n}}_\xi$ (as follows directly from Equation 5.3).

$$n_{\xi,x} = \frac{\frac{1}{2}\gamma_{xy}}{\left((\epsilon_\xi - \epsilon_x)^2 + \frac{1}{4}\gamma_{xy}^2\right)^{\frac{1}{2}}} \qquad n_{\xi,y} = \frac{\epsilon_\xi - \epsilon_x}{\left((\epsilon_\xi - \epsilon_x)^2 + \frac{1}{4}\gamma_{xy}^2\right)^{\frac{1}{2}}} \tag{5.4}$$

Because the cracks are always acting in the principal directions it is convenient to rotate the global strain into the coordinate system associated with the crack. The rotation between the local and the global coordinate system and vice versa is done by the rotation matrices $\mathbf{R}_\sigma$ and $\mathbf{R}_\epsilon$ given in Equation (5.5). This results in Equations (5.6) which give the relationship between the local stress $\widetilde{\underline{\sigma}}$ respectively strain $\widetilde{\underline{\epsilon}}$ and the global stress $\underline{\sigma}$ respectively strain $\underline{\epsilon}$.

$$\mathbf{R}_\sigma = \begin{bmatrix} n_{\xi,x}^2 & n_{\xi,y}^2 \\ n_{\xi,y}^2 & n_{\xi,x}^2 \\ n_{\xi,x}n_{\xi,y} & -n_{\xi,x}n_{\xi,y} \end{bmatrix} \qquad \mathbf{R}_\epsilon = \begin{bmatrix} n_{\xi,x}^2 & n_{\xi,y}^2 \\ n_{\xi,y}^2 & n_{\xi,x}^2 \\ 2n_{\xi,x}n_{\xi,y} & -2n_{\xi,x}n_{\xi,y} \end{bmatrix} \tag{5.5}$$

$$\underline{\sigma} = \mathbf{R}_\sigma \cdot \widetilde{\underline{\sigma}} \qquad \widetilde{\underline{\epsilon}} = \mathbf{R}_\sigma^T \cdot \underline{\epsilon} \tag{5.6a}$$

$$\underline{\epsilon} = \mathbf{R}_\epsilon \cdot \widetilde{\underline{\epsilon}} \qquad \widetilde{\underline{\sigma}} = \mathbf{R}_\epsilon^T \cdot \underline{\sigma} \tag{5.6b}$$

Note that the transformation expressed by Equations (5.6) does not only perform the rotation of the stress and strain vectors but it also eliminates the shear value by exploiting the fact that the local system is coaxial with the principal directions (the shear strain component is zero).

5.2.3 Constitutive Equations

The next thing that needs to be defined are the constitutive equations. As we have already mentioned in Section 5.2.1 we will define individual constitutive laws for both the cracks

and the bulk material. In nonlinear Finite Element Analysis the material behavior is typically given by a *constitutive law* of the type $\Delta\underline{\sigma} = \chi(\Delta\underline{\epsilon})$ that relates the incremental strains to an incremental stresses. It turns out that in the case of Smeared Crack Models it is more convenient to express the material behavior by a *compliance law* of the type $\Delta\underline{\epsilon} = \phi(\Delta\underline{\sigma})$ where ϕ is the inverse function of χ. For the uncracked bulk material we assume a linear, elastic behavior as defined by Equation (4.18) in Section 4.2.5. This leads to a compliance law for the bulk concrete as given by Equation (5.7). The elastic compliance matrix $\mathbf{C}_{co}$ is given by Equation (5.8) and it is computed as the the inverse of the elastic constitutive matrix $\mathbf{C}_{co} = \mathbf{D}_{co}^{-1}$ (see Equation 4.19).

$$\Delta\underline{\epsilon}_{co} = \phi_{co}(\Delta\underline{\sigma}_{co}) = \mathbf{C}_{co} \cdot \Delta\underline{\sigma}_{co} \tag{5.7}$$

$$\mathbf{C}_{co} = \frac{1}{E}\begin{bmatrix} 1 & -\nu & 0 \\ -\nu & 1 & 0 \\ 0 & 0 & 2(1+\nu) \end{bmatrix} \tag{5.8}$$

The cracking law is also defined in compliance format and it is conveniently formulated in the local coordinate system associated with the cracks (principal directions). It relates the local cracking strain increments $\Delta\underline{\widetilde{\epsilon}}_{cr}$ to the local cracking stress increments $\Delta\underline{\widetilde{\sigma}}_{cr}$.

The third fundamental assumption of the proposed Rotating Crack Model is that the components of the cracking law are uncoupled. This means that a set of cracks in the first principal direction ξ does not interact with a set of of cracks in the second principal direction η. Although it is a simplification this seems to be a reasonable assumption and it is standard for Rotating Crack Models. Note that a coupling between the components can still be introduced by an implicit relationship between the cracking laws. Considering all this, the compliance law for the cracks is given by Equation (5.9).

$$\Delta\underline{\widetilde{\epsilon}}_{cr} = \phi_{cr}(\Delta\underline{\widetilde{\sigma}}_{cr}) = \begin{Bmatrix} \phi_{cr,\xi}(\Delta\widetilde{\sigma}_{cr,\xi}) \\ \phi_{cr,\eta}(\Delta\widetilde{\sigma}_{cr,\eta}) \end{Bmatrix} \tag{5.9}$$

For the model presented here it is assumed that the compliance functions in both principal directions are the same ($\phi_{cr,\xi} = \phi_{cr,\eta}$) and that they are nonlinear. A schematic cracking law for High Performance Fiber Reinforced Cementitious Composites is illustrated in Figure 5.3. Note that the cracking strain remains zero as long as the total stress does not exceed the first cracking stress of the material ($\widetilde{\sigma}_{cr} < \sigma_{cc}$). During unloading it is assumed that the microcracks in HPFRCCs close completely which manifests in an unloading branch of the cracking law that returns to the origin. However, unloading with a residual cracking strain is also a viable option and the choice depends on the specific HPFRCC.

In principle this model can readily be extended to a cyclic one by simply providing a compliance curve or function that represents the material's cyclic behavior. Such a law could

per example be determined experimentally by means of a cyclic direct tension/compression test (e.g. [KBD03, KB04]).

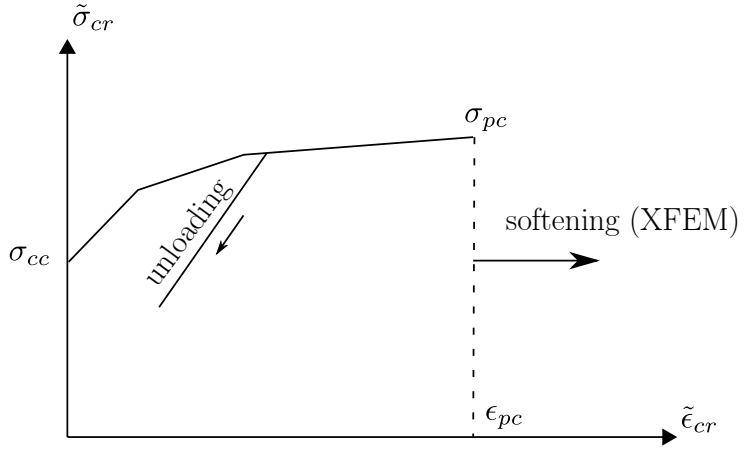

Figure 5.3: Piecewise linear cracking law for HPFRCCs

The cracking law is only valid until the post-cracking strain ϵ_{pc} and the corresponding post-cracking stress σ_{pc} are reached. After that a localized crack which is represented by a discrete cohesive discontinuity is introduced. The latter is modeled by the eXtended Finite Element Method as will be explained in Chapter 6. Furthermore, the specific details on how and when the transition between the smeared and the discrete model is performed can be found in Sections 6.4 and 6.5.

5.2.4 Algorithmic Stress Function

As we have mentioned in the introduction to this chapter one of the primary goals is to come up with an algorithmic stress function that computes the stress increment $\Delta\underline{\sigma}$ for any given total strain increment $\Delta\underline{\epsilon}_{tot}$. Such a function for the herein developed Rotating Crack Model is derived in the following.

We start out with Equation (5.1) which represents the decomposition of the total strain at the target state for which the stress should be computed. We also assume that we are currently at a state of equilibrium where all state variables (i.e. $\underline{\epsilon}_{tot}^{eq}$, $\underline{\sigma}_{tot}^{eq}$, $\underline{\epsilon}_{co}^{eq}$, $\underline{\sigma}_{co}^{eq}$, $\underline{\tilde{\epsilon}}_{cr}^{eq}$, $\underline{\tilde{\sigma}}_{cr}^{eq}$) are known. We can then express Equation (5.1) of the target state in incremental form by using Equations (5.2). This yields Equation (5.10).

$$\underline{\epsilon}_{tot}^{eq} + \Delta\underline{\epsilon}_{tot} = \underline{\epsilon}_{co}^{eq} + \Delta\underline{\epsilon}_{co} + \underline{\epsilon}_{cr}^{eq} + \Delta\underline{\epsilon}_{cr} \tag{5.10}$$

Because the constitutive law for the cracks is given in the local coordinate system associated with the cracks (corresponding to the principal directions of the target strain state $\underline{\epsilon}_{tot}$) Equation (5.10) is rotated into the crack coordinate system as was explained in Section 5.2.2. Using Equation (5.6a) this leads to Equation (5.11).

$$\mathbf{R}_\sigma^T(\underline{\epsilon}_{tot}^{eq} + \Delta\underline{\epsilon}_{tot}) = \mathbf{R}_\sigma^T(\underline{\epsilon}_{co}^{eq} + \Delta\underline{\epsilon}_{co}) + \underbrace{\mathbf{R}_\sigma^T(\underline{\epsilon}_{cr}^{eq} + \Delta\underline{\epsilon}_{cr})}_{\widetilde{\underline{\epsilon}}_{cr}^{eq} + \Delta\widetilde{\underline{\epsilon}}_{cr}} \tag{5.11}$$

Note that the rotation matrices depend on the total strain state and will change over time which introduces the characteristic rotation of the cracks. Also note that the last term in Equation (5.11) which corresponds to the cracking strain can be directly expressed in the local coordinate system where it is well known.

The next step is to use the compliance functions defined in Section 5.2.3 (Equations 5.7 and 5.9). Replacing the strain increments in Equation (5.11) with the values computed through the compliance functions results in Equation (5.12).

$$\mathbf{R}_\sigma^T\left[\underline{\epsilon}_{tot}^{eq} + \Delta\underline{\epsilon}_{tot}\right] = \mathbf{R}_\sigma^T\left[\underline{\epsilon}_{co}^{eq} + \phi_{co}(\Delta\underline{\sigma}_{co})\right] + \widetilde{\underline{\epsilon}}_{cr}^{eq} + \phi_{cr}(\Delta\widetilde{\underline{\sigma}}_{cr}) \tag{5.12}$$

In order to solve Equation (5.12) we need a relationship between the stress in the concrete and the cracking stress. This is provided by the local equilibrium of the cracks which enforces that the cracking stress $\widetilde{\underline{\sigma}}_{cr}$ and the projection of the concrete stress onto the crack system $\widetilde{\underline{\sigma}}_{co}$ are equal (Equation 5.13).

$$\widetilde{\underline{\sigma}}_{co} = \widetilde{\underline{\sigma}}_{cr} \tag{5.13}$$

Rotating Equation (5.13) back into the global system by using Equation (5.6a) the global concrete stress can be related to the local cracking stress as indicated in Equation (5.14).

$$\underbrace{\mathbf{R}_\sigma\widetilde{\underline{\sigma}}_{co}}_{\underline{\sigma}_{co}} = \mathbf{R}_\sigma\widetilde{\underline{\sigma}}_{cr} \tag{5.14}$$

In analogy to Equations (5.2) in Section 5.2.1 the incremental equations $\underline{\sigma}_{co} = \underline{\sigma}_{co}^{eq} + \Delta\underline{\sigma}_{co}$ and $\widetilde{\underline{\sigma}}_{cr} = \widetilde{\underline{\sigma}}_{cr}^{eq} + \Delta\widetilde{\underline{\sigma}}_{cr}$ can be used to transform Equation (5.14) directly into Equation (5.15). With the latter the global concrete stress increments can be computed from the local cracking stress increments.

$$\Delta\underline{\sigma}_{co} = \mathbf{R}_\sigma\left(\widetilde{\underline{\sigma}}_{cr}^{eq} + \Delta\widetilde{\underline{\sigma}}_{cr}\right) - \underline{\sigma}_{co}^{eq} \tag{5.15}$$

Using Equation (5.15) in conjunction with Equation (5.12) finally yields the following Equation (5.16) which relates the incremental stress in the crack system to the global strain increment.

$$\mathbf{R}_\sigma^T\left[\underline{\epsilon}_{tot}^{eq} + \Delta\underline{\epsilon}_{tot}\right] = \mathbf{R}_\sigma^T\left[\underline{\epsilon}_{co}^{eq} + \phi_{co}\big(\mathbf{R}_\sigma\left(\widetilde{\underline{\sigma}}_{cr}^{eq} + \Delta\widetilde{\underline{\sigma}}_{cr}\right) - \underline{\sigma}_{co}^{eq}\big)\right] + \widetilde{\underline{\epsilon}}_{cr}^{eq} + \phi_{cr}(\Delta\widetilde{\underline{\sigma}}_{cr}) \tag{5.16}$$

By simple algebraic manipulation the above Equation (5.16) can be rewritten as Equation (5.17). Note that two new terms $\Delta\underline{\widetilde{\epsilon}}^{eq}$ and $\Delta\underline{\sigma}^{eq}$ are introduced. Although they are only used to alleviate the notation there is also a physical interpretation. The term $\Delta\underline{\widetilde{\epsilon}}^{eq}$ corresponds to the local strain disequilibrium that is created by the rotation of the crack axes whereas $\Delta\underline{\sigma}^{eq}$ can be interpreted as the global stress disequilibrium between the bulk material and the cracks that is created by the rotation of the axes. If there is no rotation of the crack axes both terms are zero.

$$\underbrace{\mathbf{R}_\sigma^T\underline{\epsilon}_{tot}^{eq} - \mathbf{R}_\sigma^T\underline{\epsilon}_{co}^{eq} - \underline{\widetilde{\epsilon}}_{cr}^{eq}}_{\Delta\underline{\widetilde{\epsilon}}^{eq}} + \mathbf{R}_\sigma^T\Delta\underline{\epsilon}_{tot} = \mathbf{R}_\sigma^T\phi_{co}\big(\underbrace{\mathbf{R}_\sigma\underline{\widetilde{\sigma}}_{cr}^{eq} - \underline{\sigma}_{co}^{eq}}_{\Delta\underline{\sigma}^{eq}} + \mathbf{R}_\sigma\Delta\underline{\widetilde{\sigma}}_{cr}\big) + \phi_{cr}\big(\Delta\underline{\widetilde{\sigma}}_{cr}\big) \quad (5.17)$$

Equation (5.17) has to be solved for $\Delta\underline{\widetilde{\sigma}}_{cr}$. In the most general case the compliance functions ϕ_{co} and ϕ_{cr} are nonlinear functions of $\Delta\underline{\widetilde{\sigma}}_{cr}$ and by consequence a numerical solution procedure needs to be implemented. In Section 5.2.3 the assumption was made that the compliance function for the bulk material is linear (see Equation 5.7) but that the cracking compliance function is nonlinear. Therefore, Equation (5.17) is solved by using the Newton-Raphson iteration algorithm. In order to do so Equation (5.17) has to be linearized. The linearized versions of the compliance laws are given in Equations (5.18).

$$\phi_{co}^{lin}\big(\Delta\underline{\sigma}^{eq} + \mathbf{R}_\sigma(\Delta\underline{\widetilde{\sigma}}_{cr} + \delta\underline{\widetilde{\sigma}}_{cr})\big) = \phi_{co}\big(\Delta\underline{\sigma}^{eq} + \mathbf{R}_\sigma\Delta\underline{\widetilde{\sigma}}_{cr}\big) + \mathbf{C}_{co}\mathbf{R}_\sigma\delta\underline{\widetilde{\sigma}}_{cr} \quad (5.18a)$$

$$\phi_{cr}^{lin}(\Delta\underline{\widetilde{\sigma}}_{cr} + \delta\underline{\widetilde{\sigma}}_{cr}) = \phi_{cr}(\Delta\underline{\widetilde{\sigma}}_{cr}) + \widetilde{\mathbf{C}}_{cr}\delta\underline{\widetilde{\sigma}}_{cr} \quad (5.18b)$$

In Equation (5.18b) $\widetilde{\mathbf{C}}_{cr}$ is the *tangent* compliance matrix for the cracks at the current state in the crack coordinate system. Since the components are assumed to be uncoupled it is given by Equation (5.19).

$$\widetilde{\mathbf{C}}_{cr} = \begin{bmatrix} \frac{\partial\phi_{cr,\xi}}{\partial\Delta\widetilde{\sigma}_{cr,\xi}} & 0 \\ 0 & \frac{\partial\phi_{cr,\eta}}{\partial\Delta\widetilde{\sigma}_{cr,\eta}} \end{bmatrix} \quad (5.19)$$

Linearizing Equation (5.17) by using Equations (5.18) leads to Equation (5.20).

$$\Delta\underline{\widetilde{\epsilon}}^{eq} + \mathbf{R}_\sigma^T\Delta\underline{\epsilon}_{tot} = \mathbf{R}_\sigma^T\phi_{co}\big(\Delta\underline{\sigma}^{eq} + \mathbf{R}_\sigma\Delta\underline{\widetilde{\sigma}}_{cr}\big) + \phi_{cr}(\Delta\underline{\widetilde{\sigma}}_{cr}) + \underbrace{\big(\mathbf{R}_\sigma^T\mathbf{C}_{co}\mathbf{R}_\sigma + \widetilde{\mathbf{C}}_{cr}\big)}_{\widetilde{\mathbf{C}}_{smcr}}\delta\underline{\widetilde{\sigma}}_{cr} \quad (5.20)$$

Finally Equation (5.20) can be solved iteratively by repetitively solving for $\delta\underline{\widetilde{\sigma}}_{cr}$ as given in Equation (5.21) and then updating $\Delta\underline{\widetilde{\sigma}}_{cr}^{n+1} := \Delta\underline{\widetilde{\sigma}}_{cr}^{n} + \delta\underline{\widetilde{\sigma}}_{cr}^{n}$.

$$\delta\underline{\widetilde{\sigma}}_{cr}^{n} = \widetilde{\mathbf{C}}_{smcr}^{-1}\left[\Delta\underline{\widetilde{\epsilon}}^{eq} + \mathbf{R}_{\sigma}^{T}\Delta\underline{\epsilon}_{tot} - \mathbf{R}_{\sigma}^{T}\phi_{co}\left(\Delta\underline{\sigma}^{eq} + \mathbf{R}_{\sigma}\Delta\underline{\widetilde{\sigma}}_{cr}^{n}\right) - \phi_{cr}(\Delta\underline{\widetilde{\sigma}}_{cr}^{n})\right] \tag{5.21}$$

There are a couple of remarks that should be made about Equation (5.21). The first one is that the crack compliance matrix $\widetilde{\mathbf{C}}_{cr}$ can either be updated to the new state of $\Delta\underline{\widetilde{\sigma}}_{cr}^{n+1}$ at every iteration step (*full* Newton-Raphson) or it can be kept constant (*modified* Newton-Raphson). Here it was decided to use the full Newton-Raphson technique since it converges faster and the matrix inversion $\widetilde{\mathbf{C}}_{smcr}^{-1}$ is computationally inexpensive because it is only a 2×2 matrix. Another important thing is to realize that the rotation matrix $\mathbf{R}_{\sigma}$ does not change during the iteration since it is determined by the principal directions of the total strain $\underline{\epsilon}_{tot} = \underline{\epsilon}_{tot}^{eq} + \Delta\underline{\epsilon}_{tot}$ which remain unchanged.

One way to look at Equation (5.21) is to interpret it as a kind of "inner" equilibrium iteration during which the cracking stress and the concrete stress are brought into equilibrium. Once the iteration has converged the global stress increment $\Delta\underline{\sigma}$ follows directly from Equation (5.15). It can be returned as the result of the stress return algorithm and the standard Finite Element procedure is followed from there.

There is one final note that should be made here. The state of the cracked concrete is only saved as an equilibrium state once the "external" Finite Element iteration has reached equilibrium and not when the "inner" equilibrium of Equation (5.21) has converged. It is absolutely vital, that the stress-return algorithm is entered with the total strain increment from the last global equilibrium state. Otherwise numerical problems such as *false unloading* will negatively affect the robustness of the algorithm.

5.2.5 Tangent Constitutive Matrix

The second key parameter that needs to be computed for the proposed Rotating Crack Model is the tangent constitutive matrix $\mathbf{D}_{smcr}$ at the current strain state. The easiest way to come up with the tangent constitutive matrix is to formulate it in the local coordinate system of the crack and to rotate it into the global coordinate system afterwards. In Section 5.2.4 we already developed the tangent compliance matrices for the bulk material $\widetilde{\mathbf{C}}_{co} = \mathbf{R}_{\sigma}^{T}\mathbf{C}_{co}\mathbf{R}_{\sigma}$ and the cracks $\widetilde{\mathbf{C}}_{cr}$ in the crack coordinate system. We also found that the compliance matrix of the cracked concrete $\widetilde{\mathbf{C}}_{smcr}$ is equal to the sum of the concrete compliance matrix and the cracking compliance matrix as given in Equation (5.22).

$$\widetilde{\mathbf{C}}_{smcr} = \widetilde{\mathbf{C}}_{co} + \widetilde{\mathbf{C}}_{cr} = \mathbf{R}_{\sigma}^{T}\mathbf{C}_{co}\mathbf{R}_{\sigma} + \widetilde{\mathbf{C}}_{cr} \tag{5.22}$$

Adding up the compliance matrices of the bulk material and the cracks in order to obtain the total compliance matrix is also justified by the fact that these components act *in series* as becomes clear from Figure 5.1.

The constitutive matrix $\widetilde{\mathbf{D}}_{smcr}$ can then be obtained by inverting the compliance matrix ($\widetilde{\mathbf{D}}_{smcr} = \widetilde{\mathbf{C}}_{smcr}^{-1}$). However, there still remains a problem. The constitutive matrix $\widetilde{\mathbf{D}}_{smcr}$

only covers the behavior in the principal directions and does not allow for a rotation of the principal stresses. The situation can be remedied by introducing a shear term $\widetilde{D}_{shear}$ into the compliance matrix. This term should lead to a rotation of the principal stress directions if a local shear strain is applied. Therefore, the tangent compliance matrix takes the form given in Equation (5.23).

$$\begin{Bmatrix} \Delta\widetilde{\sigma}_{\xi} \\ \Delta\widetilde{\sigma}_{\eta} \\ \Delta\widetilde{\tau}_{\xi,\eta} \end{Bmatrix} = \underbrace{\begin{bmatrix} \widetilde{D}_{smcr,11} & \widetilde{D}_{smcr,12} & 0 \\ \widetilde{D}_{smcr,21} & \widetilde{D}_{smcr,22} & 0 \\ 0 & 0 & \widetilde{D}_{shear} \end{bmatrix}}_{\widetilde{\mathbf{D}}} \begin{Bmatrix} \Delta\widetilde{\epsilon}_{\xi} \\ \Delta\widetilde{\epsilon}_{\eta} \\ \Delta\widetilde{\gamma}_{\xi,\eta} \end{Bmatrix} \tag{5.23}$$

The components $\widetilde{D}_{smcr,11}, \widetilde{D}_{smcr,12}, \widetilde{D}_{smcr,21}, \widetilde{D}_{smcr,22}$ in Equation (5.23) are directly taken from $\widetilde{\mathbf{D}}_{smcr}$. The constitutive matrix shows that there is a coupling between the normal components. This is due to the concrete contribution which includes Poisson's effect.

What remains to be determined is the shear term $\widetilde{D}_{shear}$ of the constitutive matrix in Equation (5.23). It can be inferred from the condition that the directions of principal stress should remain coaxial with the directions of principal strain. A shear term that enforces coaxiality of the principal stress and the principal strain was first published in [Bažant83] and further elaborated in [Rot88]. It can be derived by investigating what happens to a state of principal stress (resp. principal strain) when a shear stress increment (resp. shear strain increment) is applied. The situation can be illustrated by Mohr's circle as shown in Figure 5.4.

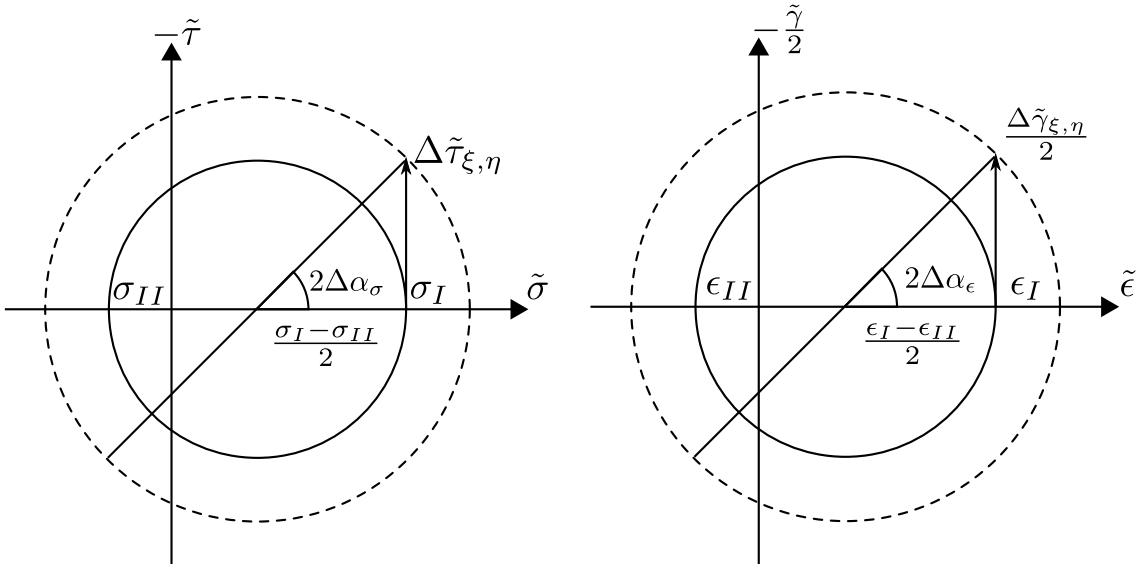

(a) Shear stress increment (b) Shear strain increment

Figure 5.4: Rotation of principal directions by shear stress or strain increment

Figure 5.4 clearly shows that the shear stress increment $\Delta\widetilde{\tau}_{\xi,\eta}$ produces a rotation of the

principal stress axes by $\Delta\alpha_\sigma$ whereas the shear strain increment $\Delta\widetilde{\gamma}_{\xi,\eta}$ results in a rotation of the principal strain axes by $\Delta\alpha_\epsilon$. Using basic trigonometry the rotation angles can be computed as given in Equation (5.24) where σ_I, σ_{II} are the principal stresses and ϵ_I, ϵ_{II} are the principal strains.

$$\tan\left(2\Delta\alpha_\sigma\right) = \frac{2\Delta\widetilde{\tau}_{\xi,\eta}}{\sigma_I - \sigma_{II}} \qquad \tan\left(2\Delta\alpha_\epsilon\right) = \frac{\Delta\widetilde{\gamma}_{\xi,\eta}}{\epsilon_I - \epsilon_{II}} \tag{5.24}$$

If the stress and the strain vector are to remain coaxial it is clear that the rotation angles $\Delta\alpha_\epsilon$ and $\Delta\alpha_\sigma$ need to be identical. The relationship between the shear stress increment and the shear strain increment that respects this condition directly follows from Equation (5.24) as given by Equation (5.25). Comparing this with Equation (5.23) the condition for coaxiality becomes apparent. The constitutive matrix explicitly enforces coaxiality between the principal strain and the principal stress directions if the shear term given in Equation (5.25) is used.

$$\Delta\widetilde{\tau}_{\xi,\eta} = \underbrace{\frac{\sigma_I - \sigma_{II}}{2(\epsilon_I - \epsilon_{II})}}_{\widetilde{D}_{shear}} \Delta\widetilde{\gamma}_{\xi,\eta} \tag{5.25}$$

Finally, the constitutive matrix has to be rotated from the local coordinate system into the global one. This is done by using the standard transformation rule given in Equation (5.26).

$$\mathbf{D} = \mathbf{R}\widetilde{\mathbf{D}}\mathbf{R}^T \qquad \text{where} \tag{5.26a}$$

$$\mathbf{R} = \begin{bmatrix} n_{\xi,x}^2 & n_{\xi,y}^2 & -2n_{\xi,x}n_{\xi,y} \\ n_{\xi,y}^2 & n_{\xi,x}^2 & 2n_{\xi,x}n_{\xi,y} \\ n_{\xi,x}n_{\xi,y} & -n_{\xi,x}n_{\xi,y} & n_{\xi,x}^2 - n_{\xi,y}^2 \end{bmatrix} \tag{5.26b}$$

Note that the rotation matrix $\mathbf{R}$ is related to the rotation matrix $\mathbf{R}_\sigma$ from Equation (5.5) but it is not identical. In fact $\mathbf{R}_\sigma$ is a reduced version of $\mathbf{R}$ that does not only perform the rotation but also eliminates the shear terms since these are not used in the stress return algorithm. The components of the unit vector $\underline{\mathbf{n}}_\xi = (n_{\xi,x}, n_{\xi,y})$ are computed as given in Equation (5.4).

Chapter 6

Strain Localization Model

6.1 Introduction

As discussed at several occasions in previous Chapters (i.e. Section 3.1.1) strain localization and localized cracking of HPFRCC structural members is a critical issue. A number of modeling approaches which tackle this problem were presented in Section 3.1.2. The most advanced concept is probably that of the eXtended Finite Element Method (XFEM) which was discussed in detail in Section 3.3. In contrast to other models such as for instance interface elements, the eXtended Finite Element Method allows for the formation of cracks which are completely *mesh-independent*. Yet the XFEM is capable of representing localized cracks by strong discontinuities as opposed to the popular continuum approaches (e.g. Smeared Crack Models or Damage and Plasticity Models) which require artificial regularization techniques. Furthermore, the cracks introduced by the XFEM are completely free of spurious stress transfer and other numerical instabilities. For this reason the crack localization phase of HPFRCC structural members (see in Section 3.4.2) is modeled by the eXtended Finite Element Method.

Although the XFEM has many advantages over the other mentioned methods these come at a price. The implementation of eXtended Finite Elements is more complicated and requires modifications of the Finite Element Method which go beyond simply adding a new "user" element to an existing Finite Element software package. The main reason for this is that the number of global degrees of freedom may change during the computation (see Section 6.4) since the extended degrees of freedom are only added when they are required. This is unusual for traditional Finite Element Analysis and standard Finite Element software is typically not prepared to handle this situation. Furthermore, the eXtended Finite Element Method entails some interaction between the crack geometry and the Finite Element mesh which is non-standard. Therefore, the eXtended Finite Elements developed during this thesis could not be implemented as "user" elements and a completely new code had to be written. The basic element used in that code was

presented in Section 4.2 and its extension is explained in the following sections.

We will begin by introducing a strong discontinuity into the isoparametric, quadrilateral element from Section 4.2 by means of the XFEM. This discontinuity represents a localized crack and can either be traction free at its surface or it can transmit cohesive forces in the spirit of the Cohesive Crack Model by Hillerborg [HMP76] (see also Section 3.1.4). First we will be focusing on stress-free cracks (Section 6.2) which will then be extended to cohesive cracks (Section 6.3). Thereafter, the crack tip and its propagation will be treated (Section 6.4) and the modifications that have to be made if the crack propagates in strain-hardening FRCCs will be discussed (Section 6.5). The latter also constitutes the main innovation and challenge of this thesis since this is the first time that a combination of the Smeared Crack Model and the eXtended Finite Element Method have been attempted.

In the following it is assumed that the reader is familiar with the basics of the XFEM which were discussed in Section 3.3.

6.2 Extended Finite Element Cracking Model

As already mentioned the isoparametric, 8-node quadrilateral element introduced in Section 4.2 is used as a starting point and it is modified by the XFEM to include a crack. For this purpose the standard Finite Element Analysis procedure has to be adapted. The basic steps of the XFEM procedure are given in the following (new steps are emphasized):

1. Discretization
2. Selection of standard shape functions
3. *Selection of a global enrichment function* Ψ
4. *Formulation of the enriched shape functions*
5. *Crack–Mesh interaction*
6. Formulation of the shape function matrix $\mathbf{N}_{enr}$
7. Formulation of the strain–displacement transformation matrix $\mathbf{B}_{enr}$
8. Computation of the element stiffness matrix $\mathbf{K}_e$ and force vector $\underline{\mathbf{F}}_e$
9. Assembly
10. Solution of the global system of equations
11. Update of the element state and computation of secondary results
12. Equilibrium check

Note that some steps do not deviate from the standard Finite Element Analysis procedure given in Section 4.2. These are not repeated here. The other steps are elaborated in more detail in the following sections.

6.2.1 Enrichment Function

We recall that the enrichment function Ψ is a function with global character which is used to improve the Finite Element approximation space (see Section 3.3.4). In order to model a localized crack in a HPFRCC structural member a generalized two-dimensional $\text{sign}(x, y)$ enrichment function centered at the crack is used. It will introduce a strong discontinuity into the approximation space of those Finite Elements crossed by a crack. The $\text{sign}(x, y)$ enrichment function takes the value $+1$ in the positive domain Ω^+ (to the left of the crack) and the value -1 in the negative domain Ω^- (to the right of the crack) as defined by Equation 6.1.

$$\Psi(x, y) = \text{sign}(x, y) = \begin{cases} +1 & \forall (x, y) \in \Omega^+ \\ -1 & \forall (x, y) \in \Omega^- \end{cases} \tag{6.1}$$

The next step in the eXtended Finite Element Method is to define a set of Partition of Unity Functions which are used to "localize" or "window" the global enrichment function (see Section 3.3.1). It is important to note that the Partition of Unity Functions will determine the opening profile of the crack as explained in Section 3.3.4. If the Partition of Unity Functions are linear the crack opening profile will also be linear over the length of an element whereas a quadratic profile is obtained with quadratic Partition of Unity Functions. In order to get a more realistic, quadratic crack opening profile and for the sake of an easier implementation the quadratic shape functions of the isoparametric, 8-node element given in Equations (4.4) are also used as Partition of Unity Functions.

6.2.2 Enriched Shape Functions

With the global enrichment function from Equation (6.1) and the Partition of Unity Functions from Equations (4.4) the enriched shape functions $N_{enr,i}$ can be determined according to the Partition of Unity Method (PUM) by Melenk and Babuška [MB96].

Since we have chosen eight Partition of Unity Functions (the standard shape functions for 8-node quadrilateral elements) the PUM will yield eight enriched shape functions. Each of them is associated with one of the element nodes. If a specific node is enriched than all elements connected to that node have to be enriched with the associated enriched shape function.

The shifted, enriched shape functions are given by Equation (6.2) (for more details on the shifting procedure see Section 3.3.1).

$$N_{enr,i}(r,s) = N_i(r,s) \cdot [\Psi(x,y) - \Psi(x_i,y_i)] \tag{6.2}$$

Equation (6.2) is directly obtained from Equation (3.19). Note that the upper index indicating the shift is omitted in order to alleviate the notation. The pair (x_i, y_i) represents the coordinates of the node with which the enriched shape function in question is associated. Also note that the enrichment function is formulated in global coordinates (x, y) – a fact which once again underlines the enrichment function's global character. In order to evaluate an enriched shape function at some natural coordinates (r, s) the corresponding global coordinates (x, y) are required. They can easily be obtained by the isoparametric coordinate mapping procedure given in Equation (4.2). Using the specific sign() enrichment function the enriched shape functions can be expressed by Equation (6.3). Figures 6.1 and 6.2 show four of the eight shifted, enriched shape functions for a basic element which is cut by a straight crack going from $(0.5, -1.0)$ to $(-0.5, 1.0)$. Note that due to the shift of the bases the shape function values can exceed 1.

$$N_{enr,i}(r,s) = N_i(r,s) \cdot [\text{sign}(x,y) - \text{sign}(x_i,y_i)] \tag{6.3}$$

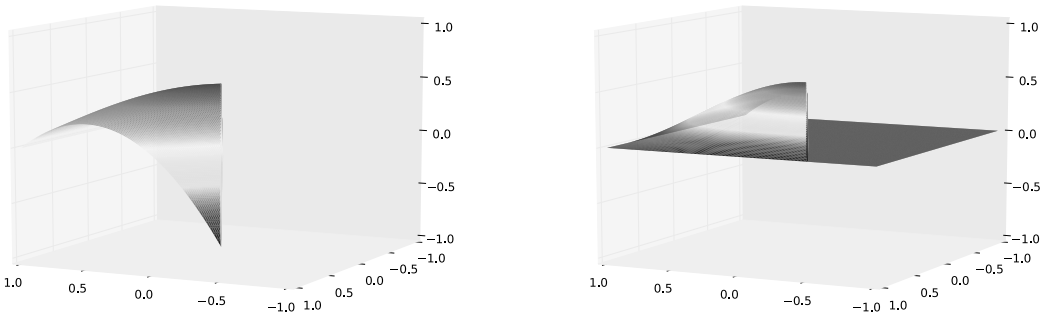

(a) $N_{enr,2}$ (b) $N_{enr,3}$

Figure 6.1: Shifted, enriched shape functions

The transition from the standard Finite Element to the eXtended Finite Element containing a crack is done by interpolating the displacement field using not only the standard shape functions N_i but also using the enriched shape functions $N_{enr,i}$ according to the fundamental equation of the eXtended Finite Element Method (3.20). Because the enriched shape functions are discontinuous the interpolation field will also be discontinuous

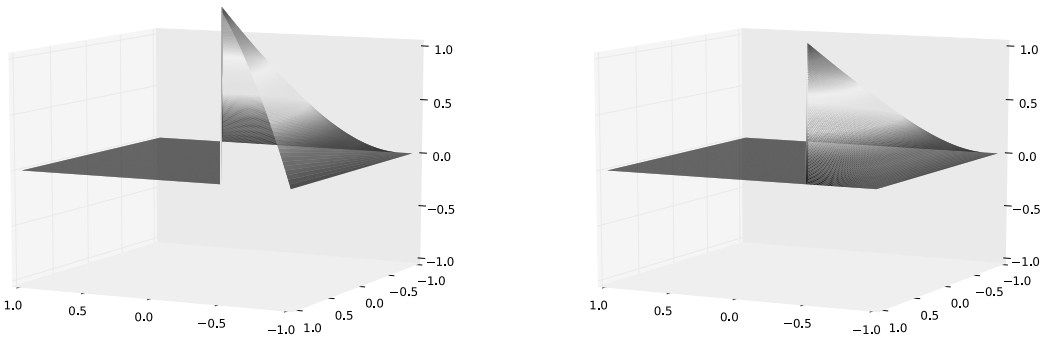

(a) $N_{enr,5}$ (b) $N_{enr,8}$

Figure 6.2: Shifted, enriched shape functions

and it will thereby introduce a crack.

$$u(r,s) = \sum_{1}^{8} N_i(r,s)u_i + \sum_{\text{enriched nodes}} N_{enr,i}(r,s)u_{enr,i} \tag{6.4a}$$

$$v(r,s) = \sum_{1}^{8} N_i(r,s)v_i + \sum_{\text{enriched nodes}} N_{enr,i}(r,s)v_{enr,i} \tag{6.4b}$$

In the above Equations (6.4) $u_{enr,i}$ and $v_{enr,i}$ are the additional degrees of freedom for the enriched nodes. Therefore, the degrees of freedom will be $\underline{\mathbf{d}}_{std,i} = (u_i, v_i)$ for a standard node and $\underline{\mathbf{d}}_{enr,i} = (u_i, v_i, u_{enr,i}, v_{enr,i})$ for an enriched node. Depending on an element's location with respect to the crack it can have between one and eight enriched nodes (see Section 6.2.3). E.g. a fully cracked element will have eight enriched nodes whereas an uncracked element will have none. Elements in the transition zone (blending elements) will have between 1 and 7 enriched nodes.

Comparing this section with Section 4.2.2 it becomes apparent that the only difference between the eXtended Finite Element and the standard Finite Element are the additional discontinuous terms in the displacement field interpolation. Note that the interpolation of the element geometry (coordinates) does not change and Equation (4.2) remains the same.

It should be emphasized, that the enrichment of the displacement field explained in this section represents the prime modification introduced by the eXtended Finite Element Method. Apart from some details concerning the selection of the enriched nodes and a slight adaptation of the numerical integration scheme the standard Finite Element Analysis procedure is followed.

6.2.3 Crack–Mesh Interaction

An issue that arises with the introduction of cracks is the geometrical interaction between the crack trajectories and the Finite Element mesh. With the eXtended Finite Element Method this interaction is restricted to a minimum because the Finite Element mesh does not have to change in order to accommodate a crack. In principle the XFEM allows the latter to take an arbitrary path through the mesh but the geometry of the crack is still limited by the underlying Finite Element formulation. More specifically the crack path is determined by the polynomial order of the shape functions of the underlying Finite Element [SBCB03].

For the isoparametric, quadrilateral elements with quadratic shape functions used in this thesis the crack could in principal have a parabolic curvature within an element and the crack geometry could be approximated by a piecewise quadratic line. However, in order to simplify the geometrical computation of the intersection segments between the crack trajectory and the individual Finite Elements as well as to alleviate the coordinate mapping procedure between the real and the natural domain it was decided to limit the crack trajectory to *element-wise linear segments*. For the same reasons the quadrilateral Finite Elements are also restricted to having straight edges (although the shape functions would allow parabolic ones). A further assumption which is made for the sake of simplicity is that an element is either uncracked or fully crack (for more details see Section 6.4.1). For typical civil engineering applications these approximations are reasonable and with mesh-refinement the Finite Element solution converges towards the exact solution. It is important to note that these restrictions are not limitations of the method but rather simplifications for the ease of implementation.

A popular way to represent the crack geometry in the Finite Element mesh is to use *Level Sets* [OS88, Set99, SCMB01b]. For this thesis it was refrained from using Level Sets because the Level Set values are typically only saved at the node locations (and interpolated using the Finite Element shape functions) which introduces an additional approximation. Although this approximation is completely acceptable for computational purposes it was found that it results in deformation plots which are not very nice.

For this reason the intersection between the crack trajectory and the elements is computed by means of traditional vector geometry. Once an intersection segment of an element with the crack is determined it can be used to distinguish the positive domain Ω^+ (to the left of the crack segment) where the enrichment function from Section 6.2.1 takes the value $+1$ from the negative domain Ω^- (to the right of the crack segment) where the enrichment function takes the value -1. This information is then used to compute the enriched shape functions (see Equation 6.3) as explained in Section 6.2.2.

The intersection information is also used to determine which nodes have to be enriched. As explained in Section 3.3.3 only a subset of nodes in the immediate vicinity of the crack have to be enriched. They are effectively determined by the *area criterion* which was given in Section 3.3.3. However, apart from some rare exceptions (due to numerical

issues) the set of enriched nodes consists of the nodes of the cracked elements.

As a part of the crack–mesh interaction, a *subtriangulation* of the cut elements is performed. It essentially consists of subdividing the positive and negative domain of a cut element into triangles. These subtriangles are then used for two different purposes. Firstly, they are used to compute the area of the positive and the negative domain of a node's support since this information is required for the area criterion (see Section 3.3.3, Figure 3.20). And secondly they are used for the numerical integration of the element stiffness matrix and the element force vector as we will see in Section 6.2.6. Since the positive and the negative domains of quadrilateral elements with straight edges always have convex polygonal shapes the subtriangles can be formed by connecting each edge of the polygon with the polygon's centroid as shown in Figure 6.3. For more complicated element geometries a *Delaunay Triangulation* has to be performed.

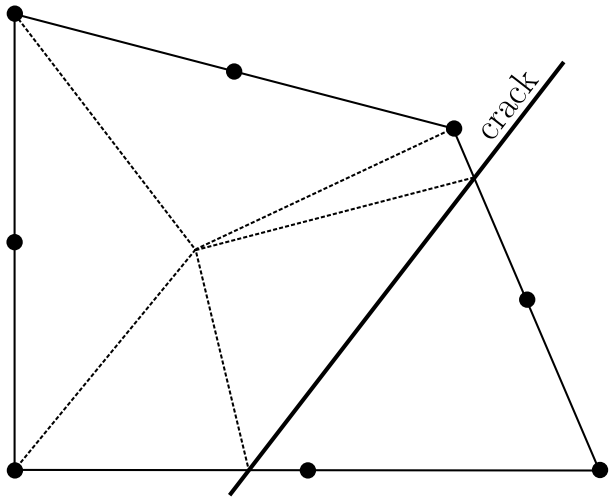

Figure 6.3: Subtriangulation of a cut element

6.2.4 Shape Function Matrix

In analogy to Section 4.2.3 the shape functions are assembled into a shape function matrix **N**. What differs from the standard procedure is that in addition to the standard shape functions N_i, the shape function matrix for an eXtended Finite Element should also contain the enriched shape functions $N_{enr,i}$ introduced in Section 6.2.2. For each enriched node two additional degrees of freedom are added to the element. Since the number of enriched nodes of an element can range from 0 to 8 the shape function matrix and the vector of element degrees of freedom have a variable size. The generic procedure in assembling the shape function matrix is to loop over all nodes of an element and to append the corresponding block of shape functions associated with that node (standard or enriched) as indicated in Equation (6.5).

$$\mathbf{N} = \begin{bmatrix} \cdots & \underbrace{\begin{matrix} N_i & 0 \\ 0 & N_i \end{matrix}}_{\text{standard}} & \cdots & \underbrace{\begin{matrix} N_j & 0 & N_{enr,j} & 0 \\ 0 & N_j & 0 & N_{enr,j} \end{matrix}}_{\text{enriched}} & \cdots \end{bmatrix} \tag{6.5}$$

The vector of element degrees of freedom is assembled analogously. Note that the enriched degrees of freedom are inserted close to the original degrees of freedom of a given node since they are mentally associated with the latter (node-wise assembly). However, this is only a matter of preference and it would also be possible to add all enriched degrees of freedom at the end of the displacement vector. The only important thing, is that the shape function matrix and the displacement vector are assembled in a consistent fashion.

$$\underline{\mathbf{d}}_e = (\dots \underbrace{u_i, v_i}_{\text{standard}} \dots \underbrace{u_j, v_j, u_{enr,j}, v_{enr,j}}_{\text{enriched}} \dots) \tag{6.6}$$

Equation (4.6) remains unchanged and it will compute the displacement field of both standard and eXtended Finite Elements in the same way. However, the shape function matrix and the nodal displacement vector used in the equation are different.

6.2.5 Strain–Displacement Transformation Matrix

The strain–displacement transformation matrix is established following the same procedure as given in Section 4.2.4. The kinematic Equation (4.8) remains the same except for the minor inconvenience that the strain cannot be evaluated at the exact location of the discontinuity (where it is infinite). However, this is of no concern because the determination of a "strain" across the crack is not meaningful and it is more reasonable to evaluate the crack opening displacement as shown in Section 6.3.

The Jacobi transformation given by Equation (4.13) is performed in the same way as for standard elements since it links the natural and the global differential operators which are independent of the function to which they are applied. The only difference in the procedure is that in the strain–displacement transformation matrix of an eXtended Finite Element the derivatives of the enriched shape functions need to be added at the appropriate locations. This is exemplarily shown in Equation (6.7).

$$\mathbf{B} = \begin{bmatrix} \cdots & \underbrace{\begin{matrix} N_i^x & 0 \\ 0 & N_i^y \\ N_i^y & N_i^x \end{matrix}}_{\text{standard}} & \cdots & \underbrace{\begin{matrix} N_j^x & 0 & N_{enr,j}^x & 0 \\ 0 & N_j^y & 0 & N_{enr,j}^y \\ N_j^y & N_j^x & N_{enr,j}^y & N_{enr,j}^x \end{matrix}}_{\text{enriched}} & \cdots \end{bmatrix} \tag{6.7a}$$

$$N^x := \partial N/\partial x \qquad N^y := \partial N/\partial y \qquad N^x_{enr} := \partial N_{enr}/\partial x \qquad N^y_{enr} := \partial N_{enr}/\partial y \tag{6.7b}$$

Equation (6.7b) indicates that the enriched shape function derivatives are needed in addition to the standard shape function derivatives. The former can be computed by differentiating Equation (6.3) by x and y. Respecting the product rule we have:

$$\frac{\partial N_{enr,i}(r,s)}{\partial x} = \frac{\partial N_i(r,s)}{\partial x} \cdot [\text{sign}(x,y) - \text{sign}(x_i,y_i)] + N_i(r,s)\frac{\partial}{\partial x} \cdot [\text{sign}(x,y) - \text{sign}(x_i,y_i)]$$
$$\frac{\partial N_{enr,i}(r,s)}{\partial y} = \frac{\partial N_i(r,s)}{\partial y} \cdot [\text{sign}(x,y) - \text{sign}(x_i,y_i)] + N_i(r,s)\frac{\partial}{\partial y} \cdot [\text{sign}(x,y) - \text{sign}(x_i,y_i)]$$

The second term in both equations requires the differentiation of $[\text{sign}(x,y) - \text{sign}(x_i,y_i)]$. The result is zero in both cases since the two functions are constant (except for the location of the discontinuity where the stain cannot be evaluated). As a consequence the second term in both of the above equations can be dropped which yields Equations (6.8).

$$\frac{\partial N_{enr,i}(r,s)}{\partial x} = \frac{\partial N_i(r,s)}{\partial x} \cdot [\text{sign}(x,y) - \text{sign}(x_i,y_i)] \tag{6.8a}$$
$$\frac{\partial N_{enr,i}(r,s)}{\partial y} = \frac{\partial N_i(r,s)}{\partial y} \cdot [\text{sign}(x,y) - \text{sign}(x_i,y_i)] \tag{6.8b}$$

Equations (6.8) show that for the specific sign() enrichment used here, the derivatives of the enriched shape functions are directly related to the derivatives of the standard shape functions. The enriched shape function derivatives are obtained by multiplying the standard shape function derivatives with a step function which is equal to the difference between the enrichment function at the location of interest and the enrichment function at the location of the node with which the enriched shape function in question is associated. Note that the derivatives of the standard shape functions in Equation (6.8) are determined by using Equation (4.13) which performs a Jacobi transformation to pass from the natural coordinate system to the global coordinate system.

The Jacobi transformation matrix $\mathbf{J}$ is computed in the same way as for the standard quadrilateral elements (see Equations 4.16). It would be wrong to include the enriched shape functions since they are used to interpolate the discontinuous displacement field and not the geometry of the element (implicit assumption of small deformations).

6.2.6 Element Stiffness Matrix and Force Vector

The equilibrium equation for an eXtended Finite Element can be derived in the same way as it was done for the standard quadrilateral elements in Section 4.2.5 (Equations 4.17 – 4.25). However, there is a slight difference between standard elements and enriched elements. In the derivation of the weak form of equilibrium the divergence theorem (a.k.a.

Green's theorem) is used which is only applicable to domains that are sufficiently regular (no singularities or discontinuities) [SP03]. Therefore, the weak form of equilibrium has to be evaluated on each side of the crack individually resulting in an integration by parts of the positive domain Ω_e^+ and the negative domain Ω_e^-. Respecting this constraint the stiffness matrix $\mathbf{K}_e$ and the force vector $\underline{\mathbf{F}}_e$ follow directly from Equation (4.23) and are given by Equations (6.9).

$$\mathbf{K}_e = \int_{\Omega_e^+} \mathbf{B}^T \mathbf{D} \mathbf{B} \; d\Omega_e^+ + \int_{\Omega_e^-} \mathbf{B}^T \mathbf{D} \mathbf{B} \; d\Omega_e^- \tag{6.9a}$$

$$\underline{\mathbf{F}}_e = \int_{\Omega_e^+} \mathbf{N}^T \underline{\mathbf{f}} \; d\Omega_e^+ + \int_{\Omega_e^+} \mathbf{N}^T \underline{\mathbf{f}} \; d\Omega_e^- \tag{6.9b}$$

For cracked elements the internal virtual work would technically have to be augmented by an integral over the surface of the crack. For the stress free cracks considered here there is evidently no work done on the crack surface and that term can be dropped. However, this will not be the case if cohesive forces are added to the crack (see Section 6.3).

The integration of Equations (6.9) is performed numerically in analogy to Section 4.2.5. However, the application of the standard Gauss-Legendre integration scheme poses a problem. Because the domain of a cracked element has to be integrated by parts the standard procedure is on longer applicable.

At this point the subtriangulation introduced in Section 6.2.3 comes into play. Because a crack can cut a quadrilateral element into two a priori unknown polygonal domains the locations and weights of the necessary Gauss points cannot be determined easily. Therefore, the two domains are decomposed into subtriangles and the integration is performed over the individual, triangular subdomains $\Omega_\triangle$. This leads to Equations (6.10).

$$\mathbf{K}_e = \sum_{\triangle} \left[\int_{\Omega_\triangle} \mathbf{B}^T \mathbf{D} \mathbf{B} \cdot d\Omega_\triangle \right] \tag{6.10a}$$

$$\underline{\mathbf{F}}_e = \sum_{\triangle} \left[\int_{\Omega_\triangle} \mathbf{N}^T \underline{\mathbf{f}} \cdot d\Omega_\triangle \right] \tag{6.10b}$$

There is one last difficulty to overcome. In Equation (4.26) the numerical integration is performed in the natural domain of the parent quadrilateral element (the strain–displacement transformation matrix is formulated in those coordinates). The positions and weights of the Gauss points on the other hand are only well known in the natural domain of the parent triangle. Therefore, the Gauss points have to be mapped from the parent triangle to the parent quadrilateral element.

Basically, the mapping is done in two steps. The first step is to perform a coordinate mapping from the parent triangle to the real quadrilateral element. This is relatively straightforward. Since the global coordinates of all subtriangle vertices $(x_{\triangle,i}, y_{\triangle,i})$ are known the standard linear shape functions for triangular elements $N_{\triangle,i}$ can be used to perform the mapping. The latter are given in Equations (6.11) ($r_\triangle$ and $s_\triangle$ are the natural coordinates of the parent triangle domain).

$$N_{\triangle,1}(r_\triangle, s_\triangle) = 1 - r_\triangle - s_\triangle \tag{6.11a}$$
$$N_{\triangle,2}(r_\triangle, s_\triangle) = r_\triangle \tag{6.11b}$$
$$N_{\triangle,3}(r_\triangle, s_\triangle) = s_\triangle \tag{6.11c}$$

The global coordinates (x, y) of any point $r_\triangle, s_\triangle$ in the natural subtriangle domain can then be computed by Equation (6.12).

$$x(r_\triangle, s_\triangle) = \sum_1^3 N_{\triangle,i}(r_\triangle, s_\triangle) \cdot x_{\triangle,i} \qquad y(r_\triangle, s_\triangle) = \sum_1^3 N_{\triangle,i}(r_\triangle, s_\triangle) \cdot y_{\triangle,i} \tag{6.12}$$

In addition to the coordinates the weights (representative areas) of the integration points need to be mapped. The relationship between the real weight α_{gp} of an integration point and its natural weight in a subtriangle $\alpha_{\triangle,gp}$ is given by Equation (6.13) where $\mathbf{J}_\triangle$ is the Jacobi matrix for the subtriangle.

$$\alpha_{gp} = \det \mathbf{J}_\triangle(r_{\triangle,gp}, s_{\triangle,gp}) \cdot \alpha_{\triangle,gp} \tag{6.13}$$

The Jacobi matrix for the transformation of differentials between the parent triangle and the real domain can be computed analogously to the procedure outlined in Section 4.2.4. Using the shape functions for a subtriangle given in Equations (6.11) this yields Equation (6.14) where $(x_{\triangle,i}, y_{\triangle,i})$ are the global coordinates of the subtriangle vertices.

$$\det \mathbf{J}_\triangle = (x_{\triangle,2} - x_{\triangle,1})(y_{\triangle,3} - y_{\triangle,1}) - (x_{\triangle,3} - x_{\triangle,1})(y_{\triangle,2} - y_{\triangle,1}) \tag{6.14}$$

The second step of the coordinate mapping procedure is more complex because it requires an *inverse mapping*. If the coordinates of a point were known in the parent quadrilateral element the shape functions for isoparametric, quadrilateral 8-node elements from Equation (4.4) could be used to map the point from the parent domain to the global domain by means of Equation (4.2). Unfortunately the inverse is the case. The real coordinates (x, y) of the point are known and the parent coordinates $(r_\square, s_\square)$ need to be found. Because the shape functions for the used quadrilateral element are quadratic the mapping equations

cannot be inverted easily (nonlinear equations). Therefore, the system of equations has to be solved numerically. This is done by using the well known Newton-Raphson algorithm. Note that if the quadrilateral element only had four nodes one could also use the analytical procedure detailed in [ZHMO99] for the inverse mapping. However, the Newton-Raphson algorithm is more general as it can be used for higher order shape functions and for linear shape functions it converges after one iteration.

The subtriangles are integrated using a 7-point Gauss-Legendre quadrature. The latter is required in order to achieve the same accuracy as for the standard quadrilateral elements with a 3×3 integration rule. The appropriate locations $(r_{\triangle,gp}, s_{\triangle,gp})$ and weights $\alpha_{\triangle,gp}$ of the Gauss-Legendre quadrature points in a natural triangle can be found in the Finite Element literature [Bat96]. Figure 6.4 shows the Gauss-quadrature points that are used to compute the stiffness matrix and the force vector of a quadrilateral element that is cut by a crack.

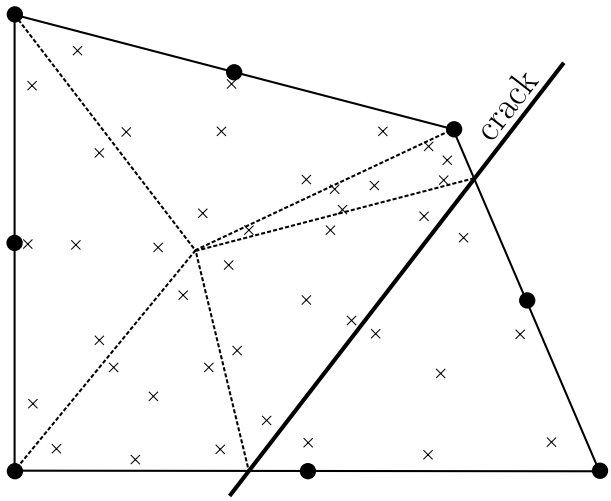

Figure 6.4: Integration points for a cut element

It should be emphasized, that the subtriangulation is only performed for the purpose of numerical integration and it has nothing to do with remeshing. No additional degrees of freedom have to be introduced and there are also no restrictions regarding the shape of the subtriangles (unlike for triangular Finite Elements which may exhibit numerical problems if they are strongly distorted).

Putting everything together, the final Finite Element matrix of a cracked element is given by Equations (6.15). Note that the shape function matrix $\mathbf{N}$ and the strain–displacement transformation matrix $\mathbf{B}$ are the eXtended Finite Element versions given in Equations (6.5) and (6.7). The coordinates of the integration points in the natural domain of the parent element $(r_{\square,gp}, s_{\square,gp})$ are computed using the mapping procedure

explained above.

$$\mathbf{K}_e = \sum_{\triangle} \left[\sum_{\text{Gauss points}} \mathbf{B}^T(r_{\square,gp}, s_{\square,gp}) \cdot \mathbf{D} \cdot \mathbf{B}(r_{\square,gp}, s_{\square,gp}) \cdot t \cdot \det \mathbf{J}_{\triangle} \alpha_{\triangle,gp} \right] \tag{6.15a}$$

$$\underline{\mathbf{F}}_e = \sum_{\triangle} \left[\sum_{\text{Gauss points}} \mathbf{N}^T(r_{\square,gp}, s_{\square,gp}) \cdot \underline{\mathbf{f}} \cdot t \cdot \det \mathbf{J}_{\triangle} \alpha_{\triangle,gp} \right] \tag{6.15b}$$

6.3 Extension to Cohesive Cracks

In Section 6.2 we focused on modeling a stress free crack with the XFEM. However, the final goal is to model localized cracking and softening of High Performance Fiber Reinforced Cementitious Composite structural members. As already discussed at length in Chapter 2, HPFRCCs do not fail in a brittle manner but exhibit a very pronounced softening phase during which fibers bridge the macroscopic cracks and transmit cohesive forces across the crack surfaces. As a consequence the model presented in Section 6.2 needs to be extended to incorporate cohesive forces at the crack locations.

This is done by means of the Cohesive Crack Model by Hillerborg [HMP76] (see also Section 3.1.4). The basic idea behind the Cohesive Crack Model is to abstract the non-linear fracture behavior due to aggregate interlock, fibers etc. by replacing it with a set of cohesive forces which act on the crack surfaces and transfer stresses in function of the crack mouth opening (see Figure 6.5). Although the Cohesive Crack Model was originally proposed for traditional concrete it makes even more sense to apply it to Fiber Reinforced Cementitious Composites since the cohesive forces in the model directly relate to the physical nature of the fiber pullout process.

6.3.1 The Separation Vector

The first thing that has to be done when analyzing a crack is to compute its opening profile. It is characterized by the *separation vector* $\underline{\mathbf{w}}$. In the eXtended Finite Element model the crack is represented by a strong discontinuity in the element displacement field which separates the computational domain into a positive and a negative part. On the discontinuity itself (i.e. the crack) it is not possible to compute the strain since it is singular. However, the separation vector can be computed. It corresponds to the "jump" in the displacement field which is equal to the difference between the displacement field in the positive domain and the displacement field in the negative domain at the location of the discontinuity. By definition the positive direction of the separation vector is pointing from the negative domain to the positive domain. It can therefore be computed

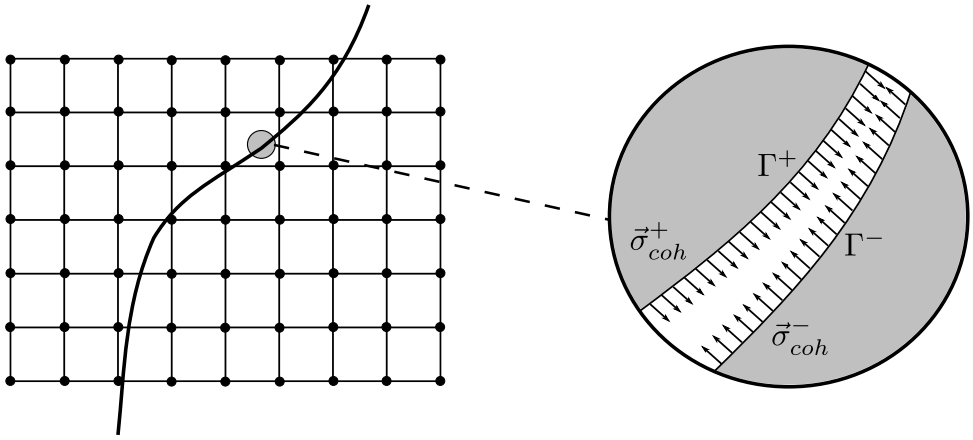

Figure 6.5: Cohesive forces on a XFEM crack

as given by Equation (6.16) where $\underline{\mathbf{w}}$ denotes the separation vector and (r_w, s_w) are the natural coordinates of any point located on the discontinuity. The vectors $\underline{\mathbf{u}}^+(r_w, s_w)$ and $\underline{\mathbf{u}}^-(r_w, s_w)$ represent the equivocal displacement field at the location of the discontinuity coming either from the positive domain or from the negative domain.

$$\underline{\mathbf{w}}(r_w, s_w) = \begin{Bmatrix} w_x \\ w_y \end{Bmatrix} = \underline{\mathbf{u}}^+(r_w, s_w) - \underline{\mathbf{u}}^-(r_w, s_w) \tag{6.16}$$

Replacing the displacement fields by their Finite Element approximations from Equations (6.4) yields Equations (6.17) and it becomes evident that the terms containing the standard shape functions cancel each other out which leads from Equations (6.16) to Equation (6.18).

$$\underline{\mathbf{u}}^+(r_w, s_w) = \sum_1^8 N_i(r_w, s_w) \begin{Bmatrix} u_i \\ v_i \end{Bmatrix} + \sum_{\text{enriched nodes}} N^+_{enr,i}(r_w, s_w) \begin{Bmatrix} u_{enr,i} \\ v_{enr,i} \end{Bmatrix} \tag{6.17a}$$

$$\underline{\mathbf{u}}^-(r_w, s_w) = \sum_1^8 N_i(r_w, s_w) \begin{Bmatrix} u_i \\ v_i \end{Bmatrix} + \sum_{\text{enriched nodes}} N^-_{enr,i}(r_w, s_w) \begin{Bmatrix} u_{enr,i} \\ v_{enr,i} \end{Bmatrix} \tag{6.17b}$$

In analogy to the displacement field, $N^+_{enr,i}$ and $N^-_{enr,i}$ denote the enriched shape functions evaluated on the discontinuity.

$$\underline{\mathbf{w}}(r_w, s_w) = \sum_{\text{enriched nodes}} N^+_{enr,i}(r_w, s_w) \begin{Bmatrix} u_{enr,i} \\ v_{enr,i} \end{Bmatrix} - \sum_{\text{enriched nodes}} N^-_{enr,i}(r_w, s_w) \begin{Bmatrix} u_{enr,i} \\ v_{enr,i} \end{Bmatrix} \tag{6.18}$$

Equation (6.18) can be further simplified by replacing the enriched shape functions with

their definition (see Equation (6.2)). Again using the notation Ψ^+ and Ψ^- for the equivocal values of the enrichment function this yields Equations (6.19).

$$N^+_{enr,i}(r_w, s_w) = N_i(r_w, s_w)\left(\Psi^+(x_w, y_w) - \Psi(x_i, y_i)\right) \tag{6.19a}$$
$$N^-_{enr,i}(r_w, s_w) = N_i(r_w, s_w)\left(\Psi^-(x_w, y_w) - \Psi(x_i, y_i)\right) \tag{6.19b}$$

Substituting Equations (6.19) in Equation (6.18) and dropping the terms which cancel each other out the separation vector can be computed by Equation (6.20)

$$\underline{\mathbf{w}}(r_w, s_w) = \sum_{\text{enriched nodes}} N_i(r_w, s_w)\left(\Psi^+(x_w, y_w) - \Psi^-(x_w, y_w)\right)\begin{Bmatrix} u_{enr,i} \\ v_{enr,i} \end{Bmatrix} \tag{6.20}$$

Because the enrichment function used here is the generalized two-dimensional $\text{sign}(x, y)$ function centered at the discontinuity it takes the values $\Psi^+ = 1$ and $\Psi^- = -1$ in the positive respectively the negative domain which finally yields Equation (6.21) for the separation vector.

$$\underline{\mathbf{w}}(r_w, s_w) = \sum_{\text{enriched nodes}} 2 \cdot N_i(r_w, s_w)\begin{Bmatrix} u_{enr,i} \\ v_{enr,i} \end{Bmatrix} \tag{6.21}$$

Or using matrix notation in analogy to Equation (6.5) this can be rewritten as Equations (6.22) where $\underline{\mathbf{d}}_e$ is the element displacement vector introduced in Equation (6.6).

$$\underline{\mathbf{w}}(r_w, s_w) = \mathbf{N}_{coh}(r_w, s_w) \cdot \underline{\mathbf{d}}_e \qquad \text{with} \tag{6.22a}$$

$$\mathbf{N}_{coh}(r_w, s_w) = \begin{bmatrix} \cdots & \underbrace{\begin{matrix} 0 & 0 \\ 0 & 0 \end{matrix}}_{\text{standard}} & \cdots & \underbrace{\begin{matrix} 0 & 0 & 2N_i & 0 \\ 0 & 0 & 0 & 2N_i \end{matrix}}_{\text{enriched}} & \cdots \end{bmatrix} \tag{6.22b}$$

Note that this derivation is the two-dimensional equivalent to Equations (3.22). As we have already discussed in Section 6.2.1 the variation of the crack opening in the herein presented XFEM model is parabolic over the length of an element due to the quadratic Partition of Unity Functions. This is reflected in Equation (6.22) which shows that the separation vector is a quadratic function of (r_w, s_w) (the shape functions $N_i(r_w, s_w)$ are quadratic).

6.3.2 The Traction–Separation Law

Typically the cohesive forces of a crack decrease with increasing crack mouth opening and the relationship between the separation vector $\underline{\widetilde{\mathbf{w}}} = (w_\xi, w_\eta)$ and the cohesive stresses $\underline{\widetilde{\sigma}}_{coh} = (\sigma_\xi, \tau_\eta)$ is called the *traction–separation law*. It is usually formulated in the local coordinate system (ξ, η) associated with the crack as illustrated in Figure 6.6.

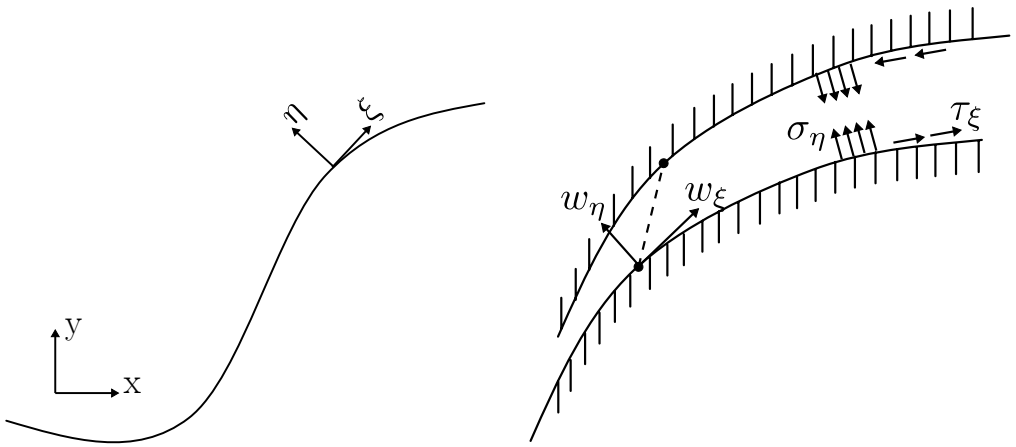

(a) Local coordinate system of a crack (b) Separation vector and cohesive forces

Figure 6.6: Cohesive crack coordinate system

Because most traction–separation laws are nonlinear they need to be expressed in incremental form. The global Finite Element solution algorithm for nonlinear problems requires that the traction–separation law provides two things [Bat96]: Firstly this is a stress return algorithm $\chi_{coh}(\Delta\underline{\widetilde{\mathbf{w}}})$ which is used for the computation of the element reaction forces (see Section 6.3.4) and secondly this is a tangent constitutive matrix $\widetilde{\mathbf{D}}_{coh}$ which is used to compute the tangent element stiffness matrix (see Section 6.3.3). This is expressed in Equations (6.23).

$$\Delta\underline{\widetilde{\sigma}}_{coh} = \chi_{coh}(\Delta\underline{\widetilde{\mathbf{w}}}) \tag{6.23a}$$

$$\Delta\underline{\widetilde{\sigma}}_{coh} = \widetilde{\mathbf{D}}_{coh} \cdot \Delta\underline{\widetilde{\mathbf{w}}} \tag{6.23b}$$

The constitutive traction–separation law can be formulated using any theory that links the crack opening $\underline{\widetilde{\mathbf{w}}}$ and the cohesive stresses $\underline{\widetilde{\sigma}}_{coh}$ (i.e. Plasticity, Damage etc.). Unfortunately, for HPFRCCs there is no conclusive experimental evidence or sophisticated model that would provide a traction–separation law for localized cracks. Such a law would have to take fiber pull-out, fiber deformation, aggregate interlock etc. into account and it is different for every specific HPFRCC. Therefore, it was decided to use a simple traction–separation law which assumes an uncoupled behavior of the normal-opening component and the shear-sliding component. However, as research in that field progresses it would

be straightforward to use a more sophisticated law that accounts for implicit or explicit coupling of the components. Using the assumption of uncoupled components the tangent cohesive matrix in the local coordinate system is given by Equation (6.24).

$$\widetilde{\mathbf{D}}_{coh} = \begin{bmatrix} D^{I}_{coh} & 0 \\ 0 & D^{II}_{coh} \end{bmatrix} \tag{6.24}$$

Although the traction–separation law is conveniently formulated in the local coordinate system associated with the crack the Finite Element Method requires a traction–separation relationship in global coordinates. By consequence a rotation of the coordinate system has to be performed. Basic trigonometry immediately yields the relationship between the local cohesive stresses $\underline{\widetilde{\sigma}}_{coh}$ and the global cohesive stresses $\underline{\sigma}_{coh}$ as well as the relationship between the local separation vector $\underline{\widetilde{\mathbf{w}}}$ and the global separation vector $\underline{\mathbf{w}}$ (Equation 6.25) ($\mathbf{T}^{-1} = \mathbf{T}^{T}$).

$$\underline{\sigma}_{coh} = \mathbf{T}^{T}(\alpha) \cdot \underline{\widetilde{\sigma}}_{coh} \qquad \underline{\widetilde{\mathbf{w}}} = \mathbf{T}(\alpha) \cdot \underline{\mathbf{w}} \qquad \text{where} \qquad \mathbf{T}(\alpha) = \begin{bmatrix} \cos\alpha & \sin\alpha \\ -\sin\alpha & \cos\alpha \end{bmatrix} \tag{6.25}$$

In Equations (6.25) α denotes the angle of rotation between the local and the global coordinate system. Introducing Equations (6.25) into Equation (6.23b) the linearized traction–separation law in global coordinates is found (Equation 6.26).

$$\Delta\underline{\sigma}_{coh}(x,y) = \underbrace{\mathbf{T}^{T} \cdot \widetilde{\mathbf{D}}_{coh} \cdot \mathbf{T}}_{\mathbf{D}_{coh}} \cdot \Delta\underline{\mathbf{w}}(x,y) \tag{6.26}$$

6.3.3 Element Stiffness Matrix and Force Vector

The next step is to modify the weak form of the element equilibrium. As we have already mentioned in Section 6.2.6 the equilibrium equation for a cracked element has to be augmented by a term δW_{coh} that accounts for the virtual work done by the cohesive forces on the crack surface. Due to the possible nonlinearity of the cohesive law the weak form of equilibrium has to be used in its linearized, incremental form [Bat96]. Equation (4.17) therefore becomes Equation (6.27).

$$\int_{\Omega_e} \delta\underline{\epsilon}^{T} \cdot \Delta\underline{\sigma} \; d\Omega_e = \int_{\Omega_e} \delta\underline{\mathbf{u}}^{T} \cdot \Delta\underline{\mathbf{f}} \; d\Omega_e + \delta W_{coh} + \delta\underline{\mathbf{d}}_e{}^{T} \cdot \Delta\underline{\mathbf{P}}_e \tag{6.27}$$

The virtual work of the cohesive forces can be computed by integrating over the crack surfaces Γ_e^{+} and Γ_e^{-} of the element (see Figure 6.5) as given by Equation (6.28) where $\delta\underline{\mathbf{u}}^{+}$ and $\delta\underline{\mathbf{u}}^{-}$ denote the virtual displacements of the positive respectively the negative field at the crack location.

$$\delta W_{coh} = \int_{\Gamma_e^+} \delta \underline{\mathbf{u}}^{+T} \cdot \Delta \underline{\sigma}_{coh}^{+} \, d\Gamma_e^+ + \int_{\Gamma_e^-} \delta \underline{\mathbf{u}}^{-T} \cdot \Delta \underline{\sigma}_{coh}^{-} \, d\Gamma_e^- \tag{6.28}$$

We recall that the positive direction of the traction vector in the local coordinate system of the crack points from the negative to the positive domain. Taking into account that the local equilibrium of the crack requires that $\Delta \underline{\sigma}_{coh}^{-} = -\Delta \underline{\sigma}_{coh}^{+} := \Delta \underline{\sigma}_{coh}$ this yields Equation (6.29).

$$\delta W_{coh} = -\int_{\Gamma_e^+} \delta \underline{\mathbf{u}}^{+T} \cdot \Delta \underline{\sigma}_{coh} \, d\Gamma_e^+ + \int_{\Gamma_e^-} \delta \underline{\mathbf{u}}^{-T} \cdot \Delta \underline{\sigma}_{coh} \, d\Gamma_e^- \tag{6.29}$$

If we make the additional assumption of small deformations we can conclude that $\Gamma_e^+ = \Gamma_e^- := \Gamma_e$ which leads from Equation (6.29) to Equation (6.30).

$$\delta W_{coh} = -\int_{\Gamma_e} \left(\delta \underline{\mathbf{u}}^{+T} - \delta \underline{\mathbf{u}}^{-T} \right) \cdot \Delta \underline{\sigma}_{coh} \, d\Gamma_e \tag{6.30}$$

In analogy to Equation (6.16) we can define a virtual separation vector as $\delta \underline{\mathbf{w}} = \delta \underline{\mathbf{u}}^{+} - \delta \underline{\mathbf{u}}^{-}$ which yields Equation (6.31). This equation also makes perfect sense from a physical point of view. It expresses the fact that the additional virtual work term for the cohesive interface is computed as the integral product of the crack opening and the cohesive forces acting along the crack.

$$\delta W_{coh} = -\int_{\Gamma_e} \delta \underline{\mathbf{w}}^{T} \cdot \Delta \underline{\sigma}_{coh} \, d\Gamma_e \tag{6.31}$$

The next step is to use the traction–separation law that was introduced in Section 6.3.2. Using Equation (6.23b) leads to Equation (6.32).

$$\delta W_{coh} = -\int_{\Gamma_e} \delta \underline{\mathbf{w}}^{T} \cdot \mathbf{D}_{coh} \cdot \Delta \underline{\mathbf{w}} \, d\Gamma_e \tag{6.32}$$

Returning to Equation (6.27) we can replace the virtual work of the cohesive interface with Equation (6.32). After also applying the constitutive law for the continuum which was given in Equation (4.18) we find the equilibrium equation for an eXtended Finite Element with a cohesive crack (Equation 6.33).

$$\int_{\Omega_e} \delta \underline{\epsilon}^{T} \cdot \mathbf{D} \cdot \Delta \underline{\epsilon} \, d\Omega_e + \int_{\Gamma_e} \delta \underline{\mathbf{w}}^{T} \cdot \mathbf{D}_{coh} \cdot \Delta \underline{\mathbf{w}} \, d\Gamma_e = \int_{\Omega_e} \delta \underline{\mathbf{u}}^{T} \cdot \Delta \underline{\mathbf{f}} \, d\Omega_e + \delta \underline{\mathbf{d}}_e{}^{T} \cdot \Delta \underline{\mathbf{P}}_e \tag{6.33}$$

Equation (6.33) can be discretized using the Finite Element approximations given by Equations (4.6) and (4.9a) as was done in Section 4.2.5. Note however, that the shape

function matrix and the strain–displacement transformation matrix are the extended versions from Equations (6.5) and (6.7a). What is needed in addition is the Finite Element approximation of the separation vector which was developed in Section 6.3.1 and is given in Equation (6.22a). Again we use the same interpolation for both the real and the virtual fields. For clarity the Finite Element approximations are repeated hereafter:

$$\begin{aligned} \Delta\underline{\mathbf{u}} &= \mathbf{N}\cdot\Delta\underline{\mathbf{d}}_e & \Delta\underline{\epsilon} &= \mathbf{B}\cdot\Delta\underline{\mathbf{d}}_e & \Delta\underline{\mathbf{w}} &= \mathbf{N}_{coh}\cdot\Delta\underline{\mathbf{d}}_e \\ \delta\underline{\mathbf{u}} &= \mathbf{N}\cdot\delta\underline{\mathbf{d}}_e & \delta\underline{\epsilon} &= \mathbf{B}\cdot\delta\underline{\mathbf{d}}_e & \delta\underline{\mathbf{w}} &= \mathbf{N}_{coh}\cdot\delta\underline{\mathbf{d}}_e \end{aligned}$$

Substituting the above approximation fields in Equation (6.33) and preforming the same algebraic simplifications as in Section 4.2.5 we find Equation (6.34).

$$\underbrace{\int_{\Omega_e}\mathbf{B}^T\mathbf{D}\mathbf{B}\;d\Omega_e}_{\mathbf{K}_e^{std}}\cdot\Delta\underline{\mathbf{d}}_e+\underbrace{\int_{\Gamma_e}\mathbf{N}_{coh}^T\mathbf{D}_{coh}\mathbf{N}_{coh}\;d\Gamma_e}_{\mathbf{K}_e^{coh}}\cdot\Delta\underline{\mathbf{d}}_e=\underbrace{\int_{\Omega_e}\mathbf{N}^T\Delta\underline{\mathbf{f}}\;d\Omega_e}_{\Delta\vec{F}_e}+\Delta\underline{\mathbf{P}}_e \tag{6.34}$$

Note that for the reasons explained in Section 6.2.6 the integration of the standard stiffness matrix $\mathbf{K}_e^{std}$ and of the incremental force vector $\Delta\underline{\mathbf{F}}_e$ in Equation (6.34) needs to be done by parts as given in Equations (6.9). Comparing Equation (6.34) and Equation (4.23) it becomes obvious that the cohesive forces in a cracked element can be handled by adding an additional stiffness matrix $\mathbf{K}_e^{coh}$ to the standard stiffness matrix $\mathbf{K}_e^{std}$. Regrouping the terms of Equation (6.34) this leads to the following Finite Element stiffness matrix for a cracked element with cohesive forces (Equations 6.35).

$$\mathbf{K}_e=\mathbf{K}_e^{std}+\mathbf{K}_e^{coh}\qquad\text{where} \tag{6.35a}$$

$$\mathbf{K}_e^{std}=\int_{\Omega_e^+}\mathbf{B}^T\mathbf{D}\mathbf{B}\;d\Omega_e^+ +\int_{\Omega_e^-}\mathbf{B}^T\mathbf{D}\mathbf{B}\;d\Omega_e^- \tag{6.35b}$$

$$\mathbf{K}_e^{coh}=\int_{\Gamma_e}\mathbf{N}_{coh}^T\mathbf{D}_{coh}\mathbf{N}_{coh}\;d\Gamma_e \tag{6.35c}$$

In the following we will focus on the new stiffness matrix term $\mathbf{K}_e^{coh}$ which accounts for the cohesive forces. The standard stiffness matrix and the force vector are computed as usual (Section 6.2.6).

The integral over the area of the cohesive crack is computed numerically in the same fashion as it is done for the body of the element. Since the Partition of Unity Functions are parabolic the variation of the separation vector along the crack interface will in general also be quadratic. By consequence the integrand of the stiffness matrix contribution that

accounts for the cohesive forces is of the 4^{th} order. Therefore, a numerical integration scheme with 3 Gauss points was chosen as it is sufficient to integrate the stiffness matrix contribution $\mathbf{K}_e^{coh}$ exactly. The numerically integrated version of the stiffness matrix term accounting for the cohesive forces is given in Equation (6.36) where $\alpha_{\curvearrowright,gp}$ are the weights of the Gauss points in the natural domain $[-1,1]$ and $\mathbf{J}_{\curvearrowright}$ is the Jacobi matrix for the coordinate transformation between the natural line segment and the crack line in the global element domain.

$$\mathbf{K}_e^{coh} = \sum_{\text{Gauss pts. } \Gamma_e} \mathbf{N}_{coh}^T(r_{\square,gp}, s_{\square,gp}) \mathbf{D}_{coh} \mathbf{N}_{coh}(r_{\square,gp}, s_{\square,gp}) \cdot t \cdot \det \mathbf{J}_{\curvearrowright} \alpha_{\curvearrowright,gp} \tag{6.36}$$

Note that a similar mapping procedure as the one described in Section 6.2.6 (for the subtriangles) has to be applied to the integration points on the cohesive interface. The coordinates of the integration points are mapped from the natural domain $[-1,1]$ to the crack in the real domain of the element Ω_e and then they are inversely mapped to the natural domain of the parent quadrilateral element where they have the coordinates $(r_{\square,gp}, s_{\square,gp})$. Simultaneously the natural weights $\alpha_{\curvearrowright,gp}$ of the quadrature points on the cohesive interface are mapped to the real domain using $\alpha_{gp} = \det \mathbf{J}_{\curvearrowright} \cdot \alpha_{\curvearrowright,gp}$.

Because straight crack segments are used the mapping from the natural domain $[-1,1]$ to the real domain can be performed using the linear shape functions given in Equation (6.37).

$$N_{\curvearrowright,1}(r_{\curvearrowright}) = \frac{1 - r_{\curvearrowright}}{2} \qquad N_{\curvearrowright,2}(r_{\curvearrowright}) = \frac{1 + r_{\curvearrowright}}{2} \tag{6.37}$$

Following the standard methodology the real coordinates (x, y) of a point with the natural coordinate $r_{\curvearrowright} \in [-1,1]$ can then be determined by Equations (6.38) where (x_1, y_1) and (x_2, y_2) are the start respectively the end point coordinates of the crack segment in the real domain.

$$\begin{aligned} x &= N_{\curvearrowright,1} x_1 + N_{\curvearrowright,2} x_2 \\ y &= N_{\curvearrowright,1} y_1 + N_{\curvearrowright,2} y_2 \end{aligned} \tag{6.38}$$

The transformation of crack segment differentials expressed by the Jacobi determinant is given in Equation (6.39).

$$\det \mathbf{J}_{\curvearrowright} = \frac{d\Gamma_e}{dr_{\curvearrowright}} = \sqrt{\left(\frac{dx}{dr_{\curvearrowright}}\right)^2 + \left(\frac{dy}{dr_{\curvearrowright}}\right)^2} \tag{6.39}$$

Applying the above Equation (6.39) to the coordinate mapping functions from Equation (6.38) finally yields the scaling factor between the crack segment in the natural domain and the same segment in the real domain (Equation 6.40).

$$\det \mathbf{J}_{\hookrightarrow} = \frac{1}{2}\sqrt{(x_2 - x_1)^2 + (y_2 + y_1)^2} \tag{6.40}$$

Although it has been mentioned before, let us emphasize a very important realization about the eXtended Finite Element Method. The XFEM enhances the kinematics of a problem (the displacement field) independently of the constitutive law. This is in contrast to Smeared Crack Models where the constitutive law is modified to account for a cracking strain (see Chapter 3.2). The above derivation of the element stiffness matrix clearly shows that any type of constitutive law for the continuum (in form of the tangent constitutive matrix $\mathbf{D}$) and any type of traction–separation law for the cohesive crack (in form of the tangent constitutive matrix $\widetilde{\mathbf{D}}_{coh}$) can be used. One can for example consider a linear, elastic continuum with a nonlinear cohesive crack whose traction–separation law is based on Damage and Plasticity. Or it is possible to envisage an elasto-plastic continuum with a crack that is described by a nonlinear law with implicit coupling of the components. This could even be taken a step further and a cyclic traction–separation law could be implemented. In fact, providing a cyclic law for both the compliance function of the smeared crack model (see Section 5.2.3) and for the traction–separation relationship in the XFEM model would be the only two steps necessary to use the model in cyclic simulations.

Of course nonlinear constitutive laws require special nonlinear computational analysis techniques such as an incremental, iterative solution procedure [Bat96]. Because the formation of macroscopic cracks will often induce structural softening and might even lead to "snap-back" behavior [CW88] an *Arc-length solution technique* was implemented [Wem71, Rik72, Rik79, Rik84, Cri81, CW88, Cri97].

6.3.4 Secondary Results and Element Reactions

Finally, the transition from a stress-free to a cohesive crack requires two other minor modifications. The first one concerns the computation of secondary results. In addition to the displacement, the strain and the stress field in the bulk material it is also possible to compute secondary results on the cohesive interface. These are the separation vector $\underline{\mathbf{w}}(r_w, s_w)$ and the cohesive stresses $\underline{\sigma}_{coh}(r_w, s_w)$ acting along the discontinuity. They can be computed as given in Equations (6.41) which follow directly from Equations (6.22) , (6.23a) and (6.25). The crack opening increment used in Equation (6.41b) can be computed as $\Delta\underline{\mathbf{w}} = \underline{\mathbf{w}} - \underline{\mathbf{w}}^{eq}$. Furthermore, the term $\underline{\mathbf{w}}^{eq}$ denotes the separation vector at the last global equilibrium state and $\widetilde{\underline{\sigma}}^{eq}_{coh}$ denotes the corresponding local cohesive stress vector.

$$\underline{\mathbf{w}}(r_w, s_w) = \mathbf{N}_{coh}(r_w, s_w) \cdot \underline{\mathbf{d}}_e \tag{6.41a}$$

$$\widetilde{\underline{\sigma}}_{coh}(r_w, s_w) = \widetilde{\underline{\sigma}}^{eq}_{coh} + \chi_{coh}\left(\mathbf{T}(\alpha) \cdot \Delta\underline{\mathbf{w}}(r_w, s_w)\right) \tag{6.41b}$$

The second modification is related to the computation of the element reaction forces. When applying the concept of virtual work in order to find the element reaction forces as was done in Section 4.2.8, the contribution of the cohesive interface has to be considered. We refrain from going through the full demonstration and simply give the result in Equation (6.42).

$$\underline{\mathbf{R}}_e = \int_{\Omega_e} \mathbf{B}^T \underline{\sigma} \; d\Omega_e + \int_{\Gamma_e} \mathbf{N}_{coh}^T \underline{\sigma}_{coh} \; d\Gamma_e \tag{6.42}$$

The global cohesive stress vector $\underline{\sigma}_{coh}$ which is used in Equation (6.42) can easily be determined from the local cohesive stress vector $\widetilde{\underline{\sigma}}_{coh}$ (Equation (6.41b)) by applying the rotation expressed in Equation (6.25).

Using numerical integration in analogy to Equation (4.28) finally yields Equation (6.43).

$$\begin{aligned} \underline{\mathbf{R}}_e = & \sum_{\text{Gauss pts. } \Omega_{all\triangle}} \mathbf{B}^T(r_{\square,gp}, s_{\square,gp}) \underline{\sigma}(r_{\square,gp}, s_{\square,gp}) \cdot t \cdot \det \mathbf{J}_{\triangle} \alpha_{\triangle,gp} + \\ & \sum_{\text{Gauss pts. } \Gamma_e} \mathbf{N}_{coh}^T(r_{\square,gp}, s_{\square,gp}) \underline{\sigma}_{coh}(r_{\square,gp}, s_{\square,gp}) \cdot t \cdot \det \mathbf{J}_{\looparrowright} \alpha_{\looparrowright,gp} \end{aligned} \tag{6.43}$$

The first sum is performed over all Gauss integration points of all subtriangles as explained in Section 6.2.6 whereas the second term sums up the contributions of all integration points on the cohesive interface. It is important to note that the locations of all integration points need to be known in the natural domain of the parent quadrilateral element $(r_{\square,gp}, s_{\square,gp})$ which requires the application of the mapping procedure explained in Sections 6.2.6 and 6.3.3.

6.4 Crack Propagation

So far we have been focusing on the body of a crack in a Finite Element mesh. We have seen how the XFEM can be used to introduce a crack (see Section 6.2) and how cohesive forces can be added to that crack (see Section 6.3). However, we have not discussed how a crack will evolve over time. In most cases a localized crack in a structural element will form at a location of very high tensile stresses and it will then propagate as the deformations increase.

There are two major issues that have to be considered when modeling crack propagation. The first one is a realistic model of the crack tip. Because the propagation of the crack is typically governed by the stress or the strain field in the vicinity of the crack tip an accurate model of that region is required. Such a crack tip model will be proposed in

Section 6.4.1. The second component of a crack propagation model is a law which governs crack evolution. It should provide a *crack propagation criterion* which determines the conditions under which a crack will grow. Furthermore, the crack propagation criterion also needs to define the direction in which the crack will propagate. This is detailed in Section 6.4.2.

In the literature there are two basic approaches that are used for quasi-static crack propagation in combination with the XFEM. The first one is oriented towards linear, elastic fracture mechanics and can be found in [BB99, MDB99, Dol99]. It employs a *maximum circumferential stress criterion* for crack propagation and it computes the necessary stress intensity factors by using domain forms of the J-integral. This approach is extended to cohesive cracks in [MB02] and [ZB03]. The length of the crack increment is typically taken as the control parameter for the nonlinear Finite Element solution procedure and it is normally set to between 1/2 and 3/2 of the characteristic element length [VBB03].
The second approach is more oriented towards cohesive crack growth. It was pioneered in [Wel01, WS01] and it is based on a nonlocal average of the stress tensor in the vicinity of the crack tip. The same approach was also used in [MKS05]. The reason for using a nonlocal average is that in the Finite Element approximation the stress at the crack tip is not known exactly and the Finite Element interpolation functions do not provide the needed accuracy to determine the latter. It is this second approach which is followed in the model presented here. A very similar method was also proposed by [MP03]. Instead of using a nonlocal average the stress at the crack tip is interpolated by a fourth-order polynomial field that is fitted to the integration point stress values in the vicinity of the crack tip with a least-squares approximation.

6.4.1 Crack Tip Model

Before the crack tip model is given let us recall that the geometry of the crack is restricted to be element-wise linear (see Section 6.2.3). Furthermore, following the model proposed in [WS01, Wel01] it is assumed that the crack grows from element edge to element edge (although it is possible that the crack grows over multiple elements in one step). By doing so it is guaranteed that an element is either completely bisected by a discrete crack or it is not cracked at all. In other words, there are no partially cut elements. This is illustrated in Figure 6.7.

Using a model in which the crack tip is always located on the edge between two elements strongly simplifies the implementation. The main condition for the crack tip element is that the displacement jump at the tip is constrained to zero. If the crack tip is located inside an element this requires special enrichment functions as described in [MDB99] or [DMB00]. For the model presented here this can be achieved in a more convenient way. The crack tip opening is constrained to zero by *not* enriching the nodes of the edge on which the crack tip lies (see Figure 6.7) since this will cause the enrichment field (and by consequence the displacement jump) to be zero along that edge [Wel01]. The latter can easily be verified by acknowledging the fact that all Partition of Unity Functions associated

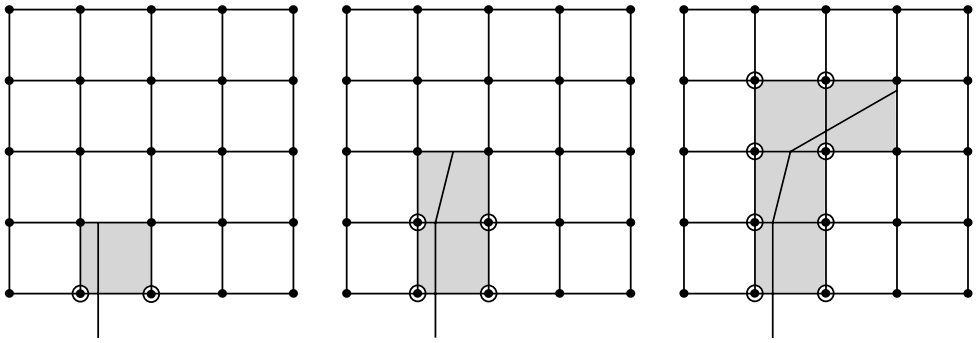

Figure 6.7: Evolution of a crack

with nodes that are not located on the edge containing the crack tip are always zero along that edge.

6.4.2 Crack Propagation Criterion

The model for crack propagation that is used here strongly follows the propositions made in [SWS03] and it is adapted to work in combination with the Rotating Crack Model that was introduced in Chapter 5. As mentioned in the introduction to this chapter the crack propagation criterion requires two things: namely a condition for crack propagation and a rule to determine the direction of propagation.

Here a relatively simple condition for crack propagation is used. The crack is extended whenever the principal strain ϵ_I or ϵ_{II} at any integration point in the element ahead of the crack tip exceeds a given *localization strain threshold* ϵ_{loc}. Note that only the principal strain component that is closer to orthogonal to the last crack segment is relevant. If more than one element ahead of the crack tip fulfill the propagation condition the crack is extended through all of those elements. An alternative is to extend the crack only when *all* integration points in the element ahead of the crack tip fulfill the propagation criterion. However, in [SWS03] it was shown that upon mesh refinement identical results are obtained with both variants. In the context of High Performance Fiber Reinforced Cementitious Composites a propagation criterion based on the maximum principal strain is justified by the fact that softening in HPFRCCs is typically triggered by excessive fiber pullout when a critical normal strain is reached.

The crack propagation criterion is only checked at the end of a load step when a new state of global equilibrium has been reached. This guarantees that the Finite Element solution algorithm remains robust and that the quadratic convergence rate of the Newton-Raphson method is conserved [WS01]. On the other hand this means that cracks will only propagate at the beginning of the next step and the localization strain threshold can be temporarily exceeded in the immediate vicinity of the crack tip. In the cohesive crack framework such a simplification is admissible since energy is dissipated upon crack opening rather the upon crack extension and according to [WS01] *"the numerical result is not particularly*

sensitive to exactly when a discontinuity is extended or the length of the discontinuity extension".

The second and more critical part of the crack propagation model is determining the direction of propagation. As already mentioned, a model based on nonlocal averaging is used. The first step is to compute a *nonlocal strain* $\underline{\hat{\epsilon}}$ at the crack tip in analogy to the procedure explained in [SWS03]. The term *nonlocal strain* means that the latter is not only a function of the properties at the exact location of evaluation, but that it is computed from the values in a circumjacent region. In this specific case the nonlocal strain is computed by averaging the strain values of all integration points in a v-shaped window (circular sector) ahead of the crack tip. The v-shaped window spans an angle of 90° and has a length of 3 times the characteristic element length as shown in Figure 6.8.

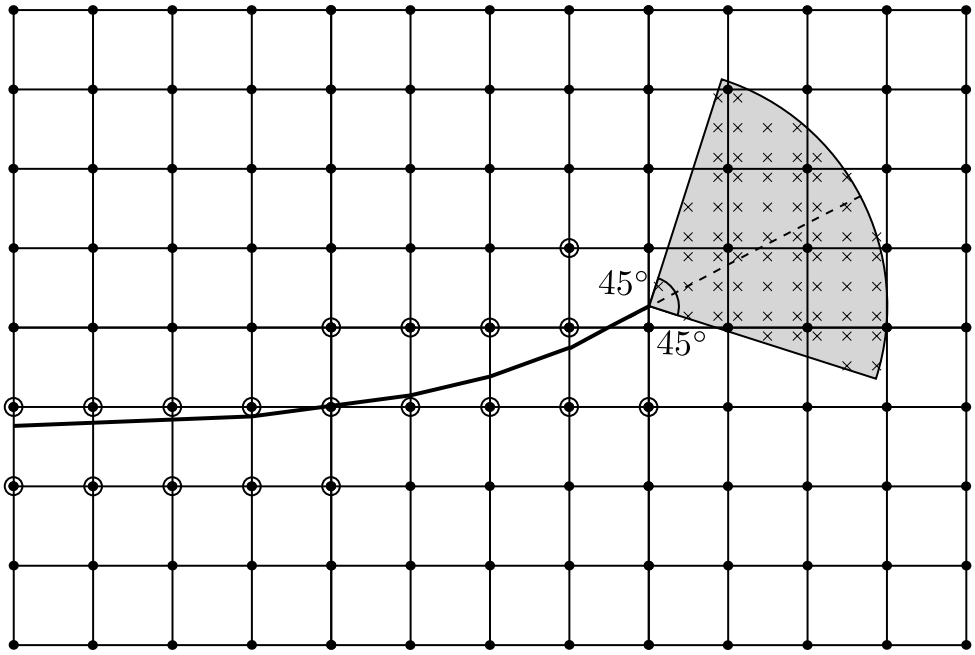

Figure 6.8: V-shaped window for computing the nonlocal cracking strain

The averaging is done by using a *Gaussian weight function* $\hat{\alpha}(r)$ as proposed in [WS01] which is given in Equation (6.44). The parameter l determines how fast the influence of the integration points decreases with increasing distance r to the crack tip and it is typically set to three times the characteristic element length.

$$\hat{\alpha}(r) = \frac{1}{(2\pi)^{\frac{3}{2}} \cdot l^3} \cdot e^{-\frac{r^2}{2l^2}} \tag{6.44}$$

The nonlocal strain at the crack tip can then be computed by averaging the strain values at the integration points $\underline{\epsilon}_{gp}$ as given by Equation (6.45) [MKS05]. Therein $\hat{\alpha}_{gp}$ is the weight determined by Equation (6.44) and α_{gp} is the standard weight (representative area) of an integration point.

$$\underline{\hat{\epsilon}} = \sum_{\text{Gauss pts.}} \underline{\epsilon}_{gp} \cdot \frac{\hat{\alpha}_{gp}\alpha_{gp}}{\sum \hat{\alpha}_{gp}\alpha_{gp}} \tag{6.45}$$

Finally, the direction of crack extension follows by assuming that the crack propagates *perpendicular to the dominant nonlocal principal strain.*

6.4.3 Discrete Crack Nucleation

So far the main focus of the explanation has been the propagation of a preexisting, discrete crack. However, in some circumstances there is no notch or starting point for a crack and the latter will localize somewhere in the middle of the Finite Element domain (see the application presented in Section 8.4). We call this process *discrete crack nucleation* and in order to handle the situation consistently a crack nucleation criterion needs to be defined. Once the localized crack has nucleated we can then revert to the crack propagation criterion which governs the propagation of the two tips of the newly nucleated crack.

For all the examples in this thesis the following numerical crack nucleation criterion is proposed: A discrete crack will nucleate within the Finite Element domain as soon as the localization strain threshold ϵ_{loc} is exceeded at any integration point of a Finite Element. Of course this has to be checked after the currently existing cracks have all propagated at the current loadstep in order to prevent a new crack from nucleating where a preexisting crack should have propagated to. The newly nucleated crack is introduced at the location of the integration point which has exceeded the localization strain threshold and with an orientation perpendicular to the principal tensile strain direction at that point. If multiple integration points within an element exceed the localization strain threshold than the integration point with the highest principal strain value is selected. The nucleated crack segment is then extended to the edges of the element within which the crack originated and its further propagation is governed by the crack propagation criterion introduced in Section 6.4.2.

6.5 Material State Transfer

In Section 6.2 a model for localized cracking with the XFEM was presented. As explained there the crack can transmit cohesive forces and the transition from a Rotating Crack Model to a discrete eXtended Finite Element model is governed by the laws detailed in Section 6.4. However, we did not discuss what happens to the bulk material during this transition. Because the transition from a Rotating Crack Model to an eXtended Finite Element model marks the onset of softening the bulk material in the vicinity of the localization zone will start to unload as governed by the Rotating Crack Model given in

Chapter 5. However, there is one key issue that remains to be solved. During cracking of an element the locations of the integration points change due to the separate integration of the positive and the negative domain and the consequential subtriangulation introduced in Section 6.2.6. And this requires a *mapping of the material history* from the old to the new integration locations.

If the bulk material is elastic the material history transfer does not pose a problem since the strain state of the new integration points $\underline{\epsilon}_{gp}$ can be recovered from the nodal degrees of freedom $\underline{\mathbf{d}}_e$ via the strain–displacement transformation matrix ($\underline{\epsilon}_{gp} = \mathbf{B} \cdot \underline{\mathbf{d}}_e$) and the stresses can be computed via the linear, elastic constitutive matrix ($\underline{\sigma}_{gp} = \mathbf{D} \cdot \underline{\epsilon}_{gp}$). However, in the present case the bulk material is nonlinear (Rotating Crack Model) and the method above is not applicable since the material law is *path dependent* and can only be expressed in incremental form. As a consequence the stress, the strain and all the material state variables need to be transfered at the time of cracking from the old set of integration points to the new one.

It is important to note that this material state mapping does not involve the primary unknowns (nodal degrees of freedom) but only the secondary unknowns such as the stresses and the material history variables. This is in contrast to remeshing techniques where the position of some nodes may change.

The literature proposes a number of different mapping techniques for the internal history variables such as the *closest point transfer*, the *shape function projection transfer* or the *least-squares projection transfer* [PJ04]. For the specific case of the XFEM in conjunction with a nonlinear bulk material there are only a handful of publications [WdBS01, WSdB02, SWS03, SS04, CMP07]. In [WdBS01] and [WSdB02] the history variables are interpolated proportionally to the distance between the old and the new integration points whereas in [SWS03] the maximum value of the history variable of the element is transfered to all new integration points.

Unfortunately, all of the above methods introduce a small error into the computation and result in a deviation from the equilibrium path which can adversely affect the robustness of the solution algorithm. More specifically, this means that a Finite Element which is in a state of equilibrium will become "unbalanced" by a change of the integration points. Moreover, this will happen during a time of drastic change when the transition from the Rotating Crack Model to the eXtended Finite Element model is performed and the stability of the solution algorithm is already critical.

In order to alleviate this problem a new transfer method based on what we call *integration point splitting* is developed. It is similar to the procedure presented in [EGC06] but in addition to integrating both sides of a cut element accurately it also simplifies the material state transfer. Following the integration point splitting technique the latter can be performed without interpolation. This new method can also be seen as an advanced version of the closest point transfer technique as will be detailed in the following Sections 6.5.1 and 6.5.2.

6.5.1 Representative Integration Point Areas

The basic idea behind the material state transfer method developed herein is that each integration point represents a certain area of the computational domain (given by its weight). The values of the stress, the strain and the material history variables are assumed to be constant over an integration point's representative area and they are given by the respective values at the location of the integration point. An integral over the entire domain is then computed as an assembly of patches with constant values corresponding to the representative areas of the integration points. Figure 6.9 shows the representative domains of the integration points for a 3×3 Gauss quadrature in both the natural and the real domain.

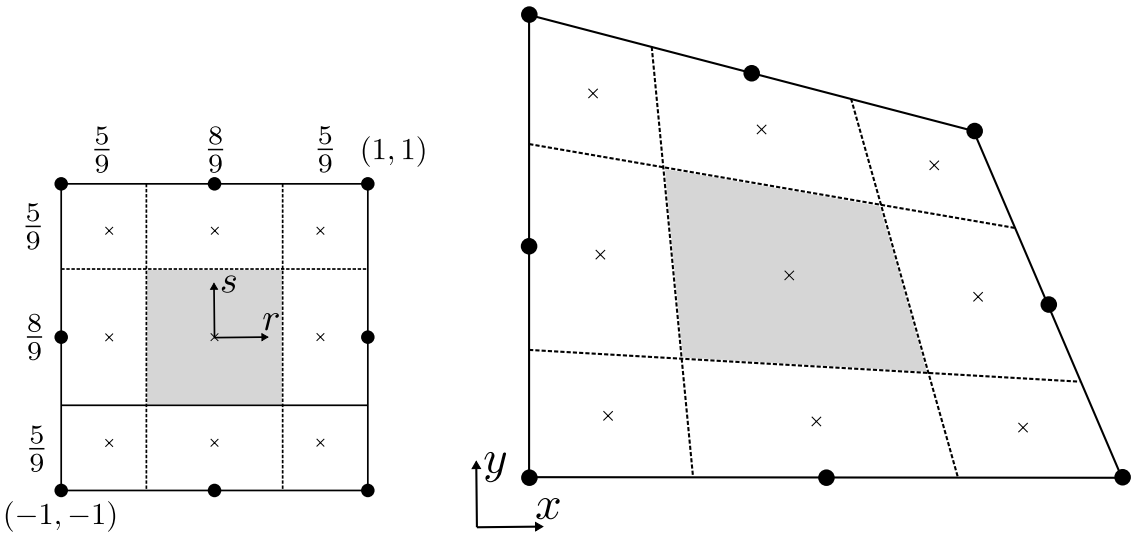

(a) Natural domain (b) Real domain

Figure 6.9: Representative areas of the integration points for a 3×3 Gauss rule

Because it was decided to use quadrilateral elements that have straight edges in the real domain (see Section 6.2.3) the isoparametric mapping procedure will project vertical and horizontal lines in the natural domain to straight lines in the real domain. By consequence the representative areas of the integration points are of quadrilateral shape.

The idea of the proposed material state transfer method is to split these subquadrilaterals into smaller patches which are each in turn represented by an integration point. In other words, the integration points and their representative areas are "split" into sub-points and their respective sub-areas. This procedure is explained in the following Section 6.5.2.

6.5.2 Integration Point Splitting

If an eXtended Finite Element is cracked the traditional procedure would be to subtriangulate the element and then integrate the individual subtriangles in order to respect

the discontinuity introduced by the crack as explained in Section 6.2.6 (see Figure 6.4). However, the innovative new procedure proposed here is to regard the representative areas of the original integration points (see Section 6.5.1) as subdomains and to integrate them individually. If a subdomain is not cut by the crack a standard 3×3 Gauss quadrature is used whereas if the subdomain is split by a crack it is subtriangulated in analogy to the standard procedure. This is shown in Figure 6.10.

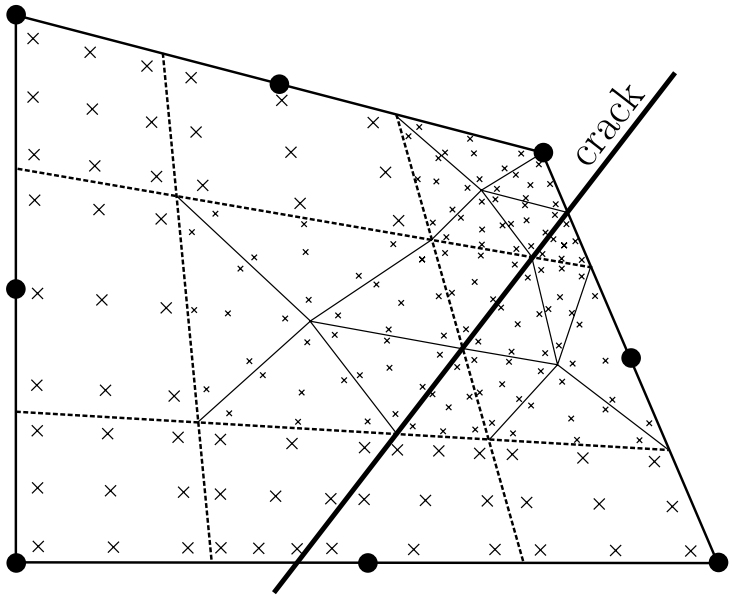

Figure 6.10: Integration of a cracked element with the integration point splitting technique

Note that if a subdomain is split into two quadrilateral parts these are integrated in the same fashion as the unsplit subquadrilaterals. The integration points for a subtriangle are found by mapping them from a natural triangle whereas those for a subquadrilateral are found by mapping them from a natural quadrilateral. The inverse mapping of all integration points to the natural domain of the parent element is then performed in the same way as explained in Section 6.2.6.

The major advantage of the integration point splitting technique is that an integration point is effectively equivalent to the sum of the subpoints within its representative area as long as the material state variables of the original point and the subpoints are identical. The integration points are "split" into subpoints so to speak. This also constitutes the key idea behind the material history transfer procedure. Because an integration point is equivalent to the sum of its subpoints the material state can be transfered one-to-one from the original point to the subpoints without changing the element energy balance.

This technique might seem excessive at first as it appears to increase the number of integration points by more than a factor of nine. However, this is not the case since typically only a very small number of elements are cut by a crack. Furthermore, the additional computational burden is only small because most of the solution time is spent during the inversion of the global stiffness matrix. And the rank of the latter is not

affected by the increased number of integration points. The reduced number of numerical instabilities due to a consistent material state transfer most likely even leads to faster convergence of the solution and by consequence less computation time (less global stiffness matrix inversions).

Chapter 7

Reinforcement Model

7.1 Introduction

Although the behavior of High Performance Fiber Reinforced Cementitious Composites is improved significantly in comparison to plain concrete the tensile strength of HPFRCCs is still not sufficient for most practical applications. In some cases the fibers in HPFRCCs can replace secondary reinforcement such as confinement and shear reinforcement (see [DBT08]) but longitudinal reinforcement is typically required. In addition, using longitudinal rebars in High Performance Fiber Reinforced Cementitious Composite structural members is also reasonable from an economical standpoint as they can be used "selectively" in regions of high tensile stresses. In order to obtain a useful simulation tool for HPFRCC structural members a steel reinforcement model has to be added to the isoparametric, quadrilateral elements presented in Chapter 4. The implementation of such a model is described in the following Section 7.2 of this chapter.

There are basically three different approaches to reinforcement modeling in concrete structures. These are namely the *Discrete Rebar Model*, the *Smeared Reinforcement Model* and the *Embedded Rebar Model*.

The most primitive one is the Discrete Rebar Model which is equivalent to using truss elements for the individual reinforcement bars. The disadvantage is that the nodes of the Finite Element mesh have to be adjusted such as to accommodate the nodes of the rebar elements. This may lead to unfavorable Finite Element meshes with an unnecessarily large number of elements or with strongly distorted elements.

The second possibility is to use a Smeared Reinforcement Model. This approach is best suited for slabs or shells with a distributed reinforcement mesh. The primary assumption of the model is that the reinforcement is distributed uniformly over the entire element and that it can therefore be approximated by an equivalent membrane layer of reinforcement steel. The latter is taken into account by modifying the constitutive equations to include a reinforcement contribution.

The third model which is adopted in this thesis is the Embedded Rebar Model by [CTC87]. The latter is based on the original formulation by [PZ76] and basically comes down to an additional term that is added to the weak form of equilibrium in order to account for the virtual work done by the reinforcement. The strain within the reinforcement bars is computed via the standard shape functions of the underlying element and the virtual work is integrated over the length of the rebars. However, only the contribution in the direction of the rebars is considered. More specific details about the model are presented in Section 7.2.

The Embedded Rebar Model was chosen here because the mesh independence of the localized crack model (see Chapter 6) should be conserved for the reinforcement model as well. In fact, there is a strong analogy between the XFEM implementation of the Cohesive Crack Model presented in Section 6.3 and the Embedded Rebar Model as was also recognized by [Hub06]. In the case of the XFEM-crack the virtual work of the cohesive forces is integrated along the crack interface whereas in the case of the Embedded Rebar Model the same is done with the virtual work of the rebars.

It should be noted, that the main goal of the rebar model presented hereafter is to come up with a simple representation for reinforcement bars in HPFRCC structural members that can be used in the computation of some example problems (see Chapter 8). However, it is not the primary focus of this thesis. Therefore, some simplifications concerning the model are made. The first one is the assumption that a reinforcement bar can be modeled by a set of element-wise straight segments. In addition perfect bond between the rebars and the concrete elements is assumed. An extension of the model to curved embedded rebars with bond slip can be found in [EH89].

Finally, it is assumed that the embedded reinforcement bars are *not* crossed by a localized crack. The elements containing rebars are allowed to undergo multiple cracking (which is modeled by the Rotating Crack Model presented in Chapter 5) but the combination of the Embedded Rebar Model and the eXtended Finite Element Method requires some additional considerations concerning the reinforcement bars at the discrete crack locations which are beyond the scope of this thesis. A more detailed discussion of this issue and an outline of what these additional considerations entail are given in Section 8.4.6.

7.2 Rebar Model

As already mentioned in the introductory Section 7.1 the Embedded Rebar Model is adopted for this thesis. The theoretical background of the model is given in the following.

One way of looking at the Embedded Rebar Model is to think of a rebar as an additional element which is superimposed on the unreinforced element. The rebar element has the same number of nodes and the same shape functions as the underlying element but it is integrated only along the line-segment where the rebar is located. This is illustrated in Figure 7.1.

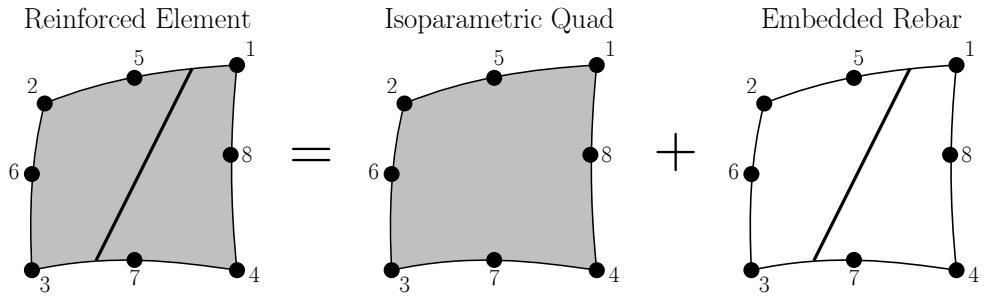

Figure 7.1: Decomposition of the Embedded Rebar Model

Following this approach results in an additional virtual work term for the reinforcement bar δW_{rebar} which has to be added to the weak form of equilibrium. For this reason Equation (4.17) has to be rewritten as Equation (7.1). Note that the latter was also transformed into incremental form because the constitutive law for the reinforcement bars is typically nonlinear which requires the *linearization* of the weak form of equilibrium.

$$\int_{\Omega_e} \delta\underline{\epsilon}^T \cdot \Delta\underline{\sigma}\; d\Omega_e + \delta W_{rebar} = \int_{\Omega_e} \delta\underline{\mathbf{u}}^T \cdot \Delta\underline{\mathbf{f}}\; d\Omega_e + \delta\underline{\mathbf{d}}_e{}^T \cdot \Delta\underline{\mathbf{P}}_e \tag{7.1}$$

The remaining task is to express the virtual work term δW_{rebar} as a function of the virtual nodal displacement increment $\delta\underline{\mathbf{d}}_e$.

The first step towards the solution is to link the nodal displacements to the strain values at the location of the reinforcement bars. Because the standard shape functions of the underlying element are also used for the embedded rebar element the strain acting on the rebar can be computed with the normal strain–displacement transformation matrix $\mathbf{B}$ (see Equation 4.9). This is expressed in Equation (7.2).

$$\begin{aligned} \Delta\underline{\epsilon}_{rebar} &= \mathbf{B}(r,s) \cdot \Delta\underline{\mathbf{d}}_e \\ \delta\underline{\epsilon}_{rebar} &= \mathbf{B}(r,s) \cdot \delta\underline{\mathbf{d}}_e \end{aligned} \qquad \forall\ (r,s) \text{ on the rebar} \tag{7.2}$$

7.2.1 Rotation into the Rebar System

The next step is to perform a rotation of the global strain into the local coordinate system associated with the rebar. This is illustrated in Figure 7.2.

Due to the assumed perfect bond between the reinforcement and the HPFRCC matrix the local strain in the direction of the rebar $\widetilde{\epsilon}_{rebar}$ has to be the same as the projection of the global strain vector $\underline{\epsilon}_{rebar}$ onto the rebar system. This is expressed in Equation (7.3).

$$\widetilde{\epsilon}_{rebar} = \mathbf{T}_{rebar} \cdot \underline{\epsilon}_{rebar} \qquad \text{where} \qquad \mathbf{T}_{rebar} = (\cos^2\alpha,\ \sin^2\alpha,\ \sin\alpha\cos\alpha) \tag{7.3}$$

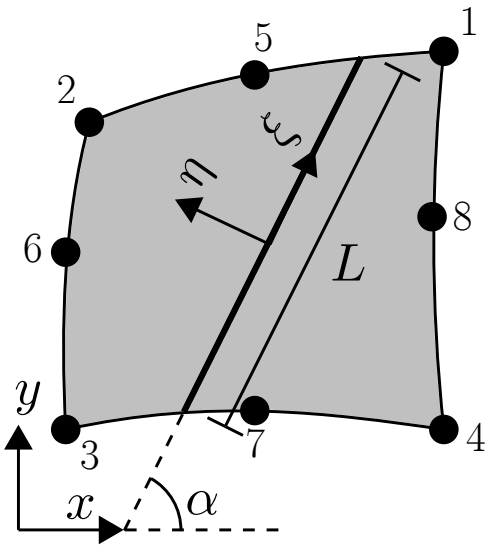

Figure 7.2: Local coordinate system associated with a rebar

Note that in this specific case the rotation matrix $\mathbf{T}_{rebar}$ reduces to a vector because we are only interested in the local strain in the direction of the reinforcement bar. The other components are ignored. The angle α in Equation (7.3) designates the rotation angle between the global axes and the local axes of the rebar as indicated in Figure 7.2.

In virtue of the principle of *duality* the local stress in the reinforcement $\widetilde{\sigma}_{rebar}$ can be rotated back into the global system according to Equation (7.4).

$$\underline{\sigma}_{rebar} = \mathbf{T}_{rebar}^{T} \cdot \widetilde{\sigma}_{rebar} \tag{7.4}$$

7.2.2 Constitutive Equation

A further component that is needed for the Embedded Rebar Model is a constitutive law. Since a rebar is a one-dimensional element the constitutive law reduces to a scalar function. It is most conveniently formulated in the local coordinate system associated with the rebar and should relate the stress in the rebar $\widetilde{\sigma}_{rebar}$ to the longitudinal rebar strain $\widetilde{\epsilon}_{rebar}$ as given by Equations (7.5). Because the constitutive law for reinforcing steel is usually nonlinear it has to be formulated in incremental form. The nonlinear algorithmic stress function χ_{rebar} is provided by Equation (7.5a) and its linearized version with the tangent constitutive modulus $\widetilde{D}_{rebar}$ is given in Equation (7.5b).

$$\Delta\widetilde{\sigma}_{rebar} = \chi_{rebar}\left(\Delta\widetilde{\epsilon}_{rebar}\right) \tag{7.5a}$$

$$\Delta\widetilde{\sigma}_{rebar} = \widetilde{D}_{rebar} \cdot \Delta\widetilde{\epsilon}_{rebar} \tag{7.5b}$$

For reasons of simplicity a standard elasto-plastic law with strain-hardening as shown in Figure 7.3 was implemented. However, this can easily be extended to a more sophisticated one such as the Ramberg–Osgood [RO43] or the Menegotto–Pinto [MP73] model.

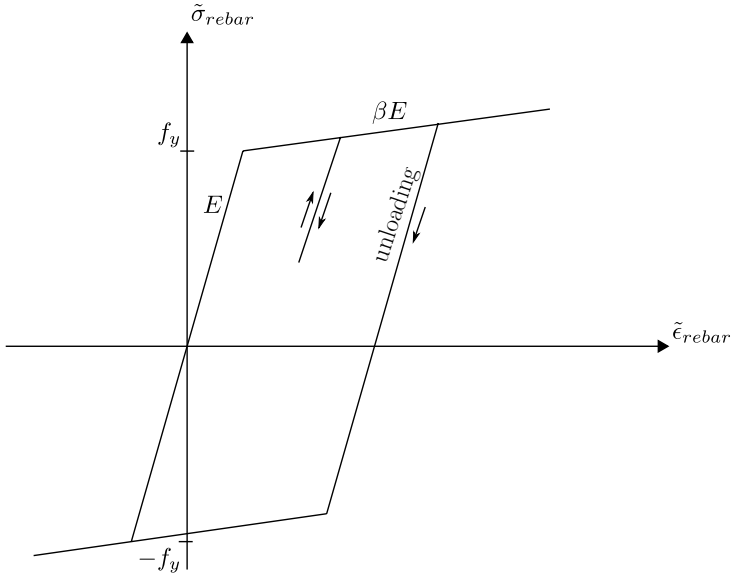

Figure 7.3: Elasto-plastic constitutive law for the embedded rebar model

In Figure 7.3 E denotes the elastic modulus of the reinforcement bars and βE is the hardening modulus after yielding. The yield strength is given by f_y.

7.2.3 Embedded Rebar Stiffness Matrix Contribution

The stiffness matrix of the embedded rebar element can be determined with the help of the weak form of equilibrium from Equation (7.1). The virtual work term δW_{rebar} which accounts for the rebars can be computed as given in Equation (7.6). The virtual work is integrated over the length L of the embedded rebar segment (see Figure 7.2) and the cross-section area of the rebar is denoted by A_{rebar}.

$$\delta W_{rebar} = \int_L \delta\widetilde{\epsilon}_{rebar}^{\,T} \cdot \Delta\widetilde{\sigma}_{rebar} \cdot A_{rebar} dL \tag{7.6}$$

Replacing the stress increment by means of the linearized constitutive law from Equation (7.5b) this can be rewritten as Equation (7.7).

$$\delta W_{rebar} = \int_L \delta\widetilde{\epsilon}_{rebar}^{\,T} \cdot \widetilde{D}_{rebar} \Delta\widetilde{\epsilon}_{rebar} \cdot A_{rebar} dL \tag{7.7}$$

Further using the rotation Equation (7.3) for both the virtual and the real local strain Equation (7.7) can be transformed into Equation (7.8).

$$\delta W_{rebar} = \int_L \left(\mathbf{T}_{rebar}\delta\underline{\epsilon}_{rebar}\right)^T \cdot \widetilde{D}_{rebar} \cdot \mathbf{T}_{rebar}\Delta\underline{\epsilon}_{rebar} \cdot A_{rebar}dL \tag{7.8}$$

Finally, Equation (7.8) is discretized with the Finite Element approximation of the strain field (Equation 7.2) which yields Equation (7.9).

$$\delta W_{rebar} = \int_L \left(\mathbf{T}_{rebar}\mathbf{B} \cdot \delta\underline{\mathbf{d}}_e\right)^T \cdot \widetilde{D}_{rebar} \cdot \mathbf{T}_{rebar}\mathbf{B} \cdot \Delta\underline{\mathbf{d}}_e \cdot A_{rebar}dL \tag{7.9}$$

After rearranging the terms and some simple algebraic transformations the stiffness matrix for an embedded rebar element is found (Equation 7.10).

$$\delta W_{rebar} = \delta\underline{\mathbf{d}}_e^T \underbrace{\int_L \mathbf{B}^T\mathbf{T}_{rebar}^T\widetilde{D}_{rebar}\mathbf{T}_{rebar}\mathbf{B} \cdot A_{rebar}dL}_{\mathbf{K}_e^{rebar}} \cdot \Delta\underline{\mathbf{d}}_e \tag{7.10}$$

Reintroducing this result into the weak form of equilibrium from Equation (7.1) and respecting the fact that the equilibrium has to be satisfied for any arbitrary variation of the virtual nodal displacements $\delta\underline{\mathbf{d}}_e$ results in the stiffness matrix given in Equations (7.11) (for the standard virtual work term see Section 4.2.5). It is composed of a stiffness contribution that accounts for the standard, isoparametric, quadrilateral element and a stiffness contribution that accounts for the embedded reinforcement.

$$\mathbf{K}_e = \mathbf{K}_e^{std} + \mathbf{K}_e^{rebar} \qquad \text{where} \tag{7.11a}$$

$$\mathbf{K}_e^{std} = \int_{\Omega_e} \mathbf{B}^T\mathbf{D}\mathbf{B}\ d\Omega_e \tag{7.11b}$$

$$\mathbf{K}_e^{rebar} = \int_L \mathbf{B}^T\mathbf{T}_{rebar}^T\widetilde{D}_{rebar}\mathbf{T}_{rebar}\mathbf{B} \cdot A_{rebar}dL \tag{7.11c}$$

At this point it becomes obvious that there is a strong similarity between the stiffness matrix contribution of a cohesive crack introduced in Section 6.3.3 and the stiffness matrix contribution of an embedded rebar. By analogy the integral in Equation (7.11c) is also evaluated numerically with a three-point Gauss integration rule. This involves the same mapping procedure of the integration points from the natural domain $[-1, 1]$ to the real domain of the rebar and then an inverse mapping from the real domain to the parent quadrilateral domain (because the strain–displacement transformation matrix is formulated in those coordinates). The details are not repeated here and the reader is referred to Section 6.3.3.

7.2.4 Secondary Results and Element Reactions

Once the global system of equations has been solved the element nodal displacements $\underline{\mathbf{d}}_e$ can be used to compute some secondary results for the embedded rebar element. The first one is the local strain in the rebar. From Equations (7.2) and (7.3) it follows directly that the local strain can be computed by Equation (7.12).

$$\widetilde{\epsilon}_{rebar} = \mathbf{T}_{rebar} \cdot \mathbf{B} \cdot \underline{\mathbf{d}}_e \tag{7.12}$$

The effective stress in the rebar can then be found through Equation (7.13). Due to the nonlinearity of the rebar material law it has to be computed via the incremental stress return algorithm (see Section 7.2.2). The local strain increment is given by $\Delta\widetilde{\epsilon}_{rebar} = \widetilde{\epsilon}_{rebar} - \widetilde{\epsilon}^{\,eq}_{rebar}$ and $\widetilde{\epsilon}^{\,eq}_{rebar}$ respectively $\widetilde{\sigma}^{\,eq}_{rebar}$ are the local strain and stress at the last global equilibrium state.

$$\widetilde{\sigma}_{rebar} = \widetilde{\sigma}^{eq}_{rebar} + \chi_{rebar}\left(\Delta\widetilde{\epsilon}_{rebar}\right) \tag{7.13}$$

The element reaction forces which are used in the global equilibrium iteration follow from the principle of virtual work. In addition to the standard term for the isoparametric, quadrilateral element (see Section 4.2.9) the virtual work contribution of the reinforcement has to be taken into account. After a rotation of the rebar stress into the global coordinate system via Equation (7.4) the element reaction forces can be computed as given by Equation (7.14).

$$\underline{\mathbf{R}}_e = \int_{\Omega_e} \mathbf{B}^T \underline{\sigma}\; d\Omega_e + \int_L \mathbf{B}^T \mathbf{T}^T_{rebar} \widetilde{\sigma}_{rebar} A_{rebar}\; dL \tag{7.14}$$

Equation (7.14) is of course evaluated numerically in analogy to Section 6.3.4.

Chapter 8

Applications

8.1 Introduction

After having explained the theoretical basis for the newly developed numerical model for High Performance Fiber Reinforced Cementitious Composites in the preceding Chapters 4 to 6, this chapter will present a couple of applications. The idea is to prove the validity of the model and to compare some simulation results with experimental test data. We will mainly focus on the model's capability to capture the general characteristics of the material response and especially the different phases of behavior. However, no major attempt will be made to calibrate the model parameters as closely as possible to the experimental results as this would equate to a "curve fitting" exercise which is deemed unreasonable. A more meaningful approach would be to determine the model parameters based on more detailed experimental knowledge about the cracking behavior of HPFRCCs (cracking-stress vs. cracking-strain law, traction–separation law, shear-transfer law) which is unfortunately not available for the materials used in the presented applications. An alternative would be to develop sophisticated micromechanical models as was done in [Kab07] but this is beyond the scope of this thesis.

In the following three different applications are presented. The first one is the simulation of a wedge splitting test (Section 8.2). In Section 8.3 the numerical model is then applied to a 4-point bending test and finally a shear beam test is simulated in Section 8.4.

8.2 Wedge Splitting Test

In this first example the newly developed numerical model is applied to an Ultra High Strength Concrete wedge splitting test [XSDK04]. The primary goal of this application is to focus on the strain-softening part of the model without involving the strain-hardening phase. For this reason an Ultra High Strength Concrete (UHSC) specimen instead of

a High Performance Fiber Reinforced Concrete (HPFRC) specimen is used. However, an application with a High Performance Fiber Reinforced Concrete will be presented in Section 8.3.

In the first two sections the test setup (Section 8.2.1) and the material of the test specimen (Section 8.2.2) are described. This is then followed by an explanation of the used Finite Element discretization (Section 8.2.3) and a description of the input parameters for the numerical model (Section 8.2.4). Finally, the results of the simulation are presented and a comparison with the experimental data is made (Section 8.2.5). The investigation of the example is concluded by a mesh-refinement analysis which demonstrates the correct convergence behavior of the model (Section 8.2.6).

8.2.1 Test Setup

The wedge splitting test which is used here to validate the crack localization phase of the numerical model is taken from [XSDK04]. A photo of the test setup is shown in Figure 8.1a. The basic goal of this kind of test is to compute the fracture energy of a material. A crack is initiated at the tip of a sawn starter notch and it is forced to propagate from the top of the specimen to its bottom. Figure 8.1b shows the geometry of the wedge splitting test specimen. Its general dimensions are $300 \times 300\ mm$ and it has a thickness of $100\ mm$. The splitting forces at the top of the specimen are applied by means of a triangular wedge (see Figure 8.1a) which redirects the vertical actuator force such that a pair of horizontal forces is created.

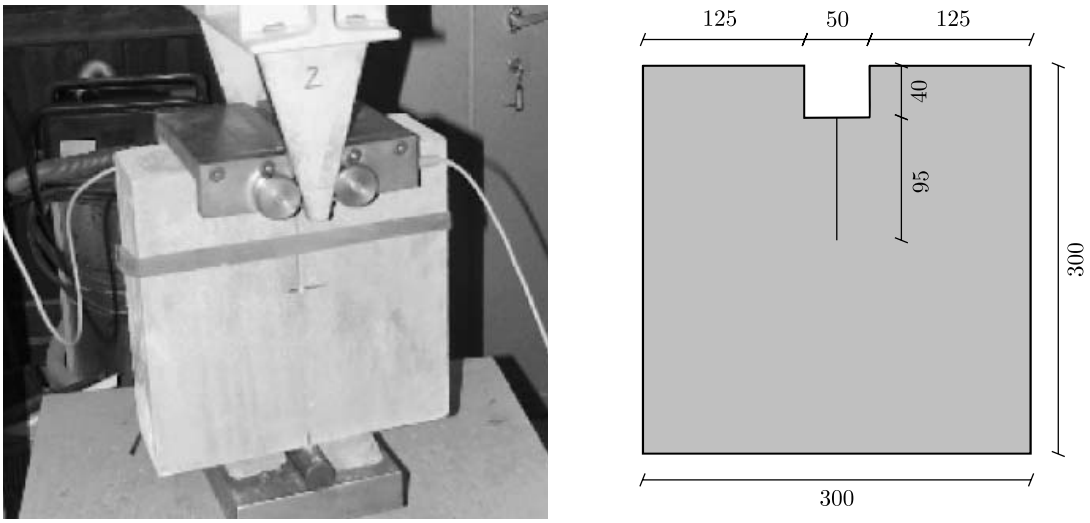

(a) Test setup (b) Specimen geometry in mm

Figure 8.1: Wedge splitting test taken from [XSDK04]

The primary result of this wedge splitting test is a relationship between the horizontal splitting force F_{sp} and the crack opening displacement (COD). According to [XSDK04],

the latter was measured by means of two high-precision displacement gauges which were located at the mouth of the starter notch. The resulting splitting force vs. crack opening displacement curve is given in Section 8.2.5.

8.2.2 Material

Because the goal of this simulation is the validation of the crack localization part of the numerical model a quasi-brittle Ultra High Strength Concrete without fiber reinforcement is chosen. Nevertheless, the UHSC does exhibits some cohesive forces in the sense of the Cohesive Crack Model by Hillerborg due to crack tortuosity and aggregate interlock. A description of the used UHSC is given in the following.

The primary constituents of the UHSC were crushed basalt (1027 kg/m^3), quartz sand (440 kg/m^3) and Portland CEM I 42.5R cement (540 kg/m^3). As fine fillers quartz powder (231 kg/m^3) and silica fume (162 kg/m^3) were used. In order to obtain the necessary workability 16.8 kg/m^3 of superplastizicer were also included in the mix. Water was added at an amount of 163 kg/m^3 resulting in a w/b ratio of 0.232. More details about the material constituents can be found in [XSDK04] where it is labeled *UHSC-2*.

The authors of [XSDK04] also determined some of the basic mechanical properties of the UHSC in question. They fond that it had a very high axial compressive strength of 147.7 MPa which is typical for Ultra High Strength Concretes. Furthermore, the tensile splitting strength was measured to be 8.6 MPa and the elastic modulus was $53'000$ MPa with a Poisson's ratio of 0.18.

8.2.3 Finite Element Discretization

The wedge splitting test is discretized using the 8-node quadrilateral elements introduced in Chapter 4. As shown in Figure 8.2a an almost regular grid of 15×13 elements is used. The elements in the critical part of the specimen are a little smaller and they are arranged in such a way as to induce crack propagation through a column of central elements instead of along element borders. The reasoning behind this is to demonstrate the correct working of the eXtended Finite Element Model. The Finite Element mesh contains a total of 189 elements and 628 nodes which results in about $1'250$ degrees of freedom.

As can be seen in Figure 8.2a the starter notch is introduced by means of the XFEM. The corresponding enriched nodes are indicated by circles. In order to avoid some numerical problems which are created if a single point of support is used (the equilibrium equations become singular because the specimen can rotate freely) all nodes of the central, bottom element are fixed. This is acceptable from a physical point of view since the pivot point in the experiment also has a certain width.

8.2.4 Model Input Parameters

The next step is to define the input parameters for the numerical model. For the most part these are directly taken from [XSDK04]. The parameters for the elastic bulk material were already introduced in Section 8.2.2 and are taken as $E = 53'000\ MPa$ and $\nu = 0.18$.

A further parameter that is needed for the simulation is the principal strain ϵ_{loc} at which crack localization and softening sets in (see Section 6.4.2). It can be estimated with the help of the splitting tensile strength which was measured to be 8.6 MPa [XSDK04]. Dividing this value by the modulus of elasticity E yields an approximate localization strain of 0.16 ‰.

Because the material is not strain-hardening (no fibers) there is no multiple cracking phase and the parameters for the Smeared Crack phase can be ignored.

Finally, the model requires a Mode I and a Mode II traction–separation law for the cohesive crack during the localization phase. For the traction–separation law in Mode I the propositions made in [XSDK04] are adopted which means that the bilinear softening curve shown in Figure 8.2b is used. It accounts for crack tortuosity as well as aggregate interlock and it assures correct energy dissipation during the cracking process.

Softening starts at the already mentioned splitting tensile strength of $\sigma_{pc} = 8.6\ MPa$ and rapidly progresses up to a crack opening of 0.0154 mm and the corresponding stress of 1.07 MPa. The traction–separation law then flattens out and the crack reaches its stress-free state at an ultimate crack opening of $w_u = 0.11\ mm$.

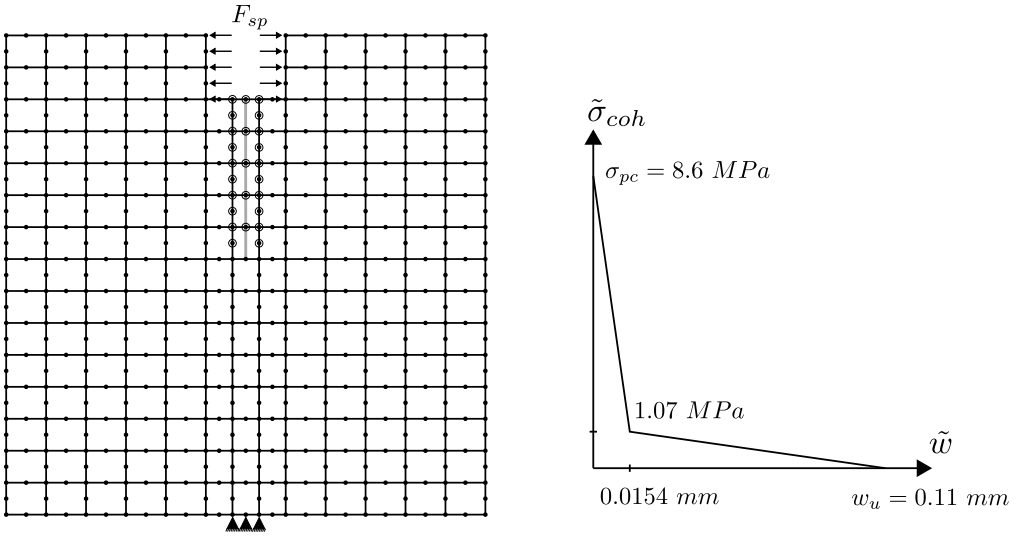

(a) Finite Element discretization (b) Mode I traction–separation law

Figure 8.2: Numerical model

Because the wedge splitting test is a pure Mode I problem the Mode II law is of no concern.

8.2.5 Results

In this section the results of the simulation are presented and they are compared to the experimental data. The experimental and the numerical splitting force vs. crack opening displacement (COD) curves are plotted in Figure 8.3. Overall there is an excellent agreement between the simulation and the experiment. The curve labeled "Test results" represents the mean value of the test measurements presented in [XSDK04].

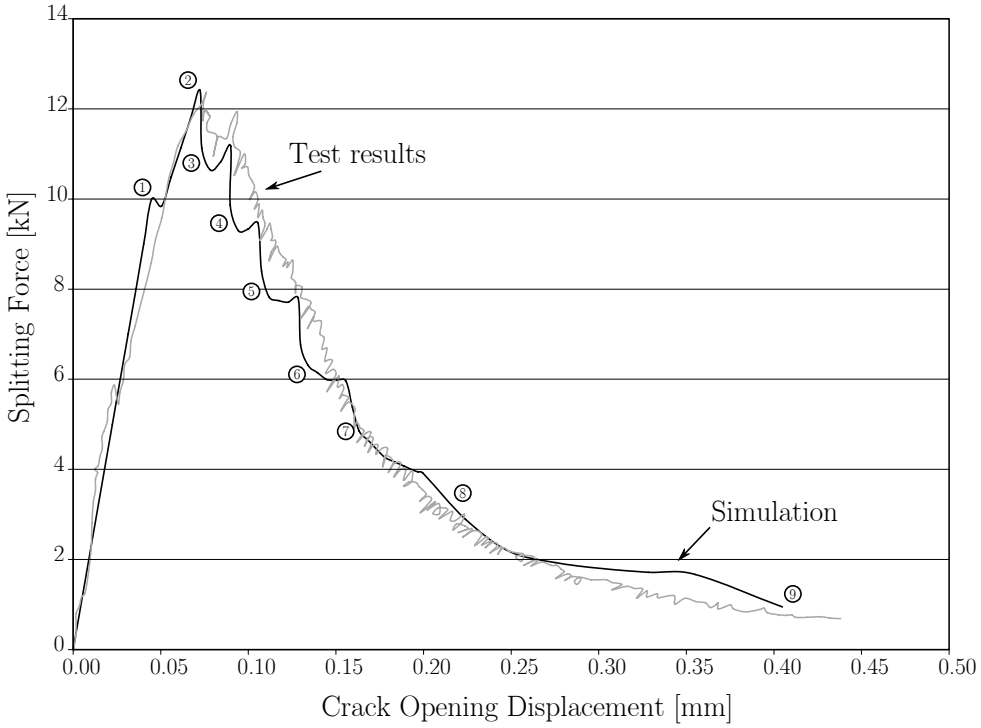

Figure 8.3: Splitting force vs. crack opening displacement (test results from [XSDK04])

The most interesting result is that the peak load is determined very accurately. This is even more astonishing when acknowledging the fact that the peak load does not correspond to the end of the elastic phase (which is marked by ①). Rather, the maximum load carrying capacity is only reached after the crack has propagated some small distance into the specimen. This can be explained by a redistribution of the internal efforts and it is typical for wedge splitting tests with cohesive materials.

The softening branch of the behavior is also captured fairly accurately even up to complete separation of the specimen.

In Figure 8.3 another interesting observation concerning the numerical model can be made. The softening curve is not completely smooth but exhibits a small number of "sawtooth-like" spikes. These are a consequence of the fact that crack growth is not continuous. More specifically, the crack is always incremented by the length of an entire element (see Section 6.4.1) which manifests itself in an artificial buildup of stresses until

the crack propagates and the excess stresses are released. However, the errors are small and the solution converges upon mesh refinement (see Section 8.2.6).

The evolution of the crack during the simulation is illustrated in Figure 8.4. Each stage of the crack is labeled by a circled number (e.g. ①) which is also used to mark the corresponding point in the splitting force – crack opening displacement curve in Figure 8.3.

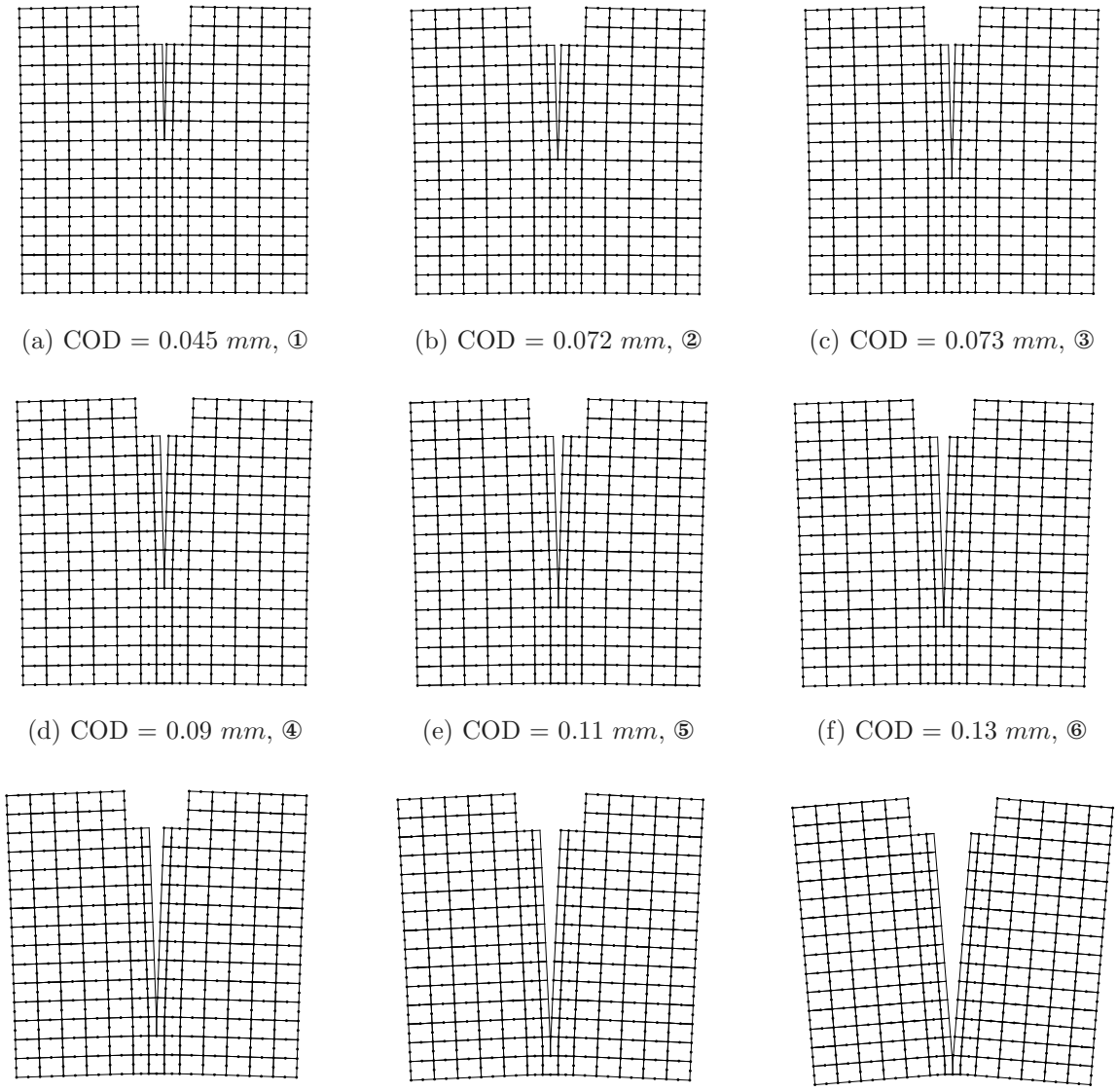

(a) COD = 0.045 mm, ① (b) COD = 0.072 mm, ② (c) COD = 0.073 mm, ③

(d) COD = 0.09 mm, ④ (e) COD = 0.11 mm, ⑤ (f) COD = 0.13 mm, ⑥

(g) COD = 0.16 mm, ⑦ (h) COD = 0.22 mm, ⑧ (i) COD = 0.4 mm, ⑨

Figure 8.4: Crack evolution (Deformation ×100)

Finally, Figure 8.5 shows a plot of the stress field in x-direction (horizontal) at peak load (see point ② in Figure 8.3). The high stresses in the vicinity of the crack tip are clearly apparent. Also note how the stresses directly behind the crack tip still remain high since the cohesive forces are large at small crack openings. On the other hand the part of

the crack which is far away from the tip has completely unloaded and the stresses in x-direction are reduced to zero.

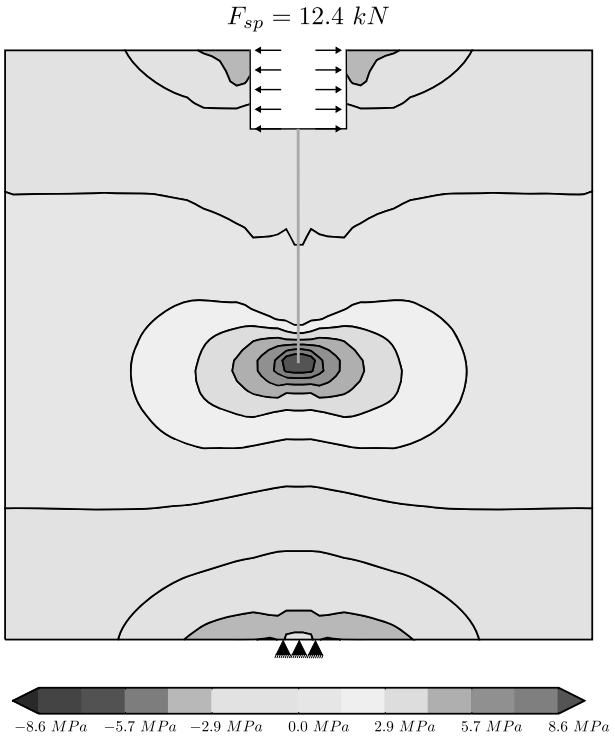

Figure 8.5: Stress field in horizontal direction at peak load

8.2.6 Mesh Refinement

Because the splitting force vs. crack opening displacement curve of the simulation exhibits a number of unconventional spikes (see Section 8.2.5) and because mesh-insensitivity is a key feature of the proposed model a mesh refinement analysis is performed. The number of elements is more or less doubled and a new mesh of 30×25 elements is generated. This results in a refined model with 750 elements, $2'309$ nodes and approximately $4'610$ degrees of freedom as is illustrated in Figure 8.6. Note that in order to keep the model consistent the width of the support zone is kept the same as in the model with the coarse mesh.

In Figure 8.7 the splitting force vs. crack opening curves that were obtained with the fine mesh (Mesh 30×25) are plotted together with those from the original simulation (Mesh 15×13). The results clearly indicate that the coarse mesh already provides fairly accurate results and that the proposed model is not sensitive to mesh refinement at all. The elastic branch of the response is identical and the peak load as well as the softening behavior are very close. The most obvious difference is that the aforementioned spikes which are related to an artificial buildup of stresses due to the element-wise propagation of the crack

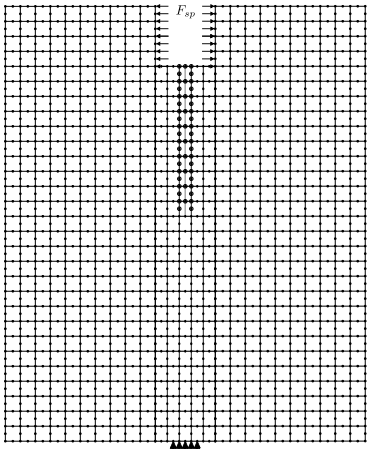

Figure 8.6: Refined mesh

are strongly reduced. This is a direct consequence of the larger number of elements which allows for a smoother crack propagation (smaller crack growth increments). However, the two curves never deviate much from one another and they coincide whenever the crack just propagated and the artificial stress buildup is released. It is interesting to note that because the crack propagates in shorter increments the spikes are smaller in magnitude but larger in number. Also note that the two results remain close even at large crack openings which is often not the case for other models. Overall, this mesh refinement analysis clearly shows that the proposed model is not particularly sensitive to the used mesh size and that the solution converges very quickly.

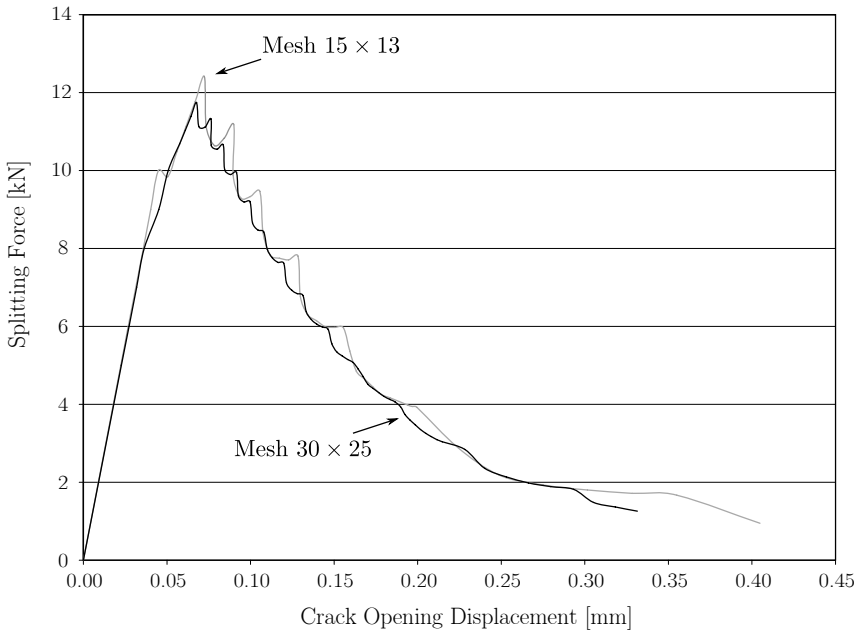

Figure 8.7: Splitting force vs. crack opening displacement for two different mesh sizes

8.2.7 Conclusions

This simulation of a wedge splitting test clearly shows the correct working of the crack localization and strain-softening part of the proposed numerical model. In the simulation the crack is able to propagate independently of the Finite Element mesh and the results are in excellent agreement with the experimental measurements. Furthermore, the model is not mesh-sensitive and the simulation is stable up to complete separation of the wedge splitting test specimen without any locking or spurious stress transfer effects.

The excellent agreement between the test and the simulation results is partly due to the particularly realistic input parameters provided by the authors of [XSDK04]. Unfortunately this publication does not explain explicitly how the input parameters were determined. However, the paper states that the input parameters are in close accordance with the global recommendations by the CEB-FIP model code [CEB90].

The next step is to use the numerical model for the simulation of a test example with a HPFRCC material in which case the strain-hardening phase of the model will have to be taken into account as well. This is done in the following Section 8.3.

8.3 4-Point Bending Test

In this second example the numerical model is applied to a HPFRCC 4-point bending test which was carried out at the University of Michigan. The test results were kindly provided by Prof. G. J. Parra-Montesinos and R. D. Lequesne. The test setup and the material properties are described in Sections 8.3.1 and 8.3.2 respectively. Thereafter, the used Finite Element discretization is given in Section 8.3.3 followed by an explanation of how the input parameters for this simulation are chosen (Section 8.3.4). Finally, the results of the simulation are presented and discussed in Section 8.3.5 and a comparison with the experimental results is made.

8.3.1 Test Setup

As already mentioned, the setup that is simulated here is a standard 4-point bending test which was performed at the University of Michigan. The results of that test are not published individually but they are part of the work leading to [LSPMW09]. A photo of the test setup is shown in Figure 8.8a.

The test was conducted following the ASTM standard [AST06], which means that the test specimen had a span of 45 *cm* and a cross-section 15 *cm* in height and 15 *cm* in width. Figure 8.8b shows the geometry and the loading conditions of the test. The two loads were applied by means of a load distribution beam and a single actuator, which was controlled by the displacement measured at mid-span.

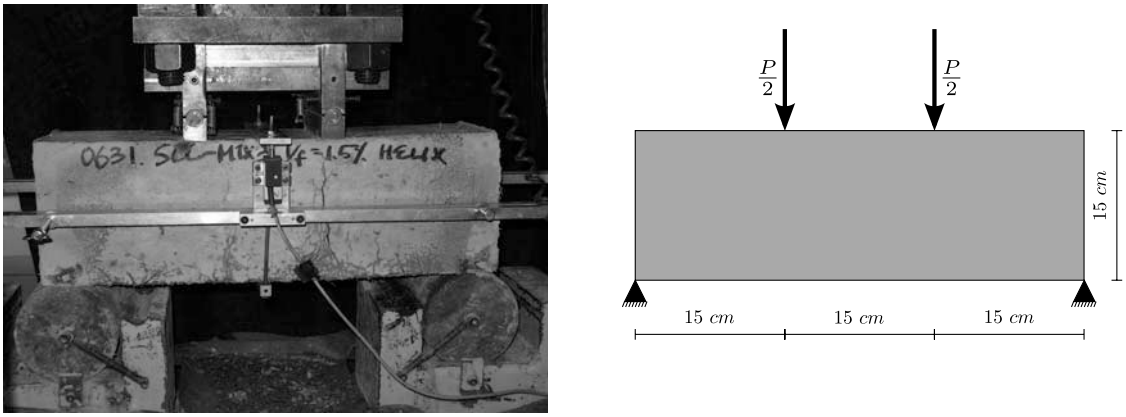

(a) Test setup (b) Specimen geometry

Figure 8.8: 4-point bending test (photo courtesy of [LSPMW09])

The beam itself consisted of a Self-Consolidating High Performance Fiber Reinforced Concrete featuring strain-hardening in direct tension. More detailed information about the material is given in the following Section 8.3.2.

8.3.2 Material

The material that was used to manufacture the test specimen was a Self-Consolidating High Performance Fiber Reinforced Concrete (SCHPFRC) that was developed at the University of Michigan [LCPN06]. Its main characteristics are summarized in the following.

The matrix of the SCHPFRC contained crushed limestone (187 g/kg) with a maximum aggregate size of about 12 mm and ASTM Type III Portland cement (155 g/kg). It also included a significant amount of fly-ash (136 g/kg) and silica sand (342 g/kg). As chemical admixtures the products Glenium® 3200 HES (0.78 g/kg) and RHEOMAC® VMA 362 (5.9 g/kg) were used. Water was added at an amount of 124 g/kg resulting in a w/c ratio of 0.8.

The fiber reinforcement of the SCHPFRC consisted of Dramix® RC-80/30-BP steel fibers which were added at a total volume fraction of 1.5 % (49 g/kg). These hooked-end fibers are made of high strength steel (2300 MPa) and have a length of 30 mm and a diameter of 0.38 mm which results in an aspect ratio of 79.

The modulus of elasticity of the Self-Consolidating High Performance Fiber Reinforced Concrete was approximately 28′000 MPa and its Poisson's ratio was 0.14. The average compressive strength was about 38 MPa. What is essential about the tensile behavior of this SCHPFRC is its pronounced strain-hardening phase. This can be seen in Figure 8.9 taken from [LCPN06]. As a consequence the concrete undergoes a prolonged phase of multiple cracking before strain localization occurs at approximately 0.5 % strain. This is in direct contrast to the Ultra High Strength Concrete presented in Section 8.2.2 which

already started softening at 0.016 % (see Section 8.2.4). More detailed information about the SCHPFRC can be found in [LCPN06] where it is labeled *Mix 6*.

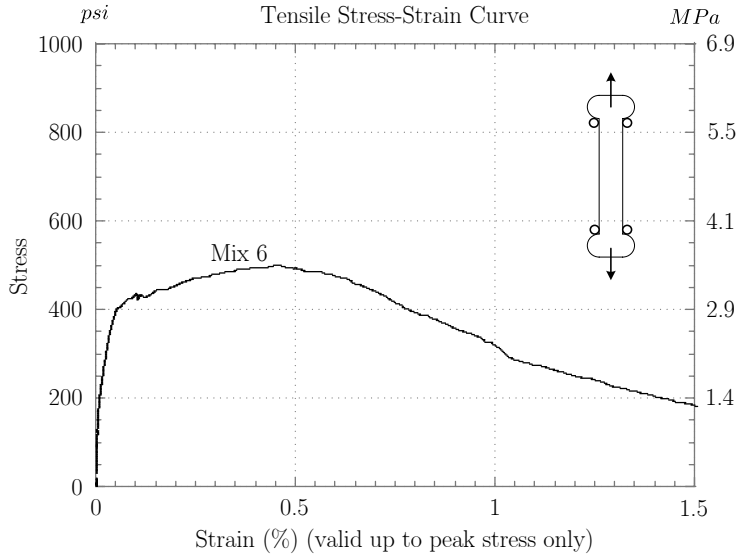

Figure 8.9: Tensile stress–strain curve of the used SCHPFRC (adopted from [LCPN06])

8.3.3 Finite Element Discretization

The first step in setting up a numerical model for the bending test described in Section 8.3.1 is to choose an appropriate Finite Element discretization. The following Figure 8.10 shows the chosen Finite Element mesh. It consists of 160 quadrilateral elements and contains a total of 531 nodes which results in about 1060 degrees of freedom. The central zone which is of primary interest is discretized with a finer mesh than the border zones. This is necessary in order to obtain more accurate strain and stress fields and also to get a more realistic crack propagation behavior.

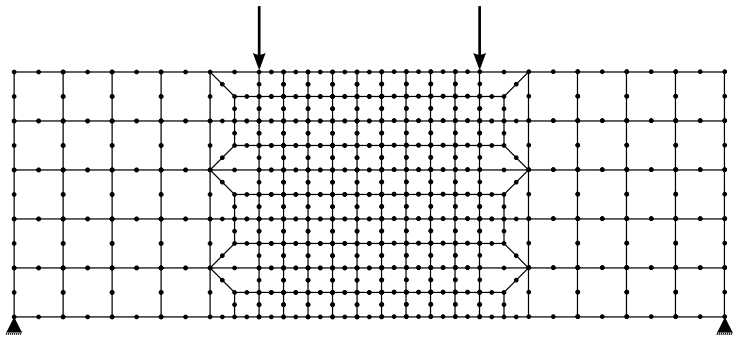

Figure 8.10: Finite Element discretization

8.3.4 Model Input Parameters

The next step in the procedure is the choice of the input parameters for the material model in accordance with the material characteristics outlined in Section 8.3.2. All parameters were chosen before the simulation was run which led to a "blind" prediction of the behavior. Each phase of the material model requires its own parameters as explained in the following.

Elastic Model

The elastic part of the model is defined by the modulus of elasticity E and Poisson's ratio ν (see Section 4.2.5, Equation 4.19). The used SCHPFRC is regarded as homogeneous and isotropic and the modulus of elasticity in compression and in tension is assumed to be the same. It is also assumed that the material remains linear-elastic in compression which is a simplification. However, this can be accepted as long as the compressive strength of the SCHPFRC (38 MPa in the simulation) is not exceeded. Following the indications given in Section 8.3.2 the modulus of elasticity and Poisson's ratio were taken as $28'000$ MPa and 0.14, respectively.

Rotating Smeared Crack Model

The Rotating Crack Model requires the input of an uniaxial stress vs. cracking-strain relationship (see Section 5.2.3). This is entered into the numerical model by means of a piecewise linear curve. Unloading is assumed to occur linearly and origin-oriented with complete closure of microcracks leaving no residual strain. The stress vs. cracking-strain curve was calibrated by means of the direct tension test results taken from [LCPN06] as shown in Figure 8.11, which is a close-up of Figure 8.9.

The Smeared Crack Model only covers the strain-hardening phase after first cracking up to the onset of softening. From the tensile test shown in Figure 8.11 the point of first cracking can be roughly identified as point ① with a stress of 2.8 MPa. Although this is probably not the point at which the first microcracks appear in the material it is clearly the beginning of multiple cracking and significant cracking-strain accumulation. The stress vs. cracking-strain relationship for the Smeared Crack Model is input into the program in form of a piecewise linear curve going from point ① to point ② (Figure 8.11). Note that such a calibration neglects the contribution of the elastic bulk material during the strain-hardening phase since it is very small in comparison. However, the cracking-strain is set to zero at point ①. As a result the input curve for the Rotating Crack Model is a polylinear line going from a first cracking stress σ_{cc} of 2.8 MPa to an ultimate stress of $\sigma_{pc} = 3.5$ MPa and a corresponding strain of $\epsilon_{pc} = 0.4$ % (see Figure 8.12b). The intermediate point on the curve is located at a stress of 3.17 MPa and a strain of 0.15 %.

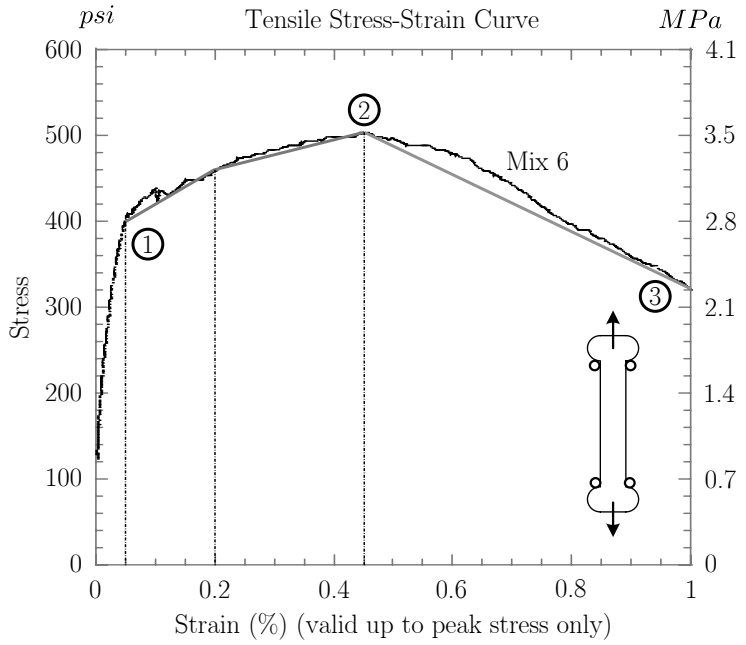

Figure 8.11: Calibration by means of a direct tension test taken from [LCPN06]

Extended Finite Element Model

The eXtended Finite Element model needs three basic input parameters. The first one is the total principal strain at which the material starts softening ϵ_{loc} (see Section 6.4.2). It can easily be identified to be 0.45 % from the direct tension test shown in Figure 8.11. The other two parameters are more difficult to determine. They are the Mode I traction–separation law and the shear vs. crack-sliding law (Mode II). Especially the latter is very difficult to express as unfortunately no experimental data on this subject are available. However, for the presented example shear sliding along the crack interface is not an issue and it can therefore be ignored.

The Mode I traction–separation law is also relatively difficult to identify. For the purpose of this simulation a rough estimation is performed as follows: The softening branch of the stress–strain curve from the direct tension test is linearly extrapolated to find the strain at total separation of the material (Figure 8.11 linear extrapolation through point ③). Of course the strain plotted in Figure 8.11 is only valid up to peak stress. Afterwards it is just an artifact that is computed from the displacement measurements of the measuring device which was attached to the central part of the tension test specimen and had a gauge length of 175 mm. In fact, the computed strain value after the peak load results from a combination of the residual strains in the bulk material and the crack opening displacement of the localized crack which is "smeared" over the length of the gauge. It is clear that at the extrapolated point of zero stress the specimen would have unloaded completely and the strain computed from the device readings would be solely caused by the localized crack. The crack opening at which the localized crack becomes completely

stress-free can therefore be estimated by multiplying the extrapolated strain with the gauge length. This procedure results in an ultimate crack opening w_u of 3.2 mm.

For the numerical model the softening curve is defined as a straight line starting at a stress of 3.5 MPa and unloading to 0 over a length of 3.2 mm. It should be emphasized, that this very crude approximation could certainly be improved by choosing a more sophisticated input curve. Unfortunately, the determination of such a curve is hindered by the limited experimental data. However, the goal of this example is not to come up with a perfect match between the numerical and experimental results but rather to demonstrate the general capabilities of the model. A more detailed calibration and a sensibility analysis of the input parameters would have to follow for any practical application.

Figure 8.12 shows the material input curves that are used for the numerical model. Note that although the curve for the eXtended Finite Element model (Figure 8.12c) is chosen to be a straight line in this simulation, the developed material model accepts any piecewise linear relationship as an input.

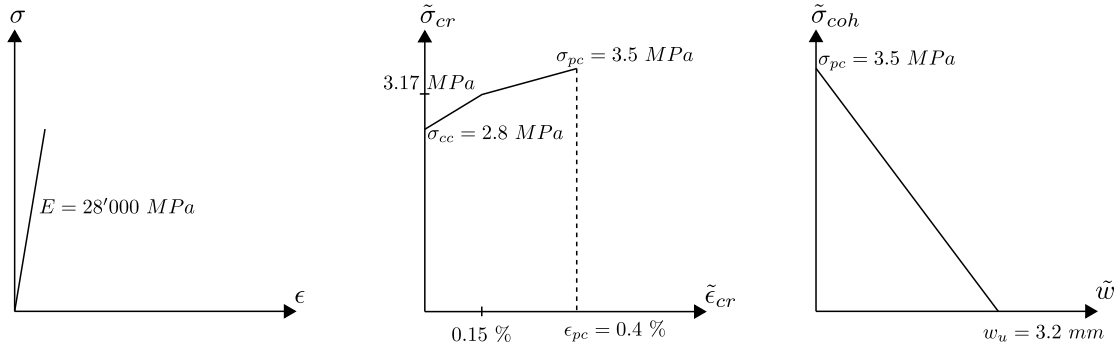

(a) Elastic (b) SMCR (c) XFEM

Figure 8.12: Input curves for the simulation

8.3.5 Results

In this section the results of the numerical simulation are discussed. In order to get a general impression of the performance of the model the experimental load–deflection curves of the 4-point bending tests mentioned in [LSPMW09] and the results of the numerical simulation are shown in the following Figure 8.13.

The overall performance of the numerical model seems to be pretty good. The computed curve looks similar to the ones measured in the test series although the peak load is slightly overestimated. One possible explanation for this is that the HPFRC tensile strength measured in a direct tension test generally overestimates the true tensile strength of the material because tension test specimen are relatively small in comparison to the fiber length, which causes a preferential alignment of the fibers in the longitudinal direction.

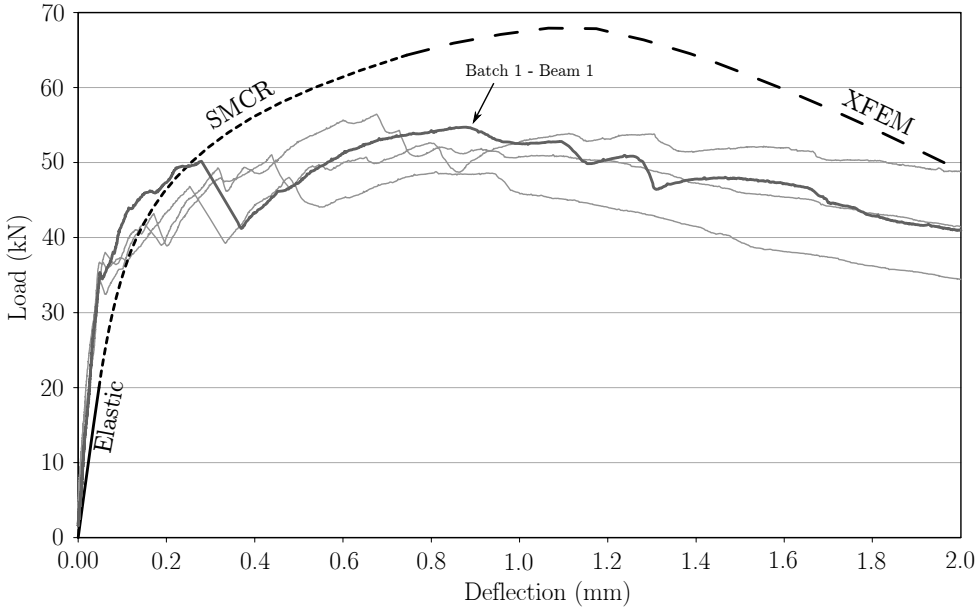

Figure 8.13: Total actuator load vs. mid-point deflection (test results from [LSPMW09])

The experimental curve which should match the simulation most closely is the one labeled "Batch 1 - Beam 1"(in that test the crack also localized at midspan).

The different behavioral phases I, II and III of the model (see Section 8.3.4) are clearly marked in the numerical load–deflection curve shown in Figure 8.13. First there is a linear, elastic phase. This is then followed by a phase of microcracking which starts at an actuator load of approximately 20 kN. During this second phase the stiffness is at first more or less retained due to a redistribution of stresses within the cross-section of the beam. Beginning at about 40 kN the simulated load–deflection curve flattens out and shortly after reaching an actuator load of 60 kN the deformations localize and a discrete crack is formed. Interestingly enough there is still some global hardening even after formation of the localized crack. This effect is analogous to the one observed for the wedge splitting test in Section 8.2.5. However, the increase in load is only minor and at a little more than 65 kN the ultimate load carrying capacity is reached and the beam enters the global softening regime.

It should be noted, that although the numerical and the experimental curves do not match exactly the general trends are captured correctly. By refining the input parameters the results could certainly be improved especially because the former are estimated so crudely. However, this requires specific experimental data on the traction–separation law of a localized crack in this type of SCHPFRC.

In the following sections the individual stages of the simulation are examined in more detail.

Elastic Phase

During the elastic phase the simulated load–deflection curve is linear (see Figure 8.13) which is of course to be expected. However, the slopes of the measured load–deflection curves are a little steeper than the slope of the simulated curve which suggests that the elastic modulus of the SCHPFRC was probably a bit higher than assumed. This could easily be the case as the modulus of elasticity that was used for the simulation (Section 8.3.4) was measured on a different batch of SCHPFRC.

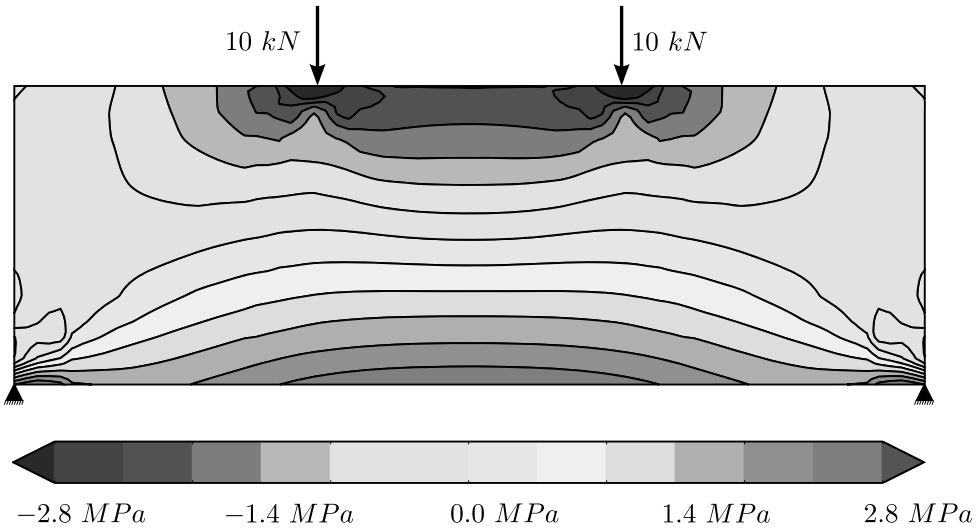

Figure 8.14: Stress in horizontal direction at a total load of 20 kN

Figure 8.14 shows a plot of the stress field in the longitudinal direction at a total load of 20 kN. This corresponds to the end of the elastic phase. The stress-profile is more or less linear and it is in accordance with the results obtained by solving the analytical Bernoulli beam equations which (at a total load of 20 kN) yield a stress of 2.67 MPa for the outermost beam fibers at midspan.

Multiple Cracking Phase

During the multiple cracking phase there is a strong redistribution of stresses within the central third of the beam due to the strain-hardening character of the material law. This is comparable to what can be observed with steel beams. The following Figures 8.15 and 8.16 show the evolution of the cracking zone. At a total load of 40 kN the cracked zone has almost reached the central axis (see Figure 8.15). As can be seen in Figure 8.13 this leads to a higher resistance of the cross-section without much loss in stiffness.

Figure 8.16 on the other hand shows the stress field towards the end of the multiple cracking phase. The beam is now cracked over almost its entire depth and only a small compression zone remains. There is also some significant cracking on the tension face of

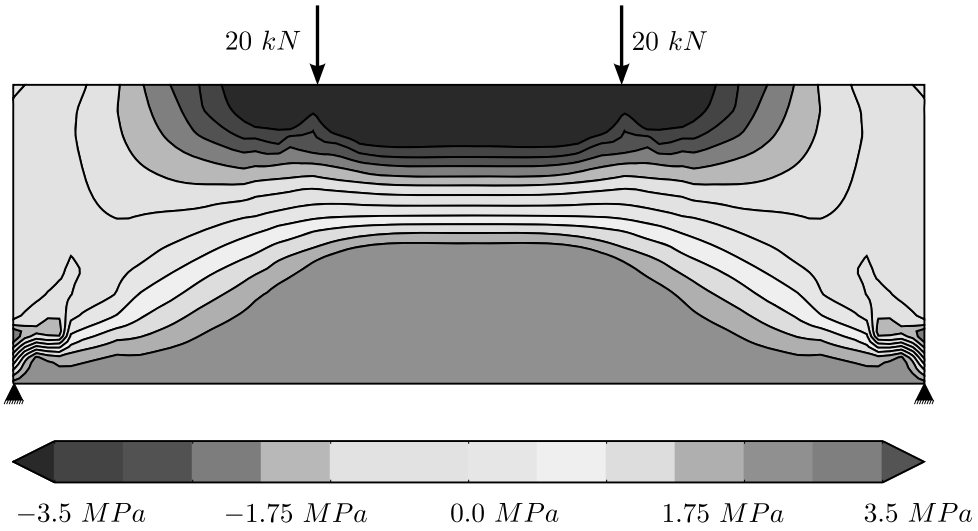

Figure 8.15: Stress in horizontal direction at a total load of 40 kN

the beam along its entire length. At this point the stiffness has dropped significantly and it represents the cracked stiffness of the beam.

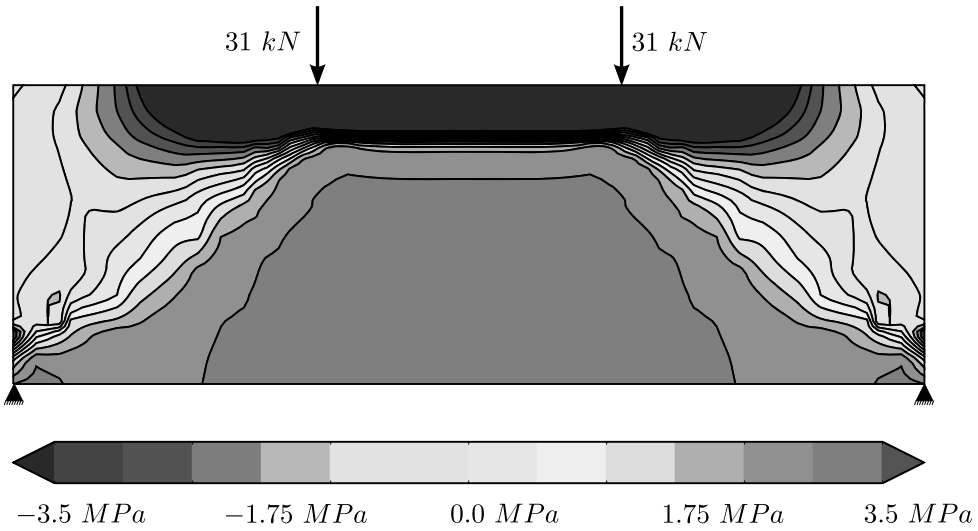

Figure 8.16: Stress in horizontal direction at a total load of 62 kN

Crack Localization Phase

During this final phase the strain starts to localize and a discrete, softening crack forms in the central region. Figure 8.17 shows the stress field at the initiation of localized cracking.

Because the softening crack can form at any location within the central region where the crack localization stress of 3.5 MPa is exceeded (in reality this depends strongly on the fiber distribution) a small notch is introduced at the center of the span.

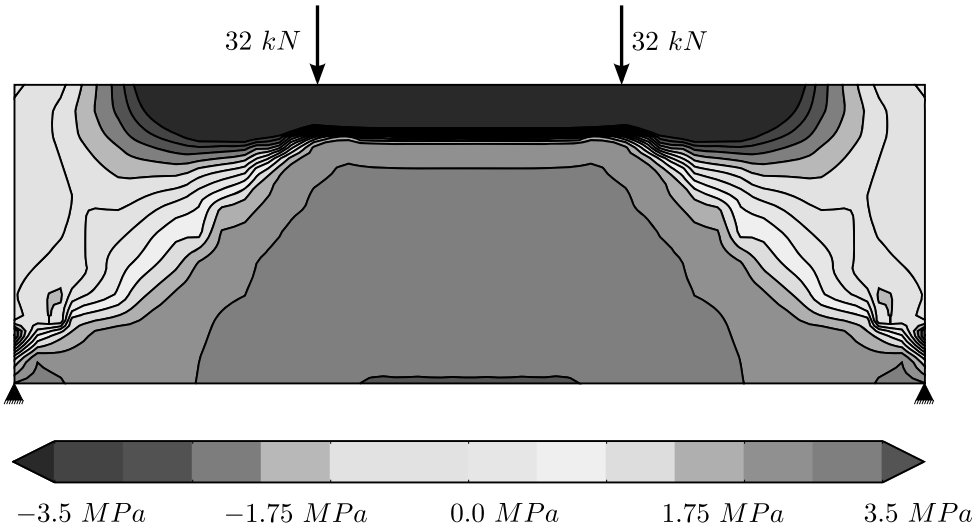

Figure 8.17: Stress in horizontal direction at a total load of 64 kN

Figure 8.18 shows the deformed beam at peak load (68 kN). The localized crack has propagated about halfway through the tension zone but it is still able to transmit a significant amount of stresses due to the fibers that bridge the crack (cohesive forces).

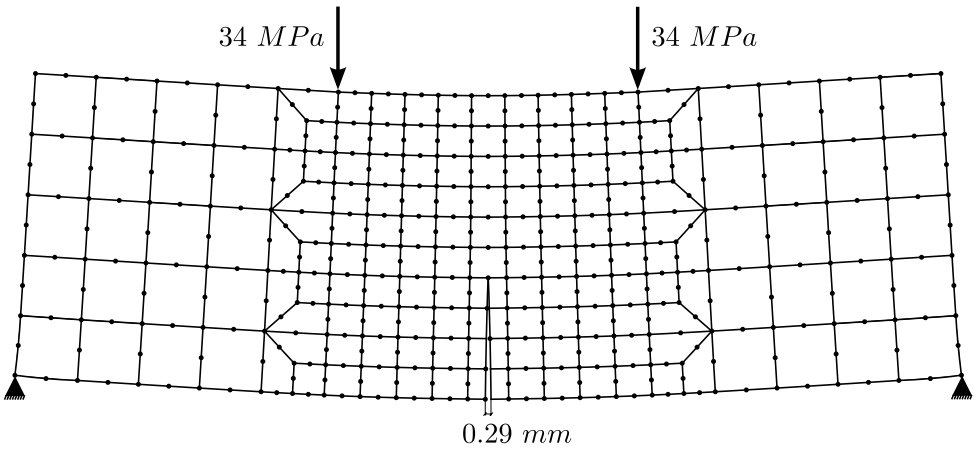

Figure 8.18: Deformation plot at a total load of 68 kN (10×)

After this point the beam starts softening. The crack quickly evolves until it crosses the entire tension zone as can be seen in Figure 8.19.

The stress field at this stage reveals that the crack has undergone significant unloading as can be seen in Figure 8.20. Only the tensile stress around the crack tip remains high.

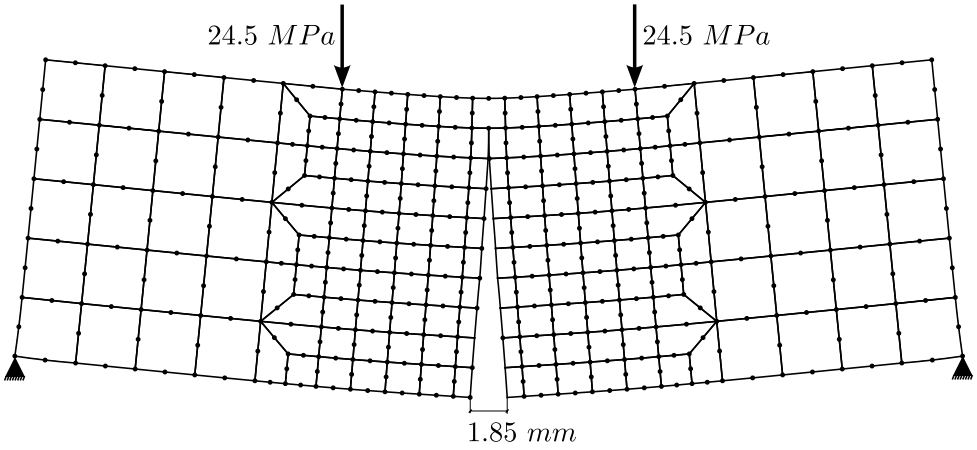

Figure 8.19: Deformation plot at a total load of 49 kN (10×)

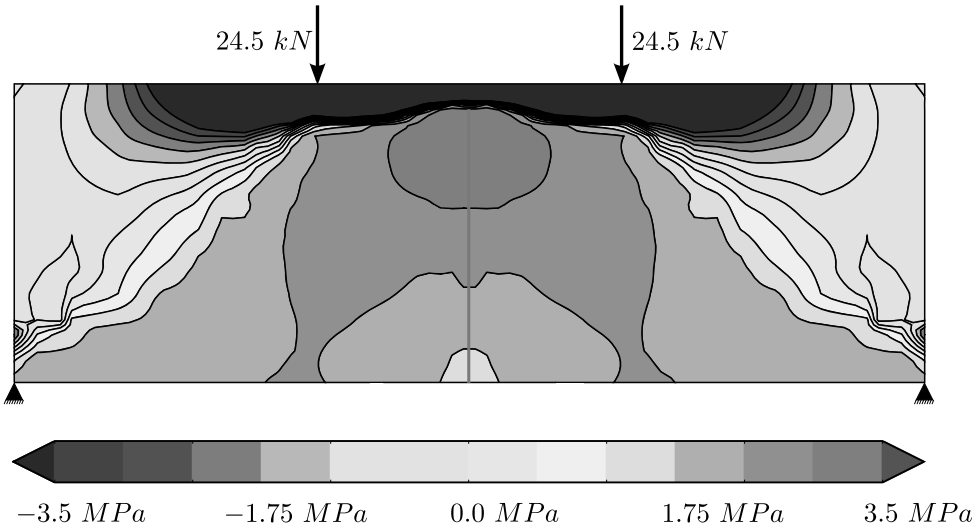

Figure 8.20: Stress in horizontal direction at a total load of 49 kN (after softening)

8.3.6 Conclusions

The numerical simulation of the presented 4-point bending test shows that the developed Finite Element model is capable of capturing the general behavior of High Performance Fiber Reinforced Cementitious Composite structures. Although some of the input parameters are only estimated very crudely the numerical results show a good agreement with the test results. Most importantly, the model is able to reproduce the different phases of behavior from the initial elastic phase through the multiple cracking phase up to crack localization and softening.

8.4 Shear Beam Test

In this final example the failure of an "Ohno shear beam" made from ECC (see Section 2.4) is simulated. The test is adopted from [Kan98] and the goal of the example is to demonstrate the full potential of the newly developed numerical model. Because the test specimen was designed to fail in shear – or more specifically in a shear failure mode called *diagonal tension* – this simulation will show the capability of the model to reproduce multiple cracking as well as crack localization in a direction that is non-orthogonal with respect to the Finite Element mesh. Furthermore, the simulation will illustrate the application of the reinforcement model presented in Chapter 7 and it will also demonstrate the use of a shear-sliding law in the context of the XFEM crack model introduced in Chapter 6. Note that the same example is also analyzed in [Kab00].

8.4.1 Test Setup

The general idea of the "Ohno shear beam" test is to set up a configuration in which the central part of a beam is subjected to a constant shear force. This is achieved by the system shown in Figure 8.21. In the tests presented in [Kan98] the loads were applied by means of a loading beam which transmitted a central actuator force to the two loading points indicated in Figure 8.21.

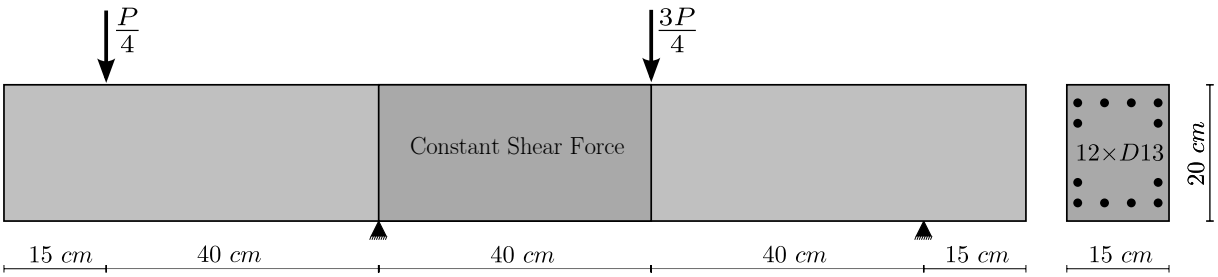

Figure 8.21: Configuration of the "Ohno shear beam" test in [Kan98]

As can be seen in Figure 8.21 the beam had a total length of 150 *cm* and a rectangular cross-section of 15 *cm* × 20 *cm*. The central region of constant shear indicated in Figure 8.21 had a length of 40 *cm* which resulted in a shear-span-to-depth-ratio of 1. In order to prevent flexural failure a longitudinal reinforcement consisting of 12 high strength steel rebars with a nominal diameter of 13 *cm* was used. However, the specimen did not include any structural shear reinforcement and the shear resistance was provided by the inherent properties of the Engineered Cementitious Composite.

8.4.2 Materials

The material which was used for the shear beam test was an Engineered Cementitious Composite with 2% Vol. Polyvinyl Alcohol fibers (PVA-ECC). The latter had a length of 12 mm and a diameter of 40 μm which results in an aspect ratio of 300. Furthermore, the fibers had an elastic modulus of 22 GPa and a shear modulus of 110 MPa.

The matrix of the composite consisted of mainly cement and fine sand as is common for ECCs. The water-to-cement ratio was 0.45 and the sand-to-cement ratio was 0.4. The matrix also included a good amount of superplasticizer and some other viscous agent. More details about the mix can be found in [Kan98].

The most important mechanical property of this Fiber Reinforced Cementitious Composite is its very pronounced strain hardening phase in direct tension which is typical for ECCs. This can be seen in Figure 8.23 which shows the results of a series of direct tension tests with this material. The compressive strength of the composite on the other hand is relatively limited due to the weak matrix (see Section 2.4.1) and it was measured to be 42 MPa. Finally, the elastic modulus of the composite was determined to be 12.8 GPa.

The reinforcement bars used in the test were made of high strength steel which had an elastic modulus of 192 GPa, a yield strength of 563 MPa and a hardening coefficient in the post yield regime of 0.01.

8.4.3 Finite Element Discretization

For the numerical simulation the discretization shown in Figure 8.22 is selected. It contains a total of 928 8-node, quadrilateral elements which corresponds to 2933 nodes and roughly 5866 degrees of freedom. The central region is discretized using a finer mesh than for the border regions. This increases the accuracy in the zone of primary interest while still limiting the overall number of nodes. Figure 8.22 also shows the discretization of the embedded reinforcement elements (dashed lines) which are implemented using the model presented in Chapter 7. Note that the location of the rebars does not impose any constraints on the Finite Element mesh. This underlines the compatibility of the reinforcement model with the general approach and particularly the XFEM.

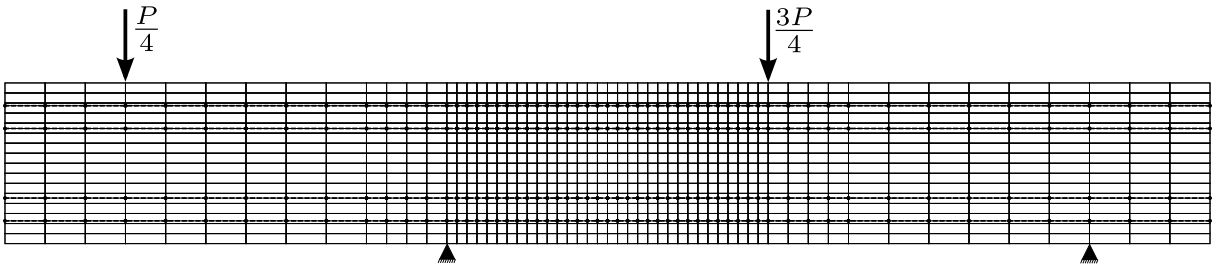

Figure 8.22: Finite Element discretization

8.4.4 Model Input Parameters

Since ECCs are High Performance Fiber Reinforced Cementitious Composites it is evident that all three proposed phases of the model (see Section 3.4.2) need to be activated. By consequence a number of input parameters for each of these phases need to be defined as is done in the following.

Elastic Model

The elastic phase is defined by the module of elasticity E and Poisson's ratio ν of the material. According to [Kan98] the elastic modulus of the composite was 12.8 GPa as already mentioned in Section 8.4.2. Furthermore, following the suggestions by [Kab00] the value of Poission's ratio is taken as 0.2 for the simulation.

Rotating Smeared Crack Model

The input parameters for the Rotating Smeared Crack Model are calibrated with the help of the direct tension tests provided in [Kan98] in analogy to the procedure presented in Section 8.3.4. This is shown in Figure 8.23. Note that there is a relatively large scatter in the direct tension test results as indicated by the different responses of the three direct tensile test specimens. In order to be on the conservative side and because the 4-point bending test suggested that direct tension tests tend to overestimate the tensile response of HPFRCCs it was decided to calibrate the numerical model with the weakest of the three specimens. The resulting input curve for the smeared crack phase is depicted in Figure 8.24b.

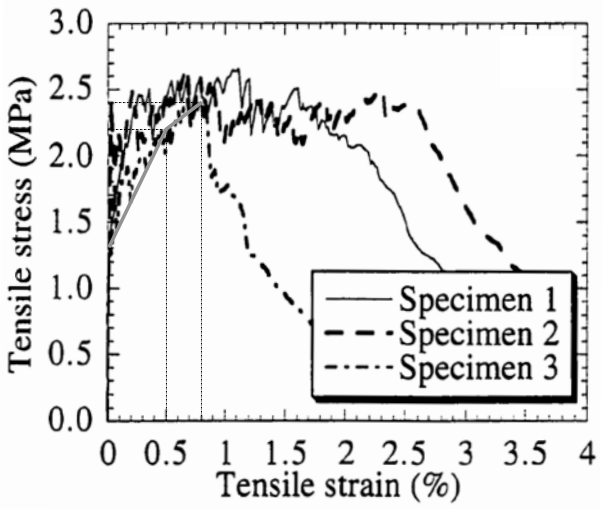

Figure 8.23: Calibration by means of a direct tension test taken from [Kan98]

The unloading model was selected based on the observation in [Kan98] that *"microcrack closure was not significant even at complete unloading"*. Therefore, the used Smeared Crack Model assumes that the cracking strain remains constant upon unloading (only the elastic strain unloads). As soon as a compressive force is applied the cracks close immediately and perfect contact is restored.

The transition from the Smeared Crack Model to the discrete XFEM model is triggered at a total strain of 0.8% which clearly marks the onset of tension softening as can be seen in Figure 8.23.

Extended Finite Element Model

Unfortunately, there is very little information available about the behavior of localized cracks in ECC. For this reason we rely heavily on the indications made in [Kab00]. The cohesive stress vs. crack opening law is assumed to be a linearly decreasing function as depicted in Figure 8.24c. The crack opening at which the crack becomes tension-free is set to 6 mm since this corresponds to the theoretical value which is predicted by the micromechanics of fiber bridging. The assumption of a linear softening law can be justified by observing the softening branches of the direct tension tests in Figure 8.23 which are also more or less linear.

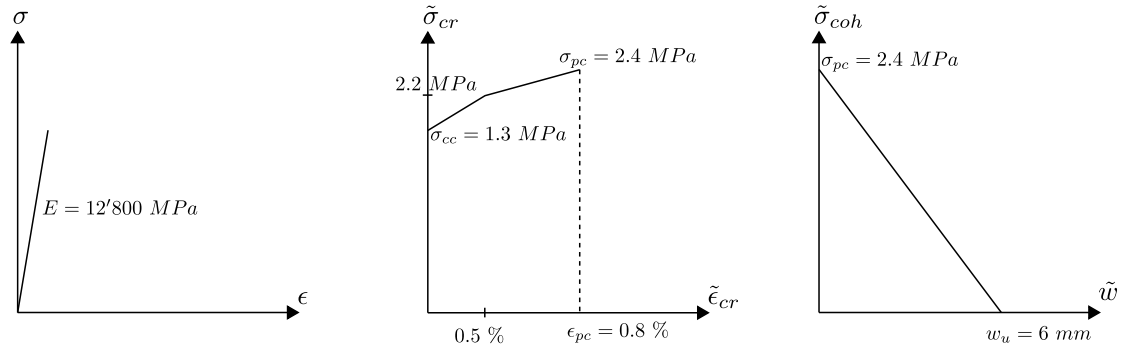

(a) Elastic (b) SMCR (c) XFEM

Figure 8.24: Input curves for the shear beam test simulation

One additional question that arises in contrast to the 4-point bending example is the definition of a shear sliding law at the localized, cohesive crack. Because there are no experimental results on this subject we have to rely on a micromechanical model. For the present example the *implicitly coupled shear law* presented in [Kab00] is used. In this context "implicitly coupled" means that the shear stress at the crack interface τ_ξ is not only a function of the shear sliding displacement w_ξ but also a function of the crack opening w_η. Following this approach the shear sliding law given in Equation (8.1) is used.

$$\tau_\xi = \begin{cases} \left(\frac{1}{2} - \frac{w_\eta}{l_{fib}}\right) \frac{V_{fib} \cdot k_{fib} \cdot G_{fib} \cdot w_\xi}{w_\eta \left[1 + \frac{4 \cdot k_{fib} \cdot G_{fib}}{3 \cdot E_{fib}} \left(\frac{w_\eta}{d_{fib}}\right)^2\right]} & w_\eta \leq \frac{l_{fib}}{2} \\ 0 & w_\eta > \frac{l_{fib}}{2} \end{cases} \tag{8.1}$$

Note that the shear stress τ_ξ is a linear function of the crack sliding displacement w_ξ. However, the former decreases exponentially with increasing crack opening w_η. The other parameters in Equation (8.1) all depend on the characteristics of the used PVA-fibers which were given in Section 8.4.2. These are the fiber volume fraction V_{fib} which is 2% $Vol.$, the fiber length l_{fib} which is 12 mm and the fiber diameter d_{fib} which is 40 μm. The parameters E_{fib} and G_{fib} denote the modulus of elasticity and the shear modulus of the fibers which are 22 GPa and 110 MPa respectively. Finally, the parameter k_{fib} is a cross-section correction factor and it is taken as 0.9 in accordance with [Kab00].

Embedded Rebar Model

For the embedded reinforcement bars the elasto-plastic material law presented in Section 7.2.2 and depicted in Figure 7.3 is adopted without modification. The parameters that are selected to represent the high strength steel reinforcement bars in the simulation are 192 GPa for the elastic modulus, 563 MPa for the yield strength and 0.01 for the hardening coefficient. This is in perfect agreement with the indications made in [Kan98].

8.4.5 Results

In the following the results of the "Ohno" shear beam test simulation are presented. The main focus will lie on a qualitative discussion of the observed behavior. Never the less, the results clearly show that the mechanics of the numerical model work correctly.

Multiple Cracking

The first observation that can be made is that the strain-hardening nature of the ECC clearly leads to multiple cracking of the test specimen. This is illustrated in Figure 8.25 which shows the evolution of the cracked zone.

Cracking of the specimen is initiated in form of flexural cracks at midspan as well as over the left support. However, the longitudinal reinforcement in those regions prevents the flexural cracks from localizing as was the case in the example presented in Section 8.3. The reason for this is that once the ECC starts cracking the additional internal loads are mostly carried by the reinforcement because the latter is much stiffer than the cracked composite (as long as the rebars have not yielded). This behavior is of course to be expected as the longitudinal reinforcement was selected with exactly this goal in mind. In fact, the

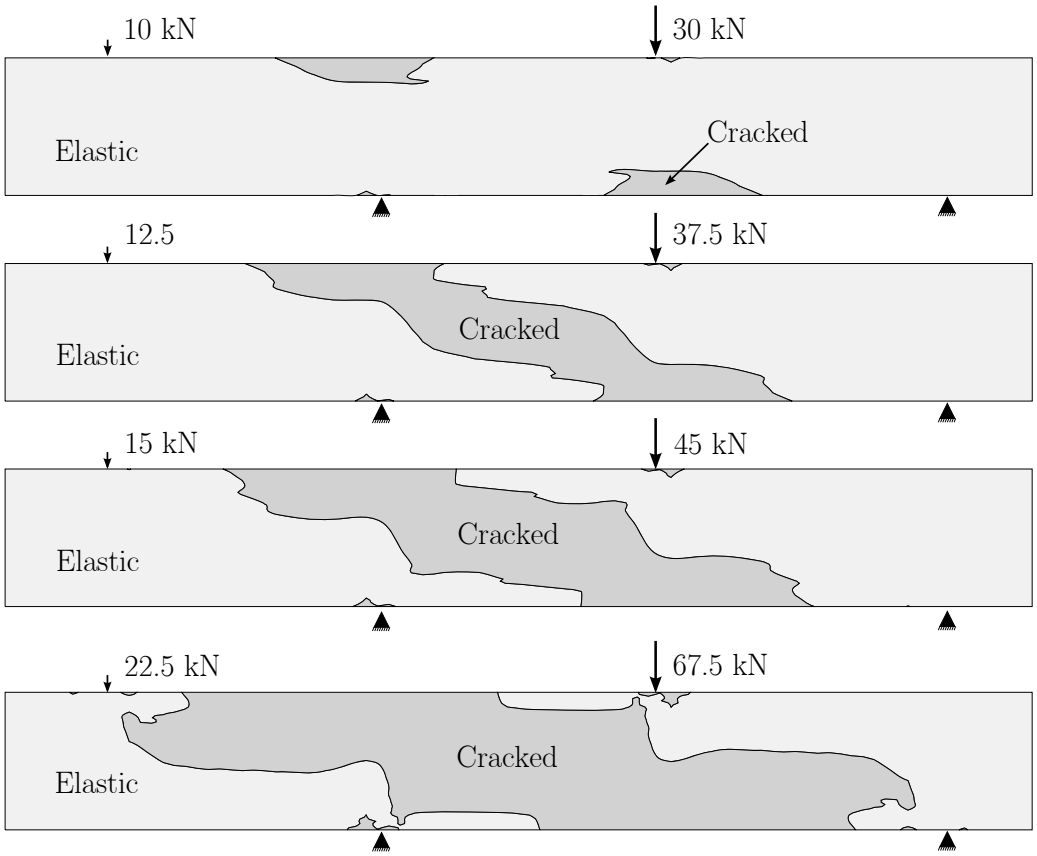

Figure 8.25: Evolution of the multiple cracking zone

longitudinal rebars remain elastic during the entire simulation and by consequence they prevent flexural failure. This is also in agreement with the experimental observations published in [Kan98].

Following the initial flexural cracks a number of fine and evenly distributed shear cracks gradually start forming predominantly in the central part of the beam as shown in Figure 8.25. This behavior is a direct consequence of the multiple-cracking nature of ECC which does not only manifest in direct tension tests but also causes a nice crack distribution in the present case of diagonal shear tension.

Strain Localization

After a certain point the multiple cracks cease to spread any further and the behavior of the flexurally and the shear dominated regions becomes distinctly different. In those regions where the cracks are of primarily flexural nature and where steel reinforcement is present the cracks begin to stabilize. The central region, on the other hand, which is mainly dominated by shear cracks is starting to experience an accumulation of strain. The latter is caused by a gradual opening of the multiple cracks and it eventually leads to

strain localization in the central region as shown in Figure 8.26. The same behavior can also be observed experimentally as can be seen in Figure 8.29a. Note however, that the photo contains a second set of multiple cracks in the opposite diagonal direction. This can be explained by the fact that a cyclic test was used in the experiment and, therefore, the second set of cracks is created by the inverse loading cycle.

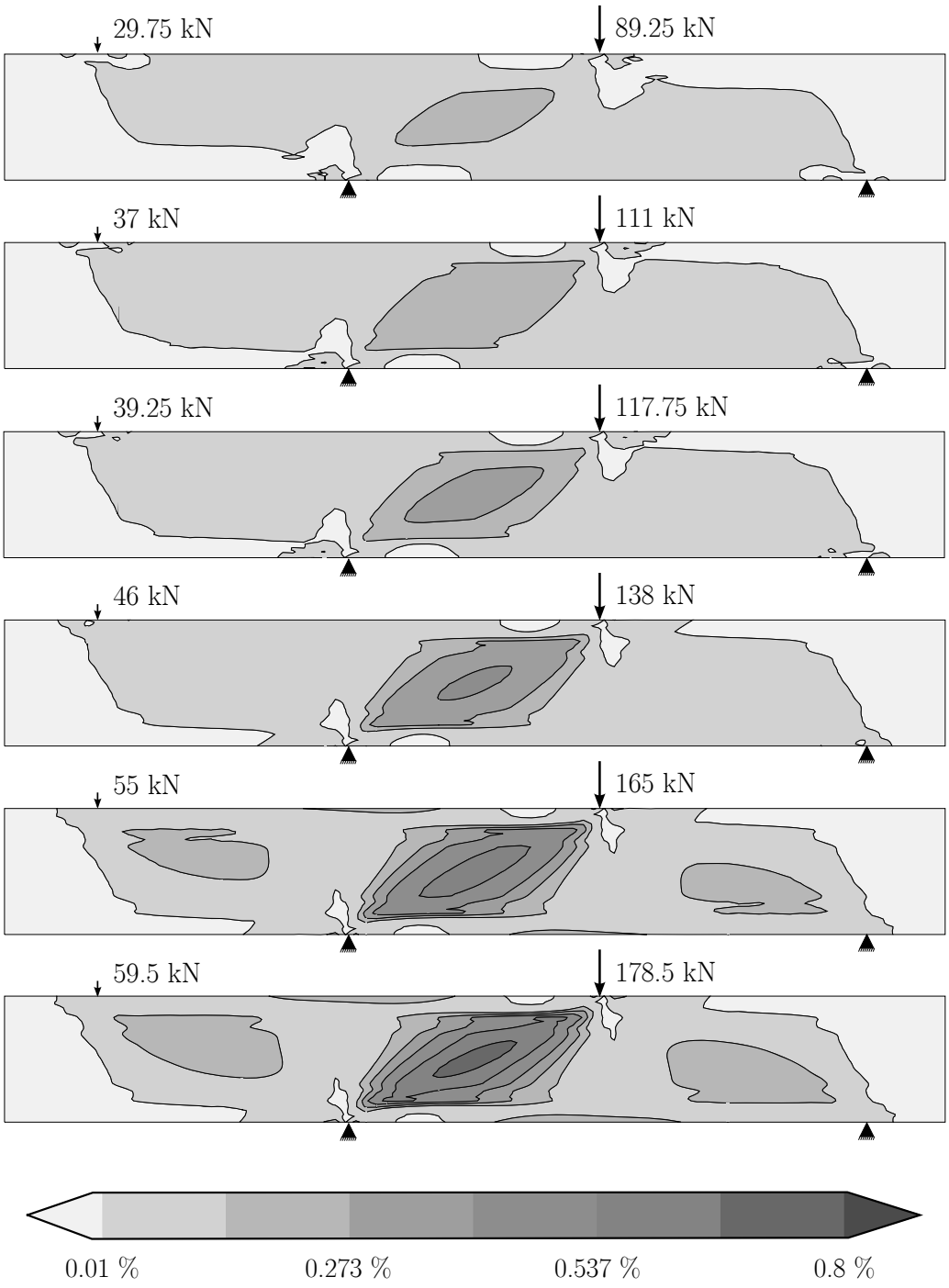

Figure 8.26: Strain localization in the shear dominated region (principal strain contours)

Discrete Cracking

Once the principal strain in the simulation reaches 0.8% the formation of a discrete crack is triggered. The principal strain contours at that stage are given in Figure 8.27. It can be clearly seen in Figure 8.27, that a discrete crack nucleates at the center of the beam as governed by the crack nucleation criterion given in Section 6.4.3. Because the formation of a shear tension crack is a relatively brittle process the localization takes place very quickly and the crack crosses the central region almost instantly.

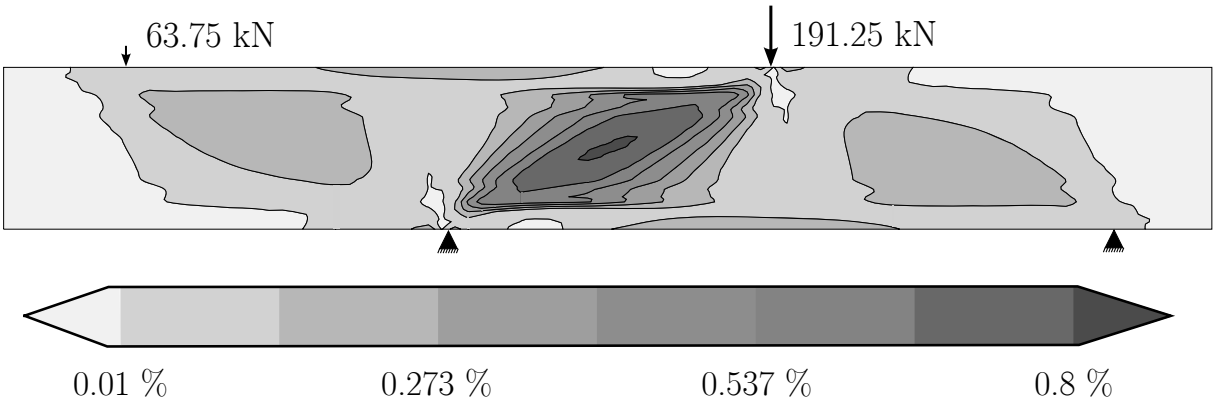

Figure 8.27: Principal strain contours at initiation of a localized crack

Figure 8.28 shows the deformed shape of the shear beam after the discrete crack has localized and propagated to the upper and lower reinforcement layers. In the numerical simulation the discrete crack forms in the diagonal between the left support and the right load at an angle of about 23°. This is in excellent agreement with the experimental observations as shown in Figure 8.29a.

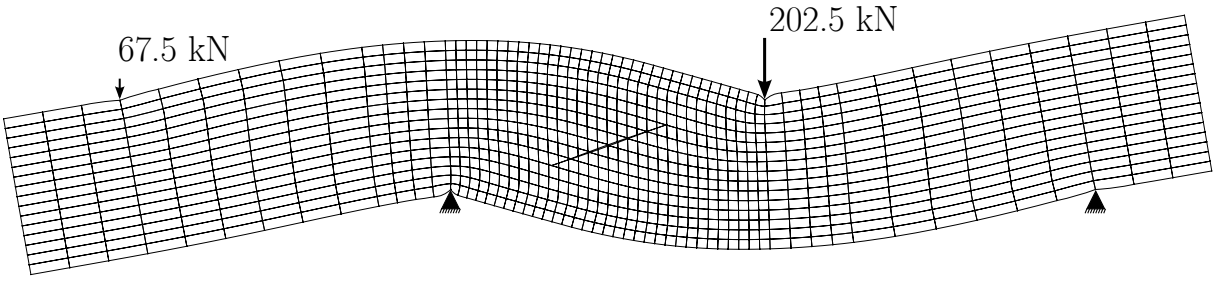

Figure 8.28: Deformation after crack localization (×40)

A closeup of the localized shear crack is shown in Figure 8.29b. Note that the deformation plot is amplified by a factor of 60 in order to visualize the crack opening profile. The latter shows the typical cusp-shaped opening of a cohesive crack which is relatively large at the center and diminishes gradually towards the crack tips. A very close observation of the crack also reveals a slight shear sliding between the crack surfaces. The latter is more significant at the center of the crack as prescribed by the shear sliding law given in Equation (8.1).

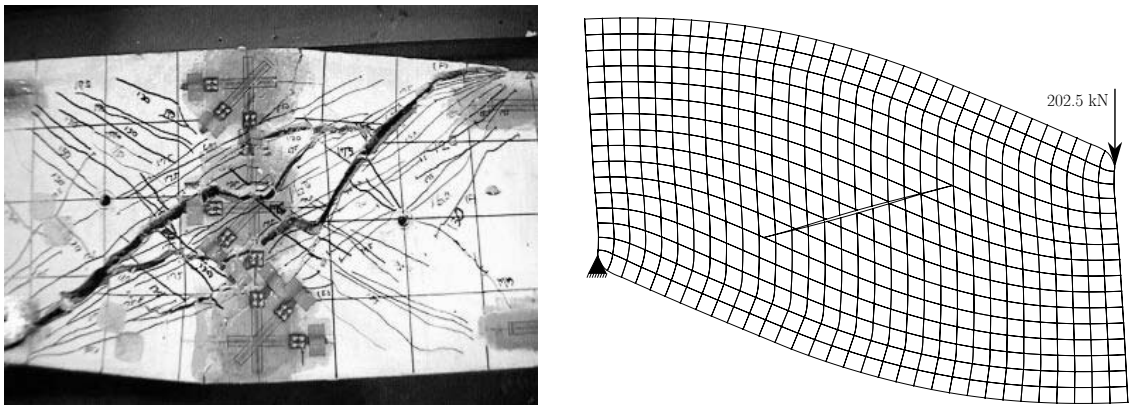

(a) Photo of the cracked test specimen (taken from [Kab00] but original by [Kan98])

(b) Localized shear crack (×60)

Figure 8.29: Comparison of the cracking pattern

Although the preceding sections clearly demonstrate the great potential of the developed numerical model the present example also presents some challenges which could not be completely overcome. These will be discussed in the following Section 8.4.6.

8.4.6 Conclusions

This last example with an "Ohno shear beam" clearly shows that the mechanics of the developed numerical model function properly. The simulation does not only prove that the multiple cracking and the crack localization phases of the model work correctly, even when the cracking does not take place in a direction orthogonal to the Finite Element mesh, but the embedded reinforcement model also performed very well in combination with the proposed material model for HPFRCCs. Furthermore, the example also demonstrates the successful use of an implicitly coupled shear sliding law.

The major issue that was encountered during this simulation is the fact that the current model is not capable of capturing the interaction between discrete, localized cracks and embedded reinforcement bars (see Section 7.1). For this reason the simulation cannot be continued up to complete shear failure of the specimen. Although at first glance the intersection of the discrete crack and the reinforcement bars seems to be a small problem this is definitely not the case. Simply smearing the crack opening over the length of the intersected reinforcement element is incorrect as this would induce an arbitrary mesh dependence which the proposed model intends to prevent in the first place. The best way to explain the difficulty is the following: If the discrete crack were to cross a reinforcement bar without any specific dispositions this would lead to an immediate plastification and complete rupture of the rebar at the location of the intersection. In reality this does of course not take place and the discrete crack causes some additional strains and possibly some plastification of the reinforcement, not only in one section but along a small segment of the rebar in the immediate vicinity of the crack. This type of

strain penetration and its extent are primarily governed by the local bond between the reinforcement and the High Performance Fiber Reinforced Cementitious Composite and a crack–rebar interaction model would have to account for this mechanism. Unfortunately, such a model is beyond the scope of this thesis, however, some further research in this direction would certainly be invaluable.

Another recurring problem is the issue of choosing suitable input curves for the hardening and the softening model which could not be solved here to complete satisfaction. There is definitely more research needed in that direction as well.

Chapter 9

Summary and Conclusions

9.1 Summary

High Performance Fiber Reinforced Cementitious Composites (HPFRCCs) are a relatively new and innovative class of Fiber Reinforced Cementitious Composites which have been developed mainly in the last decade. As we have seen in Chapter 2 they exhibit excellent mechanical properties which make them a reasonable alternative to traditional reinforced concrete for a number of structural applications. The most prominent and also characteristic feature of HPFRCCs is their strain-hardening behavior in direct tension. Although there are many different kinds of HPFRCCs all of them are based on two fundamental concepts.

The first one is that *different fiber sizes fulfill different functions*. Short fibers (i.e. 6 mm) are effective at arresting microcrack propagation and they therefore increase the tensile strength of the composite. In order to do so, they have to be added in large quantities since there is also a large number of microcracks. Long fibers (i.e. 30 mm – 60 mm) on the other hand can only be used in smaller volume fractions due to workability considerations and their numbers are not sufficient to prevent microcrack propagation. However, their advantage is that they are able to bridge macroscopic cracks even at large crack openings and they thereby increase the ductility of the composite. Of course the optimal solution from a mechanical point of view is to combine different fiber lengths in one HPFRCC. This increases both its tensile strength and its ductility and even exploits some synergetic effects (see Section 2.8).

The second core concept of High Performance Fiber Reinforced Cementitious Composites is that *dense particle packing and matrix homogeneity lead to a higher compressive strength*. This principle is exploited by using primarily small aggregates and adding a significant amount of fine fillers like silica fume and fly-ash to the cementitious matrix. Together with low water-to-binder ratios which can be obtained with the help of superplasticizers this results in a new class of Fiber Reinforced Cementitious Composites called

Ultra High Performance Fiber Reinforced Cementitious Composites. Although the dense particle packing primarily influences the compressive strength of a composite there is also a direct interaction with the fiber reinforcement. A dense, cementitious matrix provides better anchorage for the fibers which in turn improves their effectiveness. In most cases the matrix strength and its density have to be tailored carefully in order to get the desired interaction with the fibers. In some cases this can be a very dense matrix in order to improve the fibers' effectiveness in increasing the tensile strength of the composite (see Section 2.8) and in other cases this can be an extremely weak matrix which results in multiple cracking and a large ductility (see Section 2.4).

As already mentioned, the distinguishing feature of High Performance Fiber Reinforced Cementitious Composites is that they are strain-hardening in direct tension. Because this behavior is not exhibited by traditional concrete the currently existing numerical models are mostly inadequate for the simulation of HPFRCC structural elements. Furthermore, the fibers in HPFRCCs also lead to a more ductile softening behavior. And since many applications of HPFRCCs (such as those in earthquake engineering for example) exploit this ductility it is important to capture the softening part of the behavior as well. Having this in mind, a new Finite Element model for the structural simulation of HPFRCC elements was developed during this thesis. In Chapter 3 a number of possible candidate models were analyzed in respect to their suitability for a HPFRCC model. It turns out, that both the continuum model approach and the Discrete Crack Model approach on their own are not capable of modeling the complete behavior of HPFRCCs. While continuum models are well suited for the strain-hardening and multiple cracking phase they exhibit a number of problems such as mesh-sensitivity, mesh-bias and stress-locking during the strain-softening phase of the behavior. Discrete Crack Models on the other hand are well suited for the crack localization and softening phase but they cannot capture multiple cracking. Furthermore, the traditional discrete crack approach is bound to the Finite Element mesh and arbitrary crack growth requires elaborate remeshing techniques. In the framework of this thesis it was therefore decided to *combine a Smeared Crack Model with a Discrete Crack Model* in order to fully represent all behavioral aspects of HPFRCC elements. More specifically, a Rotating Crack Model was used for the strain-hardening phase of the material and a Discrete Crack Model based on the eXtended Finite Element Method (XFEM) was used for the crack localization and strain-softening phase. Especially the use of the new and innovative eXtended Finite Element Method is what distinguishes the herein presented approach from other existing models. Using the XFEM entails the significant advantage that crack localization can take place independently of the Finite Element mesh and a "true" separation of cracked structural elements with no numerical artifices can be achieved.

The numerical model itself is separated into three different phases each of which was presented in its own chapter (see Chapters 4, 5 and 6). The underlying Finite Element is a standard 8-node, quadrilateral, isoparametric element which is formulated for plane-stress conditions. This allows for a number of different structural elements (such as beams, columns, walls and beam-to-column connections) to be modeled with reasonable accuracy.

In compression and during the initial, elastic phase in tension a two-dimensional, linear, elastic Hooke law is employed.

As soon as the HPFRCC material surpasses its first cracking strength the model transitions into a *Rotating Crack Model*. Through a conscious separation of the elastic strain and the cracking-strain a clear distinction between the material law governing the elastic bulk material and the law governing the cracks is achieved. The multiple cracks are accounted for in an averaged sense by including the aforementioned cracking-strain which is computed by a nonlinear stress vs. cracking-strain law with uncoupled components. In order to achieve maximal robustness the Rotating Crack Model was implemented with an "inner" equilibrium iteration which ensures compatibility between the bulk material and the Smeared Cracks.

Once the model enters the softening regime a discrete crack is introduced by means of the *eXtended Finite Element Method*. The basic idea behind this method is to add discontinuous shape functions to the approximation space of the elements which are bisected by a discrete crack. In order to account for the crack-bridging effect of the fibers cohesive forces according to Hillerborg's Cohesive Crack Model are added to the XFEM crack model. The implementation showed that the introduction of a discrete crack with the help of the XFEM is a very "clean" and straightforward solution. Following the Partition of Unity Principle the specific knowledge about the discontinuous character of the solution can easily be incorporated into the approximation space in form of a set of additional shape functions. The developments in Chapter 6 clearly demonstrated that once the general concept of adding enriched shape functions is accepted the rest of the Finite Element procedure can be followed without modification. The only additional deviation from the standard procedure is caused by the discontinuous character of the interpolation field which requires an adaptation of the numerical integration scheme. The big difference between the XFEM and other methods for discrete crack modeling (such as for example the Embedded Discontinuities Method) is that both parts of a cut element are completely dissociated. Furthermore, inter-element continuity of the crack is guaranteed by virtue of the shared extended degrees of freedom. Possible cohesive forces are accounted for by an additional stiffness matrix contribution which is computed by integrating the virtual work along the crack surface.

During the implementation it was found that a critical part of the model is the *transition from the Rotating Crack Model to the eXtended Finite Element model*. It is governed by a set of crack propagation rules that define under which circumstances a crack propagates. In the presented model the crack propagation criterion is based on a nonlocal average of the maximum principal strain in the vicinity of the crack tip. Another key issue of the transition process that had to be solved is the transfer of the material history variables between integration points (caused by a change of the integration scheme). For this purpose a new material state transfer method called *integration point splitting* was developed. As its name suggests, the basic idea behind this method is to replace an integration point by a number of subpoints which represent the same integration domain but respect the geometry of the discontinuity. By doing so, the material state can be

transfered one-to-one without unbalancing the element equilibrium which is very beneficial to the overall robustness and consistency of the solution procedure.

Although HPFRCCs have improved tensile properties which can reduce the need for secondary reinforcement such as shear or confinement reinforcement the fibers typically cannot replace the longitudinal rebars. For this reason the numerical model was supplemented by a rebar model (see Chapter 7). In order to conserve the mesh-independent character of the procedure an *Embedded Rebar Model* was used. Looking closely at the implementation it becomes clear that this kind of model is very similar to the cohesive crack extension of the XFEM model. The virtual work performed by the embedded reinforcement bars is integrated analogously to the cohesive crack contribution. The final result is an additional stiffness matrix term for each rebar segment within a reinforced Finite Element.

In order to test the proposed model a special purpose Finite Element program was written in the programming language Python. A conscious effort was made to obtain a program which is easily extensible and modifiable by other researchers. This was achieved by following the modular design philosophy offered by the *Object-Oriented Programming paradigm*. In short, the model is split into a number of objects which all interact with one another. Every one of these objects represents a piece of the model such as for example a node, a degree of freedom, a rebar, a Finite Element or a crack. Of course the same principle can also be applied to each of the aforementioned objects and a Finite Element object for instance can be decomposed into a number of shape function objects, integration point objects and so forth. Future researchers can take full advantage of this setup by simply modifying or replacing the components they seek to improve without having to worry about the other components or risking to break existing code.

The thesis is concluded by applying the newly developed numerical model to a number of tests and then comparing the results with the corresponding experimental observations. The first example that was analyzed is a *wedge splitting test* of an Ultra High Strength Concrete. The primary goal of this first application was to focus on the crack localization phase of the model which explains why an Ultra High Strength Concrete test instead of a High Performance Fiber Reinforced Concrete test was used. The computational results showed an excellent agreement with the test results and demonstrated that the crack propagation and localization feature of the model works correctly. This first example was then followed up by a second one in which the full capabilities of the HPFRCC model could be tested. It consisted of a *4-point bending test* of an HPFRCC beam. The results illustrated that the model performed well and that the different phases of HPFRCC behavior are all represented correctly by the proposed model. Finally, the model was applied to an ECC *Ohno shear beam test* in order to verify the validity of the embedded rebar model and also to test the implementation of an implicitly coupled shear sliding law for localized cracks. The performance of the model also proved to be very satisfactory in this shear dominated setup and the multiple cracking as well as the crack localization mechanism were captured correctly.

All these observations lead to the following conclusions which are expressed in Section 9.2.

9.2 Conclusions

It is the author's strong belief that High Performance Fiber Reinforced Cementitious Composites will revolutionize the civil engineering practice in the near future. Especially in industrialized countries where labor costs are high in comparison to those of the construction materials HPFRCC structural elements are a cost-effective alternative to traditional structural elements in numerous cases. A vast majority of the experimental work cited in Chapter 2 clearly demonstrates that fibers can increase the tensile strength of a composite to the point where additional shear reinforcement becomes dispensable. Even more importantly, the right mix of fibers and a specifically tailored cementitious matrix can result in a strain-hardening behavior which turns a traditionally brittle material into a highly ductile one. By consequence a lot of time consuming and intricate reinforcement detailing can be saved as it is being taken care of by the intrinsic properties of HPFRCCs.

In spite of all these facts, HPFRCCs have not yet found their way into engineering practice. One of the main reasons for this is the lack of realistic and accurate numerical models which would allow planing engineers to incorporate HPFRCC structural elements into their design. This thesis should be seen as a first step towards overcoming this obstacle. The work and the sophisticated model presented herein provide a framework for the simulation of HPFRCC structural members.

The most outstanding feature of the proposed model is its *clear distinction between the behavioral phases of HPFRCCs* (strain-hardening, crack localization) which makes it more realistic and closely mirrors the properties of this class of materials. The input parameters all have a physical meaning and they can be determined by relatively simple material tests. Nevertheless, the model is extremely flexible both in terms of the geometry of the represented structural elements and in terms of the material laws that can be employed.

In respect to the numerical aspects of the proposed model it can be concluded that the latter is very stable, theoretically sound and shows no instabilities or inconsistencies. There is no need for "artificial", numerical parameters and the model is neither mesh-sensitive nor does it exhibit stress-locking, mesh-bias or any other kind of mesh dependency which causes many other models to fail. To a large degree this is due to the excellent performance of the eXtended Finite Element Method. In fact, the latter is an extremely useful extension of the standard Finite Element Method and it will probably see a lot more applications in the future. A related finding is that the XFEM does perform very well with the quadrilateral, higher order elements which are used in this work. To the author's knowledge this is the first time that the XFEM has been applied to non-triangular higher order elements and it is certainly the first time that it has been combined with a Smeared Crack Model.

One of the consequences of the combined Smeared Crack – eXtended Finite Element

model is that a critical transfer of the material history variables has to be performed during the transition between the aforementioned two phases. In this thesis it is shown that the innovative *integration point splitting technique* which was developed precisely for this purpose proves to be a simple and stable solution. The main benefit of this procedure is that the material state transfer does not unbalance the elements which is especially important during the transition phase because convergence of the global solution algorithm is inherently delicate at that time.

From the examples presented in Chapter 8 it can be concluded that the developed numerical model is capable of simulating the response of HPFRCC elements. All results are in good agreement with the experimental measurements and the *different phases of behavior are captured very well*. The wedge splitting test for example demonstrates that the model allows for a complete separation of the material with an arbitrary crack path. Furthermore, the 4-point bending test example nicely shows the different influences of the strain-hardening phase and the tension-softening phase of HPFRCC behavior. It also demonstrates how the material input curves can be calibrated with the help of a direct tension test and that the results are reasonable even with very crude estimates of some of the input parameters. However, this also points out one of the areas in which more research is needed. Although the developed model is very general and sets up a generic framework for how HPFRCCs can be treated it requires accurate knowledge about the stress vs. cracking-strain relationship and the traction–separation law of a specific material (see Section 9.3). Finally, the shear beam test illustrates that the embedded rebar model works well in combination with the proposed HPFRCC model and it also demonstrates that the model is not limited to flexural applications. The example proves that the multiple cracking and the crack localization mechanisms are truly mesh-independent and that cracking can be captured correctly even when it occurs in a direction that is non-orthogonal with respect to the Finite Element mesh. However, it also turned out that the model can still be improved by developing a method for the treatment of intersections between embedded rebars and discrete cracks (see Section 9.3).

A final couple of findings are related to the implementation of the numerical model. As already mentioned, the model was coded in the programming language Python. It turns out, that the latter is very well suited for scientific purposes. The syntax is intuitive and the fact that the language is not type-safe makes coding much faster and more flexible. Another significant advantage is that Python comes with a large library of preexisting tools and some additional libraries such as one for scientific computation (*SciPy*) or one for plotting (*Matplotlib*) are readily available. Furthermore, Python's full support of the Object-Oriented Programming (OOP) paradigm gives it an advantage over other commonly used scientific programming environments such as *MatLab*. In fact, using Object-Oriented Programming proved invaluable during the development process as it allowed for easy modification or exchange of certain parts of the program without having to worry about breaking the rest of the code. This also holds true for further improvements of the code as some researchers might want to base their future work on it. On a final note the author would like to recommend that researchers which are planning

to write scientific software learn about Object-Oriented Programming and also about Object-Oriented Software Design since OOP goes way beyond the paradigmatic concepts like *encapsulation* or *inheritance* and "good" Object-Oriented Programming involves a lot of important design decisions.

9.3 Outlook

The work presented in this thesis introduces a general framework for the simulation of HPFRCC structural elements. Although the resulting numerical model is theoretically sound and solves many issues there is of course always room for improvement. In the following a few possible topics for further research are suggested. They are ordered in sequence of their perceived importance beginning with the most important.

- One of the biggest difficulties with the current model is an *accurate estimation of the material input curves*. These are the stress vs. cracking-strain law and the traction–separation law. Although the former can be determined from a direct tension test the 4-point bending beam example in Section 8.3 indicated that this procedure tends to overestimate the strength of the material. In Section 8.3 it was suspected that the most likely reason for this is a preferential alignment of the fibers in the longitudinal direction of a direct tension test specimen. Another possible explanation could be that this is some kind of size effect which is caused by the fact that there is a higher probability of a "weak" cross-section in a larger specimen. However, these are just speculations and more research in this direction is needed.
  The same is true for the traction–separation law but the problem is even more pronounced. The traction–separation law which was used in the 4-point bending beam example (see Section 8.3) had to be estimated very crudely because no experimental data on this subject was available. For this reason an important research topic for further work is the investigation of the stress transfer mechanisms of a macroscopic crack in High Performance Fiber Reinforced Cementitious Composites. Such an investigation should be both experimental and theoretical and a possible goal could be to come up with a micromechanical model which links the matrix and the fiber characteristics of an arbitrary HPFRCC to its cohesive traction–separation law. Some attempts in this direction have been made in [Kab04, Kab07] but more research is needed.

- A second key improvement would be to implement an interaction model between discrete cracks and embedded reinforcement bars. As we have seen in Section 8.4.6 this would enable the simulation of the shear beam example from Section 8.4 up to complete failure. Such an extension would have to be capable of reproducing the strain penetration at the location of the discrete cracks and it probably should account for the bond behavior between HPFRCCs and embedded rebars.

- As we have seen in Chapter 2 High Performance Fiber Reinforced Cementitious

Composites are well suited for a number of seismic applications. However, the proposed numerical model is only partially useful for simulating the response of structural elements subjected to earthquake loading as it does currently not consider cyclic effects. From a theoretical standpoint the proposed model is fully capable of computing the cyclic response of structures. The only additional requirement is that a cyclic material law for all three phases of the model is implemented. This is not a major challenge since the general framework can be used without modification. For this reason a direction of further research could be to extend the material models in order to *include cyclic stiffness and strength degradation*. This also includes the material law for the reinforcement which would have to be replaced by a more sophisticated one such as the model by Ramberg–Osgood [RO43] or the model by Menegotto–Pinto [MP73].

- Another very interesting extension of the proposed model would be to implement it in a *three-dimensional solid element*. In principle the used methods (SMCR and XFEM) can easily be extended to 3D. The corresponding publications for the individual models are readily available and from the current point of view all procedures that were used to make the transition between the two models could also be extended to 3D. The greatest challenge of such an undertaking would probably be handling the computational geometry involved with the description of the crack surfaces. One possible way to go could be to use *Level Sets* as was done in [MGB02, GMB02, SCM03].

- One aspect which has been neglected in this thesis is the compressive behavior of High Performance Fiber Reinforced Cementitious Composites. Although tensile cracking is the most common cause of failure of HPFRCC elements there are still some rare cases where compressive crushing may occur. For this reason it would be interesting to extend the current model to capture nonlinear compressive failure or even more interestingly biaxial compression–tension failure. This could be done by combining the model presented herein with the one proposed in [Sir09]. Such an undertaking should not present to many difficulties because of the clear separation between the strain components. It should suffice to add a plastic strain component to the already present elastic and cracking-strain components (see [Rot88]).

- A further minor improvement that could be made is to allow for crack tips to be located inside of elements. We recall, that in the current model crack tips can only lie on element edges which forces the cracks to grow step-by-step. This can result in small "sawtooth-like" spikes in the response as was discussed in Section 8.2. In order to obtain a more continuous crack growth an additional *crack tip enrichment* along the lines of [MDB99] or [DMB00] could be introduced. In combination with this one would also have to refine the crack growth criterion. A possibility could be to only let the crack propagate through the representative domain of those integration points that have exceeded the localization strain instead of trough an entire element (see Section 6.4.2). One would possibly also have to adapt the numerical solution scheme and an imaginable option might be to modify the currently used arc-length

method to consider the crack length increment as the control parameter.

- A final proposition for improvement is not related to research but rather oriented towards the usability of the proposed model. Before the latter can be used in engineering practice it will have to be supplemented by a *graphical user interface* (GUI) which helps to input the problem geometry. Such a GUI should include a set of powerful mesh generation tools which allow automatic mesh generation and mesh refinement. On a related note the program code would also have to be optimized in respect to computational speed. This could include recoding the time critical methods in *C++* or *Fortran* and optimizing the solution algorithm for multicore-processing.

Notation

Lower Case Roman Symbols

a_i	Standard nodal unknown associated with node i
b_{ij}	Enriched nodal unknown associated with node i and enrichment j
d_{fib}	Fiber diameter
$\underline{\mathbf{d}}_e$	Finite Element displacement vector (nodal degrees of freedom)
$\underline{\mathbf{d}}_{std,i}$	Vector of nodal degrees of freedom of node i for a standard node
$\underline{\mathbf{d}}_{enr,i}$	Vector of nodal degrees of freedom of node i for an enriched node
e_i	Enriched nodal displacement degree of freedom associated with node i
f_y	Yield strength of the reinforcement steel
$\underline{\mathbf{f}}$	Vector of Finite Element surface forces
h	Numerical localization bandwidth
i	Primary index
j	Secondary index
k	Softening law factor in the Smeared Crack Model
k_{fib}	Fiber cross-section correction factor
l	Length
l_{fib}	Length of a fiber
l_c	Characteristic length of an element
m	Number of enrichment functions
n	Number of shape functions
$n_{\eta,x}$	X-component of the unit vector $\underline{\mathbf{n}}_\eta$ (projection onto the x-axis)
$n_{\eta,y}$	Y-component of the unit vector $\underline{\mathbf{n}}_\eta$ (projection onto the y-axis)
$n_{\xi,x}$	X-component of the unit vector $\underline{\mathbf{n}}_\xi$ (projection onto the x-axis)
$n_{\xi,y}$	Y-component of the unit vector $\underline{\mathbf{n}}_\xi$ (projection onto the y-axis)
$\underline{\mathbf{n}}_\eta$	Unit vector in the direction normal to the 2$^{\text{nd}}$ crack set
$\underline{\mathbf{n}}_\xi$	Unit vector in the direction normal to the 1$^{\text{st}}$ crack set
r	Horizontal natural coordinate of a Finite Element / Radius
r_{gp}	Horizontal natural coordinate of a Gauss integration point
r_w	Horizontal natural coordinate of a point on a discontinuity

$r_{\triangle}$	Horizontal coordinate in a triangular, natural domain
$r_{\triangle,gp}$	Horizontal coordinate of a Gauss point in a triangular, natural domain
$r_{\square}$	Horizontal coordinate in a rectangular, natural domain
$r_{\square,gp}$	Horizontal coordinate of a Gauss point in a rectangular, natural domain
$r_{\rightarrowtail}$	Natural coordinate in a line segment $[-1,1]$
s	Vertical natural coordinate of a Finite Element
s_{gp}	Vertical natural coordinate of a Gauss integration point
s_w	Vertical natural coordinate of a point on a discontinuity
$s_{\triangle}$	Vertical coordinate in a triangular, natural domain
$s_{\triangle,gp}$	Vertical coordinate of a Gauss point in a triangular, natural domain
$s_{\square}$	Vertical coordinate in a rectangular, natural domain
$s_{\square,gp}$	Vertical coordinate of a Gauss point in a rectangular, natural domain
t	Thickness
u	Displacement component in x-direction
u^+	Displacement on the right face of a crack (positive domain)
u^-	Displacement on the left face of a crack (negative domain)
u_i	Nodal displacement in x-direction associated with node i
$u_{enr,i}$	Enriched nodal displacement degree of freedom of node i in x-direction
$\underline{\mathbf{u}}$	Displacement vector
$\underline{\mathbf{u}}^+$	Displacement vector on the right face of a crack (positive domain)
$\underline{\mathbf{u}}^-$	Displacement vector on the left face of a crack (negative domain)
v	Displacement component in y-direction
v_i	Nodal displacement in y-direction associated with node i
$v_{enr,i}$	Enriched nodal displacement degree of freedom of node i in y-direction
w	Crack opening displacement
$\widetilde{w}$	Crack opening displacement (in crack coord. sys.)
w_u	Crack opening at which a crack becomes stress free
w_η	Crack opening component (in crack coord. sys.)
w_ξ	Crack sliding component (in crack coord. sys.)
$\underline{\mathbf{w}}$	Crack opening displacement vector (separation vector)
$\underline{\widetilde{\mathbf{w}}}$	Crack opening displacement vector (in crack coord. sys.)
$\underline{\mathbf{w}}^{eq}$	Crack opening displacement vector at the last global equilibrium
x	Cartesian coordinate in horizontal direction
$\widetilde{x}$	Cartesian x-coordinate in the local system associated with a crack
$x_{\triangle,i}$	Cartesian x-coordinate of the i$^{\text{th}}$ vertex of a subtriangle
x_i	Horizontal Cartesian coordinate of the i$^{\text{th}}$ node
x_w	X-coordinate of a location on a discontinuity (crack)
$\underline{\mathbf{x}}$	Vector of Cartesian coordinates
$\underline{\mathbf{x}}_i$	Vector of Cartesian nodal coordinates of the i$^{\text{th}}$ node

y	Cartesian coordinate in vertical direction
$\widetilde{y}$	Cartesian y-coordinate in the local system associated with a crack
$y_{\triangle,i}$	Cartesian y-coordinate of the i$^{\text{th}}$ vertex of a subtriangle
y_i	Vertical Cartesian coordinate of the i$^{\text{th}}$ node
y_w	Y-coordinate of a location on a discontinuity (crack)

Upper Case Roman Symbols

A	Area
A^+	Area of the positive domain
A^-	Area of the negative domain
A_{rebar}	Cross-section area of an embedded rebar
B_i	Crack tip enrichment function i
$\mathbf{B}$	Strain–displacement transformation matrix
$\mathbf{B}_{enr}$	Enriched strain–displacement transformation matrix
$\mathbf{C}_{co}$	Tangent compliance matrix for the bulk material (continuum)
$\widetilde{\mathbf{C}}_{co}$	Tangent compliance matrix for the bulk material (in crack coord. sys.)
$\widetilde{\mathbf{C}}_{cr}$	Tangent compliance matrix for a set of cracks (in crack coord. sys.)
$\widetilde{\mathbf{C}}_{smcr}$	Smeared Crack tangent compliance matrix (in crack coord. sys.)
D^I_{cr}	Mode I constitutive modulus associated with a multiple cracking law
D^I_{coh}	Mode I constitutive modulus associated with a cohesive crack law
D^{II}_{coh}	Mode II constitutive modulus associated with a cohesive crack law
$\widetilde{D}_{rebar}$	Constitutive modulus for a reinforcement bar (in rebar coord. sys.)
$\widetilde{D}_{shear}$	Shear term in the tangent constitutive matrix (in crack coord. sys.)
$\widetilde{D}_{smcr,ij}$	Term ij in the Smeared Crack constitutive matrix (in crack coord. sys.)
$\mathbf{D}$	Tangent constitutive matrix
$\mathbf{D}_{coh}$	Tangent constitutive matrix for a cohesive crack
$\widetilde{\mathbf{D}}_{coh}$	Tangent constitutive matrix for a cohesive crack (in crack coord. sys.)
$\mathbf{D}_{co}$	Tangent constitutive matrix for the bulk material (continuum)
$\widetilde{\mathbf{D}}_{cr}$	Tangent constitutive matrix for a set of cracks (in crack coord. sys.)
$\mathbf{D}_{smcr}$	Tangent constitutive matrix for a Smeared Crack material
$\widetilde{\mathbf{D}}_{smcr}$	Smeared Crack tangent constitutive matrix (in crack coord. sys.)
E	Modulus of elasticity
E^I_{cr}	Mode I softening modulus associated with a Smeared Crack law
E_{fib}	Modulus of elasticity of a fiber
$\underline{\mathbf{F}}_e$	Finite Element force vector (equivalent nodal forces)
F_{ls}	Level Set function
F_{sp}	Splitting force in a wedge splitting test
G	Elastic shear modulus
G_f	Mode I fracture energy

G_{fib}	Elastic shear modulus of a fiber
H	Heaviside enrichment function
H_I	Heaviside enrichment function for crack branch I
H_{II}	Heaviside enrichment function for crack branch II
J	"Junction" enrichment function
$\mathbf{J}$	Jacobi transformation matrix
$\mathbf{J}_{\triangle}$	Jacobi transformation matrix for a triangular, natural domain
$\mathbf{J}_{\rightarrowtail}$	Jacobi transformation matrix for a natural line segment domain
$\mathbf{K}_e$	Finite Element stiffness matrix
$\mathbf{K}_e^{std}$	Standard Finite Element stiffness matrix
$\mathbf{K}_e^{coh}$	Element stiffness matrix contribution accounting for a cohesive crack
$\mathbf{K}_e^{rebar}$	Element stiffness matrix contribution accounting for an embedded rebar
L	Length of a reinforcement bar segment in a Finite Element
N_i	Finite Element shape function associated with node i
$N_{\triangle,i}$	Linear shape function for a subtriangle (associated with node i)
$N_{\rightarrowtail,i}$	Linear shape function for a line segment (associated with node i)
$N_{enr,i}$	Enriched shape function associated with node i
$N_{enr,i}^s$	Shifted enriched shape function associated with node i
$N_{enr,i}^+$	Enriched shape function i on the right face of a crack (positive domain)
$N_{enr,i}^-$	Enriched shape function i on the left face of a crack (negative domain)
N_H	Heaviside enriched shape function
N_J	"Junction" enriched shape function
N_i^r	Shape function derivative by r (associated with node i)
N_i^s	Shape function derivative by s (associated with node i)
N_i^x	Shape function derivative by x (associated with node i)
N_i^y	Shape function derivative by y (associated with node i)
$N_{enr,i}^x$	Enriched shape function derivative by x (associated with node i)
$N_{enr,i}^y$	Enriched shape function derivative by y (associated with node i)
$\mathbf{N}$	Shape function matrix
$\mathbf{N}_{enr}$	Enriched shape function matrix
$\mathbf{N}_{coh}$	Interpolation matrix yielding the separation vector in the XFEM
$O()$	Polynomial order of a function
$\underline{\mathbf{P}}_e$	Vector of external element nodal forces
R	Ramp enrichment function
$\underline{\mathbf{R}}_e$	Vector of element reaction forces
$\mathbf{R}$	Coordinate system rotation matrix (local to global)
$\mathbf{R}_\epsilon$	Reduced rotation matrix associated with the strain (local to global)
$\mathbf{R}_\sigma$	Reduced rotation matrix associated with the stress (local to global)
$\mathbf{T}$	Cohesive crack rotation matrix

$\mathbf{T}_{rebar}$	Reinforcement bar rotation matrix
V_{fib}	Fiber volume fraction

Lower Case Greek Symbols

α	Crack or rebar orientation angle
$\hat{\alpha}$	Nonlocal weight (Gaussian weight function)
α_{gp}	Gauss-weight of an integration point
$\hat{\alpha}_{gp}$	Nonlocal weight of a Gauss integration point
$\alpha_{\triangle,gp}$	Gauss-weight of an integration point in a triangular, natural domain
$\alpha_{\rightarrowtail,gp}$	Gauss-weight of an integration point on a natural line segment $[-1,1]$
β	Shear retention factor / Hardening coefficient
$\widetilde{\gamma}$	Engineering shear strain in the local coord. sys. associated with a crack
γ_{xy}	Engineering shear strain component
δW_{coh}	Virtual work term accounting for a cohesive interface
δW_{rebar}	Virtual work term accounting for a reinforcement bar
$\delta\underline{\mathbf{d}}_e$	Virtual nodal displacement variation vector
$\delta\underline{\mathbf{u}}$	Virtual displacement variation vector
$\delta\underline{\mathbf{u}}^+$	Virtual displacement variation vector of the right crack face
$\delta\underline{\mathbf{u}}^-$	Virtual displacement variation vector of the left crack face
$\delta\underline{\mathbf{w}}$	Virtual separation vector variation
$\delta\underline{\epsilon}$	Virtual strain variation vector
$\delta\underline{\epsilon}_{rebar}$	Virtual strain variation vector in an embedded reinforcement bar
$\delta\underline{\widetilde{\sigma}}_{cr}$	Cracking-stress iteration increment vector (in crack coord. sys.)
$\delta\underline{\widetilde{\sigma}}^n_{cr}$	Cracking-stress iteration increment vector at step n (in crack coord. sys.)
$\widetilde{\epsilon}$	Strain in the local coordinate system associated with a crack
ϵ_I	First principal strain
ϵ_{II}	Second principal strain
$\widetilde{\epsilon}_{cr}$	Mode I cracking-strain component (in crack coord. sys.)
ϵ_{loc}	Localization strain (principal strain at which a crack localizes)
ϵ_{pc}	Post-cracking strain (maximum cracking-strain before softening)
$\widetilde{\epsilon}_{rebar}$	Strain in an embedded rebar (in rebar coord. sys.)
$\widetilde{\epsilon}^{eq}_{rebar}$	Strain in a rebar at the last global equilibrium (in rebar coord. sys.)
ϵ_u	Cracking-strain at which a crack become stress free
ϵ_x	Engineering strain component in x-direction
ϵ_y	Engineering strain component in y-direction
ϵ_η	Strain component in η-direction (2^{nd} local crack direction)
ϵ_ξ	Strain component in ξ-direction (1^{st} local crack direction)
$\underline{\epsilon}$	Strain vector (engineering notation)
$\underline{\widetilde{\epsilon}}$	Strain vector in the local coordinate system associated with a crack

$\underline{\hat{\epsilon}}$	Nonlocal strain vector at the crack tip
$\underline{\epsilon}_{co}$	Strain vector in the bulk material (continuum)
$\underline{\epsilon}_{co}^{eq}$	Continuum strain vector at the last global equilibrium state
$\underline{\epsilon}_{cr}$	Cracking-strain vector (equivalent strain contribution of a set of cracks)
$\underline{\widetilde{\epsilon}}_{cr}$	Cracking-strain vector (in crack coord. sys.)
$\underline{\epsilon}_{cr}^{eq}$	Cracking-strain vector at the last global equilibrium state
$\underline{\widetilde{\epsilon}}_{cr}^{eq}$	Cracking-strain vector at the last global equilibrium (in crack coord. sys.)
$\underline{\epsilon}_{gp}$	Strain vector at a Gauss-point location
$\underline{\epsilon}_{rebar}$	Strain vector in the embedded reinforcement bar
$\underline{\epsilon}_{tot}$	Total strain vector
$\underline{\widetilde{\epsilon}}_{tot}$	Total strain vector in the local coordinate system associated with a crack
$\underline{\epsilon}_{tot}^{eq}$	Total strain vector at the last global equilibrium state
η	Second coordinate in a crack or rebar coordinate system (Cartesian)
θ	Angle in the polar coordinate system associated with a crack
ν	Poisson's ratio
ξ	First coordinate in a crack or rebar coordinate system (Cartesian)
$\widetilde{\sigma}$	Stress in the local coordinate system associated with a crack
σ_I	First principal stress
σ_{II}	Second principal stress
σ_{cc}	First-cracking stress (crack initiation stress)
$\widetilde{\sigma}_{cr}$	Mode I cracking stress component (in crack coord. sys.)
σ_{pc}	Post-cracking stress (maximum cracking-stress before softening)
$\widetilde{\sigma}_{rebar}$	Stress in an embedded reinforcement bar (in rebar coord. sys.)
$\widetilde{\sigma}_{rebar}^{eq}$	Rebar stress at the last global equilibrium (in rebar coord. sys.)
σ_η	Cohesive crack normal stress (in crack coord. sys.)
σ_ξ	Cohesive crack shear stress (in crack coord. sys.)
$\underline{\sigma}$	Stress vector (engineering notation)
$\underline{\widetilde{\sigma}}$	Stress vector in the local coordinate system associated with a crack
$\underline{\sigma}_{coh}$	Cohesive stress vector of a localized crack
$\underline{\widetilde{\sigma}}_{coh}$	Cohesive stress vector of a localized crack (in crack coord. sys.)
$\underline{\widetilde{\sigma}}_{coh}^{eq}$	Cohesive stress vector at the last global equilibrium (in crack coord. sys.)
$\underline{\sigma}_{co}$	Stress vector acting on the bulk material (continuum)
$\underline{\widetilde{\sigma}}_{co}$	Stress vector acting on the bulk material (in crack coord. sys.)
$\underline{\sigma}_{co}^{eq}$	Stress vector acting on the bulk material at the last global equilibrium
$\underline{\sigma}_{cr}$	Stress vector acting on a set of multiple cracks
$\underline{\widetilde{\sigma}}_{cr}$	Stress vector acting on a set of multiple cracks (in crack coord. sys.)
$\underline{\widetilde{\sigma}}_{cr}^{eq}$	Cracking-stress vector at the last global equilibrium (in crack coord. sys.)
$\underline{\sigma}_{rebar}$	Stress vector in an embedded reinforcement bar
$\underline{\sigma}_{tot}$	Total stress vector

$\underline{\sigma}_{tot}^{eq}$	Total stress vector at the last global equilibrium state
τ_{pure}	Shear stress in a state of pure shear
$\widetilde{\tau}$	Shear stress in the local coordinate system associated with a crack
$\phi()$	Compliance function (material compliance law)
$\phi_{co}()$	Compliance function for the bulk material (continuum)
$\phi_{co}^{lin}()$	Linearized compliance function for the bulk material (continuum)
$\phi_{cr}()$	Compliance function for a set of multiple cracks
$\phi_{cr}^{lin}()$	Linearized compliance function for a set of multiple cracks
$\phi_{cr,\eta}()$	Compliance function for the 2$^{\text{nd}}$ crack set
$\phi_{cr,\xi}()$	Compliance function for the 1$^{\text{st}}$ crack set
φ_i	Partition of Unity function associated with node i
$\hat{\varphi}_i$	Partition of Unity function for the enrichment associated with node i
$\chi()$	Constitutive function (material law)
$\chi_{coh}()$	Cohesive crack constitutive function
$\chi_{rebar}()$	Reinforcement bar constitutive function
∂	Partial differential operator

Upper Case Greek Symbols

Γ_e	Domain of the crack face in an element
Γ_e^+	Domain of the right crack face in an element
Γ_e^-	Domain of the left crack face in an element
$d\Gamma_e$	Finite Element domain differential for the crack face
$d\Gamma_e^+$	Finite Element domain differential for the positive crack face
$d\Gamma_e^-$	Finite Element domain differential for the negative crack face
$\Delta\alpha_\epsilon$	Deviation angle from the direction of principal strain
$\Delta\alpha_\sigma$	Deviation angle from the direction of principal stress
$\Delta\widetilde{\gamma}_{\xi,\eta}$	Shear strain increment (in crack coord. sys.)
$\Delta\widetilde{\epsilon}_{rebar}$	Strain increment in an embedded reinforcement bar (in rebar coord. sys.)
$\Delta\widetilde{\epsilon}_\eta$	Strain increment in direction of η (in crack coord. sys.)
$\Delta\widetilde{\epsilon}_\xi$	Strain increment in direction of ξ (in crack coord. sys.)
$\Delta\widetilde{\sigma}_{cr,\eta}$	Stress increment in direction of the 2$^{\text{nd}}$ crack set (in crack coord. sys.)
$\Delta\widetilde{\sigma}_{cr,\xi}$	Stress increment in direction of the 1$^{\text{st}}$ crack set (in crack coord. sys.)
$\Delta\widetilde{\sigma}_{rebar}$	Stress increment in an embedded reinforcement bar (in rebar coord. sys.)
$\Delta\widetilde{\sigma}_\eta$	Stress increment in direction of η (in crack coord. sys.)
$\Delta\widetilde{\sigma}_\xi$	Stress increment in direction of ξ (in crack coord. sys.)
$\Delta\widetilde{\tau}_{\xi,\eta}$	Shear stress increment (in crack coord. sys.)
$\Delta\Psi$	Magnitude of the "jump" in a discontinuous global enrichment function
$\Delta\underline{\mathbf{f}}$	Vector of surface force increments
$\Delta\underline{\mathbf{F}}_e$	Element force vector increments (equivalent nodal force increments)
$\Delta\underline{\mathbf{P}}_e$	Vector of external element nodal force increments

$\Delta\underline{\mathbf{u}}$	Displacement vector increment
$\Delta\underline{\mathbf{w}}$	Separation vector increment
$\Delta\underline{\widetilde{\mathbf{w}}}$	Separation vector increment (in crack coord. sys.)
$\Delta\underline{\epsilon}$	Strain vector increment
$\Delta\underline{\widetilde{\epsilon}}$	Strain increment vector in the local coord. sys. associated with a crack
$\Delta\underline{\epsilon}_{co}$	Strain increment vector in the bulk material (continuum)
$\Delta\underline{\epsilon}_{cr}$	Cracking-strain increment vector (see $\underline{\epsilon}_{cr}$)
$\Delta\underline{\widetilde{\epsilon}}_{cr}$	Cracking strain increment vector (in crack coord. sys.)
$\Delta\underline{\widetilde{\epsilon}}^{eq}$	Strain increment vector due to rotation of the principal axes (crack sys.)
$\Delta\underline{\epsilon}_{rebar}$	Strain increment vector in an embedded reinforcement bar
$\Delta\underline{\epsilon}_{tot}$	Total strain increment vector
$\Delta\underline{\sigma}$	Stress increment vector
$\Delta\underline{\widetilde{\sigma}}$	Stress increment vector in the local coord. sys. associated with a crack
$\Delta\underline{\sigma}^{eq}$	Stress increment vector due to the rotation of the principal axes
$\Delta\underline{\sigma}_{coh}$	Cohesive stress increment vector
$\Delta\underline{\widetilde{\sigma}}_{coh}$	Cohesive stress increment vector (in crack coord. sys.)
$\Delta\underline{\sigma}^{+}_{coh}$	Cohesive stress increment vector on the positive crack face
$\Delta\underline{\sigma}^{-}_{coh}$	Cohesive stress increment vector on the negative crack face
$\Delta\underline{\sigma}_{co}$	Stress increment vector in the bulk material (continuum)
$\Delta\underline{\widetilde{\sigma}}_{co}$	Stress increment vector in the bulk material (in crack coord. sys.)
$\Delta\underline{\widetilde{\sigma}}_{cr}$	Stress increment vector in a set of multiple cracks (in crack coord. sys.)
$\Delta\underline{\widetilde{\sigma}}^{n}_{cr}$	Cracking-stress increment vector at iteration n (in crack coord. sys.)
$\Delta\underline{\widetilde{\sigma}}^{n+1}_{cr}$	Cracking-stress increment vector at iteration n+1 (in crack coord. sys.)
Ψ	Global enrichment function
Ψ^{+}	Global enrichment function evaluated on the right face of a crack
Ψ^{-}	Global enrichment function evaluated on the left face of a crack
Ψ_j	Global enrichment function number j
Ω	Computational domain
$\Omega_{\triangle}$	Domain of a subtriangle
Ω^{+}	Domain to the right of a discontinuity (positive domain)
Ω^{-}	Domain to the left of a discontinuity (negative domain)
Ω_e	Domain of a Finite Element
Ω^{+}_e	Domain of a Finite Element to the right of a discontinuity
Ω^{-}_e	Domain of a Finite Element to the left of a discontinuity
Ω_{enr}	Enriched domain
Ω_{pu}	Domain of a Partition of Unity
$\Omega_{all\triangle}$	Domain encompassing all subtriangles
$d\Omega_e$	Finite Element domain differential (volume element)
$d\Omega_{\triangle}$	Domain differential for a subtriangle

$d\Omega_e^+$ Finite Element domain differential for the positive domain
$d\Omega_e^-$ Finite Element domain differential for the negative domain

Bibliography

[Aar08] B. Aarup. CRC–Applications of Fibre Reinforced High Performance Concrete. CRC Technology, Denmark, April 2008.

[AB04] P. Acker and M. Behloul. Ductal®Technology: A Large Spectrum Of Properties, A Wide Range Of Applications. In *International Symposium on UHPC*, September 2004.

[ACI73] ACI Committee 544. State-of-the-Art Report on Fiber Reinforced Concrete. *ACI Journal Proceedings*, 70(11), 1973.

[AH08] Y. Abdelaziz and A. Hamouine. A survey of the extended finite element. *Computers and Structures*, 86(11–12):1141–1151, 2008.

[AKL00] B. Aarup, J. Karlsen, and G. Lindström. Fiber Reinforced High Performance Concrete for In-Situ Cast Joints. In *Proceedings from the International Symposium on High Performance Concrete*, pages 25–27, 2000.

[ALAR98] P.C. Aïtcin, M. Lachemi, R. Adeline, and P. Richard. The Sherbrooke Reactive Powder Concrete Footbridge. *Structural Engineering International*, 8(2):140–144, 1998.

[AST06] ASTM Standard C 1609/C 1609M - 05: "Standard Test Method for Flexural Performance of Fiber-Reinforced Concrete (Using Beam With Third-Point Loading)". ASTM International, 2006.

[Bac81] H.H. Bache. Densified Cement/Ultra-Fine Particle-Based Materials. In *2^{nd} International Conference on Superplasticizers in Concrete*, June 1981.

[Bac86] H.H. Bache. Shaped Article and Composite Material and Method for Producing Same, May 1986. US Patent 4,588,443.

[Bac88] H.H. Bache. The New Strong Cements: Their Use in Structures. *Physics in Technology*, 19:43–50, 1988.

[Bac90] H.H. Bache. Compact Reinforced Composite, December 1990. US Patent 4,979,992.

[Bac95] H.H. Bache. Concrete and Concrete Technology in a Broad Perspective. In *Nordic Symposium on Modern Design of Concrete Structures, Aalborg University, Denmark*, May 1995.

[Bar62] G.I. Barenblatt. The Mathematical Theory of Equilibrium Cracks in Brittle Fracture. *Advances in Applied Mechanics*, 7:55–129, 1962.

[Bat96] K.J. Bathe. *Finite Element Procedures*. Prentice-Hall, Upper Saddle River, New Jersey, 1996.

[Baž83] Z.P. Bažant. Comment on Orthotropic Models for Concrete and Geomaterials. *Journal of Engineering Mechanics*, 109(3):849–865, 1983.

[BB99] T. Belytschko and T. Black. Elastic Crack Growth in Finite Elements with Minimal Remeshing. *International Journal for Numerical Methods in Engineering*, 45(5):601–620, 1999.

[BBA02] V. Bindiganavile, N. Banthia, and B. Aarup. Impact Response of Ultra-High-Strength Fiber-Reinforced Cement Composite. *ACI Materials Journal*, 99(6), 2002.

[BCXZ03] T. Belytschko, H. Chen, J. Xu, and G. Zi. Dynamic crack propagation based on loss of hyperbolicity and a new discontinuous enrichment. *International Journal for Numerical Methods in Engineering*, 58:1873–1905, 2003.

[BDT06] D. Buzzini, A. Dazio, and M. Trüb. *Quasi-static Cyclic Tests on Three Hybrid Fibre Concrete Structural Walls*. vdf Hochschulverlag AG, 2006.

[BFE88] T. Belytschko, J. Fish, and B.E. Engelmann. A Finite Element with Embedded Localization Zones. *Computer Methods in Applied Mechanics and Engineering*, 70(1):59–89, 1988.

[BG04] N. Banthia and R. Gupta. Hybrid fiber reinforced concrete (HyFRC): fiber synergy in high strength matrices. *Materials and Structures*, 37(10):707–716, 2004.

[Bil04] S.L. Billington. Damage-tolerant cement-based materials for performance-based earthquake engineering design: Research needs. In V.C. Li, editor, *5^{th} International Symposium on Fracture Mechanics of Concrete and Concrete Structures FRAMCOS-5*, pages 53–60, Vail, Colorado, 2004.

[Bil09] S.L. Billington. Nonlinear and Sequentially Linear Analysis of Tensile Strain Hardening Cement-based Composite Beams in Flexure. In *Computational Modeling Workshop on Concrete, Masonry and Fiber-reinforced Composites*, pages 7–10, Delft, the Netherlands, 2009.

[BL05] S. Bordas and A. Legay. X-FEM Mini-Course. Course notes EPFL school of continuing education, Lausanne, Switzerland, December 2005.

[BLG94] T. Belytschko, Y.Y. Lu, and L. Gu. Element-Free Galerkin Methods. *International Journal for Numerical Methods in Engineering*, 37(2):229–256, 1994.

[BM97] I. Babuška and J.M. Melenk. The Partition of Unity Method. *International Journal for Numerical Methods in Engineering*, 40(4):727–758, 1997.

[BMUP01] T. Belytschko, N. Moës, S. Usui, and C. Parimi. Arbitrary discontinuities in finite elements. *International Journal for Numerical Methods in Engineering*, 50:993–1013, 2001.

[BO83] Z.P. Bažant and B.H. Oh. Crack band theory for fracture of concrete. *Materials and Structures*, 16(3):155–177, 1983.

[BOS95] L.R. Betterman, C. Ouyang, and S.P. Shah. Fiber-Matrix Interaction in Microfiber-Reinforced Mortar. *Advanced Cement Based Materials*, 2(2):53–61, 1995.

[BS92] P.N. Balaguru and S.P. Shah. *Fiber-reinforced cement composites*. McGraw-Hill, 1992.

[BvZ07] W.P. Boshoff and G.P.A.G van Zijl. A computational model for strain-hardening fibre-reinforced cement-based composites. *Journal of the South African Institution of Civil Engineering*, 49(2):24–31, 2007.

[BY04] S.L. Billington and J.K. Yoon. Cyclic Response of Unbonded Posttensioned Precast Columns with Ductile Fiber-Reinforced Concrete. *Journal of Bridge Engineering*, 9(4):353–363, July 2004.

[BZMB04] É. Budyn, G. Zi, N. Moës, and T. Belytschko. A method for multiple crack growth in brittle materials without remeshing. *International Journal for Numerical Methods in Engineering*, 61(10):1741–1770, 2004.

[CEB90] CEB-FIP Model Code. Comité Euro-International du Béton, 1990.

[CMF95] M. Cheyrezy, V. Maret, and L. Frouin. Microstructural Analysis of RPC (Reactive Powder Concrete). *Cement and Concrete Research*, 25(7):1491–1500, 1995.

[CMP07] C. Comi, S. Mariani, and U. Perego. An extended FE strategy for transition from continuum damage to mode I cohesive crack propagation. *International Journal for Numerical and Analytical Methods in Geomechanics*, 31(2):213–238, 2007.

[CNPM09] S.H. Chao, A.E. Naaman, and G.J. Parra-Montesinos. Bond Behavior of Reinforcing Bars in Tensile Strain-Hardening Fiber-Reinforced Cement Composites. *ACI Structural Journal*, 106(6):897–906, 2009.

[CPM10a] M.Y. Cheng and G.J. Parra-Montesinos. Evaluation of Steel Fiber Reinforcement for Punching Shear Resistance in Slab-Column Connections – Part I: Monotonically Increased Load. *ACI Structural Journal*, 107(1), 2010.

[CPM10b] M.Y. Cheng and G.J. Parra-Montesinos. Evaluation of Steel Fiber Reinforcement for Punching Shear Resistance in Slab-Column Connections – Part II: Lateral Displacement Reversals. *ACI Structural Journal*, 107(01), 2010.

[CPMW04] B.A. Canbolat, G.J. Parra-Montesinos, and J.K. Wight. Behavior of Precast High-Performance Fiber Reinforced Cement Composite Coupling Beams Under Large Displacement Reversals. In *Proceedings of the 13th world conference on earthquake engineering*, Vancouver, B.C., Canada, 2004.

[CPMW05] B.A. Canbolat, G.J. Parra-Montesinos, and J.K. Wight. Experimental Study on Seismic Behavior of High-Performance Fiber-Reinforced Cement Composite Coupling Beams. *ACI Structural Journal*, 102(1):159–166, 2005.

[CRC] www.crc-tech.com.

[Cri81] M.A. Crisfield. A Fast Incremental/Iterative Solution Procedure that Handles "Snap-Through". *Computers & Structures*, 13(1–3):55–62, 1981.

[Cri97] M.A. Crisfield. *Non-linear Finite Element Analysis of Solids and Structures*, volume 1. John Wiley & Sons, Chichester, 1997.

[CRSQ03] G. Chanvillard, S. Rigaud, and F. St Quentin. Complete Characterisation of Tensile Properties of Ductal®UHPFRC According to the French Recommendations. In *4th International RILEM Workshop on High Performance Fiber Reinforced Cement Composites (HPFRCC4)*, pages 21–34. RILEM, June 2003.

[CTC87] T.Y. Chang, H. Taniguchi, and W.F. Chen. Nonlinear Finite Element Analysis of Reinforced Concrete Panels. *Journal of Structural Engineering*, 113(1):122–140, January 1987.

[CW88] M.A. Crisfield and J. Wills. Solution Strategies and Softening Materials. *Computer Methods in Applied Mechanics and Engineering*, 66(3):267–289, 1988.

[CWB03] J. Chessa, H. Wang, and T. Belytschko. On the construction of blending elements for local partition of unity enriched finite elements. *International Journal for Numerical Methods in Engineering*, 57(7):1015–1038, 2003.

[dB02] R. de Borst. Fracture in quasi-brittle materials: a review of continuum damage-based approaches. *Engineering Fracture Mechanics*, 69(2):95–112, 2002.

[dBRN06] R. de Borst, J.J.C. Remmers, and A. Needleman. Mesh-independent discrete numerical representations of cohesive-zone models. *Engineering Fracture Mechanics*, 73(2):160–177, 2006.

[DBT08] A. Dazio, D. Buzzini, and M. Trüb. Nonlinear cyclic Behaviour of Hybrid Fibre Concrete structural walls. *Engineering Structures*, 30(11):3141–3150, 2008.

[DHB03] E. Denarié, K. Habel, and E. Brühwiler. Structural behavior of hybrid elements with Advanced Cementitious Materials (HPFRCC). In A.E. Naaman and H.W. Reinhardt, editors, *4^{th} International RILEM Workshop on High Performance Fiber Reinforced Cement Composites (HPFRCC4)*, pages 277–300. RILEM, June 2003.

[DMB00] J. Dolbow, N. Moës, and T. Belytschko. Discontinuous enrichment in finite elements with a partition of unity method. *Finite Elements in Analysis and Design*, 36(3–4):235–260, 2000.

[DMB01] J. Dolbow, N. Moës, and T. Belytschko. An extended finite element method for modeling crack growth with frictional contact. *Computer Methods in Applied Mechanics and Engineering*, 190(51–52):6825–6846, 2001.

[DMD+00] C. Daux, N. Moës, J. Dolbow, N. Sukumar, and T. Belytschko. Arbitrary branched and intersecting cracks with the extended finite element method. *International Journal for Numerical Methods in Engineering*, 48:1741–1760, 2000.

[Dol99] J. Dolbow. *An Extended Finite Element Method with Discontinuous Enrichment for Applied Mechanics*. PhD thesis, Northwestern University, 1999.

[DPMW10] H.H. Dinh, G.J. Parra-Montesinos, and J.K. Wight. Shear Behavior of Steel Fiber-Reinforced Concrete Beams without Stirrup Reinforcement. *ACI Structural Journal*, 107(9):597–606, 2010.

[DRB96] J. Dugat, N. Roux, and G. Bernier. Mechanical properties of reactive powder concretes. *Materials and Structures*, 29(4):233–240, May 1996.

[Dug60] D.S. Dugdale. Yielding of Steel Sheets Containing Slits. *Journal of Mechanics and Physics of Solids*, 8(2):100–108, May 1960.

[EGC06] T. Elguedj, A. Gravouil, and A. Combescure. Appropriate extended functions for X-FEM simulation of plastic fracture mechanics. *Computer Methods in Applied Mechanics and Engineering*, 195(7–8):501–515, 2006.

[EH89] A.E. Elwi and T.M. Hrudey. Finite Element Model for Curved Embedded Reinforcement. *Journal of Engineering Mechanics*, 115(4):740–754, April 1989.

[FL02a] G. Fischer and V.C. Li. Effect of Matrix Ductility on Deformation Behavior of Steel-Reinforced ECC Flexural Members under Reversed Cyclic Loading Conditions. *ACI Structural Journal*, 99(6), 2002.

[FL02b] G. Fischer and V.C. Li. Influence of Matrix Ductility on Tension-Stiffening Behavior of Steel Reinforced Engineered Cementitious Composites (ECC). *ACI Structural Journal*, 99:104–111, 2002.

[FL03a] G. Fischer and V.C. Li. Deformation Behavior of Fiber-Reinforced Polymer Reinforced Engineered Cementitious Composite (ECC) Flexural Members Under Reversed Cyclic Loading Conditions. *ACI Structural Journal*, 100(1):25–35, 2003.

[FL03b] G. Fischer and V.C. Li. Intrinsic Response Control of Moment-Resisting Frames Utilizing Advanced Composite Materials and Structural Elements. *ACI Structural Journal*, 100(2):166–176, 2003.

[FL03c] G. Fischer and V.C. Li. Ultra-Ductile Engineered Cementitious Composites for Seismic Resistant Structures. In *FIB Symposium*, Athens, Greece, May 2003.

[FL07] G. Fischer and V.C. Li. Effect of fiber reinforcement on the response of structural members. *Engineering Fracture Mechanics*, 74(1–2):258–272, 2007.

[FMNS99] H. Fukuyama, Y. Matsuzaki, K. Nakano, and Y. Sato. Structural Performance of Beam Elements with PVA-ECC. In *3rd International RILEM Workshop on High Performance Fiber Reinforced Cement Composites (HPFRCC3)*, pages 531–541. RILEM, 1999.

[FPH95] A. Filiatrault, S. Pineau, and J. Houde. Seismic Behavior of Steel-Fiber Reinforced Concrete Interior Beam–Column Joints. *ACI Structural Journal*, 92(5), 1995.

[FSL+00] H. Fukuyama, Y. Sato, V.C. Li, Y. Matsuzaki, and H. Mihashi. Ductile Engineered Cementitious Composite Elements for Seismic Structural Applications. In *12th World Conference of Earthquake Engineering*, volume 1672, 2000.

[Fuh04] A. Fuhlrott. Grundlagen der Extended Finite Element Method (X-FEM). Bauhaus-Universität, Weimar, March 2004. (in German).

[GMB02] A. Gravouil, N. Moës, and T. Belytschko. Non-planar 3D crack growth by the extended finite element and level sets – Part II: Level set update. *International Journal for Numerical Methods in Engineering*, 53(11):2569–2586, 2002.

[HC06] U. Häußler-Combe. Dreiaxiale Stoffgesetze für Beton – Grundlagen, Formulierungen, Anwendungen. *Beton und Stahlbetonbau*, 101(3):175–186, 2006. (in German).

[HET09] C.C. Hung and S. El-Tawil. Cyclic Model for High Performance Fiber Reinforced Cementitious Composite Structures. In *ATC & SEI Conference on Improving Seismic Performance of Existing Buildings and Other Structures*. ASCE, 2009.

[HFB03] T.S. Han, P.H. Feenstra, and S.L. Billington. Simulation of Highly Ductile Fiber-Reinforced Cement-Based Composite Components Under Cyclic Loading. *ACI Structural Journal*, 100(6):749–757, 2003.

[HHK02] M. Harajli, B. Hamad, and K. Karam. Bond-slip Response of Reinforcing Bars Embedded in Plain and Fiber Concrete. *Journal of Materials in Civil Engineering*, 14(6):503 p., 2002.

[HMP76] A. Hillerborg, M. Modéer, and P.E. Petersson. Analysis of Crack Formation and Crack Growth in Concrete by Means of Fracture Mechanics and Finite Elements. *Cement and Concrete Research*, 6(6):773–782, 1976.

[HN87] J.R. Homrich and A.E. Naaman. Stress-Strain Properties of SIFCON in Compression. *ACI Special Publication*, 105:283–304, 1987.

[Hub06] F. Huber. *Nichtlineare dreidimensionale Modellierung von Beton-und Stahlbetontragwerken*. PhD thesis, Institut für Baustatik, Universität Stuttgart, 2006. (in German).

[JB02] M. Jirásek and T. Belytschko. Computational Resolution of Strong Discontinuities. In *5^{th} World Congress on Computational Mechanics*, pages 7–12, Vienna, Austria, July 2002.

[Jir00] M. Jirásek. Numerical Modeling of Deformation and Failure of Materials. Lecture Notes, December 2000.

[Jir01] M. Jirásek. Modeling of localized damage and fracture in quasibrittle materials. *Lecture Notes in Physics*, 568:17–29, 2001.

[JP01] M. Jirásek and B. Patzák. Models for Quasibrittle Failure: Theoretical and Computational Aspects. In *European Conference on Computational Mechanics*, June 2001.

[JZ98] M. Jirásek and T. Zimmermann. Analysis of Rotating Crack Model. *Journal of Engineering Mechanics*, 124(8):842–851, 1998.

[Kab00] P. Kabele. Assessment of Structural Performance of Engineered Cementitious Composites by Computer Simulation. Habilitation Thesis, Czech Technical University in Prague, 2000.

[Kab02] P. Kabele. Equivalent continuum model of multiple cracking. *Engineering Mechanics (Association for Engineering Mechanics, Czech Republic)*, 9(1/2):75–90, 2002.

[Kab03] P. Kabele. New Developments in Analytical Modeling of Mechanical Behavior of ECC. *Journal of Advanced Concrete Technology*, 1(3):253–264, 2003.

[Kab04] P. Kabele. Linking scales in modeling of fracture in high performance fiber reinforced cementitious composites. In V.C. Li, editor, *5th International Symposium on Fracture Mechanics of Concrete and Concrete Structures FRAMCOS-5*, pages 71–80, Vail, Colorado, 2004.

[Kab06] P. Kabele. Fracture Behavior of Shear-Critical Reinforced HPFRCC Members. In *International RILEM Workshop on High Performance Fiber Reinforced Cementitious Composites (HPFRCC) in Structural Applications*, pages 383–392. RILEM, 2006.

[Kab07] P. Kabele. Multiscale framework for modeling of fracture in high performance fiber reinforced cementitious composites. *Engineering Fracture Mechanics*, 74:194–209, 2007.

[Kan98] T. Kanda. *Design of Engineered Cementitious Composites for Ductile Seismic Resistant Elements*. PhD thesis, University of Michigan, 1998.

[KB02] K. Kesner and S.L. Billington. Experimental Response of Precast Infill Panels Made with DFRCC. In *JCI International Workshop on Ductile Fiber Reinforced Cementitious Composites (DFRCC)*, pages 289–298, Takayama, Japan, 2002.

[KB03] K.E. Kesner and S.L. Billington. Experimental Response of Precast Infill Panel Connections and Panels Made with DFRCC. *Journal of Advanced Concrete Technology*, 1(3):327–333, 2003.

[KB04] K.E. Kesner and S.L. Billington. Tension, Compression, and Cyclic Testing of Engineered Cementitious Composites. Technical report, MCEER Technical Report, March 2004.

[KB05] N. Kaptijn and J. Blom. A new CRC (Compact Reinforced Composite) bridge deck. In *18th BIBM International Congress*, Amsterdam, The Netherlands, May 2005.

[KBD03] K.E. Kesner, S.L. Billington, and K.S. Douglas. Cyclic Response of Highly Ductile Fiber-Reinforced Cement-Based Composites. *ACI Materials Journal*, 100(5):381–390, 2003.

[KBL03] H.J. Kong, S.G. Bike, and V.C. Li. Constitutive rheological control to develop a self-consolidating engineered cementitious composite reinforced with hydrophilic poly(vinyl alcohol) fibers. *Cement and Concrete Composites*, 25(3):333–341, 2003.

[KEKK02] Y.K. Kwak, M.O. Eberhard, W.S. Kim, and J. Kim. Shear Strength of steel Fiber-Reinforced Concrete Beams without Stirrups. *ACI Structural Journal*, 99(4), 2002.

[KH96] P. Kabele and H. Horii. Analytical Model for Fracture Behaviors of Pseudo Strain-Hardening Cementitious Composites. *Journal of Materials, Concrete Structures and Pavements*, 532:209–220, 1996.

[KLL00] T. Kanda, Z. Lin, and V.C. Li. Tensile Stress-Strain Modeling of Pseudostrain Hardening Cementitious Composites. *Journal of Materials in Civil Engineering*, 12(2):147–156, May 2000.

[KTIH99] P. Kabele, S. Takeuchi, K. Inaba, and H. Horii. Performance of Engineered Cementitious Composites in Repair and Retrofit: Analytical Estimates. In *3rd International RILEM Workshop on High Performance Fiber Reinforced Cement Composites (HPFRCC3)*, pages 617–627, Mainz, Germany, May 1999. RILEM.

[KWL98] T. Kanda, S. Watanabe, and V.C. Li. Application of Pseudo Strain Hardening Cementitious Composites to Shear Resistant Structural Elements. In *3rd International Symposium on Fracture Mechanics of Concrete and Concrete Structures FRAMCOS-3*, pages 1477–1490, 1998.

[KX03] B.L. Karihaloo and Q.Z. Xiao. Modelling of stationary and growing cracks in FE framework without remeshing: a state-of-the-art review. *Computers and Structures*, 81(3):119–129, 2003.

[Lan84] D.R. Lankard. Properties, applications: Slurry Infiltrated Fiber Concrete (SIFCON). *Concrete International*, 6:44–47, 1984.

[Lan85] D.R. Lankard. Slurry Infiltrated Fiber Concrete (SIFCON): Properties and Applications. *Very High Strength Cement Based Materials*, 42, 1985.

[LCPN06] W-C. Liao, S-H. Chao, S-Y. Park, and A.E. Naaman. Self-Consolidating High Performance Fiber Reinforced Concrete (SCHPFRC) - Preliminary Investigation. Technical Report UMCEE 06-02, Department of Civil and Environmental Engineering, University of Michigan, December 2006.

[LF99] V.C. Li and G. Fischer. Interaction Between Steel Reinforcement and Engineered Cementitious Composites. In *3rd International RILEM Workshop on High Performance Fiber Reinforced Cement Composites (HPFRCC3)*, pages 361–370. RILEM, May 1999.

[Li93] V.C. Li. From Micromechanics to Structural Engineering – The Design of Cementitious Composites for Civil Engineering Applications. *Journal of Structural Mechanics and Earthquake Engineering*, 10(2), 1993.

[Li02a] V.C. Li. Advances in ECC research. *ACI Special Publication*, 206:373–400, 2002.

[Li02b] V.C. Li. Large Volume, High-Performance Applications of Fibers in Civil Engineering. *Journal of Applied Polymer Science*, 83(3):660–686, 2002.

[Li02c] V.C. Li. Reflections on the Research and Development of Engineered Cementitious Composites (ECC). In *JCI International Workshop on Ductile Fiber Reinforced Cementitious Composites (DFRCC)*, pages 1–21, 2002.

[Li03] V.C. Li. On Engineered Cementitious Composites (ECC). *Journal of Advanced Concrete Technology*, 1(3):215–230, 2003.

[Li08] V.C. Li. *Concrete Construction Engineering Handbook*, chapter 24. CRC Press, 2008.

[LK98] V.C. Li and T. Kanda. Engineered Cementitious Composites for Structural Applications. *Journal of Materials in Civil Engineering*, 10(2):66–69, May 1998.

[LMN+94] V.C. Li, D.K. Mishra, A.E. Naaman, J.K. Wight, J.M. LaFave, H.C. Wu, and Y. Inada. On the Shear Behavior of Engineered Cementitious Composites. *Advanced Cement Based Materials*, 1(3):142–149, 1994.

[LMW95] V.C. Li, D.K. Mishra, and H.C. Wu. Matrix design for pseudo-strain-hardening fibre reinforced cementitious composites. *Materials and Structures*, 28(10):586–595, 1995.

[LN84] D.R. Lankard and J.K. Newell. Preparation of Highly Reinforced Steel Fiber Reinforced Concrete Composites. *ACI Special Publication*, 81:286–306, 1984.

[LSPMW09] R.D. Lequesne, M. Setkit, G.J. Parra-Montesinos, and J.K. Wight. Seismic Detailing and Behavior of Coupling Beams Incorporating High-Performance Fiber Reinforced Concrete. In *Antoine E. Naaman Symposium – Four decades of progress in prestressed concrete, fiber reinforced concrete, and thin laminate composites*. American Concrete Institute, Farmington Hills, MI, 2009.

[LWW01] V.C. Li, S. Wang, and C. Wu. Tensile Strain-Hardening Behavior of Polyvinyl Alcohol Engineered Cementitious Composite (PVA-ECC). *ACI Materials Journal*, 98(6):483–492, 2001.

[Mar06] I. Marković. *High-Performance Hybrid-Fiber Concrete*. PhD thesis, Delft University of Technology, Delft, the Netherlands, 2006.

[MB96] J.M. Melenk and I. Babuška. The partition of unity finite element method: Basic theory and applications. *Computer Methods in Applied Mechanics and Engineering*, 139(1–4):289–314, 1996.

[MB02] N. Moës and T. Belytschko. Extended finite element method for cohesive crack growth. *Engineering Fracture Mechanics*, 69(7):813–833, 2002.

[MDB99] N. Moës, J. Dolbow, and T. Belytschko. A Finite Element Method for Crack Growth without Remeshing. *International Journal for Numerical Methods in Engineering*, 46(1):131–150, 1999.

[MF08] A.R. Malik and S.J. Foster. Behaviour of Reactive Powder Concrete Columns without Steel Ties. *Journal of Advanced Concrete Technology*, 6(2):377–386, June 2008.

[MGB02] N. Moës, A. Gravouil, and T. Belytschko. Non-planar 3D crack growth by the extended finite element and level sets – Part I: Mechanical model. *International Journal for Numerical Methods in Engineering*, 53(11):2549–2568, 2002.

[MKS05] J. Mergheim, E. Kuhl, and P. Steinmann. A finite element method for the computational modelling of cohesive cracks. *International Journal for Numerical Methods in Engineering*, 63(2):276–289, 2005.

[ML94] M. Maalej and V.C. Li. Flexural/Tensile-Strength Ratio in Engineered Cementitious Composites. *Journal of Materials in Civil Engineering*, 6(4):513–528, 1994.

[MM02] T. Matsumoto and H. Mihashi. JCI-DFRCC Summary Report on DFRCC Terminologies and Application Concepts. In *Proceedings of the JCI International Workshop on Ductile Fiber Reinforced Cementitious Composites–Application and Evaluation*, pages 59–66. Citeseer, 2002.

[MP73] M. Menegotto and P.E. Pinto. Method of Analysis for Cyclically Loaded Reinforced Concrete Plane Frames Including Changes in Geometry and Nonelastic Behavior of Elements Under Combined Normal Force and Bending. In *IABSE Symposium on the Resistance and Ultimate Deformability of Structures Acted on by Well Defined Repeated Loads*, pages 15–22, 1973.

[MP03] S. Mariani and U. Perego. Extended finite element method for quasi-brittle fracture. *International Journal for Numerical Methods in Engineering*, 58:103–126, 2003.

[MWvM03] I. Marković, J.C. Walraven, and J.G.M. van Mier. Development of High Performance Hybrid Fibre Concrete. In A.E. Naaman and H.W. Reinhardt, editors, *4th International RILEM Workshop on High Performance Fiber Reinforced Cement Composites (HPFRCC4)*, pages 277–300. RILEM, 2003.

[MWvM04a] I. Markovic, J.C. Walraven, and J.G.M. van Mier. Tensile behaviour of high performance hybrid fibre concrete. In V.C. Li, editor, *5th International Symposium on Fracture Mechanics of Concrete and Concrete Structures FRAMCOS-5*, pages 1113–1121, Vail, Colorado, 2004.

[MWvM04b] I. Marković, J.C. Walraven, and J.G.M. van Mier. Tensile Response of Hybrid Fibre Concrete. In M. di Prisco, R. Felicetti, and G.A. Plizzari,

editors, *6th International RILEM Symposium on Fibre-Reinforced Concretes (BEFIB 2004)*, pages 1341–1352. RILEM, 2004.

[Naa03] A.E. Naaman. Engineered Steel Fibers with Optimal Properties for Reinforcement of Cement Composites. *Journal of Advanced Concrete Technology*, 1(3):241–252, 2003.

[Naa07] A.E. Naaman. Tensile strain-hardening FRC composites: Historical evolution since the 1960. *Advances in Construction Materials*, pages 181–202, 2007.

[ND87] R. Narayanan and I.Y.S. Darwish. Use of Steel Fibers as Shear Reinforcement. *ACI Structural Journal*, 84(3):216–227, 1987.

[ND88] R. Narayanan and I.Y.S. Darwish. Fiber Concrete Deep Beams in Shear. *ACI Structural Journal*, 85(2):141–149, 1988.

[NH89] A.E. Naaman and J.R. Homrich. Tensile Stress-Strain Properties of SIFCON. *ACI Materials Journal*, 86(3), 1989.

[NKKM04] S. Nagai, T. Kaneko, T. Kanda, and M. Maruta. Structural Capacity of Reinforced PVA-ECC Dampers. In M. di Prisco, R. Felicetti, and G.A. Plizzari, editors, *6th International RILEM Symposium on Fibre-Reinforced Concretes (BEFIB 2004)*, pages 1227–1263. RILEM, 2004.

[NR95] A.E. Naaman and H.W. Reinhardt, editors. *High Performance Fiber Reinforced Cement Composites 2*, chapter 3, pages 232–269. E. & F.N. Spon, 1995.

[NR06] A.E. Naaman and H.W. Reinhardt. Proposed classification of HPFRC composites based on their tensile response. *Materials and Structures*, 39(5):547–555, 2006.

[NRF92] A.E. Naaman, H.W. Reinhardt, and C. Fritz. Reinforced Concrete Beams with a SIFCON Matrix. *ACI Structural Journal*, 89(1), 1992.

[NS79] A.E. Naaman and S.P. Shah. Fracture and Multiple Cracking of Cementitious Composites. In S.W. Freiman, editor, *Fracture Mechanics applied to Brittle Materials. Proceedings of the 11th National Symposium on Fracture Mechanics*, pages 183–201. ASTM, 1979.

[NWA87] A.E. Naaman, J.K. Wight, and H. Abdou. SIFCON Connections for Seismic Resistant Frames. *Concrete International*, 9(11):34–39, November 1987.

[ODA00] G. Orange, J. Dugat, and P. Acker. DUCTAL®. New Ultra High Performance Concrete. Damage Resistance and Micromechanical Analysis. In *5th International RILEM Symposium on Fiber-Reinforced Concretes (BEFIB 2000)*, pages 781–790, 2000.

[OS88] S. Osher and J.A. Sethian. Fronts Propagating with Curvature-Dependent Speed: Algorithms Based on Hamilton-Jacobi Formulations. *Journal of Computational Physics*, 79(1):12–49, 1988.

[PJ03] B. Patzák and M. Jirásek. Process zone resolution by extended finite elements. *Engineering Fracture Mechanics*, 70(7):957–977, 2003.

[PJ04] B. Patzák and M. Jirásek. Adaptive Resolution of Localized Damage in Quasi-brittle Materials. *Journal of Engineering Mechanics*, 130(6):720–732, June 2004.

[PM05] G.J. Parra-Montesinos. High-Performance Fiber-Reinforced Cement Composites: An Alternative for Seismic Design of Structures. *ACI Structural Journal*, 102(5):668–675, 2005.

[PMAG07] G. Pons, M. Mouret, M. Alcantara, and J.L. Granju. Mechanical behaviour of self-compacting concrete with hybrid fibre reinforcement. *Materials and Structures*, 40(2):201–210, 2007.

[PMC07] G.J. Parra-Montesinos and P. Chompreda. Deformation Capacity and Shear Strength of Fiber-Reinforced Cement Composite Flexural Members Subjected to Displacement Reversals. *Journal of Structural Engineering*, 133(3):421–431, 2007.

[PMCJ06] G.J. Parra-Montesinos, B.A. Canbolat, and G.R. Jeyaraman. Relaxation of Confinement Reinforcement Requirements in Structural Walls Through the Use of Fiber Reinforced Cement Composites. In *Proceedings of the 8th national conference on earthquake engineering*, San Francisco, California, 2006.

[PMK04] G.J. Parra-Montesinos and K.Y. Kim. Seismic Behavior of Low-Rise Walls Constructed With Strain-Hardening Fiber Reinforced Cement Composites. In *Proceedings of the 13th world conference on earthquake engineering*, Vancouver, B.C., Canada, 2004.

[PMPC05] G.J. Parra-Montesinos, S.W. Peterfreund, and S.H. Chao. Highly Damage-Tolerant Beam–Column Joints Through Use of High-Performance Fiber-Reinforced Cement Composites. *ACI Structural Journal*, 102(3):487–495, 2005.

[PMW00] G. Parra-Montesinos and J.K. Wight. Seismic Response of Exterior RC Column-to-Steel Beam Connections. *Journal of Structural Engineering*, 126(10):1113–1121, October 2000.

[PZ76] D.V. Phillips and O.C. Zienkiewicz. Finite Element Nonlinear Analysis of Concrete Structures. In *Proc. Inst. Civ. Engr.*, volume 61, pages 59–88, 1976.

[RAM87] P. Rossi, P. Acker, and Y. Malier. Effect of steel fibres at two different stages: the material and the structure. *Materials and Structures*, 20(6):436–439, 1987.

[RAPF05] P. Rossi, A. Arca, E. Parant, and P. Fakhri. Bending and compressive behaviors of a new cement composite. *Cement and Concrete Research*, 35(1):27–33, 2005.

[RAS96] N. Roux, C. Andrade, and M.A. Sanjuan. Experimental Study of Durability of Reactive Powder Concretes. *Journal of Materials in Civil Engineering*, 8(1), February 1996.

[RB03] M. Rouse and S.L. Billington. Behavior of Bridge Piers with Ductile Fiber Reinforced Hinge Regions and Vertical, Unbonded Post-Tensioning. In *FIB Symposium on Concrete Structures in Seismic Regions*, Athens, Greece, 2003.

[RBCS80] V. Ramakrishnan, T. Brandshaug, W.V. Coyle, and E.K. Schrader. A Comparative Evaluation of Concrete Reinforced with Straight Steel Fibers and Deformed End Fibers Glued Together into Bundles. *ACI Journal*, 77(3):135–143, 1980.

[RC95] P. Richard and M. Cheyrezy. Composition of Reactive Powder Concretes. *Cement and Concrete Research*, 25(7):1501–1511, 1995.

[RCD86] H.W. Reinhardt, H.A.W. Cornelissen, and Hordijk D.A. Tensile Tests and Failure Analysis of Concrete. *Journal of Structural Engineering*, 112:2462–2477, 1986.

[RdB89] J.G. Rots and R. de Borst. Analysis of Concrete Fracture in "Direct" Tension. *International Journal of Solids and Structures*, 25(12):1381–1394, 1989.

[RdBN03] J.J.C. Remmers, R. de Borst, and A. Needleman. A cohesive segments method for the simulation of crack growth. *Computational Mechanics*, 31(1):69–77, 2003.

[Rik72] E. Riks. The Application of Newton's Method to the Problem of Elastic Stability. *Journal of Applied Mechanics,*, 39:1060–1065, 1972.

[Rik79] E. Riks. An Incremental Approach to the Solution of Snapping and Buckling Problems. *International Journal of Solids and Structures*, 15(7):529–551, 1979.

[Rik84] E. Riks. Some Computational Aspects of the Stability Analysis of Nonlinear Structures. *Computer Methods in Applied Mechanics and Engineering*, 47(3):219–259, 1984.

[RM64] J.P. Romualdi and J.A. Mandel. Tensile Strength of Concrete Affected by Uniformly Distributed and Closely Spaced Short Lengths of Wire Reinforcement. *ACI Journal Proceedings*, 61(6):657–671, 1964.

[RO43] W. Ramberg and W.R. Osgood. Description of Stress-Strain Curves by Three Parameters. *National Advisory Committee For Aeronautics, Technical note*, 902, 1943.

[Ros97] P. Rossi. High Performance Multimodal Fiber Reinforced Cement Composites (HPMFRCC): The LCPC Experience. *ACI Materials Journal*, 94(6), 1997.

[Ros00] P. Rossi. Ultra-High Performance Fibre Reinforced Concretes (UHPFRC): An overview. In *5^{th} RILEM Symposium on Fibre-Reinforced Concretes (FRC)*, page 87 p., Lyon, France, September 2000. RILEM Publications.

[Ros05] P. Rossi. Development of new cement composite materials for construction. *Proceedings of the Institution of Mechanical Engineers, Part L: Journal of Materials: Design and Applications*, 219(1):67–74, 2005.

[Rot86] J.G. Rots. Strain-Softening Analysis of Concrete Fracture Specimens. *Fracture Toughness and Fracture Energy of Concrete*, pages 137–148, 1986.

[Rot88] J.G. Rots. *Computational Modeling of Concrete Fracture*. PhD thesis, Delft University of Technology, Delft, the Netherlands, 1988.

[Rot91] J.G. Rots. Smeared and discrete representations of localized fracture. *International Journal of Fracture*, 51(1):45–59, 1991.

[RP08] P. Rossi and E. Parant. Damage mechanisms analysis of a multi-scale fibre reinforced cement-based composite subjected to impact and fatigue loading conditions. *Cement and Concrete Research*, 38(3):413–421, 2008.

[SBC00] T. Strouboulis, I. Babuška, and K. Copps. The design and analysis of the Generalized Finite Element Method. *Computer Methods in Applied Mechanics and Engineering*, 181:43–69, 2000.

[SBCB03] F.L. Stazi, E. Budyn, J. Chessa, and T. Belytschko. An extended finite element method with higher-order elements for curved cracks. *Computational Mechanics*, 31(1):38–48, 2003.

[SCB01] T. Strouboulis, K. Copps, and I. Babuška. The generalized finite element method. *Computer Methods in Applied Mechanics and Engineering*, 190(32–33):4081–4193, 2001.

[SCM03] N. Sukumar, D.L. Chopp, and B. Moran. Extended finite element method and fast marching method for three-dimensional fatigue crack propagation. *Engineering Fracture Mechanics*, 70(1):29–48, 2003.

[SCMB01a] M. Stolarska, D.L. Chopp, N. Moës, and T. Belytschko. Modelling crack growth by level sets in the extended finite element method. *International Journal for Numerical Methods in Engineering*, 51(8):943–960, 2001.

[SCMB01b] N. Sukumar, D.L. Chopp, N. Moës, and T. Belytschko. Modeling holes and inclusions by level sets in the extended finite-element method. *Computer Methods in Applied Mechanics and Engineering*, 190(46–47):6183–6200, 2001.

[Set99] J.A. Sethian. *Level Set Methods and Fast Marching Methods.* Cambridge University Press, 1999.

[Sha86] A.K. Sharma. Shear Strength of Steel Fiber Reinforced Concrete Beams. *ACI Journal Proceedings*, 83(4):624–628, 1986.

[Sim03] A. Simone. *Continuous-Discontinuous Modelling of Failure.* PhD thesis, Delft University of Technology, Delft, the Netherlands, 2003.

[Sir09] K. Sirijaroonchai. *A Macro-scale Plasticity Model for High Performance Fiber Reinforced Cement Composites.* PhD thesis, University of Michigan, 2009.

[SL04] H. Stang and V.C. Li. Classification of Fibre Reinforced Cementitious Materials for Structural Applications. In *6^{th} RILEM Symposium on Fibre-Reinforced Concretes (FRC)*, pages 197–218, Varenna, Italy, September 2004. RILEM Publications.

[SLH+09] M. Sahmaran, M. Lachemi, K.M.A. Hossain, R. Ranade, and V.C. Li. Influence of Aggregate Type and Size on Ductility and Mechanical Properties of Engineered Cementitious Composites. *ACI Materials Journal*, 106(3), 2009.

[SMK05] M.N. Soutsos, S.G. Millard, and K. Karaiskos. Mix Design, Mechanical Properties, and Impact Resistance of Reactive Powder Concrete (RPC). In *International RILEM Workshop on High Performance Fiber Reinforced Cementitious Composites (HPFRCC) in Structural Applications*, pages 549–560. RILEM Publications, May 2005.

[SMMB00] N. Sukumar, N. Moës, B. Moran, and T. Belytschko. Extended finite element method for three-dimensional crack modelling. *International Journal for Numerical Methods in Engineering*, 48:1549–1570, 2000.

[SP03] N. Sukumar and J.H. Prévost. Modeling quasi-static crack growth with the extended finite element method Part I: Computer implementation. *International Journal of Solids and Structures*, 40(26):7513–7537, 2003.

[SS04] A. Simone and L.J. Sluys. The use of displacement discontinuities in a rate-dependent medium. *Computer Methods in Applied Mechanics and Engineering*, 193(27–29):3015–3033, 2004.

[Stä08] P. Stähli. *Ultra-Fluid, Oriented Hybrid-Fibre-Concrete*. PhD thesis, ETH Zürich, 2008.

[SvM04] P. Stähli and J.G.M. van Mier. Rheological Properties and Fracture Processes of HFC. In M. di Prisco, R. Felicetti, and G.A. Plizzari, editors, *6th International RILEM Symposium on Fibre-Reinforced Concretes (BEFIB 2004)*, pages 299–308. RILEM, 2004.

[SvM05] P. Stähli and J.G.M. van Mier. Fracture Testing of Hybrid-Fibre Concrete. In *11th International Conference on Fracture (ICF-11)*, Torino, Italy, 2005.

[SvM07] P. Stähli and J.G.M. van Mier. Manufacturing, fibre anisotropy and fracture of hybrid fibre concrete. *Engineering Fracture Mechanics*, 74:223–242, 2007.

[SvMW00] Y. Sato, J.G.M. van Mier, and J.C. Walraven. Mechanical Characteristics of Multi-Modal Fiber Reinforced Cement Based Composites. In P. Rossi and G. Chanvillard, editors, *5th International RILEM Symposium on Fibre-Reinforced Concretes (BEFIB 2000)*, pages 791–800. RILEM, 2000.

[SWS03] A. Simone, G.N. Wells, and L.J. Sluys. From continuous to discontinuous failure in a gradient-enhanced continuum damage model. *Computer Methods in Applied Mechanics and Engineering*, 192(41–42):4581–4607, 2003.

[VBB03] G. Ventura, E. Budyn, and T. Belytschko. Vector level sets for description of propagating cracks in finite elements. *International Journal for Numerical Methods in Engineering*, 58(10):1571–1592, 2003.

[VFG06] Y.L. Voo, S.J. Foster, and R.I. Gilbert. Shear Strength of Fiber Reinforced Reactive Powder Concrete Prestressed Girders without Stirrups. *Journal of Advanced Concrete Technology*, 4(1):123–132, February 2006.

[vM03] J.G.M. van Mier. High Performance Fibre Reinforced Concrete. In *9th Betontagung (HOLCIM)*, pages 15–29, 2003.

[VM04a] D. Vachon and B. Massicotte. Seismic Retrofitting of Rectangular Bridge Piers with FRC Jackets. In *6th RILEM Symposium on Fibre-Reinforced Concretes (FRC)*, pages 1247–1256, Varenna, Italy, September 2004. RILEM Publications.

[vM04b] J.G.M. van Mier. Cementitious Composites with High Tensile Strength and Ductility Through Hybrid Fibres. In M. di Prisco, R. Felicetti, and G.A. Plizzari, editors, *6th International RILEM Symposium on Fibre-Reinforced Concretes (BEFIB 2004)*, pages 219–236. RILEM, 2004.

[VMT96] J.G.M. Van Mier and G. Timmers. Method and Apparatus for Manufacturing a Reinforced Constructional Element, and such Constructional Element, 1996. Patent WO 9634727.

[vR06] G. van Rossum. www.python.org (version 2.5), 2006.

[vZ07] G.P.A.G. van Zijl. Improved mechanical performance: Shear behaviour of strain-hardening cement-based composites (SHCC). *Cement and Concrete Research*, 37(8):1241–1247, 2007.

[WdBS01] G.N. Wells, R. de Borst, and L.J. Sluys. An Enhanced Finite Element Method for Analysing Failure in Elasto-Plastic Solids. In *International Conference on the Trends in Computational Structural Mechanics*, pages 397–406, 2001.

[Wel01] G.N. Wells. *Discontinuous modelling of strain localisation and failure*. PhD thesis, Delft University of Technology, July 2001.

[Wem71] G.A. Wempner. Discrete Approximations Related to Nonlinear Theories of Solids. *International Journal of Solids and Structures*, 7(11):1581–1599, 1971.

[WS01] G.N. Wells and L.J. Sluys. A new method for modelling cohesive cracks using finite elements. *International Journal for Numerical Methods in Engineering*, 50(12):2667–2682, 2001.

[WSdB02] G.N. Wells, L.J. Sluys, and R. de Borst. Simulating the propagation of displacement discontinuities in a regularized strain-softening medium. *International Journal for Numerical Methods in Engineering*, 53(5):1235–1256, 2002.

[XSDK04] J. Xiao, H. Schneider, C. Dönnecke, and G. König. Wedge splitting test on fracture behaviour of ultra high strength concrete. *Construction and Building Materials*, 18(6):359–365, 2004.

[YWYL08] E.H. Yang, S. Wang, Y. Yang, and V.C. Li. Fiber-Bridging Constitutive Law of Engineered Cementitious Composites. *Journal of Advanced Concrete Technology*, 6(1):181–193, 2008.

[ZB03] G. Zi and T. Belytschko. New crack-tip elements for XFEM and applications to cohesive cracks. *International Journal for Numerical Methods in Engineering*, 57(15):2221–2240, 2003.

[ZHMO99] C. Zhao, B.E. Hobbs, H.B. Mühlhaus, and A. Ord. A Consistent Point-Searching Algorithm for Solution Interpolation in Unstructured Meshes Consisting of 4-Node Bilinear Quadrilateral Elements. *International Journal for Numerical Methods in Engineering*, 45(10):1509–1526, 1999.